



AFRL-RQ-WP-TR-2014-0062

POWER AND THERMAL TECHNOLOGIES FOR AIR AND SPACE – SCIENTIFIC RESEARCH PROGRAM

Delivery Order 0020: Advanced Conductors and Thermal Science

Evan L. Thomas, Qihong N. Zhang, Helen Shen, Serhiy N. Leontsev, John P. Murphy, Jack L. Burke, Lyle Brunke, and Charles Ebbing

University of Dayton Research Institute

MARCH 2014

Final Report

Approved for public release; distribution unlimited.

See additional restrictions described on inside pages

STINFO COPY

**AIR FORCE RESEARCH LABORATORY
AEROSPACE SYSTEMS DIRECTORATE
WRIGHT-PATTERSON AIR FORCE BASE, OH 45433-7542
AIR FORCE MATERIEL COMMAND
UNITED STATES AIR FORCE**

NOTICE AND SIGNATURE PAGE

Using Government drawings, specifications, or other data included in this document for any purpose other than Government procurement does not in any way obligate the U.S. Government. The fact that the Government formulated or supplied the drawings, specifications, or other data does not license the holder or any other person or corporation; or convey any rights or permission to manufacture, use, or sell any patented invention that may relate to them.

This report was cleared for public release by the USAF 88th Air Base Wing (88 ABW) Public Affairs Office (PAO) and is available to the general public, including foreign nationals.

Copies may be obtained from the Defense Technical Information Center (DTIC)
(<http://www.dtic.mil>).

AFRL-RQ-WP-TR-2014-0062 HAS BEEN REVIEWED AND IS APPROVED FOR
PUBLICATION IN ACCORDANCE WITH ASSIGNED DISTRIBUTION STATEMENT.

*//Signature//

GREGORY L. RHOADS
Program Manager
Mechanical and Thermal Systems Branch
Power and Control Division

//Signature//

THOMAS L. REITZ, Technical Advisor
Mechanical and Thermal Systems Branch
Power and Control Division
Aerospace Systems Directorate

//Signature//

JOHN G. NAIRUS, Chief Engineer
Power and Control Division
Aerospace Systems Directorate

This report is published in the interest of scientific and technical information exchange, and its publication does not constitute the Government's approval or disapproval of its ideas or findings.

*Disseminated copies will show “//Signature//” stamped or typed above the signature blocks.

REPORT DOCUMENTATION PAGE				Form Approved OMB No. 0704-0188	
<p>The public reporting burden for this collection of information is estimated to average 1 hour per response, including the time for reviewing instructions, searching existing data sources, gathering and maintaining the data needed, and completing and reviewing the collection of information. Send comments regarding this burden estimate or any other aspect of this collection of information, including suggestions for reducing this burden, to Department of Defense, Washington Headquarters Services, Directorate for Information Operations and Reports (0704-0188), 1215 Jefferson Davis Highway, Suite 1204, Arlington, VA 22202-4302. Respondents should be aware that notwithstanding any other provision of law, no person shall be subject to any penalty for failing to comply with a collection of information if it does not display a currently valid OMB control number. PLEASE DO NOT RETURN YOUR FORM TO THE ABOVE ADDRESS.</p>					
1. REPORT DATE (DD-MM-YY) March 2014		2. REPORT TYPE Final		3. DATES COVERED (From - To) 02 April 2010 – 28 February 2014	
4. TITLE AND SUBTITLE POWER AND THERMAL TECHNOLOGIES FOR AIR AND SPACE – SCIENTIFIC RESEARCH PROGRAM Delivery Order 0020: Advanced Conductors and Thermal Science				5a. CONTRACT NUMBER FA8650-04-D-2403-0020	
				5b. GRANT NUMBER	
				5c. PROGRAM ELEMENT NUMBER 62203F	
6. AUTHOR(S) Evan L. Thomas, Qiuhong N. Zhang, Helen Shen, Serhiy N. Leontsev, John P. Murphy, Jack L. Burke, Lyle Brunke, and Charles Ebbing				5d. PROJECT NUMBER 3145	
				5e. TASK NUMBER N/A	
				5f. WORK UNIT NUMBER Q0LQ	
7. PERFORMING ORGANIZATION NAME(S) AND ADDRESS(ES) University of Dayton Research Institute Energy Technology and Materials Division 300 College Park Dayton, OH 45469-0170				8. PERFORMING ORGANIZATION REPORT NUMBER UDR-TR-2010-0063	
9. SPONSORING/MONITORING AGENCY NAME(S) AND ADDRESS(ES) Air Force Research Laboratory Aerospace Systems Directorate Wright-Patterson Air Force Base, OH 45433-7542 Air Force Materiel Command United States Air Force				10. SPONSORING/MONITORING AGENCY ACRONYM(S) AFRL/RQQM	
				11. SPONSORING/MONITORING AGENCY REPORT NUMBER(S) AFRL-RQ-WP-TR-2014-0062	
12. DISTRIBUTION/AVAILABILITY STATEMENT Approved for public release; distribution unlimited.					
13. SUPPLEMENTARY NOTES PA Case Number: 88ABW-2014-1811; Clearance Date: 18 April 2014.					
14. ABSTRACT The objectives of this delivery order were to 1) Develop new superconductors and improve state-of-the-art yttrium barium copper oxide (YBCO)-coated conductors for optimal performance as a coated conductor in high-temperature superconductor (HTS) generators and magnets by flux pinning mechanisms but also thicker films 2) Conduct research to advance thermoelectric materials by exploring novel chemistries and processes, including combinatorial methodologies, for tailoring thermoelectric responses 3) Investigate carbon nanotube growth on various materials, especially metals and diamonds, with emphasis on thermal and electrical properties for power generation and cooling applications 4) Conduct magnetic material research by investigating high energy product permanent magnets, improvements in soft magnet mechanical strength, and modeling magnetic structures such as rotors and stators, and also provide additional support for thermal physics issues on an as-needed basis 5) Develop improved measurement techniques and standards of measurement as needed for properties of HTSs, thermoelectrics, carbon nanotubes, and thermal and magnetic materials.					
15. SUBJECT TERMS superconductivity, thermoelectrics, magnetic materials, carbon nanotubes					
16. SECURITY CLASSIFICATION OF:			17. LIMITATION OF ABSTRACT: SAR	18. NUMBER OF PAGES 220	19a. NAME OF RESPONSIBLE PERSON (Monitor) Gregory L. Rhoads 19b. TELEPHONE NUMBER (Include Area Code) N/A
a. REPORT Unclassified	b. ABSTRACT Unclassified	c. THIS PAGE Unclassified			

TABLE OF CONTENTS

<u>Section</u>	<u>Page</u>
1. Microstructure and Critical Current Density of $\text{YBa}_2\text{Cu}_3\text{O}_{7-x} + \text{BaSnO}_3$ Thick Films Grown with Pre-mixed Pulsed Laser Ablation Target.....	1
1.1 Introduction.....	1
1.2 Experimental.....	1
1.3 Results and Discussion	2
1.4 Summary	5
1.5 References.....	5
2. Experimental Setup for Calorimetric Measurements.....	7
2.1 Introduction.....	7
2.2 Experimental.....	8
2.2.1 Apparatus	8
2.2.2 Measurement Procedures	9
2.2.3 Operation.....	10
2.3 Self-field Summary.....	12
2.4 Integrating the Isothermal Cryogenic Calorimeter into the SAM Machine to Expose the Samples to a Substantial Alternating Magnetic Field.....	12
2.4.1 Introduction.....	12
2.4.2 Experimental	13
2.4.3 Summary	20
2.5 Description of Bulmer Circle Terahertz Emitter.....	21
2.6 References.....	22
3. Growth of High-quality Carbon Nanotubes on Free-standing Diamond Substrates.....	24
3.1 Introduction.....	24
3.2 Experimental.....	24
3.3 Results and Discussion	25
3.4 Summary	30
3.5 References.....	30
4. Growth and Characterization of Carbon Nanotubes for Thermal Management and Electrical Applications.....	32
4.1 Research Objectives.....	32
4.2 Approaches	33
4.2.1 Growth of CNT Layer with Controllable Structure/Morphology on Metal Foil Substrates	33
4.2.2 Growth and Functionalization of Nanotubes on Porous Cellular (Foam) Carbon Materials.....	33
4.2.3 Characterization of the Structure and Thermal and Mechanical Properties of CNT Based Nano-composites	34
4.3 Growth of CNT on Copper and Metal Foil.....	34
4.3.1 Introduction.....	34
4.3.2 Experimental	36
4.3.3 Results and Discussion.....	38
4.3.4 Summary	51
4.4 Growth of CNTs on Carbon Foam.....	52
4.4.1 Introduction.....	52
4.4.2 Experimental	53
4.4.3 Results and Discussion.....	54
4.4.4 Summary	60
4.5 References.....	60

5.	Enhancement of Thermoelectric Materials to Provide Solutions for Power and Thermal Challenges.	62
5.1	Research Objectives.....	62
5.2	Introduction.....	62
5.2.1	Thermoelectric Materials Challenges	64
5.2.2	Nano-structure Engineering to Achieve High TE Performance.....	64
5.2.3	Advantages of Complex Oxide Materials for TE Applications and Current Technology Barriers for Applications	64
5.3	Results and Discussion	65
5.3.1	Approach 1: Microstructural Self-assembly to Fabricate Nano-dimensional Materials with Nano-inclusions.....	65
5.3.2	Approach 2: High-throughput Combinatorial Approach for Rapid Identification of Novel TE Materials	83
5.3.3	Thick and Thin Film TE Device Fabricated from Oxide-based Materials: Design and Synthesis of Textured Ca-Co-O Films	96
5.4	Summary	104
5.5	References.....	104
6.	Magnetically Hard/Soft Nanocomposite Magnets	107
6.1	Introduction.....	107
6.2	Experimental	107
6.3	Results and Discussion	108
6.3.1	Isotropic Sm-Co/Fe Nanocomposite Bulks.....	108
6.3.2	Anisotropic Sm-Co/Fe Nanocomposite Particles.....	127
6.4	Summary	145
6.5	References.....	146
7.	Development of Hard-Soft Bulk Nanocomposite Magnets	147
7.1	Introduction.....	147
7.2	Experimental	147
7.3	Results and Discussion	149
7.3.1	SmCo ₅ Nano-flake Powder Preparation via Wet Milling Route using Oleic Acid Surfactant.....	149
7.3.2	SmCo ₅ Nano-flake Powder Preparation via Wet Milling Route using Valeric Acid Surfactant.....	151
7.3.3	Surfactant Removal Study for Nanoscale SmCo ₅ Powder Prepared by High Energy Ball Milling	153
7.3.4	UDRI Gas Gun Target Fixture Design.....	159
7.3.5	UDRI Gas Gun Powder Compaction Experiment	162
7.3.6	SmCo ₅ Powder Microwave Sintering	168
7.3.7	Computer Simulation of Magnetic Inductor Components using FEM	170
7.3.8	Magnetic Field Comparison for Solid and Wound Coil in Maxwell 3D	171
7.3.9	Eddy Current Power Loss Test in Maxwell 3D: Single Bar Model.....	174
7.3.10	Eddy Current Single Bar Model in Maxwell 3D: Mesh Size Optimization.....	176
7.3.11	Ferrite Core Single Grain Eddy Loss Calculation in Maxwell 3D	181
7.3.12	Summary of Inductor Eddy-current Loss Simulation using ANSYS Maxwell 3D Software.....	184
7.3.13	Finite Element Modeling in Maxwell 3D: Permanent Magnet Plate Design.....	187
7.4	Other Ongoing Magnetic Material Research Projects	200
7.4.1	SmCo ₅ -FeNi Hard-Soft Composite Magnet.....	200
7.5	References.....	201
	List of Acronyms, Abbreviations and Symbols	203

List of Figures

<u>Figure</u>	<u>Page</u>
Figure 1.1. T_c in YBCO + 20 mol% BSO Films with varying thickness	2
Figure 1.2. J_c values for varying thickness YBCO + 20 mol% BSO films at 77 K and $H // c$	3
Figure 1.3. VSM J_c data for selected YBCO + 20 mol% BSO film thicknesses compared with 300 nm YBCO at 77 K and $H // c$	3
Figure 1.4. θ -2 θ x-ray scans of YBCO + 20 mol% BSO of varying thickness	3
Figure 1.5. SEM photomicrograph showing surface microstructure of (a) 260 nm sample and (b) 2.8 μ m sample	4
Figure 1.6. SEM photomicrograph showing uniform BSO distribution in YBCO on (a) 260 nm sample and (b) 2.8 μ m sample	4
Figure 1.7. Cross sectional TEM image showing through-thickness, uniform BSO nanocolumns in (a) 780 nm film and (b) 2.8 μ m film	5
Figure 2.1. Schematic diagram of Self Field Calorimeter	8
Figure 2.2. Horizontal Cross Section of Self-Field Calorimeter	9
Figure 2.3. Graph depicting calibration offset derived from a resistance heater with known power input	11
Figure 2.4. Total calorimetric loss measurement compared to electrical field partial loss measurement	12
Figure 2.5. Horizontal Cross Section	14
Figure 2.6. Vertical Cross Section	15
Figure 2.7. Cross section of sample holder	16
Figure 2.8. Calculated magnetic field strength and field line vectors	16
Figure 2.9. Measured vertical field profiles	17
Figure 2.10. Mapping coil, 10mm diameter	17
Figure 2.11. Field map around the rotor	18
Figure 2.12. Magnetic field frequency sensing coil	18
Figure 2.13. N_2 flow change and measured magnetic field frequency as drive motor speed is reduced in 100RPM steps	20
Figure 3.1. SEM micrograph of as-grown diamond sample showing facets of crystals	26
Figure 3.2. X-ray diffraction pattern taken from a diamond substrate	26
Figure 3.3. Raman spectra taken from a diamond substrate as compared to CNT/diamond samples	26
Figure 3.4. Partial coverage of CNTs grown on diamond substrate partially covered with Ni-W-Fe deposited by using initial sputtering conditions	27
Figure 3.5. Complete coverage of CNTs on diamond substrates with Ni catalysts deposited by sputtering using optimized conditions	28
Figure 3.6. Higher magnification photomicrograph showing the CNTs grown on a diamond substrate	28
Figure 3.7. Cross-sectional SEM image showing CNTs grown on a diamond substrate	29
Figure 3.8. (a) TEM micrograph showing 20 nm diameter CNTs grown on diamond substrates, and (b) high resolution TEM micrograph showing 16 walls of highly crystalline MWCNT	29
Figure 4.1. Scheme of assembling VA-CNT/Cu as a TIM	36
Figure 4.2. Schematic of substrate preparation procedure	36
Figure 4.3. Scheme of processing for CNTs grown on Cu substrate by THCVD (<i>Not to scale</i>)	37
Figure 4.4. Floating catalyst thermal CVD (FCCVD) system	37
Figure 4.5. Scheme of processing for CNTs grown on Cu substrate by FCCVD (<i>Not to scale</i>)	38

Figure 4.6. CNTs grown on Fe/Cu substrate with varying thickness of Fe layer and temperature. A=700°C; B=750°C; C=800°C	39
Figure 4.7. CNTs grown on Ni/Cu substrate with varying thickness of Ni layer and temperature. A=700°C; B=750°C; C=800°C	39
Figure 4.8. CNTs growth on Fe/ Al ₂ O ₃ /Cu substrate	40
Figure 4.9. CNTs growth on Fe/Al ₂ O ₃ /Cu substrate with varying thickness of Al ₂ O ₃ , Left to right = 5 nm, 10 nm, 15 nm 30 nm.....	41
Figure 4.10. CNTs growth on pure Cu (<i>left</i>) and Al ₂ O ₃ /Cu (<i>right</i>) substrate by FCCVD.....	42
Figure 4.11. CNTs growth on Al ₂ O ₃ /Cu substrate with varying thickness of Al ₂ O ₃ (Left to right = 5 nm, 10 nm, 15 nm, 30 nm)	42
Figure 4.12. Alignment of CNTs grown on Cu substrate with varying thickness of Al ₂ O ₃ layer Growth Time: A = 20 min; B = 40 min	42
Figure 4.13. Diameter of CNT grown on Cu substrate with varying thickness of Al ₂ O ₃ layer	42
Figure 4.14. SEM images: areal density and alignment (insets) of CNTs	44
Figure 4.15. Raman spectroscopy of the CNT/Cu THCVD (<i>left</i>) and FCCVD (<i>right</i>)	45
Figure 4.16. ASTM D5470 TIM Testing System	45
Figure 4.17. The effect of CNT layer on CNTs/Cu impedance Test condition: Pressure=80psi (without grease)	46
Figure 4.18. The effect of various interface materials on thermal impedance Test condition: Pressure=80psi	47
Figure 4.19. The image of CNTs-Cu interface after peel-off test	48
Figure 4.20. Scheme of interfacial force testing by a pull-off tester (<i>not to scale</i>).....	48
Figure 4.21. The effect of Al ₂ O ₃ thickness on interfacial adhesion	49
Figure 4.22. Schematic of sample electrical property testing	50
Figure 4.23. Example of a power device packaging layer	53
Figure 4.24. SEM image of as-received carbon foam from Ultramet, Inc.....	55
Figure 4.25. SEM image of CNTs grown on as-received carbon foam surface	55
Figure 4.26. SEM image of nitric acid treated CF before (<i>top</i>) and after CNTs growth (<i>bottom</i>).....	56
Figure 4.27. SEM image of oxygen treated CF before (<i>top</i>) and after CNTs growth (<i>bottom</i>).....	56
Figure 4.28. SEM image of HDS treated CF after CNTs growth	57
Figure 4.29. SEM image of Al ₂ O ₃ (various thicknesses) coated CF after CNTs growth	57
Figure 4.30. Netzsch LFA instrument schematic.....	58
Figure 4.31. Thermal conductivity of CNT/Carbon foam substrate	59
Figure 4.32. SEM image of Nickel Electroplating CNT/CF.....	59
Figure 4.33. SEM image of Nickel Electroless plating CNT/CF.....	59
Figure 5.1. Power output dependence on both <i>ZT</i> and temperature differential (ΔT)	63
Figure 5.2. BSO nano-columns (highlighted by arrows) in YBCO matrix grown by PLD.....	66
Figure 5.3. Schematic illustration of the crystal structure of Ca ₃ Co ₄ O ₉ (CCO-349). Adapted from [18]. .	67
Figure 5.4. XRD patterns for a (a) CCO-349 target and (b) 200 nm CCO-349 thin film on Si (100).....	69
Figure 5.5. Temperature-dependent electrical resistivity (ρ) measured using the van der Pauw method for a film grown on Si (100). <i>Inset</i> : Thermopower behavior measured at room temperature using our custom thermopower screening tool. For comparison, the thermopower was measured for samples grown on Si (100) and LaAlO ₃ (100).	70
Figure 5.6. TEM and HR-TEM images of the three Ca-Co-O phases in the “pure” CCO-349 film	71

Figure 5.7 STEM Z-contrast images, EDS spectrum and EDS elemental mapping of CCO-349 (Spec 1) and CCO-225 (Spec 2)	72
Figure 5.8. <i>Left panel:</i> Temperature-dependent electrical resistivity (ρ) measured using the van der Pauw method for films grown on Si (100). <i>Inset:</i> Blow-up of high temperature data. <i>Right panel:</i> Thermopower behavior measured at room temperature using the PFSI. For comparison, the thermopower was measured for samples grown on Si (100) and LaAlO ₃ (100).....	74
Figure 5.9. BZO-doped CCO film with increased mis-orientation and low angle grain boundaries perpendicular to the film plane.....	74
Figure 5.10. BZO-doped film with CCO-349 as the main phase and nano-lamellar CCO-225 (B) and CCO-unknown (C) phases.....	75
Figure 5.11. Zr is uniformly distributed throughout the film, while Ba segregates into Ca-deficient phases and GBs	76
Figure 5.12. (<i>Top</i>) Ca-Co-O film with interface reaction layer highlighted. (<i>Bottom</i>) Element distribution at interface reaction layer (<i>note scale</i>).....	77
Figure 5.13. HR-TEM micrograph revealing the epitaxial growth of the Ca-Co-O phases on the interface reaction layer of crystalline Co ₃ O ₄ (<i>note scale</i>)	77
Figure 5.14. Nano-layer Co ₃ O ₄ alternating with Ca-Co-O deposited using a sector target PLD approach	79
Figure 5.15. (<i>top</i>) Temperature-dependent Power Factor data for Ca-Co-O-based thin film samples deposited on insulating substrates. A reference curve (Wang, et al.) is shown for comparison. (<i>bottom</i>) 4-probe configuration for thin film measurement using the PPMS/TTO.	80
Figure 5.16. zT data for bulk Ca-Co-O-based samples measured using the PPMS/TTO (<i>note temperature range</i>). The reference curves were calculated from reported data by Kenfau, et al.....	81
Figure 5.17. Fully-automated combinatorial deposition process. (a) Depiction of PLD chamber components with laser entry and rotating targets and substrate. (b) Alternating targets are ablated to deposit single layers at various substrate positions. (c) After reaching desired thickness based on material calibrations, a ternary diagram is achieved where the three materials overlap.	85
Figure 5.18. (a) Custom Power Factor Screening Instrument (PFSI) and components. (b) Close-up of sample stage and measurement head. (c) Detail of measurement head components. (d) PFSI wiring diagram	89
Figure 5.19. Custom LabVIEW-generated interface for (a) designing the wafer scan and (b) physical property data collection.....	92
Figure 5.20. (a) Post-deposition processing via standard photolithography techniques (negative resist NR71-3000) followed by 1 μ m Au sputtering and removal of Au with RR41 photoresist remover to generate discrete composition units in the calibration sample. The same process was followed for the (b) Ni standard sample and the (c) Ca ₃ (Fe,Ni,Co) ₄ O ₉ combinatorial ternary sample (with HCl etchant).	93
Figure 5.21. (a) Ca ₃ Co ₄ O ₉ (Material 1) – CaMnO ₃ (Material 3) Binary combinatorial sample. (b) Electrical property data collected using PFSI. (c) XRD data from diagonal line scan from Material 1 to Material 2.....	94
Figure 5.22. Electrical property data collected using PFSI of a 500 μ m Nickel standard film (non-patterned).....	95

Figure 5.23. Overlay of electrical resistivity short scan data from PFSI on optical image of a 3 in dia. $\text{Ca}_3(\text{Ti, Fe, Co})_4\text{O}_9$ sample grown on Si/SiO ₂ . Experiment parameters are shown below the figure.	96
Figure 5.24. Textured Ca-Co-O film grown on 2 μm thick layer of amorphous SiO ₂	97
Figure 5.25. In-plane thin film TE device schematic (<i>not to scale</i>).....	98
Figure 5.26. Ordinary design for TE power generation module	98
Figure 5.27. Custom-built water-cooled power generation measurement system. (<i>Right panel</i>) Close-up of thin film unicouple mounting schematic	100
Figure 5.28. (<i>Left panel</i>) Voltage output and (<i>Right panel</i>) Power generated from a thin film unicouple as a function of the temperature gradient across the sample	100
Figure 5.29. Temperature dependence of electrical resistivity ρ (<i>top</i>) and Seebeck coefficient S (<i>bottom</i>) for CMO bulk sample.....	102
Figure 5.30. Morphology of clean GBs and nano-domains within the grains of an as-sintered CMO sample.....	102
Figure 6.1. DM-HP process for preparation of bulk Sm-Co/Fe nanocomposite magnets	108
Figure 6.2. XRD patterns for SmCo_5 + 10 wt % Fe starting mixture, after 4 hours of milling, and the bulk sample after subsequent compaction at 600 °C	109
Figure 6.3. SEM/BSE images of bulk Sm-Co/Fe compacted at 600 °C using 8 h milled powder with a starting composition of SmCo_5 + 10 wt % Fe	110
Figure 6.4. SEM/BSE image and corresponding EDS patterns for the bulk Sm-Co/Fe sample compacted at 600 °C using 8 hour milled powder.....	110
Figure 6.5. Demagnetization curves of bulk SmCo_5 and Sm-Co/Fe samples compacted at 600 °C using 12 h milled powder for starting composition of SmCo_5 and SmCo_5 + 10 wt % Fe	111
Figure 6.6. Demagnetization curves of bulk Sm-Co/Fe magnets as a function of milling time	112
Figure 6.7. Magnetic properties of bulk Sm-Co/Fe magnets vs. milling time.....	113
Figure 6.8. XRD patterns for bulk Sm-Co/Fe magnets with different milling time	114
Figure 6.9. SEM images of bulk Sm-Co/Fe samples pressed at 600 °C using the powders milled 4, 8, 12, and 16 hours with starting composition of SmCo_5 + 10 wt% Fe (Magnification 5000 x)	115
Figure 6.10. Demagnetization curves of Sm-Co/Fe bulk magnets pressed at 600 °C using the powders milled 4h with BPR of 5, 10, and 20	116
Figure 6.11. Demagnetization curves of Sm-Co/Fe bulk magnets pressed at 600 °C using the powders milled 8h with BPR of 5, 10, and 20	117
Figure 6.12. Magnetic properties vs. BPR for Sm-Co/Fe bulk samples pressed at 600 °C with milling of 8 h.....	117
Figure 6.13. Demagnetization curves of Sm-Co/Fe bulk samples pressed at different temperatures.....	119
Figure 6.14. Magnetic properties of Sm-Co/Fe bulk samples vs. HP temperature.....	119
Figure 6.15. SEM/BSE images of Sm-Co/Fe bulk samples with pressing temperature of: A -HP600°C; B - HP700°C; C - HP800°C	120
Figure 6.16. XRD patterns of the starting powder and Sm-Co/Fe bulk samples pressed at different temperatures: A – HP 600 °C; B – HP 700 °C; C – HP 800 °C	121
Figure 6.17. Demagnetization curves of bulk Sm-Co/Fe magnets with different amount of Fe(M) addition and maximum energy product vs. Fe content (inset).....	123
Figure 6.18. Demagnetization curves of Sm-Co/Fe bulk magnets with starting composition of SmCo_5 + 15 wt% soft phase (Fe(M), Fe(N), and FeCo).....	124

Figure 6.19. SEM/BSE images for Sm-Co/Fe bulk samples with different soft phase precursor	125
Figure 6.20. XRD patterns for as-milled powders (a) and bulk samples (b) with starting composition of SmCo ₅ + 15 wt% Fe(M), Fe(N), and FeCo	126
Figure 6.21. XRD patterns for as-milled powders with the starting composition of SmCo ₅ + 15 wt% FeCo after milling for 2, 4, 6, and 8 hours	127
Figure 6.22. DM-WM process	128
Figure 6.23. Demagnetization curves of bulk Sm-Co/Fe magnets pressed at different temperature	129
Figure 6.24. SEM images of the milled Sm-Co/Fe particles prepared with precursors pressed at 650 °C (a) and 850 °C (b)	130
Figure 6.25. Demagnetization curves of Sm-Co/Fe particle epoxy samples tested along both parallel () and perpendicular (⊥) to the magnetic aligning direction	131
Figure 6.26. Degree of anisotropy vs. pressing temperature	132
Figure 6.27. Demagnetization curves of bulk Sm-Co/Fe magnets pressed at 650 °C with different heat treatment (HT) temperature for 10 min	133
Figure 6.28. Demagnetization curves of Sm-Co/Fe particles epoxy samples tested along both parallel () and perpendicular (⊥) to the magnetic aligning direction	134
Figure 6.29. Degree of anisotropy vs. heat treatment temperature	135
Figure 6.30. XRD patterns for Sm-Co/Fe composite bulk precursors prepared by DM-HP process: (a) Pressed at 650-940 °C; (b) Pressed at 650 °C and HT at 650-950 °C	137
Figure 6.31. BM-WM process	138
Figure 6.32. SEM images of Sm-Co + Fe mixed powders milled 4h by BM	139
Figure 6.33. Demagnetization curves of Sm-Co and composite Sm-Co/Fe bulk magnets pressed at 650 °C	139
Figure 6.34. SEM images for Sm-Co/Fe composite particles milled 1h with different BPR by WM	142
Figure 6.35. Demagnetization curves of Sm-Co/Fe powder epoxy samples tested along parallel () and perpendicular (⊥) to the magnetic aligning direction. (Insert is demagnetization curves of SmCo ₅ particles prepared with same process)	143
Figure 6.36. Dependence of degree of anisotropy of Sm-Co/Fe particles on BPR	143
Figure 6.37. XRD patterns of SmCo ₅ as-cast random powders, Sm-Co/Fe as-milled random powders and aligned powders prepared with BPR of 0.8 (⊥ aligned – X-ray detected surface perpendicular to magnetic aligning direction; aligned – X-ray detected surface parallel to the magnetic aligning direction during epoxy sample preparation)	144
Figure 6.38. XRD patterns of Sm-Co/Fe powder (milled with different BPR) epoxy samples (X-ray detected surface perpendicular to magnetic aligning direction in epoxy sample preparation)	145
Figure 7.1. Powder flake thickness dependence on the milling time	149
Figure 7.2. SEM micrographs for SmCo ₅ powder batches	150
Figure 7.3. (Left) DSC data. (Right) Powder flake thickness dependence on the milling time	151
Figure 7.4. SEM micrographs for SmCo ₅ powder batches before and after DSC tests	152
Figure 7.5. SEM images of as-milled (a), heat treated in argon at 200 °C (b) and 400 °C (c) SmCo ₅ nano- flake powders prepared by HEBM using valeric acid; clusters of SmCo ₅ nano-flakes (d) ...	155
Figure 7.6. DSC heat flow (heating) for as-milled and heat treated SmCo ₅ nano-powders	155
Figure 7.7. Powder x-ray diffraction data for as-milled and heat treated SmCo ₅ nano-scale powder	156

Figure 7.8. Demagnetization data for epoxy bound as-milled and heat treated SmCo ₅ nano-powders. Inset table: coercivity H_{ci} , remanence B_r and maximum energy product $(BH)_{max}$	157
Figure 7.9. Schematic of three-capsule palte-impact recovery fixture used with the 80 mm diameter gas-gun for dynamic densification experiments	159
Figure 7.10. Target fixture and flyer plate assembly used in the shock consolidation. Note that only the sample, and not the containment assembly, is impacted	160
Figure 7.11. Preliminary target fixture design	161
Figure 7.12. Powder capsule modifications	161
Figure 7.13. SmCo ₅ experimental powder preparation flowchart.....	163
Figure 7.14. Target fixture drawing	164
Figure 7.15. Machined and welded target fixture with and without the target assembly mounted	164
Figure 7.16. (a) Projectile schematic. (b) Set of 4 machined projectiles	165
Figure 7.17. SEM imaging of shock compacted SmCo ₅ nano-scale powder	167
Figure 7.18. Magnetic hysteresis data for shock compacted and as-milled SmCo ₅ nano-scale powder ..	167
Figure 7.19. SEM images of CIP compacted as-milled SmCo ₅ nanopowder (a) and microwave sintered sample at 600°C for 15 min (b)	168
Figure 7.20. Magnetic hysteresis data for as-milled and microwave sintered nano-scale SmCo ₅	169
Figure 7.21. XRD data for SmCo ₅ samples sintered at 300, 450 and 600 °C	170
Figure 7.22. Model of a laminated inductor core in Maxwell 3D software.....	171
Figure 7.23. Simulated and theoretical Eddy loss frequency dependence	171
Figure 7.24. Rendering of a tape core inductor 3D model and a 2D cross-section used for accurate Eddy-current calculation	184
Figure 7.25. Simulated Eddy-current distribution and corresponding mesh discretization in a single lamination layer	185
Figure 7.26. Eddy power loss as a function of frequency, logarithmic scale.....	185
Figure 7.27. Eddy power loss as a function of frequency, linear scale.....	186
Figure 7.28. Eddy power loss as a function of lamination thickness	186
Figure 7.29. Eddy power loss as a function of material resistivity	187

List of Tables

<u>Table</u>	<u>Page</u>
Table 4-1. CNT synthesis conditions and results using FCCVD	43
Table 4-2. Impedance testing results (3 tests on each sample)	46
Table 4-3. Interface Adhesive of CNTs/Cu	47
Table 4-4. Interfacial adhesion of CNTs on Al ₂ O ₃ coated Cu substrate	49
Table 4-5. Electrical Property of CNT/Cu Measurement	50
Table 4-6. Effect of Growth method and buffer layer on CNT growth	52
Table 6-1. Magnetic properties of Sm-Co/Fe bulk samples with different milling time	112
Table 6-2. Milling ball type	116
Table 6-3. Magnetic properties of Sm-Co/Fe bulk samples pressed at different temperature.....	118
Table 6-4. Soft phase precursors.....	122

FOREWORD

The work documented in this report (UDRI report number UDR-TR-2010-0063) was performed by the University of Dayton Research Institute (UDRI) between April 2010 and February 2014, for the Aerospace Systems Directorate of the Air Force Research Laboratory, Wright-Patterson Air Force Base, Ohio. The effort was performed as Delivery Order 0020 on Contract No. FA8650-04-D-2403, Power and Thermal Technologies for Air and Space – Scientific Research Program (SRP).

Technical support and direction of this delivery order was provided by Dr. Timothy Haugan and Mr. Greg Rhoads and their staff of AFRL/RQQM (RZPG). Dr. Evan Thomas was the Delivery Order Principal Investigator and is the primary author of the report. Dr. Thomas was supported by his staff, Dr. Qihong Zhang, Dr. Serhiy Leontsev, Helen Shen, Jack Burke, John Murphy, Lyle Brunke, and Charles Ebbing.

The author would like to thank Lt. Breanna Ruter-Schoppman for providing the delivery order government administration. The author also wishes to acknowledge the assistance of Ms. Karoline Hoffman and Dr. Bang H. Tsao of the UDRI, who provided the administrative support to make this work possible. Dr. Tsao is the SRP Program Manager.

1. Microstructure and Critical Current Density of $\text{YBa}_2\text{Cu}_3\text{O}_{7-x}$ + BaSnO_3 Thick Films Grown with Pre-mixed Pulsed Laser Ablation Target

1.1 Introduction

$\text{YBa}_2\text{Cu}_3\text{O}_{7-x}$ (YBCO)-coated conductors have excellent self-field critical current density (J_c) but need improvement in applied magnetic fields like in motors, generators, and other electrical power applications [1,2]. To provide this improvement, flux pinning centers are introduced to the YBCO. Pinning in YBCO films can be provided via crystalline defects or other non-superconducting materials in nanodimensional additions. Examples of such material inclusions are Y_2BaCuO_5 , BaZrO_3 (BZO), Y_2O_3 , etc. when dispersed in a controlled manner in a sufficiently high density, to provide this enhancement [3-6]. In the case of BaSnO_3 (BSO), it has been shown to create nanocolumns in YBCO when proper processing conditions were used [7], similar to BZO. These BSO nanocolumns particularly contribute to pinning in the c-axis orientation, with J_c increasing by more than 2 orders of magnitude in high fields.

In the literature, undoped YBCO also shows rapid degradation in J_c as the thickness of the film is increased ($>1\text{ }\mu\text{m}$) [8,9]. In a previous study, thick YBCO + BSO films were grown with a sectored target approach to address this issue [10]. By only varying the time of the deposition, thick ($3\text{ }\mu\text{m}$) YBCO + BSO films were grown and found to maintain J_c in applied magnetic fields due to the presence of the nanocolumns. These nanocolumns were uniformly straight and extended throughout the thickness of the films, for thicknesses ranging from 300 nm to $3\text{ }\mu\text{m}$. The study presented here was performed to investigate if thick YBCO + BSO films with a pre-mixed target in place of a sectored target can achieve similar results. This is not clear since the supply of BSO is fairly continuous during film growth in the pre-mixed target case as opposed to an intermittent supply of BSO in the case of a YBCO/BSO sectored target.

1.2 Experimental

All the films were made by pulsed laser deposition (PLD). The PLD target used in this experiment was made using NEXANS YBCO powder and Cerac BSO powder (-325 mesh, 99%). The powders were mixed and ground together in the appropriate ratio to yield a final composition of YBCO + 20 mol% BSO. This ratio was used for its similarity to the BSO content of the previous experiment that used a YBCO + BSO sectored target. The mixed powder was pressed and then sintered for 72 hours at $850\text{ }^\circ\text{C}$ and 168 hours at $920\text{ }^\circ\text{C}$ to an approximate density of ~ 90 percent.

The film depositions were carried out in a Neocera chamber with a target to substrate working distance of $\sim 6\text{ cm}$. A Lambda Physik excimer laser ($\lambda=248\text{ nm}$) was used to ablate the target. The laser was operated at 4 Hz, 625 mJ with an energy density on the target of ~ 2 to 4 J/cm^2 . The films were deposited on single crystal (100) LaAlO_3 substrates in a 300 mTorr O_2 atmosphere at $780\text{ }^\circ\text{C}$. Samples were oxygenated during cool down at $500\text{ }^\circ\text{C}$, 600 torr O_2 for $\frac{1}{2}$ hour, and then cooled to room temperature. The thickness of the films was varied by changing only the deposition time. Final film thicknesses ranging from 250 nm to $3\text{ }\mu\text{m}$ were obtained by varying the deposition times from 20 minutes up to 4 hours.

Magnetization hysteresis loops were taken in a Quantum Design PPMS Vibrating Sample Magnetometer (VSM). The Bean model was used for calculation of magnetization J_c from the data taken from these loops. The magnetic dipole moment of the sample was also measured as temperature was varied in the VSM to obtain the critical transition temperature (T_c) of the

samples. The film thickness was measured with a KLA Tencor profiler. X-ray diffraction data was obtained on the samples using a Rigaku DMAX B. A FEI Sirion high resolution scanning electron microscope (SEM) was used to obtain electron micrographs of the samples' microstructure. A FEI Tecnai F20 analytical electron microscope with a point-to-point resolution of 0.21 nm (TEM) was used after standard sample preparation to observe the nanocolumns of BSO in the YBCO matrix.

1.3 Results and Discussion

The T_c data of YBCO + BSO samples of different thickness are shown in Figure 1. All the films for this study showed a T_c of ~ 87 K. It can be seen that the T_c does not degrade as the film thickness is increased, even up to 3 μm . This offers initial confirmation that 30 min of oxygenation is sufficient for even the thick films. A slight reduction of T_c to 87 K is consistent with the thin films of YBCO + BSO as reported earlier [11].

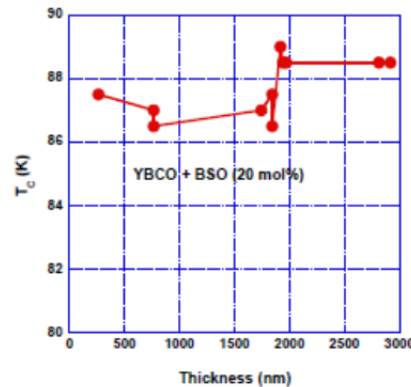


Figure 1.1. T_c in YBCO + 20 mol% BSO Films with varying thickness

A plot of the J_c of different thickness samples is shown as a function of applied magnetic fields in Figure 2. The results show that the samples continue to maintain their J_c very well even when the thickness is increased, especially at higher fields. At 8 Tesla of applied magnetic field, the J_c of a YBCO + BSO sample of 2.8 μm thickness was $1.5 \times 10^4 \text{ A/cm}^2$, which is similar to the J_c of a 260 nm thick YBCO + BSO sample. Although there is some reduction in J_c evident at very low fields, there appears to be a slight improvement at the higher fields as the thickness approaches the 1 μm range.

Figure 3 displays several magnetization J_c curves of thick YBCO + BSO samples. These are compared with a YBCO 300 nm film standard. After 1.8 Tesla, all YBCO + BSO films show improvement from YBCO. At 8 T, it can be seen that the YBCO + BSO films are at least 2 orders of magnitude better than the undoped YBCO.

Theta - two theta x-ray diffraction data taken from different samples is shown in Figure 1.4. The area of interest has been expanded and compared for four representative thickness samples. All the samples show good texture for (00l) type YBCO peaks. However, an additional peak appears in the thicker samples which corresponds to YBCO (103) peak. This peak becomes more intense in the 2.8 μm thickness sample. These misoriented grains are expected as the temperature at the growing surface could be lower in thicker films than thin films as the films are heated from the back of the substrate. Although all YBCO + BSO films show some drop in self-field J_c and T_c , the misoriented grains could be the primary cause for the greater drop in self-field J_c as observed in films with thickness $> 2 \mu\text{m}$.

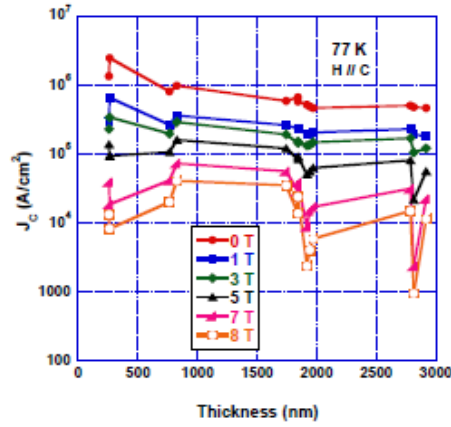


Figure 1.2. J_c values for varying thickness YBCO + 20 mol% BSO films at 77 K and $H // c$

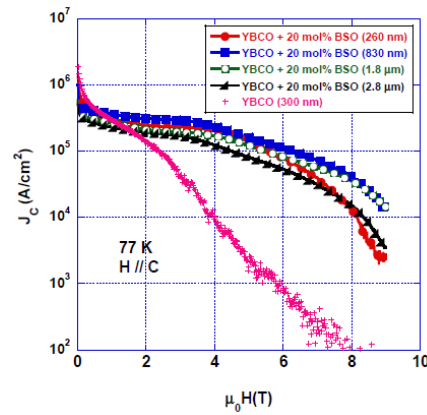


Figure 1.3. VSM J_c data for selected YBCO + 20 mol% BSO film thicknesses compared with 300 nm YBCO at 77 K and $H // c$

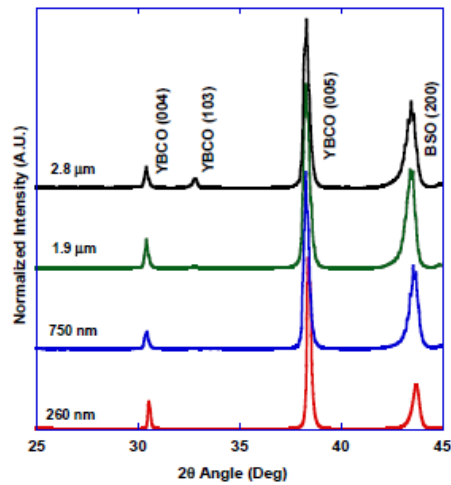


Figure 1.4. θ -2 θ x-ray scans of YBCO + 20 mol% BSO of varying thickness

Figure 1.5 shows the low magnification (1.5 kx) scanning electron surface micrographs of (a) 260 nm and (b) 2.8 μm thick YBCO + BSO samples. The 260 nm shows standard surface features for YBCO + BSO with small particles (note that these particles are not the planar view

of the nanocolumns) on the surface that can be observed at low magnification. The 2.8 μm sample, however, shows misoriented grains such as *a*-axis grain growth occurring in the sample. Despite the misoriented grain growth (possibly created by the lower surface temperature as discussed before) in thick films, the YBCO + BSO microstructure still shows nanocolumn formation of BSO continuing into the upperparts of the films. Figure 1.6 shows at higher magnification (150 kx) the (a) 260 nm sample and (b) 2.8 μm sample. Both display a uniform distribution of BSO nanoparticles at the surface. These are the cross-sections (*a-b* planar view) of the BSO nanocolumns as observed in cross-sectional transmission electron micrographs shown later.

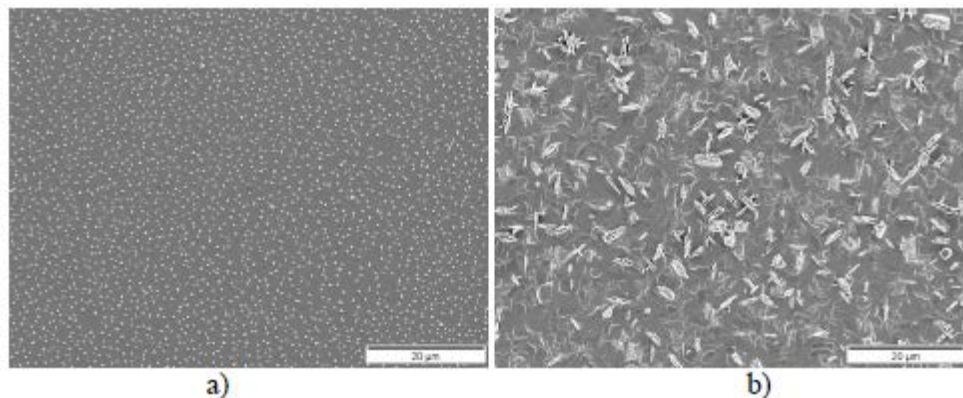


Figure 1.5. SEM photomicrograph showing surface microstructure of (a) 260 nm sample and (b) 2.8 μm sample

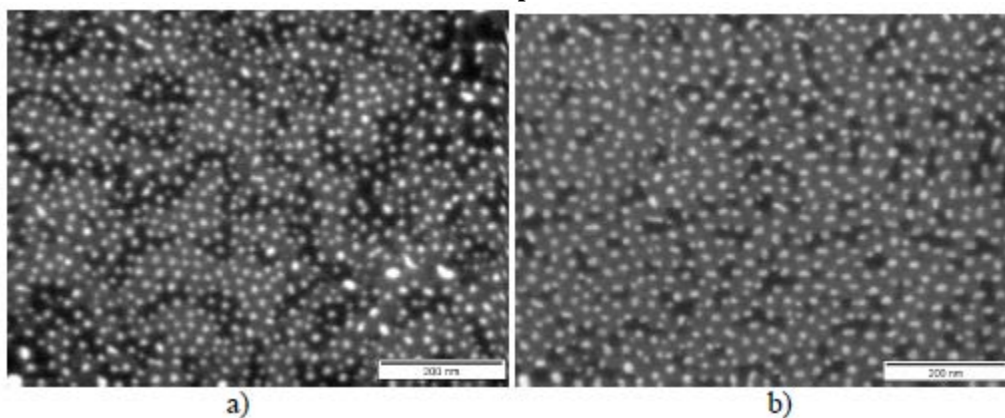


Figure 1.6. SEM photomicrograph showing uniform BSO distribution in YBCO on (a) 260 nm sample and (b) 2.8 μm sample

Cross-sectional TEM was done on the samples to investigate the extent of the BSO nanocolumnar formation in the samples as well. Figure 1.7 shows a YBCO + BSO film of (a) 750 nm thickness and (b) 2.8 μm thickness. Both samples show nanocolumns with a diameter of ~ 8 -11 nm. Both also show continuous nanocolumns that extend through the thickness of the film. They appear to be relatively unaffected by the appearance of *a*-axis growth. The nanocolumns were similar to the nanocolumns shown in the YBCO + BSO thick film made with a sector target.

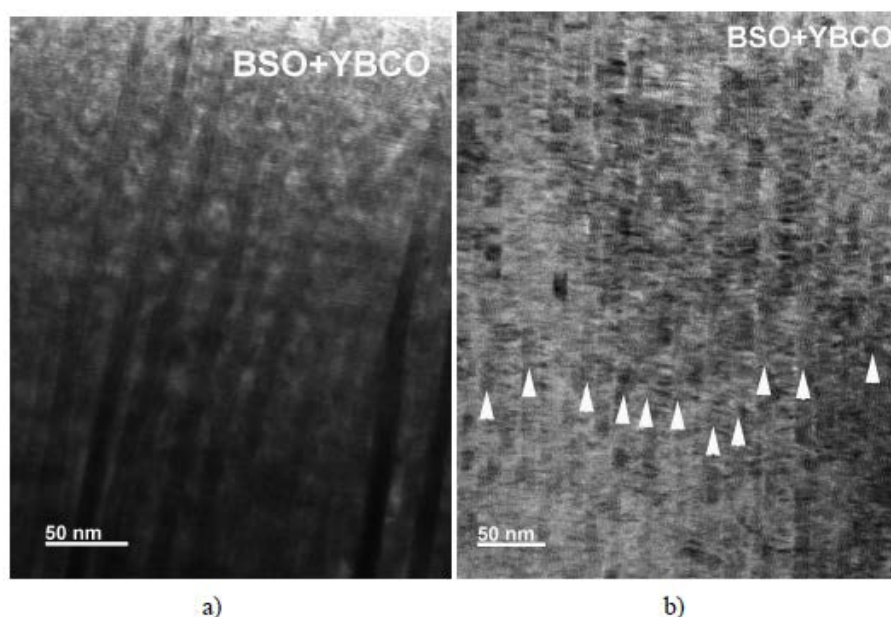


Figure 1.7. Cross sectional TEM image showing through-thickness, uniform BSO nanocolumns in (a) 780 nm film and (b) 2.8 μm film

1.4 Summary

It has been shown that quality, thick YBCO + 20 mol% BSO films up to 3 μm can be grown by just varying the deposition time. This quality growth occurs whether BSO is supplied from a continuous source like a pre-mixed target or intermittent source as the sectorized target. The YBCO + BSO thick films show a T_c of $\sim 87\text{K}$ regardless of the thickness. The samples show little degradation of J_c as thickness is increased, with samples ranging from 260 nm to 2.8 μm showing $>104 \text{ A/cm}^2$ at 8 T, H//C. The samples also all show continuous 8-11 nm nanocolumns of BSO extending throughout the sample despite the presence of a-axis growth in the thicker samples.

1.5 References

- [1] Larbalestier, D., Gurevich A., Feldman, D.M., and Polyanski, A., *Nature* **414**, pp 368-377 (2001).
- [2] Barnes, P.N., Sumption, M.D., and Rhoads, G.L., *Cryogenics* **45**, pp. 670-686 (2005).
- [3] Haugan, T.J., Barnes, P.N., Wheeler, R., Meisenkothen, F., and Sumption M., *Nature* **430**, pp. 867-870 (2004).
- [4] MacManus-Driscoll, J.L., Foltyn, S.R., Jia, Q.X., Wang, H., Serquis, A., Civale, L., Maiorov, B., Hawley, M.E., Maley, M.P., and Peterson, D.E., *Nat. Mater.* **3**, pp. 439-443 (2004).
- [5] Kang, S., Goyal, A., Li, J., Gapud, A.A., Martin, P.M., Heatherly, L., Thomson, J.R., Christen, D.K., List, F.A., Paranthaman, M., and Lee, D.F., *Science* **311**, pp. 1911-1914 (2006).
- [6] Campbell, T.A., Haugan, T.J., Maartense, I., Murphy, J., Brunke, L., and Barnes, P., *Physica C* **423**, pp1-8 (2005).
- [7] Varanasi, C., Barnes, P.N., Burke, J., Carpenter, J., and Haugan, T.J., *Appl. Phys. Lett.* **87**, pp 262510-262510-3 (2005).

- [8] Foltyn, S.R., Tiwari, P., Dye, R.C., Le, M.Q., and Wu, X.D., *Appl. Phys. Lett.* **63**, pp 1848-1850 (1993).
- [9] Foltyn, S.R., Civale, L., Macmanus–Driscoll, J.L., Jia, Q.X., Mairov, B., Wang, H., and Maley, M., *Nat. Mater.* **6**, pp. 631-642 (2007).
- [10] Varanasi, C.V., Burke, J., Wang, H., Lee, J.H., and Barnes, P.N., *Appl. Phys. Lett.* **93**, pp 092501-092501-3 (2008)
- [11] Varanasi, C.V., Burke, J., Brunke, L., Wang, H., Lee, J.H., Barnes, P.N., *J. Mater. Res.* **23**, pp 3363-3369 (2008).

2. Experimental Setup for Calorimetric Measurements

2.1 Introduction

The goal of this project is to measure total AC losses from self-field and external fields. As the high temperature superconducting (HTS) wires, specifically the $\text{YBa}_2\text{Cu}_3\text{O}_{7-x}$ (YBCO) coated conductors, have been extended to long lengths, development has been initiated to implement them in practical devices, such as field windings in motors and generators [1], transformers [2], superconductor magnet energy storage devices [3], power transmission cables [4], etc. A critical characteristic to understand for these YBCO coated conductors in several applications is their ac tolerance [5]. The need to measure ac losses of the wire in device relevant environments have led to the development of several techniques [6,7]. Some of them use electromagnetic measurements, such as the measurement of the electric potential across the sample in phase with the driving current [8], others use calorimetric methods based on the measurement of the temperature increase of the sample or the rate of cryogen boil-off [9]. All these methods have their strengths and weaknesses and for particular experimental conditions some are more suitable than others [10].

For the calorimetric system discussed here, the principle of operation is based on recording the total mass and rate of the N_2 gas evaporating from the LN_2 bath in which the sample is immersed. The driving current applied through the particular sample is turned on for a set period of a few minutes. For the total mass data, the total amount of excess N_2 gas evaporated due to the losses caused by the time-varying current is a measure of the total energy deposited in the sample. From this the power of dissipation is calculated. This protocol differs from the commonly used approach [11] when the current is driven through the sample until the equilibrium between the power of dissipation and the evaporation rate is established. In some cases, such as a slow current ramp, equilibrium cannot be reached. In other cases the wait for the equilibrium to be established may lead to excessive heating of the sample, so that its temperature cannot be reliably determined. By restricting the amount of current-on time we can not only avoid boiling of the LN_2 , which can produce a great deal of irregularity in the gas flow, but it will allow quicker collection of data. This can also reduce the risk of thermal runaway associated with the temperature differential methods [12].

An important part of the design that went into the ac loss measurement system presented here is to particularly minimize the background boil-off allowing the potential differentiation of a few milliwatts in power loss as opposed to 100 milliwatts or more. Although the system design and construction allows the measurement of losses caused by irregular current perturbations, the results presented here for illustration of its operation used the flow rate data collection. In this case, a pancake coil made out of YBCO coated conductor was supplied with harmonic driving current at different frequencies. Again, the data collection did not wait until equilibrium was achieved. Calibration determined that the rate of mass flow increase correlated directly with the applied current level. Although this did allow data to be more rapidly collected, it was critical to ensure that the data was collected during the linear ramping in the cryogen boil-off flow rate.

2.2 Experimental

2.2.1 Apparatus

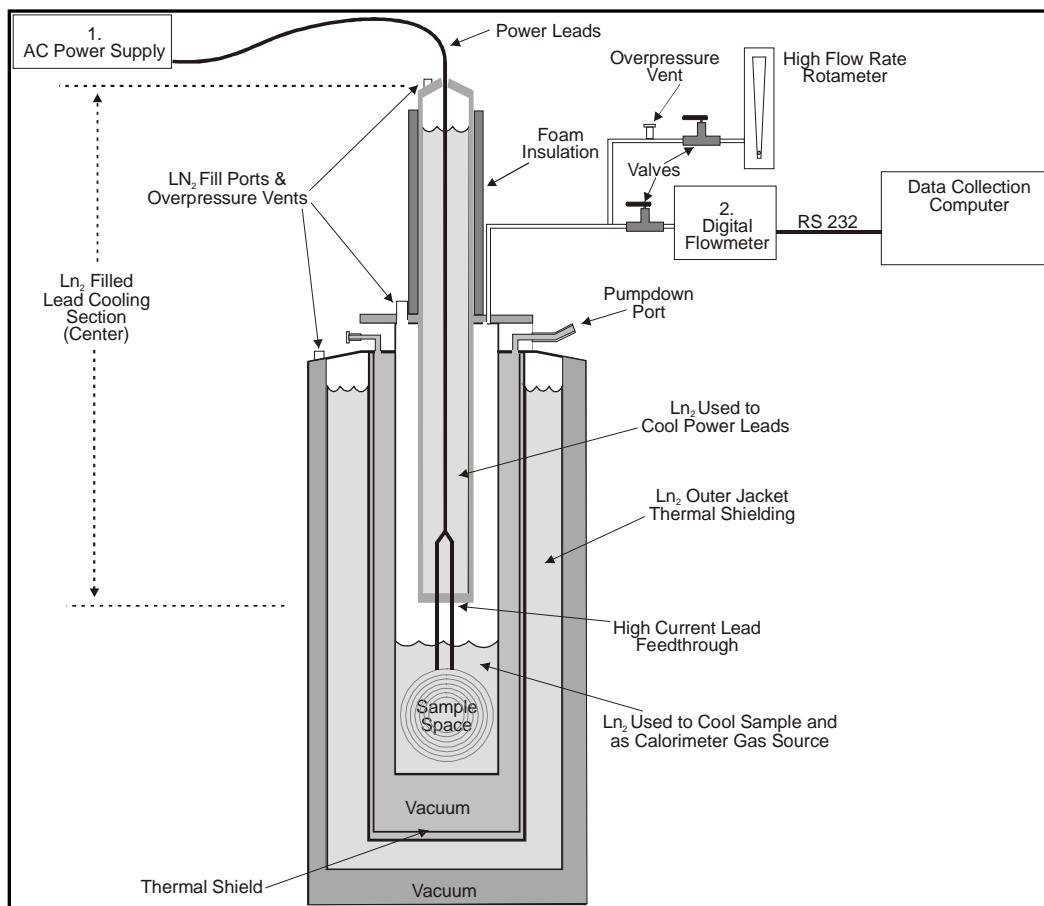


Figure 2.1. Schematic diagram of Self Field Calorimeter

The system, as shown in Figure 2.1, was built using a surplus, LN₂ shielded, liquid helium (LHe) Dewar that was previously used for low temperature superconducting magnet operations. This was selected to provide the best possible thermal insulation since the heat leaks were expected to be the main noise source, limiting the sensitivity of the system.

As shown in Figure 2.2, the original LHe cooled magnet space was divided into two annular cylinders consisting of the center sample space surrounded by the insulating vacuum space. This was done by fabricating a gas tight, cryogenically stable, sample holder made of G-10 fiberglass and suspending it inside the former magnet space which was then evacuated to provide thermal insulation for the LN₂ cooled sample space. The original outer LN₂ jacket and shield structure is still used as a thermal radiation barrier, as shown in Figure 2.2.

Samples are immersed in LN₂ inside the central fiberglass canister. This sample space is sealed so that all evaporating N₂ gas can be directed through one of the 2 flow meters. A relatively high capacity rotameter (a floating ball type flowmeter) is used primarily to verify that the actual gas flow is low enough to not damage the low flow/high sensitivity digital mass flow meter. The rotameter is closed off during data collection, when all the gas goes through the

digital meter. The low flow/high sensitivity digital mass flow meter is an M series mass and volumetric laminar flow meter from Alicat Scientific, Inc. This meter was chosen for its dynamic range and automatic temperature compensation.

The dimensions of the cylindrical sample chamber are approximately 10 cm in diameter and 25 to 50 cm in height. This volume is sufficiently large to test different innovative coil geometries and samples other than coils. In order to reduce the heat leaks through the high capacity current leads, the leads are cooled in LN₂ before entering the sample space and are fabricated from braided copper to increase surface area and facilitate heat removal. Any heat loss from the sample out through the leads will be a result of the current lead connections which is intentionally evaluated and eliminated as discussed later. As such, this loss if it exists is immaterial. The currently installed LN₂ filled lead cooling section reduces the overall sample space to about 15 cm in height. However, the sample space can be substantially increased with simple modifications to the mounting of the lead cooling section.

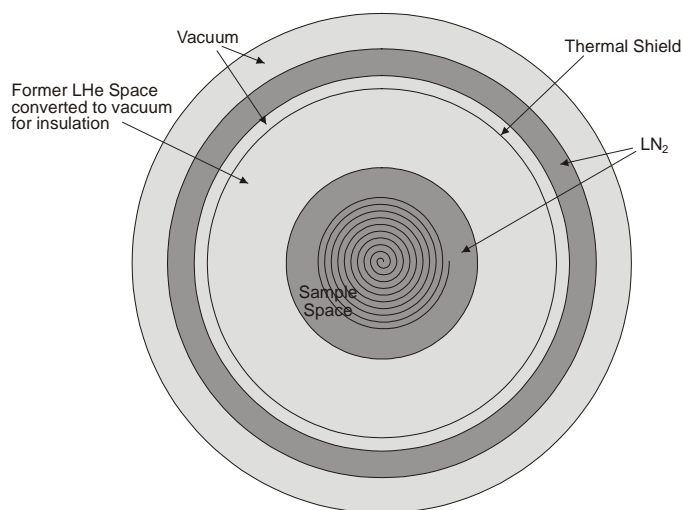


Figure 2.2. Horizontal Cross Section of Self-Field Calorimeter

2.2.2 Measurement Procedures

The total thermal losses of a sample are determined by measuring the mass of LN₂ converted to gas during current flow and calculating the energy necessary to produce that volume. The ohmic losses are found prior to AC measurement in order to facilitate isolation of the AC hysteretic loss from the total thermal loss.

By measuring the total mass of the N₂ gas coming from this sample space during characterization, subtracting the background flow, and inserting the system specific correction factor, we have repeatedly correlated the mass of the N₂ gas to various power levels input to a resistance heater simulating an HTS coil in the system. The energy input is calculated based on the heat of vaporization of LN₂ (199J/g or 0.225J/scc) and the time duration of power applied to the heater or sample. The ohmic losses are found prior to AC measurement to facilitate isolation of the AC hysteretic loss from the total thermal loss. A system-specific calibration maps the input heat load onto the change in output mass flow rate, allowing the data reduction process to be simplified to a single step [13].

The best base background gas flows due to vaporized LN₂ from the sample space have ranged from 2 sccm to 4 sccm, indicating ~44mW to ~88mW respectively. These flow variations seem to follow changes in the level of LN₂ in the outer jacket used as a radiation shield more so than room temperature changes. This represents the vast majority of background noise to be dealt with.

Initial sample simulation tests used a 0.25 W, 75 ohm resistor as a heater. A heater this small tends to form an insulating gas bubble very readily, which is not anticipated to happen with a superconductor sample. A coil of superconductor would be physically much larger than a 0.25W resistor, presenting much more surface area to dissipate the similar power.

To avoid damaging the sample HTS coils it is desirable to not initiate a quench condition. This means that the sample temperature will not go above the boiling point of the LN₂, and should not trigger nucleate boiling. To more closely simulate the planned samples, the tiny 0.25W resistor heater was changed to a physically large, low power per surface area heater. This heater consists of two 1.5 by 3 by 0.125-inch aluminum plates with a 50-ohm kapton encapsulated resistance heater sandwiched between them. A Lakeshore model 340 temperature controller operated in current control mode was used as a power supply to drive the heater. Using this arrangement we were able to directly measure heater inputs as low as 10 mW.

It should be noted that at this stage it was observed that lower power inputs were easier to measure consistently than power levels high enough to cause nucleate boiling on the sample. Since the goal is to measure small heat losses during normal operation of HTS components, it is desirable to avoid this active boiling anyway.

2.2.3 Operation

The initial operations of the cryogenic calorimeter were tests to characterize the system. By using a dc powered resistance heater designed to simulate a substantial sized coil of superconducting tape we were able to plot the expected N₂ gas output from a variety of power levels and operating conditions.

The basic operating procedure consists of installing a sample, cooling the system, energizing the sample and measuring the mass of evolving gas.

The heater used to simulate a HTS coil was connected to an electric power feed through at the bottom of the lead cooling section and inserted into the sample space while the system was at room temperature.

The next step of properly cooling the system requires more care than initially anticipated. During initial efforts to characterize the calorimetry system it rapidly became apparent that the presence of condensates in the LN₂ tends to cause unpredictable errors. This appears to be due to the fact that, when condensation does occur, the quantity and type of condensate is unknown. It has been speculated that O₂ and water are the principle condensates, based on the temperature of LN₂. It is known that mixing LO₂ with LN₂ has been a simple way to raise the boiling point of LN₂ [14].

Small changes in the boiling point of the test fluid, to an unknown temperature, cause large differences in the gas output during experiments. Theoretically, an operator could re-characterize the system after each LN₂ fill using the same techniques used to initially set up the system.

Rather than compensating for the changes in thermal properties of the cryogen mixture it was decided that avoiding the contamination was the more viable course to take. This was

accomplished by performing a sealed LN₂ transfer via pressurized lines directly from a bulk dewar.

By putting LN₂ into the warm sample space and lead cooling space first, adequate positive pressure is maintained by the boiling cryogen to prevent cryopumping into those spaces while the outer thermal radiation shielding jacket is being filled. The sample space is vented through the high volume rotameter, whose reading drops as the outer jacket cools. When the gas volume drops below the resolution of the rotameter the flow rate is low enough to open the valve to the Alicat digital meter without the gas surge harming it. It is not unusual at this point for the system to take several hours to become usably stable, when starting at room temperature. Once the system is cool it will stabilize after a refill in a few minutes.

During these characterization tests, background noise/continuous gas evolution due to environmental heat leakage, tended to stay consistent over short time periods (~20 minutes). Since heater test runs and lower power coil tests tended to take less than this amount of time it seemed to be a good start. Topping off the lead cooling section would restabilize the system.

The basic data collection sequence consisted of recording the base gas flow rate as background noise to be subtracted, resetting the mass total to zero and energizing the heater. This still being a manual operation, the operator would switch on the power for a set length of time and then turn off the heater power. When the N₂ flow rate dropped back to the background rate, data collection would be stopped.

This sequence of operations was modified several times, varying the time the power was on and selecting which section of the data curve was the most meaningful. Ultimately a shorter power on time was selected and the increasing gas flow section of the curve was deemed to be all that was required to determine AC losses.

Naturally, simply dividing the energy input to the heater by the difference in gas generated did not give the right results. There is however a consistent offset when the power input and run times are factored in. Figure 2.3 illustrates the well behaved power to gas flow rate offset ratio.

This produced a system-specific calibration, mapping the input heat load onto the change in output mass flow rate, and provided a single step data reduction process.

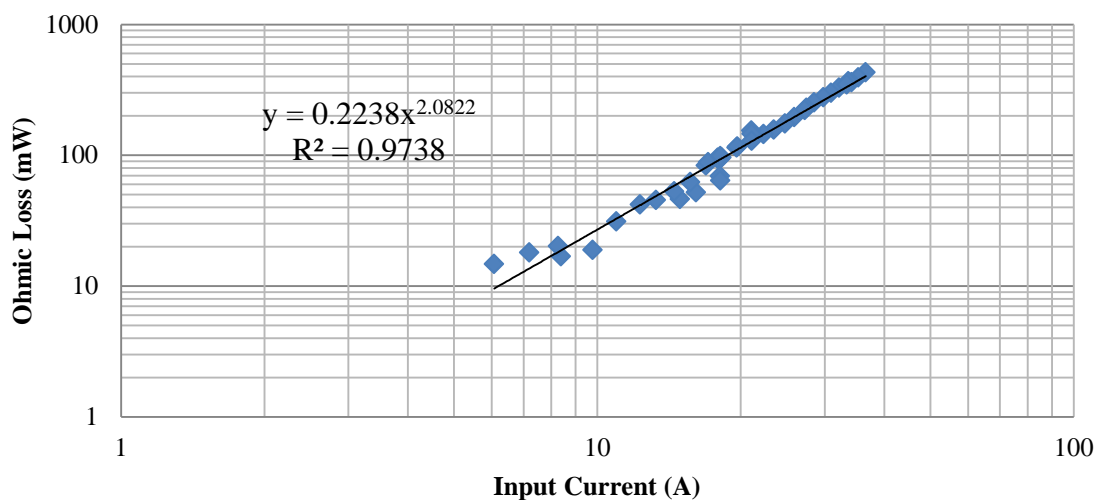


Figure 2.3. Graph depicting calibration offset derived from a resistance heater with known power input

Initial tests have been done using a 1M coil of HTS ribbon. This permitted validating the use of our Elgar TrueWave 5250-1 variable frequency, current controlled, power supply. The results, shown in Figure 2.4, from these measurements fell within the expected range for this particular sample, fabricated using a 1 m $\text{YBa}_2\text{Cu}_3\text{O}_{7-\delta}$ (YBCO), coated conductor coil. The coil was produced and partial losses measured by Dr. Milan Polak, as described in the *Applied Physics Letters* article, “AC Losses in a $\text{YBa}_2\text{Cu}_3\text{O}_{7-x}$ Coil” [17].

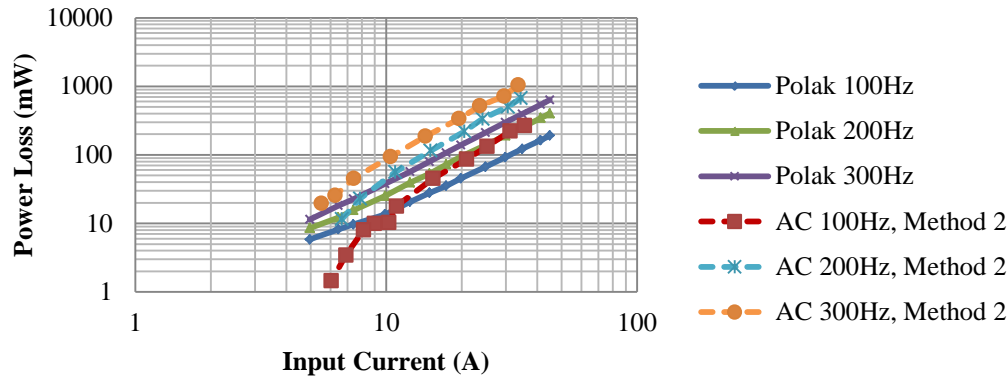


Figure 2.4. Total calorimetric loss measurement compared to electrical field partial loss measurement

2.3 Self-field Summary

An isothermal cryogenic calorimeter of increased sensitivity has been designed and built to determine the total electrical losses from a variety of different sized coils of high temperature superconductor.

Electrical losses from the HTS coil are integrated and given off as heat, slightly increasing the evaporation rate of the LN_2 used to cool the coil. Boiling of the LN_2 does not occur because quenching of the coil is avoided. Heat loss calculations from the energized coil are based on standard nitrogen heat of vaporization while the actual measurement is of the gas evolving from evaporating LN_2 using a commercial mass flow meter to record flow rate and gas temperature.

The coil being measured is connected to a current controlled power supply which provides alternating current to the coil at a selectable frequency, ranging from 100Hz to 300Hz for these experiments. Initial tests of the calorimeter were done with a resistance heater for calibration and a one meter length of HTS tape as a real-world sample. The maximum length of conductor that can be measured is only limited by dimension of the existing 4 inch diameter sample space.

2.4 Integrating the Isothermal Cryogenic Calorimeter into the SAM Machine to Expose the Samples to a Substantial Alternating Magnetic Field

2.4.1 Introduction

The goal of this project was to measure total AC losses resulting from AC transport current in an external reversing magnetic field and controlled combinations thereof. In the SAM machine, the system used for external field measurements, an HTS sample is exposed to a reversing magnetic field of variable frequency. Space is provided to also connect high current

loads, AC or DC, to small linear samples or substantial sized coils. This will permit self-field and external field measurements, in and out of phase, on a sample at the same time. An important feature is the high $d\phi/dt$ that the sample is exposed to. The test rig rotor is an eight-pole (four north and four south) permanent magnet design, spinning at 1,800 rpm in this example, and producing 0.5 Tesla. The $d\phi/dt$ in the annular test space will be $0.5T \cdot (2 \cdot \pi \cdot \text{freq}) = 377$. The rotor is designed to reach 3,000 rpm. Losses are calculated from the measured flow of N_2 gas from the LN_2 calorimeter containing the test sample and installed into the reversing magnetic field. This calorimeter is based on the prior 10 mW sensitivity system.

By mounting the sample in a fixed location between a rotating permanent magnet and a laminated back iron the sample is swept by a rapidly reversing magnetic field with the frequency controlled by the rotation speed of the magnet. Using the previous 1,800 rpm example this would provide a complete field reversal in about 3 ms where a similar field reversal in a 60 Hz sine wave system would take 8 msec.

2.4.2 Experimental

2.4.2.1 External Field Apparatus

The mechanism for providing the time varying magnetic field consists of the 8 pole magnet rotor, nested inside an annular, laminated backiron stack, supported by four sets of ball bearings to hold it in position vertically and horizontally while permitting free rotation. Instead of the extremely small gap found between the rotor and stator in an electric motor this instrument has a 1.5 inch gap to permit placing the HTS sample in the center of the magnetic field to expose the sample to the most uniform part of the field.

Figures 2.5 and 2.6 show where the sample holder is nested inside a fiberglass LN_2 cell shaped to fit in the magnet-backiron gap. This gap, along with the rest of the instrument, is evacuated to provide insulation for the LN_2 cell. The sample is held inside a thin walled fiberglass box with a long fiberglass tube extending from the sample space up through the open top of the LN_2 cell to the Alicat model M-1SLPM mass flow meter. This sample holder contains enough LN_2 to completely cover the sample under test with enough to spare so it will remain covered throughout the test.

The LN_2 cell is supported at three points along its length and is stiff enough to not bulge when the insulating space is evacuated or bend when the magnet “pulls” on the sample.

Similar to the description in the abstract, an important characteristic of the protocol of our measurements is that the magnetic field is oscillated (and, if desired, the current is also turned on) for a specific, but relatively short, period of time so that the sample and liquid nitrogen do not come to equilibrium at the end of this period.

In this system the LN_2 in the large LN_2 cell boils, at least a little, continuously due to radiant heating from the surrounding machinery. This layer of LN_2 shields the sample holder from the external heating source. The limited time of exposure to magnetic field and/or AC current limits the sample temperature rise to the double digit milli-Kelvin range, and avoids extra boiling of liquid nitrogen, allowing us to determine the losses at different field and/or current frequencies, but at the same (or closely comparable) temperature of the sample. This technique also greatly reduces signal drift, avoids quench conditions, and more closely mimics the environment inside an operating HTS equipped machine such as a motor or generator where there would be more robust cooling. Since the temperature of the sample does not need to rise

substantially, having the sample holder immersed in the LN₂ cell does not reduce the signal when using the methodology described here.

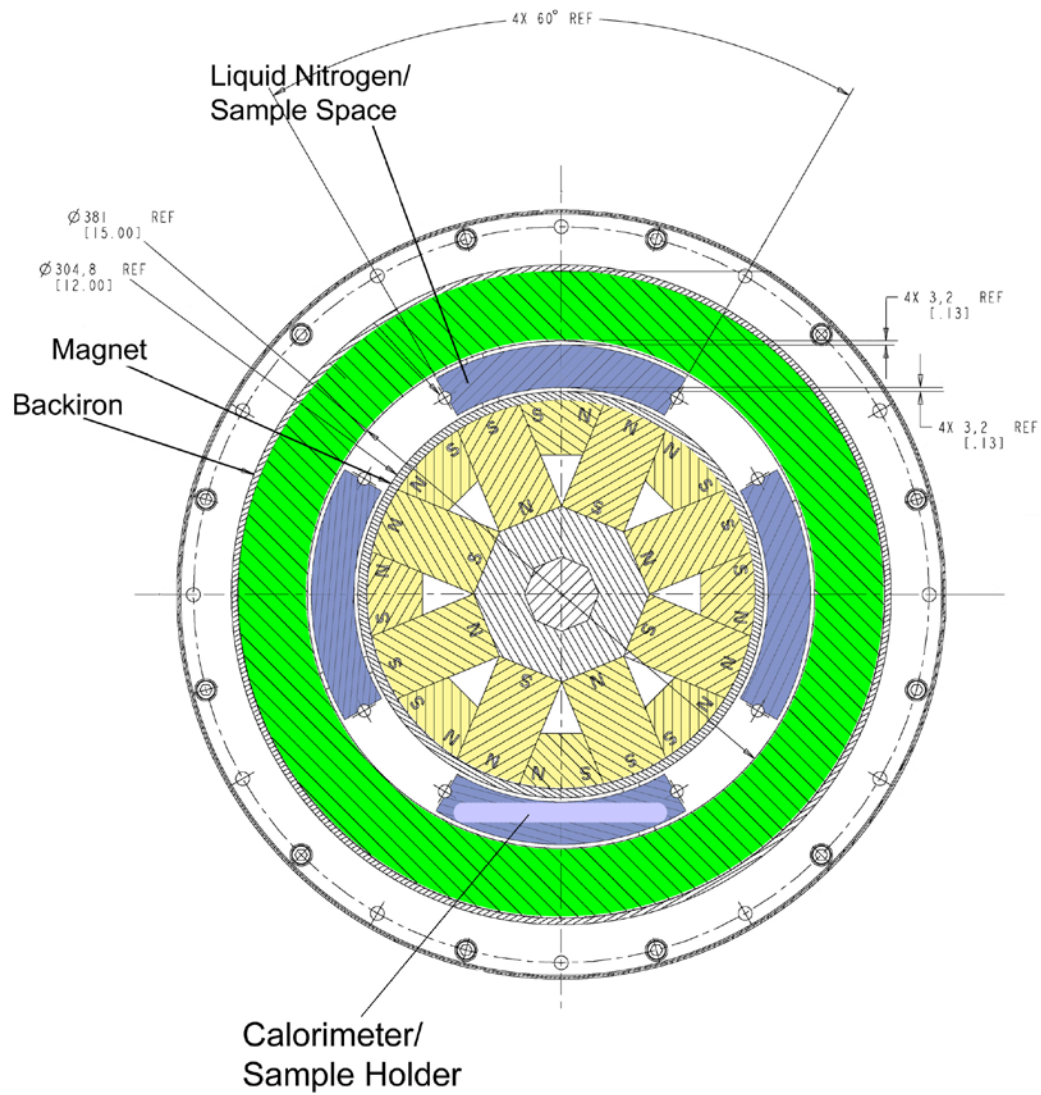


Figure 2.5. Horizontal Cross Section

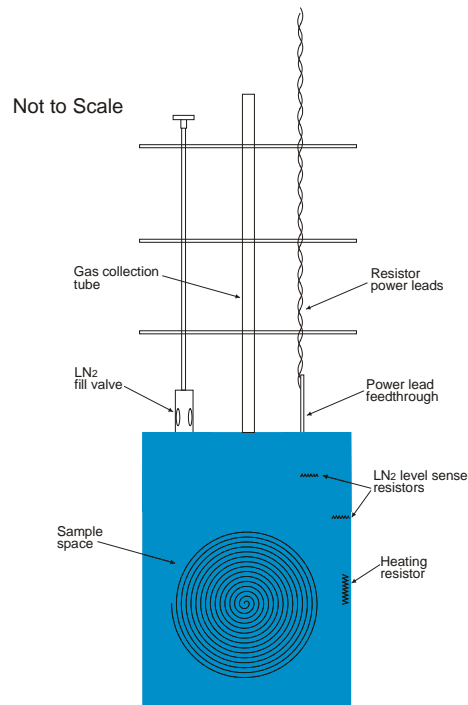


Figure 2.7. Cross section of sample holder

The sample holder is filled by submerging it inside the filled LN₂ cell and opening the valve on the top using the stem extension reaching outside the top of the LN₂ cell. When the resistance of one resistor changes the valve is closed. The sample is accessed via an opening in the bottom of the sample holder which is closed off with a fiberglass plug. An alternate sample holder opens at the top and has two additional, high current, leads to energize the sample.

The design phase of the rotating magnet includes computer modeling of the magnetic field shape and predicted field strength as depicted in Figure 2.8. Measurements using a Lakeshore Model 450 Gaussmeter showed that samples under test can be exposed to the calculated maximum field of 0.6 Tesla. In the vertical axis the field is acceptably uniform over about 17 cm of the 22 cm height of the magnet as shown in Figure 2.9.

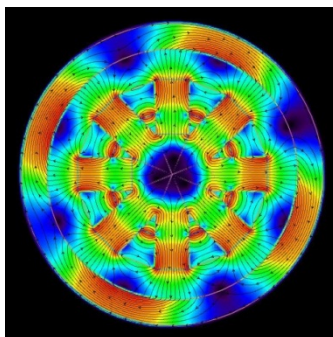


Figure 2.8. Calculated magnetic field strength and field line vectors

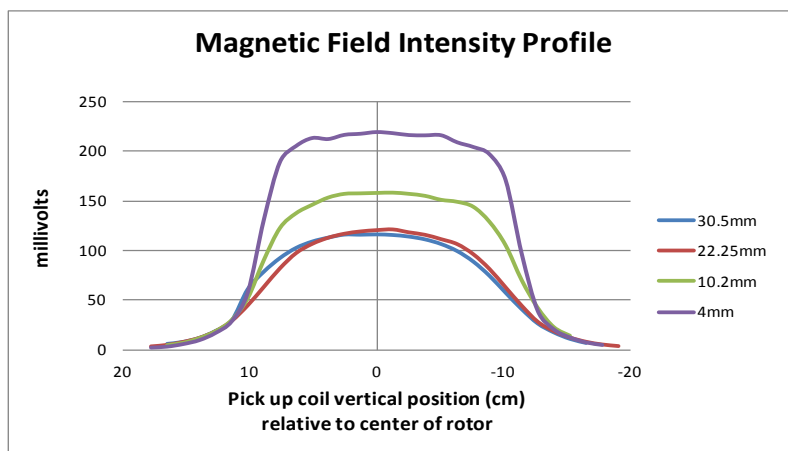


Figure 2.9. Measured vertical field profiles

The 10mm diameter coil of copper wire shown in Figure 2.10 was used to map the relative field intensity along the vertical axis in 12.5mm (0.5in) vertical increments at four radial positions. The coil was mounted on a section of fiberglass 'U' channel that was machined to fit into the space between the rotor and back iron without moving. Measurement positions were indexed by bolting the coil to evenly spaced holes in the channel. The radial position was indexed by bolting the coil mounting bracket to a block with a series of holes. To avoid having the changing magnetic field induce movement of this assembly all mounting mount parts were fiberglass and screws were nylon. Since the field is strong enough to "pull" non-magnetic metals when the magnet is rotating, the wire used to measure the voltage generated across the coil also was tied down to the channel in several places. The asymmetry in the curve in Figure 2.7 is due to voltage generated in this wire as it stretched across the magnet to reach the coil when measuring the far end.

The horizontal profile of the field was mapped with the same coil mounted near the center of the vertical axis of the sample space, as the magnet rotated past the stationary coil. This profile was measured at different distances from the rotor, as shown with the vertical profile in Figure 2.9. Figure 2.11 represents the plot closest to the magnet rotor.

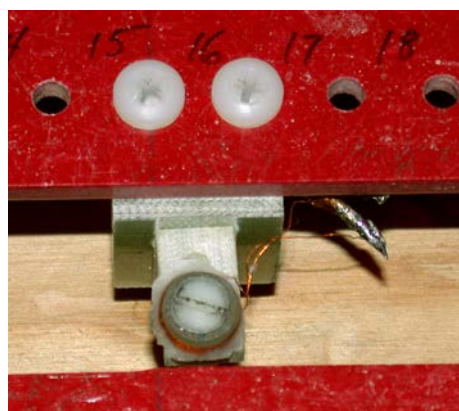


Figure 2.10. Mapping coil, 10mm diameter

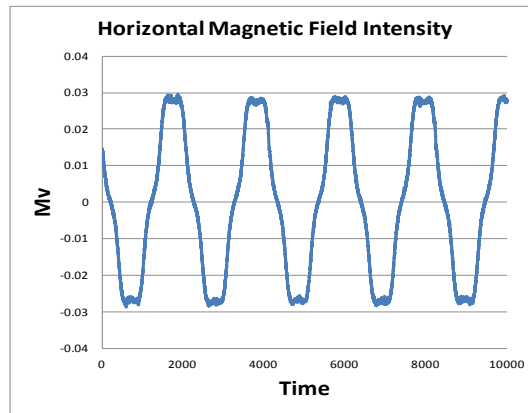


Figure 2.11. Field map around the rotor

A 10cm x 0.25cm coil, shown in test configuration in Figure 2.12, was fabricated and permanently installed, by mounting to a fiberglass channel in the magnet-to-backiron gap. This is connected to an oscilloscope to provide a sync signal for AC current relative phase control, for better simulations [15], and to indicate the actual frequency that the samples are being exposed to. Both of these copper wire coils were oriented so the magnetic field lines would pass through the loops of the coils as in a current sense transformer or similar to a Rogowski coil. These were not calibrated for specific field strength measurements, but were constructed for adequate sensitivity and stable, repeatable, relative strength measurements. The usable sample space is approximately 170 mm tall x 100 mm wide x 70 mm thick. The calorimeter/sample holder will hold a range of sample sizes and geometries inside the 170 mm x 100 mm x 40 mm range. The linear portion of the magnetic field is about 43 mm wide as it travels along the 100 mm axis of the sample holder. The steep part of the transition from north to south is about 89 mm wide. Using the previous 1800 rpm example this would provide a field reversal in about 3 msec.

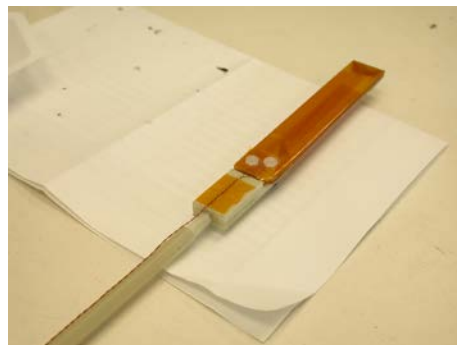


Figure 2.12. Magnetic field frequency sensing coil

2.4.2.2 Measurement Procedures

Once the main body of the system, containing the magnet and back iron, is evacuated the LN₂ cell can be filled from a dewar. This is done very slowly, blowing cold N₂ gas deep into the cell for several minutes before actually introducing liquid. The LN₂ cell is tall and narrow so it is desirable to limit the thermal stresses as much as possible. The sample holder, containing the

sample, is lowered into the filled LN₂ cell very slowly as well, sitting in cold gas above the liquid most of the wait time, to reduce the thermal shock from immersion. Filling takes ten minutes and insertion takes another five or six minutes.

Typically the samples are held in place, in the desired orientation, inside the sample holder with small styrofoam spacers, making contact in as small an area as is practical to maintain maximum contact with the LN₂ for cooling. Both small sections of HTS tape and 1M coils have been briefly tested to verify fit and functionality.

When the sample holder is inserted into the LN₂ cell the gas collection tube to the mass flow meter is valved off to ensure that only the dry N₂ surrounding the sample holder is pulled into the cell as it cryopumps, and not moist air backwards through the flowmeter. After immersion the valve on the sample cell is opened, while monitoring the resistance on the level indicating resistors, and is closed again when the resistance goes up on one of them. When this valve is closed the valve to the flow meter must be opened to prevent an exciting, but time wasting, pressure buildup in the sample holder. At this point the LN₂ cell is topped off since it will now be about half empty.

Once the system has stabilized, that is, the LN₂ is boiling off at a steady but relatively sedate rate, the flowmeter can be zeroed and data collected in the same way as with the self-field calorimeter described above. The difference being that, instead of, or in addition to, turning on the AC current, the magnet is rotated at the proper speed to deliver the desired frequency of magnetic field.

Using a 5HP variable speed motor the rotor is ramped up to high speeds in about 20 seconds, the data is recorded and the rotor is ramped to stop, to limit inductive heating of the backiron and magnet. This heating will increase the radiant heating of the LN₂ cell and can cause an increase signal noise.

2.4.2.3 Sample Demonstration

In order to visualize system response and sensitivity a comparison was made between controlled power input to a resistance heater and a 12x5mm copper strip inductively heated by the rotating magnet rotor. Resistor power and rotor RPM's were stepped down from a higher starting point to approach the base system noise regime. This procedure is also basically the method for determining offsets and correlating sample response to known heat loads. It was determined that starting at the highest power in the planned test range and stepping down through the lowest provided more repeatability and a clearer chart than starting low and going up in excitation energy. This appears to be due to the sudden surge which occurs with the onset of boiling when approaching that state very slowly. Figure 2.13 illustrates an example of using the same stepping down method with 100rpm (*HERTZ*) changes in motor speed. The dip at "Time 1900" was caused and interruption in the drive motor. The magnet drive motor was stepped through even motor speeds, the actual magnetic field frequency was measured. The steps in the graph above represent stepping through the following magnetic frequencies: 0, 42.2, 40.5, 38.9, 35.6, 32.3, 38.9, 30.7, 29.1, 27.5, 25.9, 32.3, 0 Hz (motor off). Illustrated are losses of 0.45mW (0Hz), 106mW (42.2Hz), 96.75mW (40.5Hz) etc. This graph represents initial operational tests and does not include any correction calculations or noise reduction. Data points were collected at 1hz. The rotor speed was increased at two points to observe how well the system behaved with non-sequential power input settings.

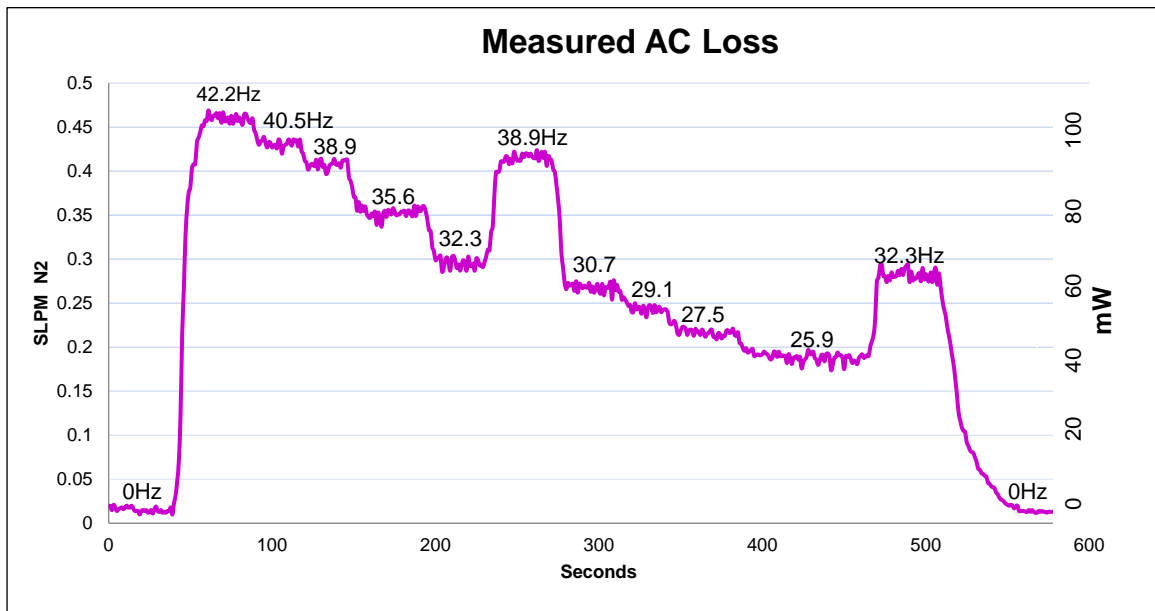


Figure 2.13. N₂ flow change and measured magnetic field frequency as drive motor speed is reduced in 100RPM steps

2.4.3 Summary

An isothermal cryogenic calorimeter has been designed and built to determine the total AC transport and alternating magnetic field losses from a variety of different sized coils and small samples of high temperature superconductor when exposed to strong, varying frequency, external magnetic fields, and/or variable frequency AC current.

Electrical and magnetization losses from the HTS coil are integrated and given off as heat, slightly increasing the boiling rate of the LN₂ used to cool the coil. Very slight boiling of the LN₂ occurs continuously due to the radiant heating of the magnet and backiron. However the entire sample is in contact with LN₂ at all times for uniform cooling and to collect all heat losses as quickly as possible without waiting for equilibrium.

Heat loss calculations from the energized coil are based on standard nitrogen heat of vaporization while the actual measurement is of the gas evolving from evaporating LN₂ using a commercial mass flow meter to record flow rate, gas temperature and atmospheric pressure. Reduced sensitivity is believed to be caused by radiant heating from the proximity of the magnet and back iron. Cryogenically cooling the interior of the instrument, as was done with the self-field calorimeter, could reduce background signal and increase sensitivity.

The ability of the system to measure reasonably small external magnetic field induced eddy current losses in a small sample has been demonstrated.

The sensitivity of the systems are such that they can individually measure low end losses from a few mW in a current transport generated self-field mode, or from several hundred mW low end, in dynamic magnetic field with or without AC transport current.

2.5 Description of Bulmer Circle Terahertz Emitter

- Terahertz radiation will not penetrate metal and is substantially attenuated by some plastics. This means that the sample cannot be in a metal or inappropriate plastic container during emission tests.
- Emissions radiate from the edge of the circle. Because of this it is best if the sample is not on a metal mount since this can affect the far field pattern and complicate measurements.
- The Bulmer Circles are superconducting YBCO and need to be cooled to about 77 K. LN₂ is the favored coolant for this material, but does not pass the infrared laser very well.
- YBCO is somewhat moisture sensitive, so the cooled sample must be shielded from the air to prevent condensation. The YBCO is deposited as a thin film (<300nm) on a sapphire wafer.
- The circles must be connected to a DC power supply and also have a solenoid coil very near-by (within 2 or 3 mm) to charge the circle under test.
- The emissions are triggered using a very short pulse near infrared laser. The housing must admit this wavelength and high peak energy laser and not excessively distort the beam.
- Measurements were performed at the University of Dayton, because that is the location of one of the femtosecond lasers that was available.

From the initial planning stage, the laser based triggering method and specifications have not been changed. The sample mounting and cooling method has gone through three distinct iterations, typically with time and funding constraints. The first iteration used a LN₂ bath for cooling. The LN₂ container was double wall polyethylene with expanded polystyrene for insulation, since these are the most transmissive plastics for the terahertz band. The sample was mounted on the end of a section of vertically mounted aluminum bar stock. The aluminum was sized to hold the sample above the surface of the LN₂ to provide laser access. The aluminum also provided thermal conduction from the LN₂ bath to cool the sample which was affixed with N-grease to maximize conduction. Since there is some latitude in the required temperature for superconductivity this was adequate cooling, but time limited due to the finite amount of LN₂ in the bath.

Two methods were tried for charging the circles. Power leads were directly connected to gold pads intersecting the rings on the sapphire substrates and one hundred turns of copper wire were wrapped around the aluminum bar to form the solenoid coil for the alternate method of charging the coil. Both methods appeared to work, however the solenoid was the easiest to use and analyze/explain. The gold pads were fragile and easily damaged and there was some concern about knowing the path of the current through the ring.

To prevent condensation on the cold sample the entire assembly was placed inside a plastic box, made of PMMA, since polycarbonate attenuates the terahertz band. A quartz window was installed as a laser window to permit triggering emissions. The box was purged with dry nitrogen, from the boiled off LN₂ coolant. This eliminated condensation problems during tests. Changing samples was very difficult however largely because it took so long for the aluminum rod to warm up above the dew point of the room and the sample could not be separated from it until the N-grease would soften, at around 0 °C.

The experiments verified that the concept was valid: It was shown that using a laser pulse it is possible to generate terahertz radiation directly from a DC current without intermediate electronics.

For the second set of experiments, intended to measure the radiation emitted, it was decided that extending the actual cold time of the sample would permit making comparative emission measurements. If possible, controlling the temperature was also desirable to see if approaching the T_c of the superconductor would change the emissions.

A set of mechanical cryocoolers were selected because they can run for hours at a time and have more than adequate cooling capacity. They were mounted in parallel in a vacuum chamber, one to cool the sample and one to cool the two sets of power leads and eight temperature sensor leads, to limit parasitic heating along the wires. Operating in a vacuum eliminated condensation problems and provided insulation for the cold ends of the cryocoolers. The cryocoolers are metal, so to move the sample from the immediate proximity a sapphire rod was fixed to the end of the cryocooler and the sample was once again mounted with N-grease onto the sapphire. Sapphire has thermal conductivity similar to steel and the cryocooler would be operated at well below the T_c of the YBCO so it was more than adequately cooled.

The solenoid coil was wrapped around the sapphire rod. The cryocoolers vibrated vigorously during operation so the vacuum chamber was about 15 kg of steel with a pyrex and quartz bell jar assembly to transmit the laser trigger beam and the terahertz emissions. The cryocoolers also required officially obsolete software to control so there was substantial difficulty in that area, enough so that it was decided to not use them for the third session of experiments. The sapphire rod proved to work well for conductive cooling except for the vibration of the cryocooler causing repeated failure of the thermal joint between them and the rod.

The third set of experiments, currently under development, is using vacuum pumped LN_2 . The cryocooler vacuum chamber was modified to hold an expanded polystyrene foam cup as a LN_2 container, the sapphire rod is mounted in the cup and cools the YBCO circle as before. By controlling the vacuum pressure the temperature of the LN_2 can be controlled within useful limits.

2.6 References

- [1] P. N. Barnes, M. D. Sumption, G. L. Rhoads, Review of high power density superconducting generators: Present state and prospects for incorporating YBCO windings. *Cryogenics* 45 (2005) 670–686
- [2] M. Yamamoto, M. Yamaguchi, K. Kaiho, Superconducting Transformers. *IEE Transactions on Power Delivery*, Vol. 15, No. 2, April 2000
- [3] A. Ishiyama, H. Ueda, Y. Aoki, K. Shikimachi, N. Hirano, and S. Nagaya, Quench Behavior and Protection in Cryocooler-Cooled YBCO Pancake Coil for SMES *IEEE Transactions on Applied Superconductivity*, Vol. 21, No. 3, June 2011
- [4] C. Træholt, E. Veje, O. Tønnesen, Electromagnetic losses in a three-phase high temperature superconducting cable determined by calorimetric measurements. *Physica C* 372–376 (2002) 1564–1566
- [5] S P Ashworth, M Suenaga Local Calorimetry to Measure AC Losses in HTS Conductors. *Cryogenics* 41 (2001) 77-89
- [6] G. Coletta, L. Gherardi, F. Giimiiry, E. Cereda, V. Ottoboni, D. Daney, M. Maley, S. Zannella. Application of Electrical and Calorimetric Methods to the AC Loss

- Characterization of Cable Conductors *IEEE Transactions on Applied Superconductivity*, Vol. 9, No. 2, June 1999
- [7] F. Darmann, S. Dou, C. Cook, Determination of the AC Losses of Bi-2223 HTS Coils at 77 K at Power Frequencies Using a Mass Boil-Off Calorimetric Technique *IEEE Transactions on Applied Superconductivity*, Vol. 13, No. 1, March 2003
 - [8] Polak, M., et al. "AC Losses in a YBa₂Cu₃O_{7-x} Coil." *Applied Physics Letters* 88 (2006).
 - [9] N Magnusson, S Hornfeldt, JJ Rabbers, B ten Haken, HHJ ten Kate. Comparison Between Calorimetric and Electromagnetic Total AC Loss Measurement on a BSCCO/Ag Tape. *Supercond. Sci. Technol.* **13** (2000) 291-294
 - [10] S. Bernd, Handbook of Applied Superconductivity. Institute of Physics Publishing, 1998 Pg 347
 - [11] S. Bernd, Handbook of Applied Superconductivity. Institute of Physics Publishing, 1998 Pg 346
 - [12] J A Demko, J W Lue, U Sinha, R L Hughey, L Dresner and SK Olsen Testing of the Dependence of the Number of Layers on the Performance of One-Meter HTS Transmission Cable Section. *IEEE Transactions on Applied Superconductivity*, Vol. 9, No. 2, June 1999
 - [13] Matthew J. Mullins, Verification of AC Hysteretic Thermal losses of a Superconducting Tape Device using a Novel Calibration Method. *In fulfillment of the requirements of the course ME-595 Mechanical Engineering Special Projects* Dr. Hallinan Department of Mechanical Engineering University of Dayton 2011
 - [14] A P Beloshitski. The Use of the Boiling Point of Nitrogen to Calibrate Thermometers. *Measurement Techniques*, Vol. 45, No. 9, 2002
 - [15] DN Nguyen, PVPSS Sastry, GM Zhang, DC Knoll, J Schwartz, *Fellow, IEEE*. AC Loss Measurement with a Phase Difference Between Current and Applied Magnetic Field. *IEEE Transactions on Applied Superconductivity*, Vol. 15, No. 2, June 2005.

3. Growth of High-quality Carbon Nanotubes on Free-standing Diamond Substrates

3.1 Introduction

Three carbon-based materials have demonstrated the potential for high thermal conductivity: graphite, diamonds and carbon nanotubes (CNTs). Due to the high thermal conductivity (~ 1800 W/km) of diamond, heat spreaders made of diamond plates are useful for thermal management in high power electronic devices [1] such as laser diodes, RF power transistors, etc. Diamond heat spreaders help to quickly transfer heat from the devices to heat sinks and thus improve the reliability and device performance [2]. Diamond coatings deposited by chemical vapor deposition (CVD) were also investigated to serve as heat spreading films for thermally limited high-power high-frequency devices [3]. In addition to diamond films, discrete CNTs also were found to have very high thermal conductivity (~ 3000 W/km) along with high mechanical compliance and thus offer a potential for the development of the next generation thermal interface materials [4–6]. CNTs can make excellent thermal interface materials if the proper quality can be maintained along with a robust attachment to the desired devices. For example, chip cooling with CNT microfin architectures have been recently proposed by Kordas et al. [5]. CNT films as thermal interface materials were also discussed by Zhu et al. [6]. Initial results by this group showed that an assembly with CNTs has a thermal conductivity of 81 W/m K and a thermal resistance of $0.43 \text{ cm}^2 \text{ K/W}$.

As an interface material, CNTs have been demonstrated to grow on a variety of materials/substrates. Cola et al. studied the performance of a thermal interface material consisting of Cu foil and CNT arrays and reported that thermal interface resistances of less than $10 \text{ mm}^2 \text{ K/W}$ are possible [7]. Xu and Fisher [8] reported enhancements in thermal conductance using CNT arrays grown on Si wafers by plasma enhanced CVD and reported a thermal interface resistance of $19.8 \text{ mm}^2 \text{ K/W}$. Cola et al. [9] investigated CNT arrays grown on SiC to serve as thermal interface materials for high temperature SiC devices and achieved thermal resistances less than $10 \text{ mm}^2 \text{ K/W}$. CNTs were grown by Wang et al. on both sides of metallic substrates to fabricate thermal interface materials [10]. Samples fabricated in this study were measured to have thermal interface resistance of $12 \text{ mm}^2 \text{ K/W}$. CNTs were also grown on constantan substrates for similar applications without the use of catalysts [11]. Carbon nanofiber-Cu composite films have been reported by Ngo et al. to have very low thermal resistances ($0.25 \text{ cm}^2 \text{ K/W}$) to serve as thermal interface materials for microelectronic packaging [12].

It is therefore reasonable to consider the growth of CNTs on diamond, since both can have superior thermal conductance. A structure containing a composite of diamond substrates for heat spreading and CNTs for heat radiation on top of them could provide a useful combination to efficiently conduct away the heat. Enhancement of thermal diffusivity properties of the diamond spreaders can be expected by combining CNTs grown on diamond substrates. In the present work, initial results of growth and characterization of CNTs grown on diamond substrates are presented.

3.2 Experimental

Diamond substrates were grown in a 5 kW microwave plasma CVD system on 2 in. diameter silicon wafers. Prior to the diamond growth, the Si wafers were thoroughly cleaned and scratched with diamond crystals (pre-seeding) in an ultrasonic bath to initiate nucleation [13]. Diamond growth was carried out in a low concentration of CH_4 (1.5–2%) as the carbon source

gas in a carrier gas of hydrogen. Diamond films were grown using microwave powers between 2500 and 4000 W at temperatures of 850–900 °C for 6–7 days to obtain films of ~100 μm thick. Free-standing diamond substrates were subsequently obtained by dissolving away the silicon wafer using chemical etchants. A catalyst layer (Ni or Ni–9% W–1.5% Fe) was then deposited by sputtering directly onto the diamond substrates without using any intermediate layers. In addition to pure Ni, alloy catalysts were also used to encourage base growth. [14]. All the depositions were done at room temperature and the metal catalyst layers from 2 to 10 nm thickness were deposited by varying the deposition time. While some samples were treated in Ar/5% H₂ atmosphere for 30 min to create catalyst islands prior to CNT growth, other samples were directly used for CNT growth without a prior heat treatment.

CNT growth was done in a lab-constructed thermal CVD system using a 1 in. diameter quartz tube in a horizontal furnace. Initially, the tube furnace was evacuated by using a rough pump and then purged with Ar/5% H₂ for 20 min. The furnace with the samples was heated in an Ar/5% H₂ atmosphere to 750–800 °C. A precursor gas of 10 vol.% C₂H₂ in an argon carrier gas was introduced as the carbon source at a flow rate of 50–400 sccm. The CNTs were grown for different lengths of time varying from 30 to 120 min. The samples were then cooled in an Ar/5% H₂ mixture to room temperature. Some samples were also grown at a total pressure of 90 torr to observe the effect of low pressure growth.

Both diamond and CNT/diamond samples were analyzed by using a high resolution FEI Sirion scanning electron microscope (SEM) and a Delta Nu Raman microscope using a 532 nm diode laser. A Rigaku powder X-ray diffractometer (XRD) was used to obtain theta-two theta scans from the samples. CNTs from the diamond substrate were separated and then transferred to a copper grid and analyzed in a FEI Tecnai F20 analytical transmission electron microscope (TEM) with a point-to-point resolution of 0.21 nm to determine the crystalline-quality.

3.3 Results and Discussion

Using microwave plasma CVD, diamond coatings up to 100 μm thick were processed. Figure 3.1 shows a SEM image of a diamond substrate processed in the present study. It can be seen that these substrates have large crystals of diamonds with sharp facets and as a result have rough surfaces. Figure 3.2 shows a theta-two theta XRD pattern taken from a diamond substrate. Peaks corresponding to different orientations of the diamond were noted, indicating the polycrystalline nature of the diamond substrates. Figure 3.3 shows Raman spectra taken from one of the large crystal diamond substrates. A sharp peak at 1332 cm⁻¹ at room temperature is observed with a very low G peak at 1550 cm⁻¹, indicating a high degree of sp³ bonding in the carbon and that the samples are of high quality. Similar sharp peaks were also noted in high-quality diamond substrates in the literature [15,16].

The free-standing diamond substrates obtained by dissolving the Si substrate were found to be fairly translucent, providing an additional indication of very low impurity levels (*sp*² carbon etc.) in these substrates. The lower impurity levels in the diamond films are desirable due to their better thermal conductivities [1]. In addition, the microstructure of polycrystalline diamond films with grain boundaries also influences thermal conductivity [17,18]. Since the large crystal diamond substrates have a reduced grain boundary area, the in-plane thermal conductivity is expected to be better in large crystal diamond substrates as compared to small crystal diamond substrates. The quality of the diamond substrates just described under the conditions in this study appears to be most suitable for growing CNTs for thermal management studies.

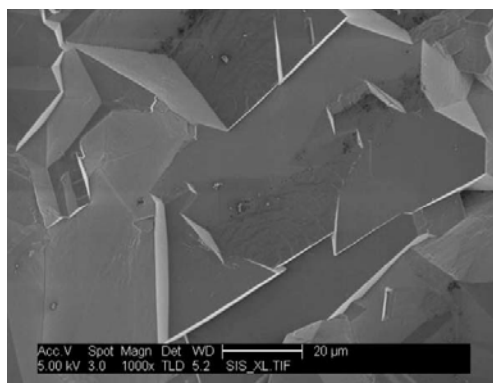


Figure 3.1. SEM micrograph of as-grown diamond sample showing facets of crystals

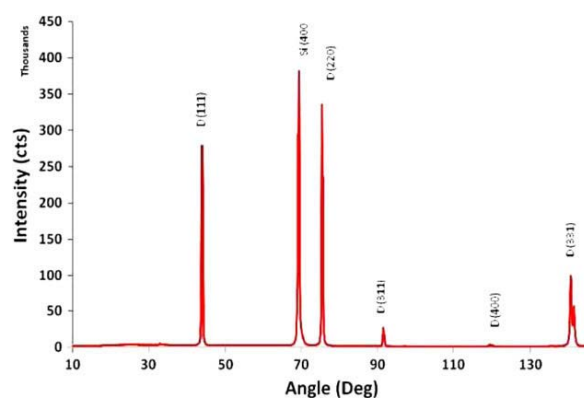


Figure 3.2. X-ray diffraction pattern taken from a diamond substrate

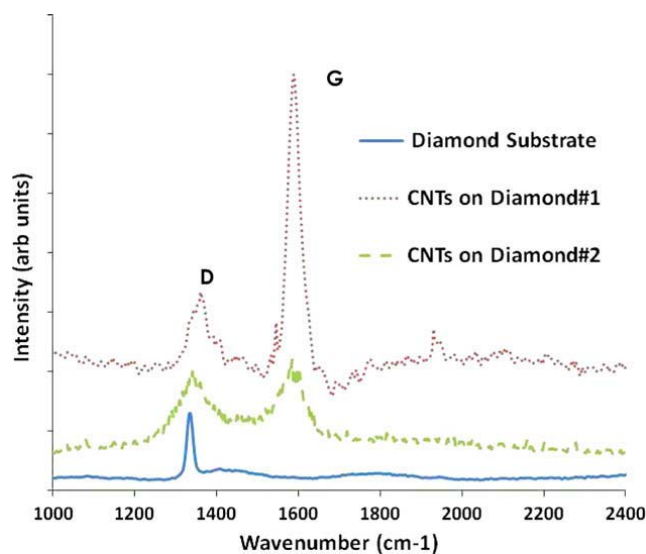


Figure 3.3. Raman spectra taken from a diamond substrate as compared to CNT/diamond samples

Complete CNT coverage of rough diamond substrates is very important for improved thermal contact. Experiments were conducted with several samples of different metal layer thicknesses and sputtering parameters to determine the effect on catalyst coverage, as coverage

of the catalyst particles will determine the final CNT coverage. Since intermediate layers were not used, catalyst particle coarsening was likely to occur during annealing. In addition, the facets present in the diamond could assist in the rapid coarsening of the catalyst particles due to the presence of the valleys between grains. Figure 3.4 shows a CNT grown on a diamond sample deposited with a 2–5 nm thick Ni–9%W–1.5%Fe catalyst using initial set of sputtering conditions (30 mA, 0.44 kV, 200 mtorr Ar, 10 min). After the CNT growth on these samples, it can be seen that only certain facets were found to be covered with a high density of CNTs (bright areas), whereas other areas appear to have a very low density (dark areas). Although the whole area of the substrate was exposed to CNT growth, only certain areas had the appropriate metal catalysts necessary for the growth and this resulted in partial coverage of the surface.

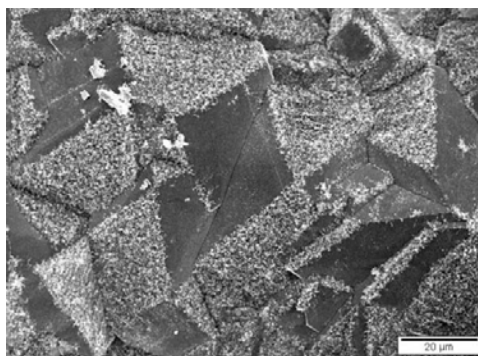


Figure 3.4. Partial coverage of CNTs grown on diamond substrate partially covered with Ni–W–Fe deposited by using initial sputtering conditions

Proper coverage of the surface was obtained using optimized sputtering conditions (190 mA, 0.32 kV, 200 mtorr Ar, 2 min) and around 5–9 nm thick Ni was deposited to create the catalyst nanoparticles. As shown in Figure 3.5, complete coverage of the substrate with CNT growth is possible with a catalyst layer. Although the initial diamond substrate surface was rough due to the faceting, the surface is completely covered with a thin layer of CNT carpet. A higher magnification photomicrograph of the samples is shown in Figure 3.6, where randomly-oriented CNTs can be clearly seen. A cross-sectional SEM micrograph of the sample shown in Figure 3.7 demonstrates that 3–5 μm thick CNT carpet is present on the samples. Samples processed with the optimized sputtering conditions for Ni–9%W–1.5%Fe also provided similar CNT coverage. Although the initial diamond substrate surface was rough due to the faceting, the surface is completely covered with a thin layer of CNT carpet. A higher magnification photomicrograph of the samples is shown in Figure 3.6, where randomly-oriented CNTs can be clearly seen. A cross-sectional SEM micrograph of the sample shown in Figure 3.7 demonstrates that 3 to 5 μm thick CNT carpet is present on the samples. Samples processed with the optimized sputtering conditions for Ni–9%W–1.5%Fe also provided similar CNT coverage.

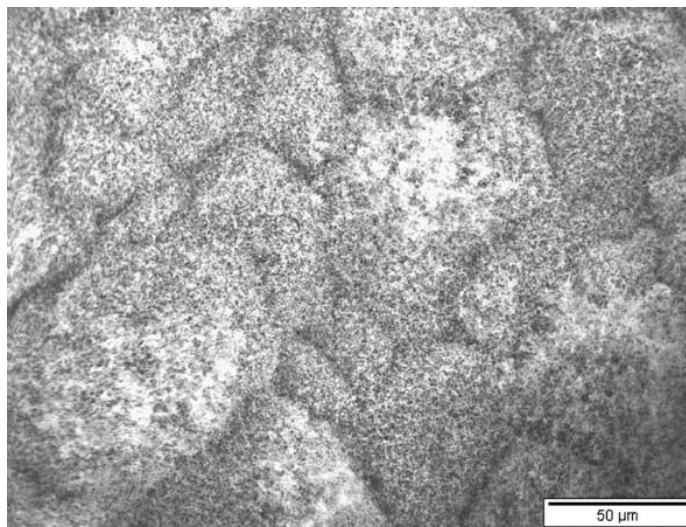


Figure 3.5. Complete coverage of CNTs on diamond substrates with Ni catalysts deposited by sputtering using optimized conditions

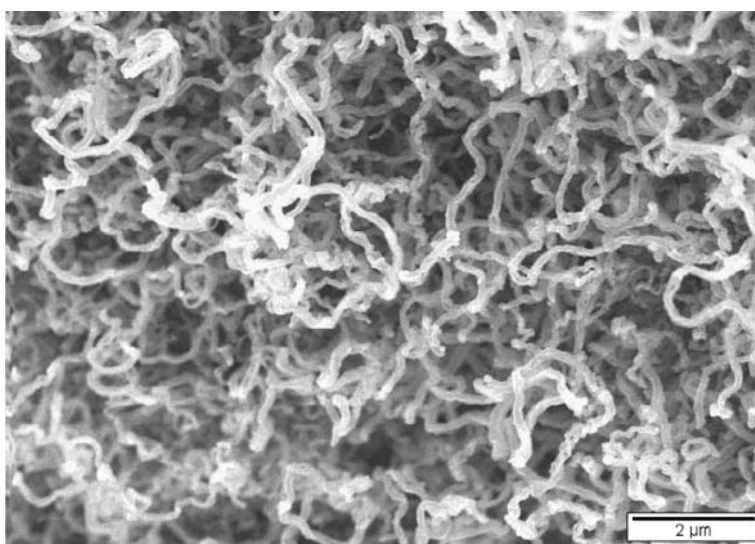


Figure 3.6. Higher magnification photomicrograph showing the CNTs grown on a diamond substrate

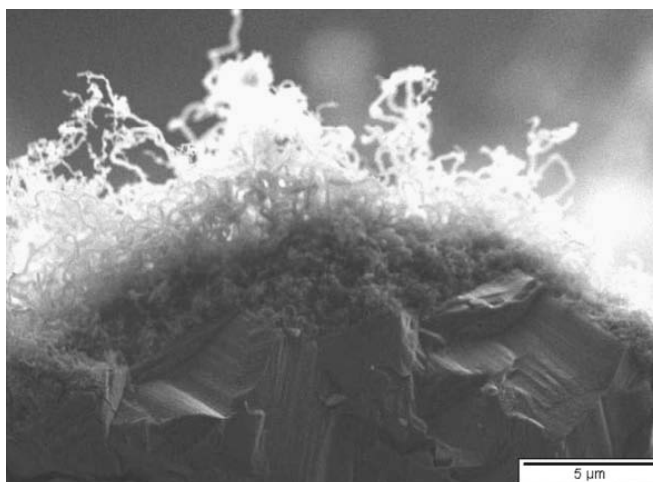


Figure 3.7. Cross-sectional SEM image showing CNTs grown on a diamond substrate

CNTs observed by TEM, as shown in Figure 3.8 (a), indicate that the diameter of the samples is around 20 nm. High resolution TEM of the samples show that growth of high crystalline- quality CNTs on diamond substrates is possible. This particular image is of a MWCNT where 16 walls are present as shown in Figure 3.8 (b). In order to further confirm the quality of these CNTs, Raman spectra were taken on different samples. Figure 3.3 shows a D/G peak ratio of 0.89 for the sample grown in atmospheric pressures (CNT/diamond #2). However, in other samples (CNT/diamond #1) grown with Ni islands and 400 sccm of C_2H_2 flow rate in 90 torr of pressure, a D/G ratio as low as 0.3 was obtained as shown in Figure 3.3 indicating the possibility of growing high-quality MWCNTs on diamonds. It is shown in the literature that smaller the D/G ratio, the better the structural purity of the graphitic materials [19] and in the present study samples showed D/G ratios of 0.2–0.3 when grown in low pressure.

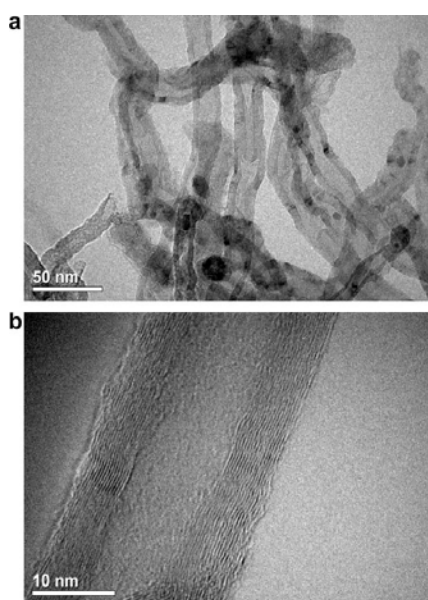


Figure 3.8. (a) TEM micrograph showing 20 nm diameter CNTs grown on diamond substrates, and (b) high resolution TEM micrograph showing 16 walls of highly crystalline MWCNT

The lower pressure growth seems to improve the D/G ratio of CNTs grown on diamond as opposed to atmospheric pressure growth. While increasing the growth times resulted in longer tubes, the growth temperature variations between 750 and 800 °C did not show much noticeable changes in CNTs. Also, prior heat treatment of the catalyst islands did not appear to influence the growth of CNTs, as the samples heated in Ar/H₂ environment prior to CVD or the samples treated in the CNT furnace yielded similar quality CNTs. With the growth of CNT on diamond substrates demonstrated as possible for thermal applications, thermal resistance measurements of these substrates are underway.

3.4 Summary

It is shown that high-quality multi-wall CNTs can be grown on diamond substrates without using intermediate oxide buffer layers. Both Ni and Ni–9% W–1.5% Fe catalysts deposited by optimized sputtering conditions were found to produce CNTs on rough diamond substrates. Proof of the good CNT crystallinity was provided by TEM and Raman spectroscopy, with a D/G ratio of 0.2–0.3 in Raman spectra being observed on such samples.

3.5 References

- [1] Hartmann J, Reichling M. Thermal transport in diamond. In: Nazare MH, Neves AJ, editors. Properties, growth and applications of diamonds. London: INSPEC; 2001. p. 32–9.
- [2] Bigelow LK. Diamond coatings. *J De Phys IV* 1993;3:897–902.
- [3] Seelmann-Eggebert M, Meisen P, Schaudel F, Koidl P, Vescan A, Leier H. Heat spreading diamond films for GaN-based high power transistor devices. *Diam Relat Mater* 2001;10:744–9.
- [4] Tong T, Zhao Y, Delzeit L, Kashani A, Meyyappan M. Dense vertically aligned multiwalled carbon nanotube arrays as thermal interface materials. *IEEE Trans Compon Pack Technol* 2007;30(1):92–100.
- [5] Kordas K, Toth G, Moilanen P, Kumpumaki M, Vahakangas J, Uusimaki A, et al. Chip cooling with integrated carbon nanotube microfin architectures. *Appl Phys Lett* 2007; 90: 123105-1–123105-3.
- [6] Zhu L, Hess DW, Wong CP. Assembling carbon nanotube films as thermal interface materials. In: Conference on electronic computing technology IEEE proceedings; 2007. p. 2006–10.
- [7] Cola BA, Xu X, Fisher T. Increased real contact in thermal interface: a carbon nanotube/foil material. *Appl Phys Lett* 2007; 90: 093513-1–093513-3.
- [8] Xu J, Fisher T. Enhancement of thermal interface materials with carbon nanotube arrays. *Int J Heat Mass Trans* 2006;49:1658–66.
- [9] Cola BA, Xu X, Fisher T, Capano M, Amana P. Carbon nanotube array thermal interfaces for high temperature silicon carbide devices. *Nano Micro Thermo Eng* 2008;12:228–37.
- [10] Wang H, Feng J, Hu X, Ng KM. Synthesis of aligned carbon nanotubes on double-sided metallic substrates by chemical vapor deposition. *J Phys Chem C* 2007;111:12617–24.
- [11] Varanasi C, Bulmer J, Brunke L, Burke J, Baca J, Yost K, et al. Growth and characterization of carbon nanotubes on constantan Ni–Cu–Mn alloy metallic substrates without adding additional catalysts. *J Vac Sci Technol A* 2008; 26: 832– 835.

- [12] Ngo Q, Cruden BA, Cassell AM, Sims G, Meyyappan M, Li J, et al. Thermal interface properties of Cu-filled vertically aligned carbon nanofiber arrays. *Nanoletters* 2004;4(12):2403–7.
- [13] Barnes PN, Wu R. Nucleation enhancement of diamond with amorphous films. *Appl Phys Lett* 1993;62(1):37–9.
- [14] Mia HY, Lue JT, Chen SY, Chen SK, Ouyang MS. Growth of carbon nanotubes on transition metal alloys by microwave enhanced hot-filament deposition. *Thin Solid Films* 2005;484:58–63.
- [15] Fabisiak K, Banaszak A, Kaczmarek M, Kozanecki M. Structural characterization of CVD diamond films using Raman and ESR spectroscopy methods. *Opt Mater* 2006;28:106–10.
- [16] Ramamurthi R, Shanov V, Singh RN, Mamedov S, Boolchand P. Raman spectroscopy study of the influence of processing conditions on the structure of polycrystalline diamond films. *J Vac Sci Technol A* 2006;24(2):179–89.
- [17] Morelli DT, Beetz CP, Perry TA. Thermal conductivity of synthetic diamond films. *J Appl Phys* 1988;64(6):3063–6.
- [18] Verhoeven H, Floter A, Reib H, Zachai R, Wittoerf D, Jager W. Influence of the microstructure on the thermal properties of thin polycrystalline diamond films. *Appl Phys Lett* 1997;71(10):1329–31.
- [19] Antunes EF, Lobo AO, Corat EJ, Trava-Airoldi VJ, Martin AA, Verissimo C. Comparative study of first-and second-order Raman spectra of MWCNT at visible and infrared laser excitation. *Carbon* 2006;44:2202–11.

4. Growth and Characterization of Carbon Nanotubes for Thermal Management and Electrical Applications

4.1 Research Objectives

This research mainly addresses (1) basic scientific issues related to the direct growth of CNTs on substrates applicable to advanced electronics packaging solutions such as ceramics, metals, and carbon based foam structures; (2) functionalization and/or metallization of the CNT arrays to form thin CNT-metal composite layers on the surfaces of these substrates; and (3) characterization of the resulting thermo-mechanical properties of the integrated micro-composite layers. The effort is also focused on investigating how CNT growth methods along with pre- and post-processing techniques affect the thermo-mechanical properties and performance of CNTs grown on various substrates and foams. The goal and impact of this effort is to grow CNTs onto strategically selected substrates to act as an interface layer in the packaging of high temperature power electronic components such as silicon carbide (SiC) devices. In addition to potential reductions in interfacial thermal and electrical resistance, using CNT based layers should act as an elastic heat sink or heat spreader layer. Specifically, it may allow for the joining of two thermally incompatible packaging layers, resulting in improved reliability of devices that are thermally cycled within lamellar compact packages. The primary benefit potential is both an enhancement of thermal interfacial impedances and improved thermal expansion coefficient mismatch stress reduction.

Specific objectives and subcategories under this effort include:

- *Expand CNT growth processing capabilities.* Modify thermal chemical vapor deposition (ThCVD) procedure and institute new floating catalyst chemical vapor deposition (FCCVD) method for deposition on two and three-dimensional (3D) substrates; and develop processes to realize CNT growth on metal foils for the purpose of creating a micro-carbon composite layer on the surface of Cu and other candidate foils.
- *Investigation of the growth and functionalization of nanotubes on porous cellular carbon materials.* Demonstrate CNT growth on vitreous carbon based foam structures for heat transfer applications such as heat sinks for electronics cooling applications; Determine the effects of carbon foam surface pre-treatment on CNT growth and morphology/structure
- *Development of processes to grow CNT with controllable structure/morphology on metal foil substrates.* Create a flexible thermal interface CNT layer by using a chemical vapor deposition (CVD) method; Determine the effects of CVD processes and buffer layer on CNT morphology, quality, thermal and interfacial properties

4.2 Approaches

4.2.1 *Growth of CNT Layer with Controllable Structure/Morphology on Metal Foil Substrates*

Compared to growing CNTs on conventional inert substrates (e.g., SiO_2), direct growth of CNTs onto reactive metallic substrates (such as Cu or Al foil) is still a challenge. The main difficulty lies in controlling the CNT growth structure and morphology due to diffusion of metallic catalysts, such as Fe or Ni, into metallic substrates. To solve this problem, a thin buffer layer, such as Al_2O_3 or SiO_2 , is pre-coated on the metal foil substrate, followed by CNT growth using the THCVD and FCCVD method. Results indicate that the buffer layer plays a key role in influencing the CNT growth and morphology such as density, alignment and thickness. Therefore, the effect of materials and thickness of buffer layer as well as layer deposited method on CNT growth and quality are investigated in order to gain an understanding of the parametric control required to achieve specific CNT characteristics and properties.

Using a CNT layer as a thermal interface material, the large thermal contact resistances and weak interfacial adhesion are two of the most pressing challenges due to the low fraction of CNT-substrate contact and lack of chemical bonding between the CNT and the substrate surface. Therefore, managing the CNT/substrate interface to effectively reduce the thermal contact resistance and simultaneously improve the interfacial adhesion is another beneficial research focus area. To address these challenges, we use different surface treatment methods such as varying buffer layer material, thickness, deposition method, and substrate roughness modification.

4.2.2 *Growth and Functionalization of Nanotubes on Porous Cellular (Foam) Carbon Materials*

Carbon foam (CF) is a low cost, light weight, and thermally conductive material. CNTs have impressive mechanical, electrical, and thermal properties. Growing CNTs on carbon foam provides a large surface area that is ideal for heat transfer or heat spreader applications. Preliminary experiments are ongoing to determine the best methods to evenly distribute the growth of CNTs throughout the entire depth of the foam to enhance the appealing properties of the foam. To reach this goal, the effort during this reporting period is focused on using different surface treatment methods on carbon foam substrates, followed by CNT growth using a floating catalyst chemical vapor deposition (FCCVD) method. Five types of surface modifications on carbon foam are used to investigate the effect of CF surface treatment on CNT growth. In comparing the CNT growth results, we find that samples coated with an Al_2O_3 thin layer by atomic layer deposition (ALD) yield dense, aligned CNT forest growth.

Aligned CNTs with different lengths and density were successfully grown throughout carbon foam substrates by changing the buffer layer material and thickness. This controllable growth capability allows us to determine the effect of the CNT layer structure on the thermal and mechanical properties. In addition, using both electrode and electro-less plating methods, we deposited a nickel layer onto the CNTs to further enhance the interfacial properties of the CNT layer with mating substrate, which resulted in improved thermal and electrical transport properties. This metallization step also can serve as active sites/catalysis for further modification and assembling of CNTs.

4.2.3 Characterization of the Structure and Thermal and Mechanical Properties of CNT Based Nano-composites

As with any scientific analysis, methodical experimentation is important. It is important to use what is learned and improve on the experimental methods to achieve the goals and objectives. As known, the properties and performance of the integrated nanotube structures (nanocomposite) depend on CNT structure, morphology and interface connection. Therefore, the characterization of the nanostructures and the determination of the nanomaterial properties are important for improving the growth methods and techniques, which is necessary to achieve our research objectives. In order to control the CNT layer structure quality, the samples made by different growth methods – before and after substrate pre-treatment and post-CNT growth – will be analyzed and characterized. The primary characterization methods will involve samples generated for atomic force microscopy (AFM), high resolution scanning electron microscopy (HR-SEM), Raman spectroscopy, laser flash, thermal impedance measurements and a custom pull-off tester. Details of the structure/property characterizations will be described in the next section.

4.3 Growth of CNT on Copper and Metal Foil

4.3.1 Introduction

Carbon nanotubes (CNTs) with unique thermal/electrical/mechanical properties and inherently large surface area are an attractive candidate for integration into thermal structures and for a flexible thermal interface material in power electronics packages. Although vertically-aligned (VA) CNT synthesis on silicon substrates has been widely investigated and has shown great promise [1-3], integrating these CNT/Si composites into an actual package configuration is not a trivial endeavor. Namely, the high temperatures needed for CNT growth would ruin most conventional Si based electronic devices. Hence, trying to grow CNTs directly on the back of a Si die would be ill-advised. Instead, growth of CNTs directly onto one of the metallic substrates typically used for packaging would be preferred [4, 5]. Copper is one of the most common of these metallic components and has been used in many applications due to its high thermal and electrical conductivity and with respect to low cost. The direct growth of nanotubes on Cu or other metal substrates would not only provide a thermally conductive transition layer between materials of varying thermal expansion rates, but it would also eliminate some processing steps and reduce the number of resistive junctions in the package. Furthermore, these CNTs/metal composite structures could be used as a conductive support for different applications such as energy storage, sensing, and nano-electronics etc. [4].

Using Vertically Aligned CNTs (VA-CNT) as a thermal interface material has been extensively reported [6-12]. Compared to CNT growth on conventional inert substrates (such as SiO₂), controlling CNT growth, structure and morphology on active metallic substrates is much more of a challenge. The reason is because the diffusion between metallic catalyst (such as Fe or Ni) and metallic substrate (for example Cu) under CNT synthesis conditions will reduce catalyst activity. So far, VA-CNT direct growth on various metal substrates has been reported by several groups, and growth of CNT directly on copper substrate is still not completely understood. For example, Wang et al. grew VA-CNTs on a copper foil surface by water-vapor-assisted CVD [13], but the quality and the structure of the “VA-CNTs” on copper were not clearly described. Recently, Yin et al. reported growing multi-walled CNTs on an oxygen-free copper substrate

with a poor CNT alignment [14]. VA-CNTs made in Fisher's research group by PECVD for thermal management [6, 9] exhibited different average diameters, diameter distributions and CNT coverage on the growth substrates even though the same synthesis conditions were used. Overall, quality, alignment and reproducibility of CNTs with desired structure/morphology are main issues for direct growth CNTs on metal substrates.

To grow CNTs directly on a metallic substrate, most researchers have paid more attention to CNT growth rather than the interfacial properties of CNTs/substrate, specifically, quantification of CNT to substrate bond strength. Therefore, the growth of CNTs on selected substrates with controllable structure and properties as application requirement, finding out the relationship of CNT structure/morphology with performance of CNT-based nanocomposites as well as increasing interface bonding strength between CNTs and metal substrate by varying catalyst and buffer layer, all of these as remained significant challenges and an active continuing area of research, have led us to begin further investigation.

As mentioned earlier, CNTs grown on an appropriate substrate is the first step towards providing a scientific basis for using CNT arrays as thermal interface materials (TIMs). To be able to advance from basic research to applied research, more needs to be understood with the connection of a CNT forest to a mating substrate, as illustrated in Figure 4.1. Several test methods have been used to measure the thermal contact resistance between VA-CNT arrays and the surface of a free mating substrate from a different interface connection method, such as compression force or solder anchoring, with varying results [6,7,9,15,16]. Throughout the referenced works' conclusions, two main issues of interface are common: 1) the thermal contact resistance at the CNT/mating substrate interface was large, and 2) the interfacial adhesion was extremely weak [17]. One reason for the large contact resistance is that there is a low fraction of CNT to substrate contact. More importantly, weak interfacial adhesion is because there is no chemical bonding or special association between the CNTs and the substrate surface. Thus, finding methods to modify the CNT/mating substrate interface to effectively reduce the thermal contact resistance and simultaneously improve the interfacial adhesion is a challenge. To solve these problems, we have just recently begun to focus on surface modification or functionalization by different methods, followed by an optimum CNTs surface metallization processing. This procedure not only increases the fraction of CNT to substrate contact, but it also can introduce proper active groups on CNT surface as a bridge to enhance adhesion of CNTs to the metal surface, such as that of a solder layer. As a result, this should provide a significant reliability improvement.

In our study, the interfacial adhesion between the CNT layer and substrate are measured using a custom-built pull-off tester. Thermal contact resistance data is collected using an *ASTM D5470 TIM Testing System* to measure pairs of Cu foil substrates with different interface materials, such as solder, thermal grease, and a CNT layer grown directly on one of the Cu foils. The electrical resistance of CNT grown on Cu as well as surface metalized CNT/Cu was also tested by a modified electrical testing system.

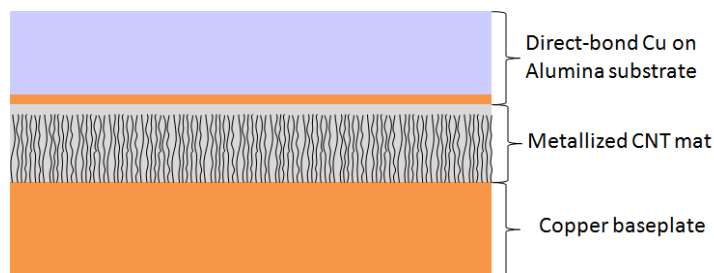


Figure 4.1. Scheme of assembling VA-CNT/Cu as a TIM

4.3.2 Experimental

4.3.2.1 Cu Substrate Preparation

As Figure 4.2 shows, the 99.99% pure copper foil (Cu) (300~400 μm thick, purchased from Vortex metals, Inc.) was cut into 8 x8 mm and 12.2x12.2 mm samples. The Cu samples were then cleaned via ultra-sonication in acetone followed by isopropanol for about 30 min per bath. The dried Cu substrates were then loaded into either a RF sputtering or an ALD system for thin film deposition. The sputter coating system (DV-502A) was employed to deposit a thin catalyst (Fe or Ni) layer (varying thickness) when applicable onto either bare Cu or Al_2O_3 coated Cu. The Al_2O_3 buffer layer (varying thicknesses) was applied to the Cu substrates at 200 $^{\circ}\text{C}$ with an ALD (Atomic Layer Deposition) system (Savannah S-100) or the sputter coating system (DV-502A).

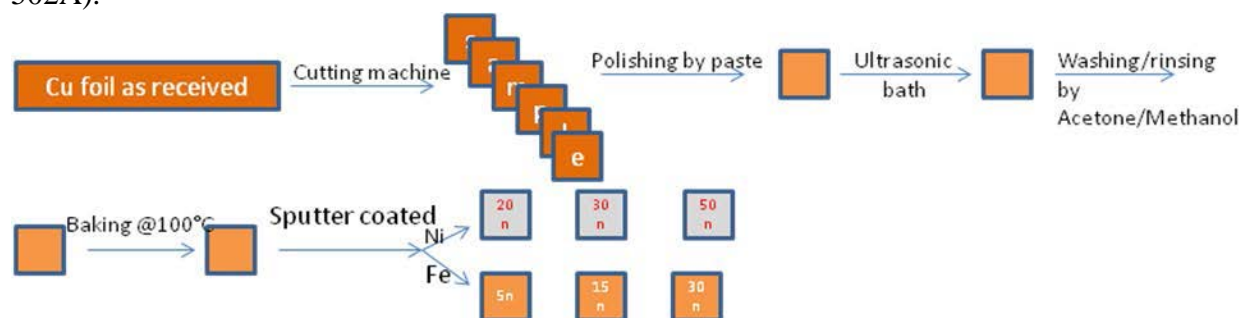


Figure 4.2. Schematic of substrate preparation procedure

4.3.2.2 Growth of CNTs on Cu substrate: Pre-coated catalyst thermal chemical vapor deposition (THCVD)

For THCVD growth of the CNTs, The general experimental processing scheme is shown in Figure 4.3. A tube furnace was set up as a horizontal CVD reactor for use in both annealing (catalyst thin film) treatment and CNT growth. First, the Cu substrates (loaded on a quartz tray) are put in the middle of the tube, and then the tube is pumped down to 7 mTorr, where it remained for 30 minutes. The furnace is then ramped to the desired annealing temperature in 300 sccm $\text{Ar}+\text{H}_2$ (5%) at 90 Torr. After this, the samples were annealed in-situ at the desired temperature (700 $^{\circ}\text{C}$, 750 $^{\circ}\text{C}$ or 800 $^{\circ}\text{C}$). When the desired annealing time was reached, the sample was quenched by immediately opening the furnace lid. Upon cooling, the CVD system was reheated to the desired growth temperature and a $\text{Ar}+\text{C}_2\text{H}_2$ (10%) precursor mixture was

introduced at 300 sccm along with 300 sccm Ar+H₂(5%); the pressure was kept at 90 Torr for 30 minutes. The precursor mixture was then turned off, and 300 sccm Ar+H₂(5%) was used to purge the tube of any residual carbon contaminants while holding at temperature for 5-10 minutes. The samples were then cooled to room temperature under the same purge gas flow conditions.

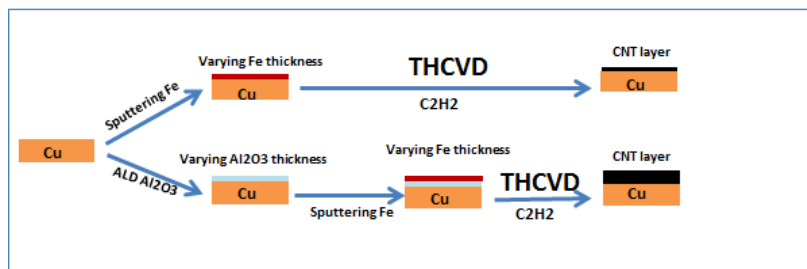


Figure 4.3. Scheme of processing for CNTs grown on Cu substrate by THCVD (Not to scale)

4.3.2.3 Growth of CNTs on Cu substrate: Floating catalyst thermal chemical vapor deposition (FCCVD)

A new FCCVD system has been implemented in our research Lab as shown in Figure 4.4. This liquid–vapor–solid phase precursor floating catalyst process allows for CNT growth on a variety of reactive substrates such as metal and carbon. It also provides a method to achieve highly conformal growth on non-planar or complex structure substrates such as foams.

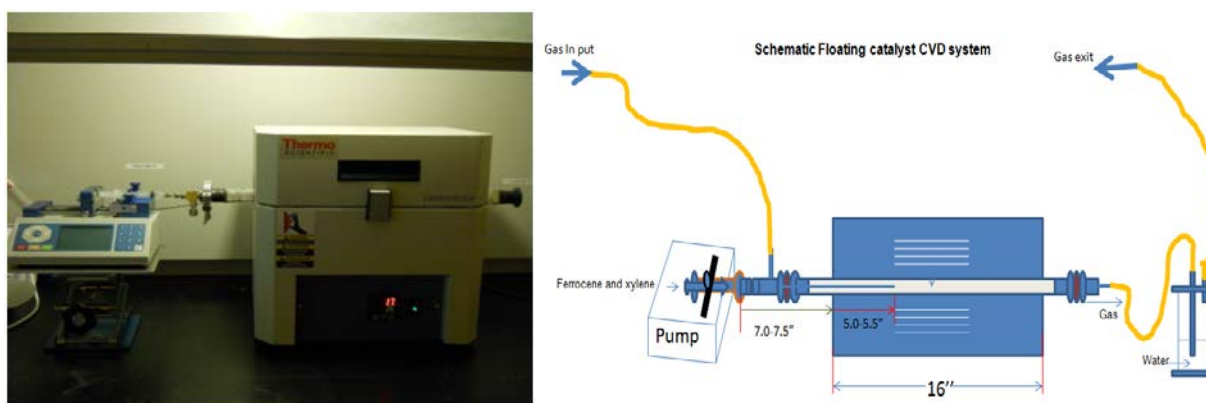


Figure 4.4. Floating catalyst thermal CVD (FCCVD) system

For FCCVD growth of the CNTs, the general experimental processing (scheme) is shown in Figure 4.5. A tubular furnace was also set up as a horizontal CVD reactor, and Cu substrates were placed in the middle of the quartz tube on the quartz tray. Ar and H₂ were used as the carrier gas with an Ar flow rate of 100 sccm (standard cubic centimeters per minute) and a H₂ flow rate of 50 sccm. A mixture of ferrocene/m-xylene (0.012 g/ml concentration) was used as the iron catalyst and carbon source, and was continuously fed into the furnace via a digital syringe pump at a desired feed rate during the reaction (at 750 °C). After the reaction, the samples were cooled to room temperature in flowing Ar and then removed from the quartz tube for characterization.

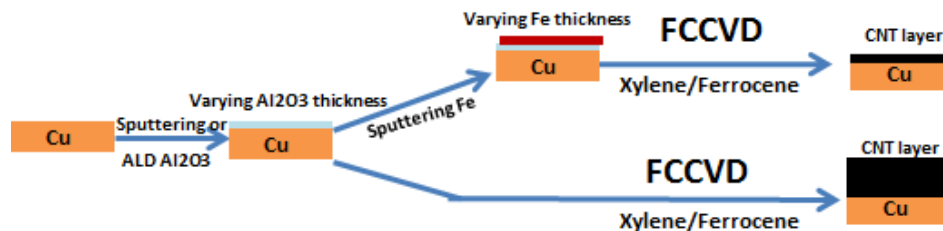


Figure 4.5. Scheme of processing for CNTs grown on Cu substrate by FCCVD (Not to scale)

4.3.2.4 Characterization of CNTs on Cu substrate

The properties and performance of integrated nanotube structures (nanocomposites) depend on CNT structure, morphology and interface connection. Therefore, systematic characterization of the nanostructures is important for improving the growth methods and techniques necessary to achieve research goals. The structure and morphology of CNTs grown on the Cu substrates at different method/conditions was studied using scanning electron microscopy (Jeol JSM-6060). Raman spectroscopy was performed using a Renishaw inVia Reflex Spectrometer System to determine the quality of the CNTs grown on Cu substrates (CNTs/Cu) by D/G peak ratio. The interfacial thermal impedance is determined by ASTM D5470 Thermal Interface Material (TIM) Testing System. A peel off tester was used to quantify CNT/substrate interfacial adhesion.

4.3.3 Results and Discussion

4.3.3.1 THCVD-grown CNTs

It has been reported that Cu alone can act as effective catalyst for CNT growth under certain conditions [18,19]. However, compared to Fe, or Ni, etc. the catalytic activity of Cu is much lower, and the grown CNTs catalyzed by Cu are “spaghetti-like” [20]. Therefore, to grow dense aligned CNTs on Cu substrates, a more active catalyst (such as Fe, Ni) needs to be introduced on the Cu surface. In order to eliminate processing steps and hopefully minimize contact resistance between CNT and Cu substrate, in our early experiments, Fe and Ni thin film catalyst was directly sputter deposited onto the Cu substrates. The studies were focused to investigate the effect of annealing/growth temperature and thickness of catalyst (Fe or Ni) layer on CNT quality. SEM is used to determine the CNT/Cu sample structure and orientation/morphology. The results of CNTs growth under different annealing/growth temperature and varying catalyst layer thicknesses are shown in Figures 4.6 and 4.7.

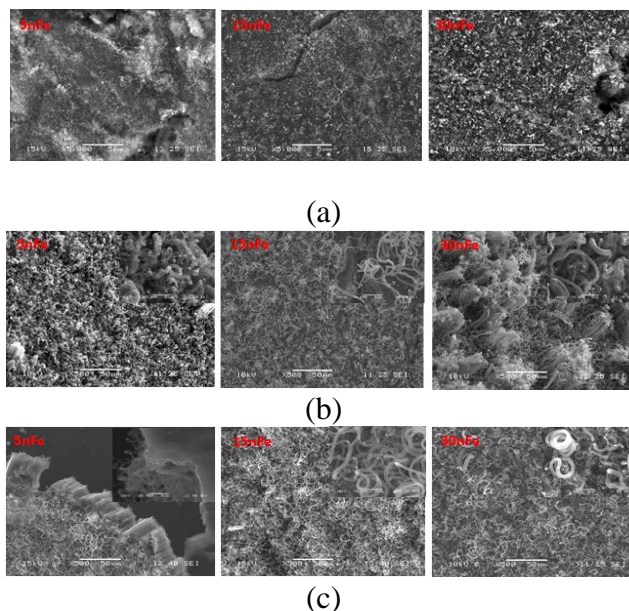


Figure 4.6. CNTs grown on Fe/Cu substrate with varying thickness of Fe layer and temperature. A=700°C; B=750°C; C=800°C

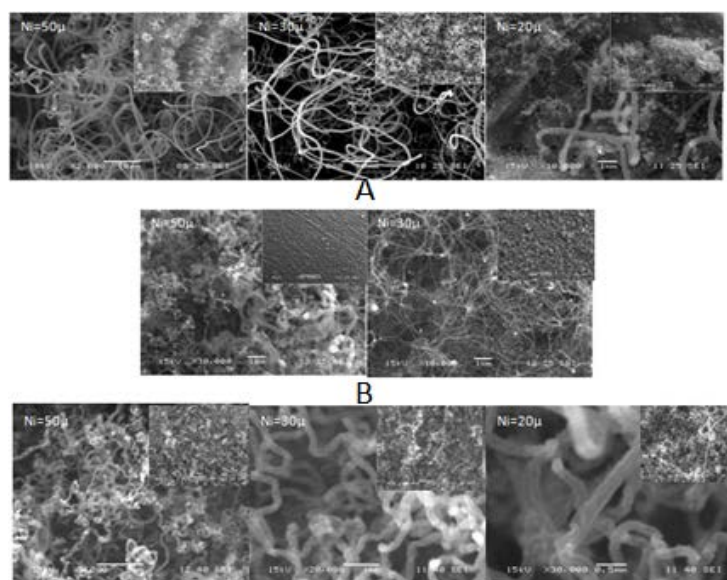


Figure 4.7. CNTs grown on Ni/Cu substrate with varying thickness of Ni layer and temperature. A=700°C; B=750°C; C=800°C

The SEM images indicate that through an optimized THCVD process, CNTs could be grown on Fe or Ni coated Cu substrates. As expected, the quality and morphology (such as diameter, density, coverage, etc.) of CNTs was affected by annealing/growth temperature and the thickness of catalyst as well as material. When annealing temperature or catalyst layer thickness was increased, the CNTs areal density increased on both Fe and Ni coated Cu substrate, and the CNTs were more likely to grow individually rather than as bundles on Fe coated Cu. Although a uniform, non-aligned CNT layer was achieved at 750 °C with 15 nm Fe and 30nm Ni coated Cu

substrate respectively, the most of CNTs were randomly distributed and tangled yielding a non-uniform film on the majority of the Fe/Cu and Ni/Cu substrates. The reason for this outcome was that Cu (substrate) tends to form a solid solution with the common CNT catalysts (such as Fe, Ni) at high temperature. Namely, the diffusion between catalyst and copper substrate inhibited catalyst activity and the resulting CNT growth. To overcome this problem, an effective method would be to deposit a thin barrier layer to restrains the diffusion reaction between catalyst and substrate [21].

A proper combination of the catalyst and the buffer layer material can result it uniform and dense catalyst islands for seeding CNT growth [22]. In our study, the Al_2O_3 buffer layer was deposited on the Cu surface by ALD. The effect of both Al_2O_3 and Fe layer thickness on CNTs growth, structure, morphology, and overall quality was investigated. The experimental results indicated that a uniform CNT layer could be grown on a bilayer (a thin layer of Fe on a support Al_2O_3 layer) coated Cu substrate by using THCVD, and the morphology of the CNTs was affected by the thicknesses of both the Fe and Al_2O_3 layers. For example, at a set Al_2O_3 layer thickness, when the Fe thickness was increased from 2 nm to 5 nm, the areal density/uniformity and the alignment of CNTs layer increased (Figure 4.8). Similarly, at a constant Fe layer thickness (5 nm), when the Al_2O_3 thickness was increased from 5 nm, to 10 nm, to 15 nm, and to 30 nm, we observed several trends (Figure 4.9). First, there was an overall, howbeit subtle, increase with the height of CNT forest; however, the highest CNT forest corresponded to the 15nm Al_2O_3 coated sample as opposed to the 30 nm. Secondly, as the buffer layer thickness increased, the morphology of top surface seemed to change. This was more likely due to changes in CNT length and areal density. Finally, the diameter of the CNTs tended to remain constant regardless of the thickness of the buffer layer.

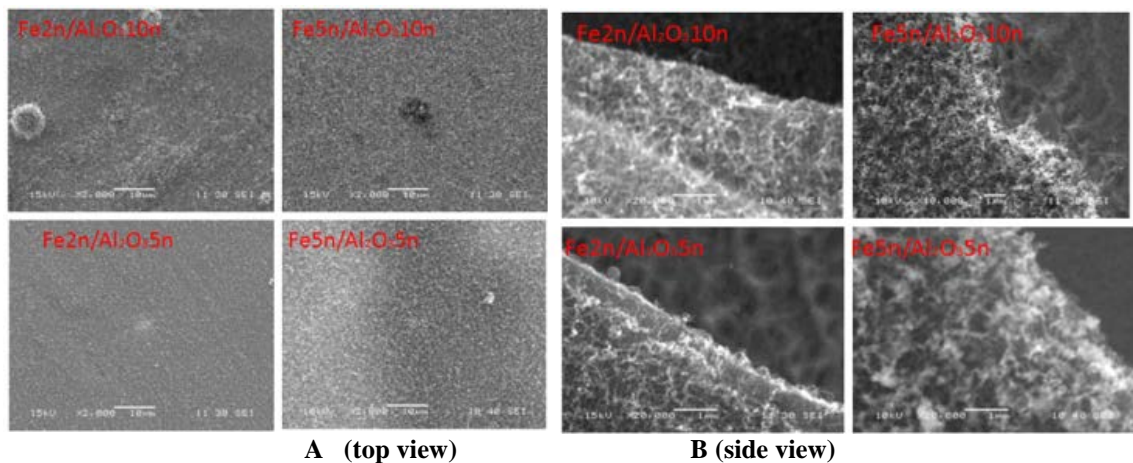


Figure 4.8. CNTs growth on Fe/ Al_2O_3 /Cu substrate

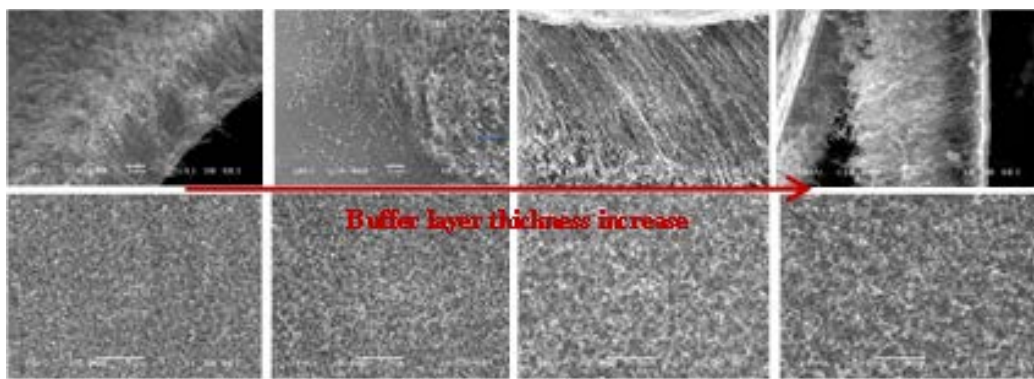


Figure 4.9. CNTs growth on Fe/Al₂O₃/Cu substrate with varying thickness of Al₂O₃, Left to right = 5 nm, 10 nm, 15 nm 30 nm

As it is known, the size and morphology of catalyst plays a key role in CNT growth, morphology, and structure. They can greatly affect where CNT nucleation occurs at the catalyst surface and lead to distinctly different growth scenarios [23]. For the THCVD method, under same growth conditions (temperature, time, and pressure, etc.), the catalyst size and morphology will be controlled solely by catalyst and buffer layer thickness. Hence, this was the reason why the CNT growth was so greatly affected by Fe and Al₂O₃ layer thickness as discussed above.

4.3.3.2 FCCVD-grown CNTs

Compared with traditional CVD methods, the advantage of FCCVD is that it allows the catalyst and carbon source to be introduced into the reactor simultaneously to produce well-aligned CNTs on various substrates [16]. With this method, keeping all other CNT growth parameters constant (temperature = 750 °C, Xylene/Ferrocene concentration = 0.012 g/ml), the effect of Al₂O₃ buffer layer thickness and growth time on CNT morphology/quality was investigated. The thickness of the Al₂O₃ film was either 0 nm (pure Cu substrate without buffer layer), 5 nm, 10 nm, 15 nm or 30 nm; the growth time was either 20 min or 40 min. Based on the SEM results of this set of experiments as shown in Figure x-y, several observations were made. First, as expected, the choice of buffer layer certainly played an important role in the growth of a uniform, dense and aligned CNT forest on the Cu substrate (Figure 4.10). Second, at a growth time of 20 min, when the Al₂O₃ thickness was increased from 5nm to 10nm, the CNT layer length is increased from 15μm to 20μm. Interestingly, there was no effect on CNTs length when buffer layer was increased to 15 and 30 nm in thickness. Thirdly, at 40 min growth, there was a significant increase in CNT layer thickness when the buffer layerthickness was increases from 5 nm to 10 nm and from 15 nm to 30 nm. For some yet unexplained reason, however there was no noticeable effect on CNTs length when buffer layer thickness changed from 10nm to 15nm (Figure 4.11). Forth, for all thicknesses except the 5 nm Al₂O₃, an increase in growth time resulted in an increase in CNT length (the maximum length ranged from 22μm to 80μm). Fifth, the areal density, CNT layer surface flatness and CNT bundle alignment all increased with increasing Al₂O₃ thickness, regardless of growth time (Figure 4.11). The alignment improvement wasperhaps most noticable when the buffer layer thickness was increased from 5nm to 10nm (Figure 4.12). Finally, the diameter of the CNTs (Figure 4.13, d=40nm~50nm) was independent of buffer layer thickness and growth time.

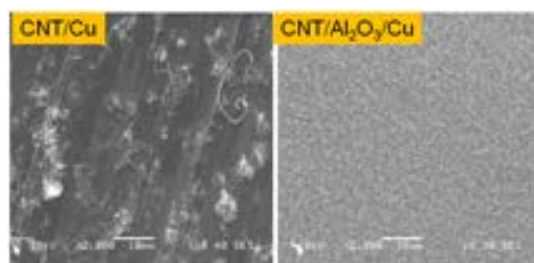


Figure 4.10. CNTs growth on pure Cu (*left*) and Al₂O₃/Cu (*right*) substrate by FCCVD

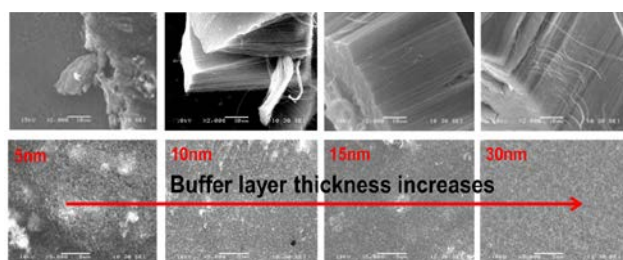


Figure 4.11. CNTs growth on Al₂O₃/Cu substrate with varying thickness of Al₂O₃ (Left to right = 5 nm, 10 nm, 15 nm, 30 nm)

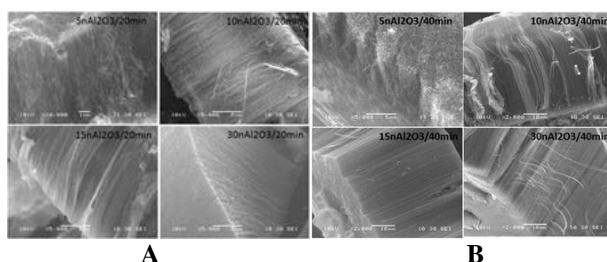


Figure 4.12. Alignment of CNTs grown on Cu substrate with varying thickness of Al₂O₃ layer Growth Time: A = 20 min; B = 40 min

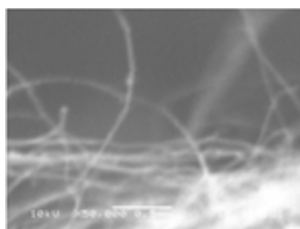


Figure 4.13. Diameter of CNT grown on Cu substrate with varying thickness of Al₂O₃ layer

In order to investigate the effects of the buffer layer, including thickness and coating methods, we have grown CNTs on metal foil substrates such as copper (Cu), stainless steel (SS), nickel (Ni) and aluminum (Al), which were coated with Al₂O₃ by sputtering and atomic layer deposition (ALD). For comparison with Al₂O₃, SiO₂ is also used as a buffer layer on the Cu foil. The FCCVD system was used to run all experiments. The procedure and conditions of CNT growth on different metal foils as well as foil surface treatment method are described in Table 4.1.

Scanning electron microscopy was employed to characterize the morphology/structure of CNTs on the metal substrates. Some SEM images are shown in Figure 4.14. Results indicate that the buffer layer plays a key role in controlling CNT growth and morphology. High quality CNTs can be successfully grown on Cu, SS or Al and Ni substrates when the metal substrate is first coated with a thin layer of Al_2O_3 using ALD or sputtering, followed by growth of CNT using the FCCVD method. SEM analyses also reveal that the thickness of the Al_2O_3 buffer layer influences the density and alignment of CNT arrays grown on a Cu foil. Initial test results indicate that when using CNTs as a thermal interface material, the structure/morphology and thickness of the CNTs play an important role in the thermal performance. Therefore, the significant impact of these controllable growth capabilities is that they allow us determine the optimum CNT layer structure for eliminating resistive junctions and provides improved thermal and electrical transport properties, which will greatly increase the reliability and performance of thermal management of electronic power devices in modern aircrafts.

Compared to Al_2O_3 , when using SiO_2 as buffer layer, less dense and shorter CNTs are produced under the same growth conditions. Further research is needed to investigate the effect of different materials as buffer layers (such as TiN, Ti and SiO_2) with CNT growth and their performance.

Table 4-1. CNT synthesis conditions and results using FCCVD

Substrate	Buffer layer/ thickness/coating Method	Growth Temperature (°C)	Growth Time (min)	Ratio (Fe/Xylene) (g/10ml)	Feed rate (Fe/Xylene) (ml/Hr)	CNT Growth Result
Cu foil	Al_2O_3 /5, 10, 15, 30nm/ Sputter	730-750	20-40	0.10-0.24	1-3	Uniform, high dense
Cu foil	Al_2O_3 /5, 10, 15, 30, 160nm/ ALD	730-750	20-40	0.10-0.24	1-3	Uniform, high dense
Cu foil	SiO_2 /10nm / ALD	730-750	20-40	0.10-0.24	1-3	Uniform, Thin dark layer
SS foil	Al_2O_3 /10nm/ Sputter	730-750	20-40	0.10-0.24	1-3	Uniform, high dense
Ni foil	Al_2O_3 /10nm/ Sputter	730-750	20-40	0.10-0.24	1-3	Thin uniform dark layer
Al foil	Al_2O_3 /10nm/ Sputter	620-650	15-20	0.10-0.24	1-3	Thin uniform dark layer

*Gas flowing rate ratio: $\text{Ar}:\text{H}_2 = 100:50$ (2:1) sccm.

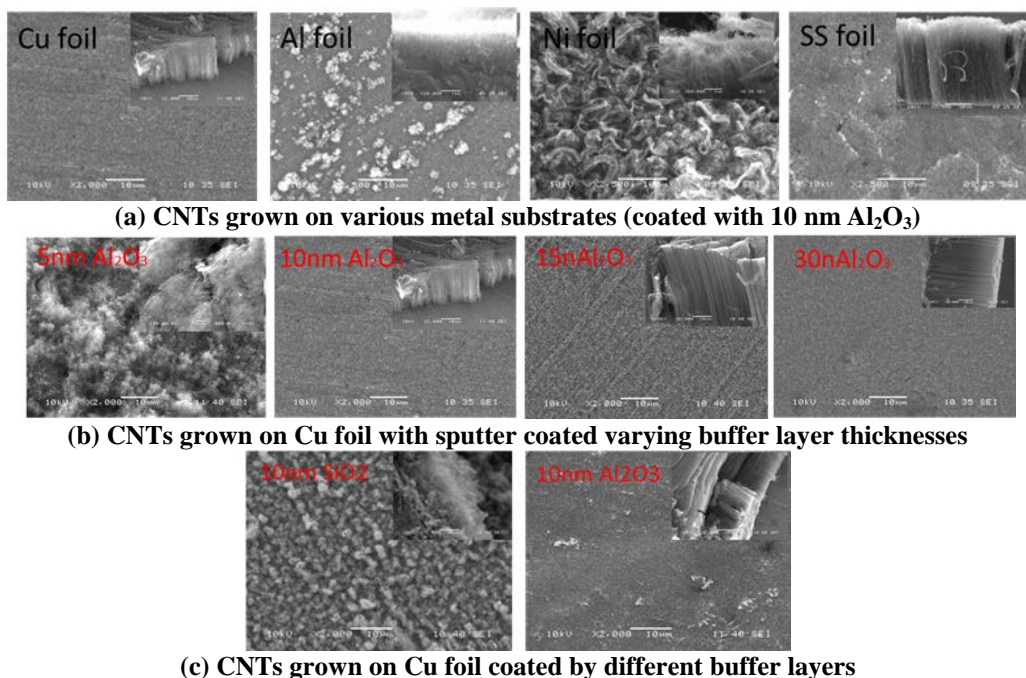


Figure 4.14. SEM images: areal density and alignment (insets) of CNTs

4.3.3.3 Quality of CNTs Grown on Cu Substrates

The quality of the CNTs in our study was determined by Raman spectroscopy using the D/G peak ratio with green (532 nm) laser radiation. D and G Peak for CNTs were observed at 1354cm^{-1} and 1588cm^{-1} , respectively. Upon compilation of the results (Figure 4.15), it was concluded that the CNTs grown on the Al_2O_3 coated Cu substrates via both THCVD and FCCVD resulted in acceptable D/G ratios (range 0.65-0.74). As a comparison, CNTs grown by THCVD resulted in a consistent D/G ratio of 0.74, which meant that the thickness of Al_2O_3 layer did not affected quality of the CNTs. Whereas the D/G ratio of the FCCVD samples showed a slight variation with increasing Al_2O_3 thickness: 0.65, 0.69, 0.73 and 0.68 corresponding to 5 nm, 10 nm, 15 nm and 30 nm, respectively.

From additional Raman results (*not shown*), we also found that (1) when using a different method (ALD or Sputtering) to coat Al_2O_3 on Cu foil as a thin buffer layer, the D/G ratio is almost identical, which means the quality of CNTs is not affected by Al_2O_3 coating method; and (2) when the buffer layer thickness is increased from 15 to 160 nm under same CNT growth conditions, the CNT quality decreases as confirmed by an increased D/G ratio from 0.63 to 0.86.

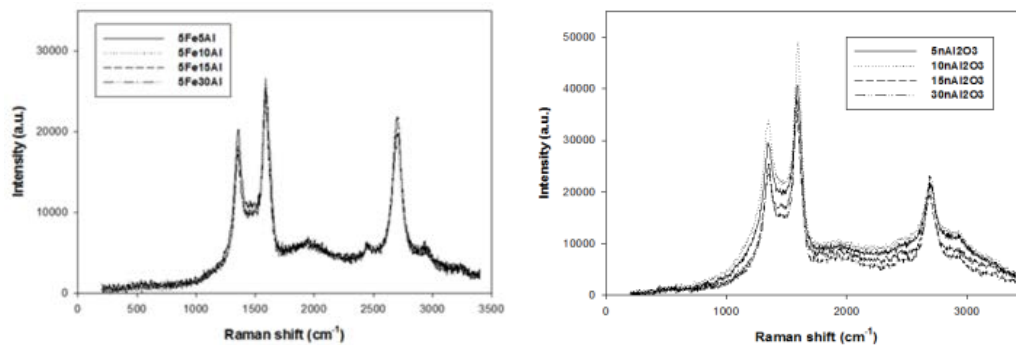


Figure 4.15. Raman spectroscopy of the CNT/Cu THCVd (left) and FCCVD (right)

4.3.3.4 Thermal Properties

According to ASTM D5470, the thermal impedance of Cu and CNTs/Cu samples were measured by using a TIM testing system as Figure 4.16 shows. The initial results are shown in Figure 4.17. As seen in the figure, when CNTs were grown on Cu substrate, the thermal impedance was lower than that of pure Cu foil. The reason for this improvement might be that CNT layer can provide a substantial increase in contact area at the cost of only a slight thickness increase. The experiment results also showed that when areal density and CNT length was increased, the impedance value was reduced. To fully understand these initial testing findings, more indepth studies are required in the future.

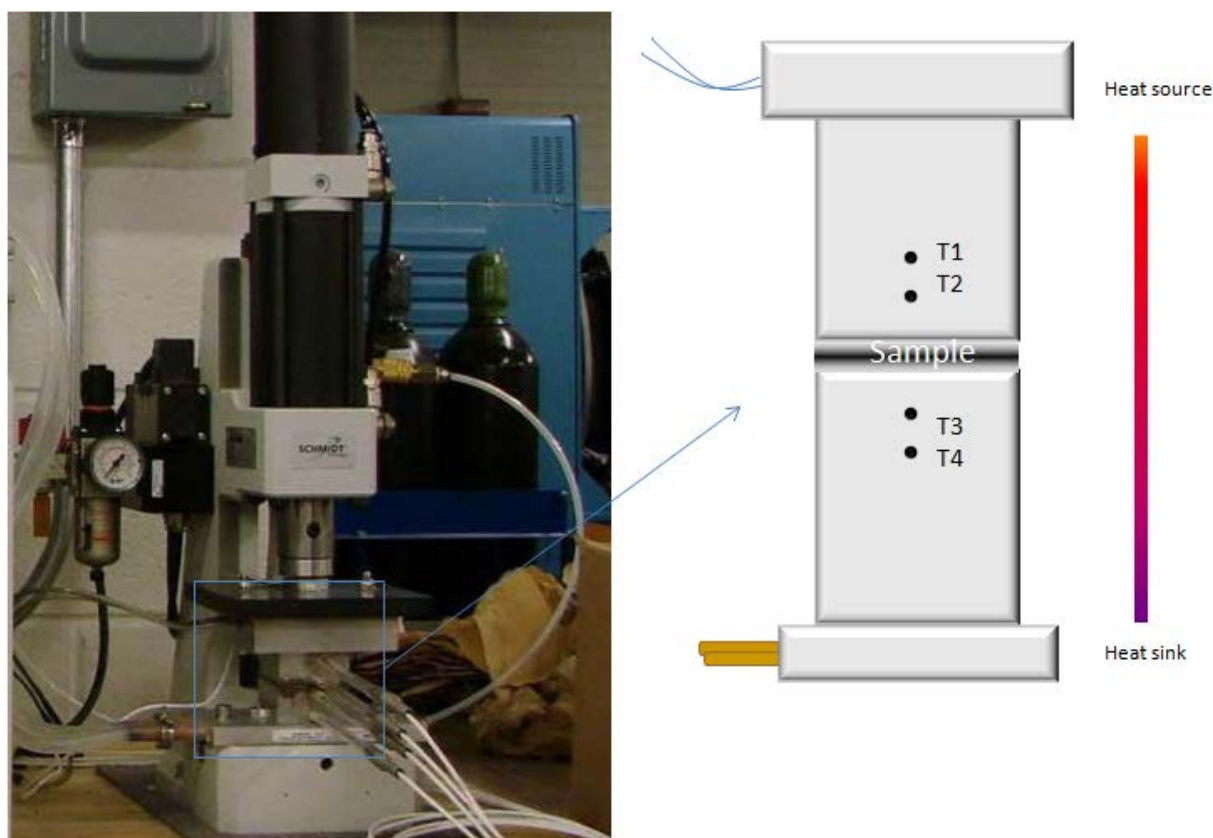


Figure 4.16. ASTM D5470 TIM Testing System

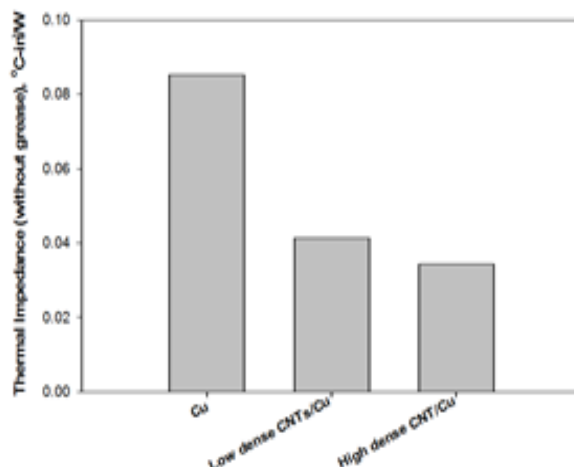


Figure 4.17. The effect of CNT layer on CNTs/Cu impedance Test condition: Pressure=80psi (without grease)

The initial thermal impedance results of pure Cu foil and CNT/Cu samples indicate that when short CNTs are grown on a Cu substrate, the thermal impedance is reduced as compared to pure Cu foil. In order to find out the different thermal interface materials effects on the thermal impedance, we did a series of tests with various interface materials including CNTs, grease, and Au/Sn solder under the same testing conditions (temperature and pressure) and then compared the results to a pair of cleaned Cu foils. The testing results of all samples with different interface materials are listed in Table 4.2.

Figure 4.18 shows the influence of different materials when used as thermal interface materials on the thermal impedance. From the initial experimental results, we can see that (1) using a CNT layer as an interface reduces the thermal impedance; and (2) solder (Au:Sn = 80:20) as an interface shows an increased impedance value. The reason for this is likely due to the thickness of solder layer and Cu foil surface oxidation during processing.

Table 4-2. Impedance testing results (3 tests on each sample)

Sample (Pair) Number	Thickness (μm)/Area (in ²)	Impedance-1 (°C in ² /w)	Impedance-2 (°C in ² /w)	Impedance-3 (°C in ² /w)	Impedance-Avg (°C in ² /w)
061013Cu/CNT/Cu-1	296,291 /0.25	0.0233	0.0242	0.0242	0.0239
061013Cu/CNT/Cu-2	303,296/0.25	0.1029	0.1047	0.1033	0.1036
061013Cu/CNT/Cu-3	303,298/0.25	0.0339	0.0341	0.0331	0.0337
061013Cu/Au-Sn/Cu-5	290,306/0.25	0.0782	0.0768	0.0774	0.0775
061013Cu/Au-Sn/Cu-6	300,307/0.25	0.0823	0.0806	0.0812	0.0814
061013Cu/Au-Sn/Cu-7	302,314/0.25	0.0788	0.0777	0.0770	0.0778
061013Cu/grease/Cu-8	303,300/0.25	0.0368	0.0366	0.0364	0.0366
061013Cu/grease/Cu-9	303,305/0.25	0.0334	0.0378	0.0332	0.0348
061013Cu/grease/Cu-12	299,306/0.25	0.0544	0.0537	0.0539	0.0540

*Test conditions: Pressure = 80 psi; Power = 20.8 W; Temperature = room temperature.

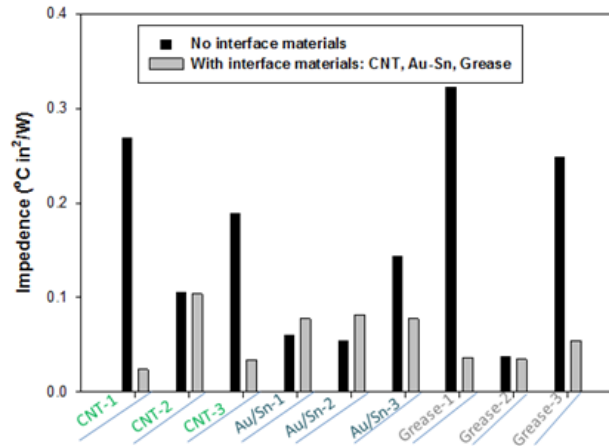


Figure 4.18. The effect of various interface materials on thermal impedance Test condition: Pressure=80psi

4.3.3.5 Interface Adhesion

The interfacial adhesion between the CNT layers and Cu substrates was first time measured with a peel-off tester (in Case Western Reserve University) with a preloading force around 4lbs (~0.3MPa). The results are summarized in Table 4.3. From the table, we can see that values for shear force was higher than normal force for all samples. The reason for this was that the contact area for the shear force test was larger than that of the normal force test. These initial experimental results also showed that the highest normal force and the highest shear force values corresponded to the with 5nm and 30nm Al₂O₃ coated samples, respectively. An SEM image of the CNTs-Cu interface of a sample after peel-testing supports these findings (Figure 4.19). As seen in the image, there was good adhesion between the CNT layer and Cu substrate. More research is needed to better understand the effect of buffer layer on interfacial properties.

Table 4-3. Interface Adhesive of CNTs/Cu

Sample: CNT/Cu	Buffer layer (nm)	Force (g)	Size (mm ²)
Normal Force	5nm Al ₂ O ₃	146	4.0x3.5
Shear Force		163	4.0x4.7
Normal Force	10nm Al ₂ O ₃	26	4.6x4.7
Shear Force		79	4.1x5.0
Normal Force	15nm Al ₂ O ₃	29	4.1x3.9
Shear Force		332	3.4x3'6
Normal Force	30nm Al ₂ O ₃	59	4.1x3.7
Shear Force		386	4.2x4.6

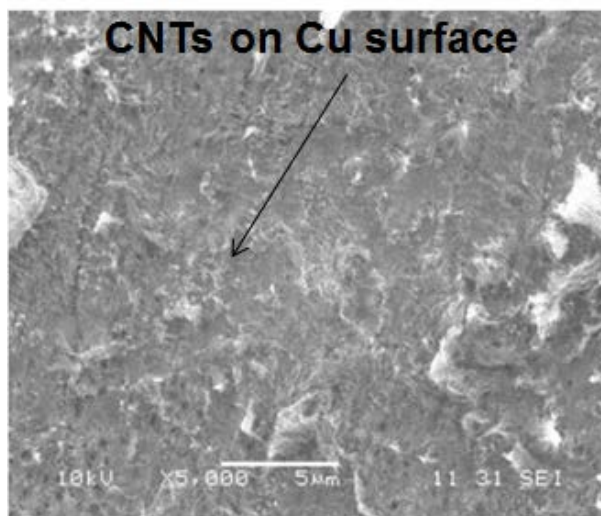


Figure 4.19. The image of CNTs-Cu interface after peel-off test

In order to better understand the effect of buffer layer on interfacial properties, more research is needed. Therefore, a custom-designed interfacial force tester is set up in our lab (Figure 4.20). Using this testing machine, several groups of samples were measured. The preliminary experimental results shown in Table 4.4 and Figure 4.21 indicate that (1) the interfacial adhesion is affected by the Al_2O_3 thickness when varied from 5 to 160 nm; and (2) when the Al_2O_3 buffer layer thickness is increased, the value of interfacial adhesion is reduced. Further investigation and characterization of interfacial relationship between the CNTs and substrate following the pull-off tests are needed to confirm and explain the preliminary results.

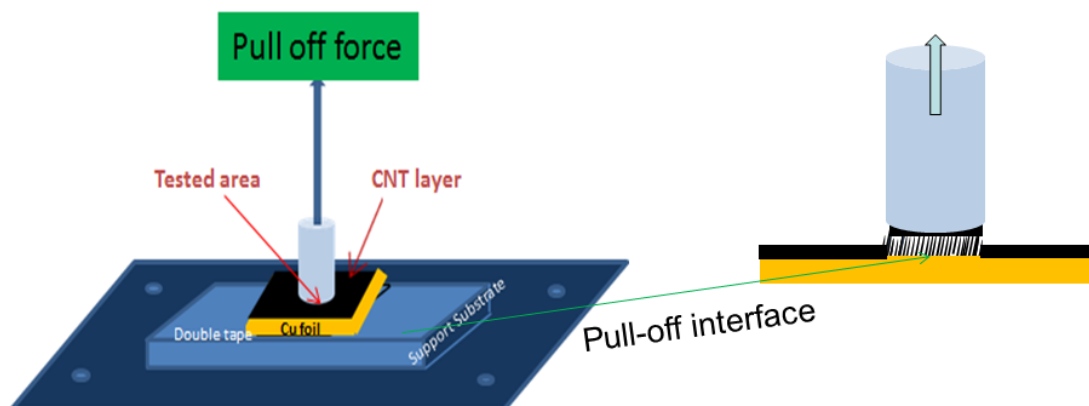


Figure 4.20. Scheme of interfacial force testing by a pull-off tester (*not to scale*)

Table 4-4. Interfacial adhesion of CNTs on Al₂O₃ coated Cu substrate

Sample	Buffer layer thickness/method	Pre-load (kg)	Pre-load time(m)	Normal pulley force (g)	Connect area (cm ²)	Interfacial adhesive strength (Mpa)
052913FCNT/Cu5n	5nmAl ₂ O ₃ /ALD/RQ	0.9700	5	784.0	0.1570	0.4994
		1.0809	5	307.5	0.1236	0.2488
052913FCNT/Cu10n	10nmAl ₂ O ₃ /ALD/RQ	0.9965	5	593.0	0.1943	0.3052
		1.0558	5	389.0	0.1229	0.3165
052913FCNT/Cu15n	15nm Al ₂ O ₃ /ALD/RQ	1.0870	5	476.0	0.1963	0.2425
		1.1060	5	280.0	0.1325	0.2113
052913FCNT/Cu30n	30nm Al ₂ O ₃ /ALD/RQ	1.0375	5	439.0	0.1861	0.2359
		1.1080	5	403.0	0.1904	0.2117
053113FCNT/Cu5n	5nm Al ₂ O ₃ /ALD/RQ	1.0960	5	345.5	0.0765	0.4516
		1.1170	5	154.5	0.0500	0.3090
053113FCNT/Cu15n	15nm Al ₂ O ₃ /ALD/RQ	1.1910	5	338.0	0.1589	0.2127
		1.0970	5	312.0	0.1684	0.1853
		1.1455	5	428.0	0.1230	0.3480
053113FCNT/Cu30n	30nm Al ₂ O ₃ /ALD/RQ	1.0670	5	402.5	0.2205	0.1825
		1.1975	5	337.5	0.2355	0.1433
		1.1330	5	416.5	0.2591	0.1607
053113FCNT/Cu160n	160nm Al ₂ O ₃ /ALD/RQ	1.0525	5	124.5	0.2355	0.0529
		1.1450	5	70.0	0.2159	0.0324
		1.0875	5	85.0	0.1809	0.0470
		1.0865	5	114.5	0.1590	0.0720

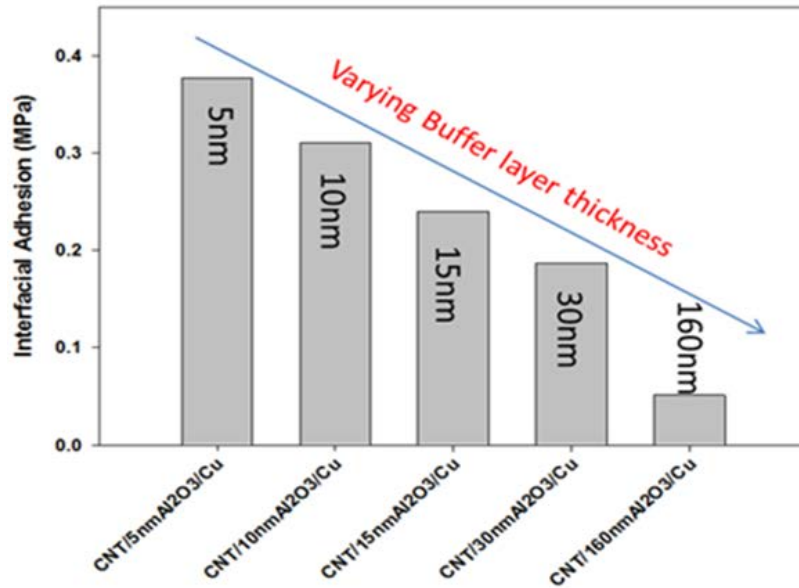


Figure 4.21. The effect of Al₂O₃ thickness on interfacial adhesion

4.3.3.6 Electrical Resistance Measurements of CNT/Cu

Using a custom-designed sample holder combined with an electrical testing system, the electrical resistance of Cu/Cu and Cu-CNTs-Cu (various thickness of CNT layer) samples have

been measured. Sample set up and testing results are shown in Figure 4.22 and Table 4.5, respectively.

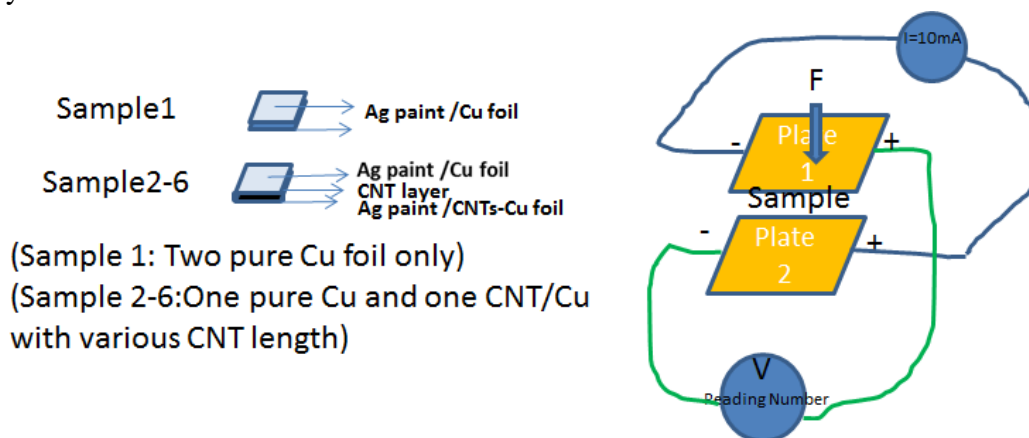


Figure 4.22. Schematic of sample electrical property testing

Table 4-5. Electrical Property of CNT/Cu Measurement

Sample	Pressure (Lb)	Reading value (mV)	Supplied Current (mA)	Contact area (in ²)	Resistance (Ω)
Ag/Cu-Cu/Ag (No CNT layer)	158	0.0428	10mA	1/2''x1/2''	0.0043
	163	0.0270			0.0027
	159	0.0198			0.0020
Ag/Cu-Cu/Ag (No CNT layer)	252	0.0117	10mA	1/2''x1/2''	0.0012
	254	0.0120			0.0012
	259	0.0130			0.0013
Ag/Cu- CNTCu/Ag Buffer (5nmAl ₂ O ₃)-s	250	0.0877	10mA	1/2''x1/2''	0.0088
	251	0.0875			0.0088
	251	0.0860			0.0086
Ag/Cu- CNTCu/Ag Buffer (10nmAl ₂ O ₃)-s	251	0.0356	10mA	1/2''x1/2''	0.0036
	251	0.0374			0.0037
	253	0.0360			0.0036
Ag/Cu- CNTCu/Ag Buffer (15nmAl ₂ O ₃)-s	253	0.0190	10mA	1/2''x1/2''	0.0019
	253	0.0198			0.0020
	250	0.0209			0.0021
Ag/Cu- CNTCu/Ag Buffer (30nmAl ₂ O ₃)-s	252	0.0191	10mA	1/2''x1/2''	0.0019
	250	0.0185			0.0019
	251	0.0168			0.0017
	250	0.0165			0.0017
Ag/Cu- CNTCu/Ag Buffer (15nmAl ₂ O ₃)- A	252	0.0369	10mA	1/2''x1/2''	0.0037
	252	0.0459			0.0046
	250	0.0451			0.0045
	253	0.0351			0.0035
	250	0.0335			0.0034

*Ag=Silver Paint; s-Sputter coating Al₂O₃; A-ALD coating Al₂O₃

According to Ohm's law for circuit theory, the resistance of a material is the applied voltage divided by the current drawn across the material across two electrodes.

$$R = V/I \text{ (1)}$$

Where: • R=Resistance (ohms,Ω) • V= Voltage (volts,V) • I = Current (amperes,A)

This electrical resistance is proportional to the sample's length and the resistivity and inversely proportional to the sample's cross sectional area.

$$R = \rho l/A \text{ (2)}$$

Where: • ρ = Resistivity • A =cross- sectional area • l = length

Based on Equation (1), using I and V value, we calculated R for each sample and shows in table 5. From results, we can see 1). When pressure is increased, the resistance is reduced with same sample. 2). Compared to pure Cu-Cu, Cu/CNT-Cu appears a higher resistance value 3). When CNT layer thickness /density is increased (determined by increased Al_2O_3 thickness), the resistance of Cu/CNT-Cu goes down. By equation (2), we can easily understand results 1) and 2) due to A and l changed. For result 3), we can also explain it by equation (2) because compared to thin and low dense CNT layer, the thicker /denser CNT layer with nano-size CNT diameter will make more contact area (A), and this contribution is much stronger than that of CNT length changed (l). The result also indicated that when using different method to coating same thickness Al_2O_3 on Cu substrate, and then to make CNT/Cu, the sample resistance is different. To verify this result, more testing is required.

4.3.4 Summary

As summarized in Table 4.6, a CNT layer could be grown on Cu and some metal foil by using both THCVD and FCCVD. If Fe was used as a catalyst, without a buffer layer on the Cu or metal foil surface, only sparse, poorly-aligned CNT forests are grown. When Al_2O_3 was used as a buffer layer, uniform/dense /aligned CNT forests could be grown on the Cu and some metal substrates via both THCVD and FCCVD. If the thickness of Al_2O_3 layer was increased (from 5 nm to 30 nm), the length and alignment of CNTs is increased as well. Additionally, the areal density and uniformity of the CNT forest was also improved. There was almost no effect on CNT diameter when the buffer layer thickness and CNT growth time were varied for both THCVD and FCCVD. Experiment results indicated that CNT length could be controlled by varying growth time in the FCCVD method. The Raman analysis suggested that the CNTs grown on the Al_2O_3 coated Cu substrates via both THCVD and FCCVD resulted in acceptable D/G ratios (range 0.65-0.74). The SEM image of a sample post peel-off testing showed good interfacial integrity between CNT layer and substrate. Initial thermal impedance testing results suggest that the CNT layer can improve interface connection and reduce contact resistance. Hence, the CNTs could be used a promising a thermal interface material.

Table 4-6. Effect of Growth method and buffer layer on CNT growth

CNT Growth Method	THCVD		FCCVD	
Al ₂ O ₃ Buffer layer	0nm	5 - 30nm	0nm	5 - 30nm
CNTs Areal Density / Uniformity	Low/No	High/Yes	Low/No	High/Yes
Alignment of CNTs	No	Yes	No	Yes

4.4 Growth of CNTs on Carbon Foam

4.4.1 Introduction

Carbon foam is thermally conductive as well as mechanically stable over wide temperature ranges, even at high temperatures. It has a high surface area, and when tailored with CNTs on its surfaces, the amounts of functional surfaces are further increased without significantly increasing in size or weight. Groups such as Nakagawa, Chakrapani, and Li, have all published typical uses and applications for carbon foams and methods of fabrication [24-26]. Various approaches have been reported for assembling CNTs onto macroscopic solids and have resulted in various CNT-based structures that includes but is not limited to fibers, mats, forests, and foams. Several groups reported ways of getting CNTs onto the macroscopic solids by deriving aqueous solution coatings of loose CNTs onto the surface of the substrate [25-29]. By doing so, the CNTs may lose some electrical or thermal properties. Another approach is selecting appropriate binding agent such as glue to adhesively attach loose CNTs onto the foam surfaces. This often results in randomly oriented CNTs and added weight from the binding agent. Compared to the above methods, growing CNTs directly onto the carbon foam surfaces has many benefits. Growing CNTs directly provided some challenges due to carbon foam surface wettability and reactivity during high temperature annealing and resulting in carbides that inhibit CNT growth. To solve this wettability issue, Mukhopadhyay's group reported using SiO₂ as the buffer layer [30]. This method resulted in dense CNT growth; however the growth is not aligned. Aligned CNTs are more beneficial to our thermal application, due to the low thermal resistance [31]. With this geometry, each CNT can be thought to act as an individual radiating fin of a heat sink.

In order to grow uniform and aligned CNTs on the carbon foam surface to enhance the appealing properties of the foam, several different method has been used to investigate the effect of carbon foam surface treatment/modify on CNT growth and their structure/ morphology. Experimental results indicated that, used a dielectric material Al₂O₃ as a buffer layer deposited via ALD onto the carbon foam surface, CNT growth resulted in a densely aligned forest that is fitted nicely on every contour surface of the carbon foam. This new capability can be applied to the heat sink component of power device as depicted in Figure 4.23. The near term challenge has been to find a way to attach this new cooling component to the material that we currently use on the electrical component side of the power module. A possible solution we are exploring is to use the electro-less plating, sputter or ALD technique to coat Ni or proper metal layer on pre-surface treated CNTs-foam composite and solder the resulting components together.

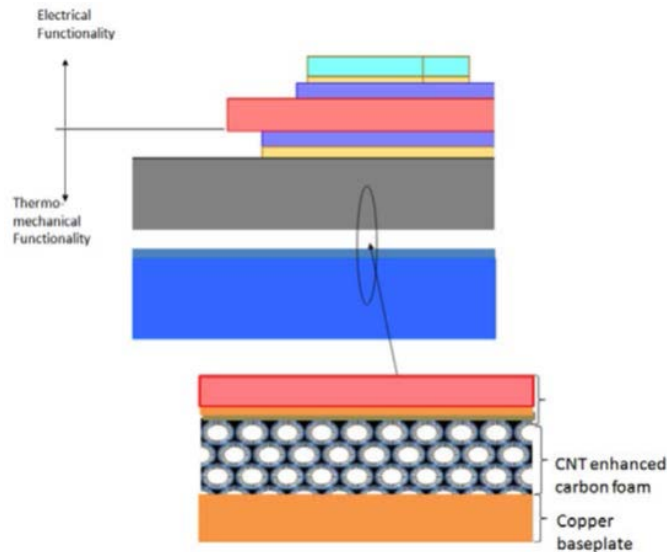


Figure 4.23. Example of a power device packaging layer

4.4.2 Experimental

4.4.2.1 Carbon foam (CF) substrate preparation and CNT growth method

Forty-five (45) pore per inch (PPI) reticulated vitreous carbon foam was purchased from Ultramet, Inc. The foam was then cut down to the experimental size of 10 mm x 10 mm x 5mm for growth analysis and 10 mm x 10 mm x 3 mm for thermal testing analysis. The CF samples were then cleaned via ultra-sonication in acetone followed by isopropanol for about 30 min per bath. The dried CF substrates were then ready for surface treatment and followed by CNT growth. CNTs were grown using the floating catalyst thermal chemical vapor deposition (FCCVD) method. The FCCVD system is equipped with both pure hydrogen and argon gas sources. During growth, the hydrogen to argon flow ratio was set to 1:2 standard cubic centimeters per second (sccm). Ferrocene was dissolved into xylene solvent in 0.012g/1ml concentration. The xylene/ferrocene liquid mixture serves as carbon feed stock as well as an iron catalytic particle source carrier. During growth, xylene/ferrocene was introduced at a flow rate of 3 ml/hr via a digital syringe pump. The CNT growth time was set for 20 minutes at 750 °C.

4.4.2.2 Method of Carbon Foam Surface Treatment

In this study, so far, the carbon foam surface was modified using five different methods in an attempt to overcome the interfacial challenges by means of introducing surface defects as well as depositing buffer layers. It is worthwhile to note that since the substrate is three-dimensional carbon foam, well-developed thin film deposition methods such as sputtering or e-beam evaporation will not suffice here. In theory, all of the modification methods performed in this study should have the ability to perform treatments at all depths and surfaces of the carbon foam. It is our goal to identify which of the surface modifications presented can provide a good foundation for dense growth of CNTs. Descriptions of each type of the treatments attempted are listed below:

1. As received: After cutting and cleaning into the sample size described above, the as-received carbon foam was first put through the CNT growth parameter. The growth results are used as a baseline to be compared with other growths
2. Thermal Oxidation Treated: According to Ultramet, the reticulated carbon foam is stable up to 350 °C in air and 3500 °C in an inert environment. Thus the carbon foam will start to decompose in oxygen environment above 350 °C. One way to functionalize the surface of carbon foam with oxygen is to treat it in an elevated temperature filled with oxygen [32]. The reticulated carbon foam was treated at temperatures of 350 – 500 °C with 50 °C increments for one hour each in a pure oxygen filled environment. The oxygen was introduced at a flow rate of 2 sccm.
3. Nitric acid treated: This method provided by Yuzun Fan, et al [33] is said to provide better surface adhesion for carbon surfaces. The clean carbon foam samples was first soaked in acetone for 2 hours and rinsed with DI water. Following this step, the samples were dried at 120 °C for 4 hours before being soaked for either 4 hours or 8 hours in 70% nitric acid solution. The resulting foam was then placed into the FCT-CVD for CTNs growth.
4. HMDS treated: It has been reported that CNTs grows well on silica surfaces [34]. MP-P20, a commercially available product containing HMDS, is commonly used in semiconductor processing to coat the surfaces of a substrate with a layer of organic silica. This process is usually done using a spin coater. In this study, the foam was simply dropped into a beaker of MP-P20 solution and allowed to soak for 30 seconds. The foam was then taken out of the solution and baked on a hot plate to cure the silica layer. The sample was left on the plate for 5 minutes at 112 °C.
5. Atomic layer deposition (ALD) of alumina buffer layer: ALD use the trimethylaluminium as the alumina precursor source to deposit 2 nm, 5nm, 10nm and 50 nm of alumina on to the carbon foam surface. The ALD deposits a uniform self-limiting monolayer of alumina on the surface of the carbon foam with each pulsed cycle [35]. The thickness of monolayer is estimated to be 1 Å per cycle. This cycle was repeated until the desired thin film thickness was achieved.

Once the treatments were completed on the carbon samples, CNT growth was achieved using the FCCVD method.

4.4.3 Results and Discussion

4.4.3.1 Characterization of CNTs Growth on CF Substrate

SEM is used to determine the CNT/CF sample structure and orientation/morphology after growth of CNTs on different surface treated CF substrates. The results are shown in Figures 4.24-4.29 . Figure 4.24 shows the surface morphology of the as-received carbon foam from Ultramet, Inc. The pore size is estimated to be 300 µm in diameter. From the image, it showed that the surface of the carbon foam is smooth and glassy- like

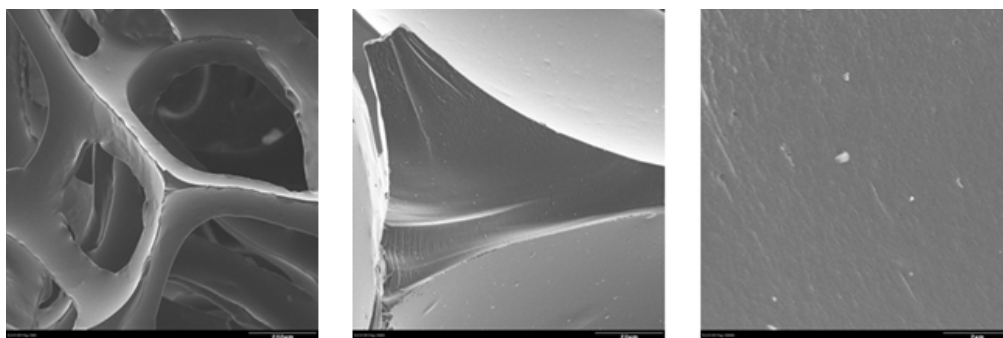


Figure 4.24. SEM mage of as-received carbon foam from Ultramet, Inc

Prior to surface treatments, the carbon foams were first cleaned by sonication in acetone and isopropanol solutions. CNTs were grown on a carbon foam sample without any surface treatments as a reference. Figure 4.25 shows sparse CNT growth on the surface of the untreated carbon foam. The image shows low amount of CNTs was grown on the surface of untreated sample. Areas with CNTs seem to cluster together. This pattern was seen throughout the sample. According to Zhang, it is challenging to grow CNTs directly onto carbon surfaces due to carbon and metal catalysis reactions [36]. The low CNT growth may be resulted from this type of reaction described by Zhang [36].

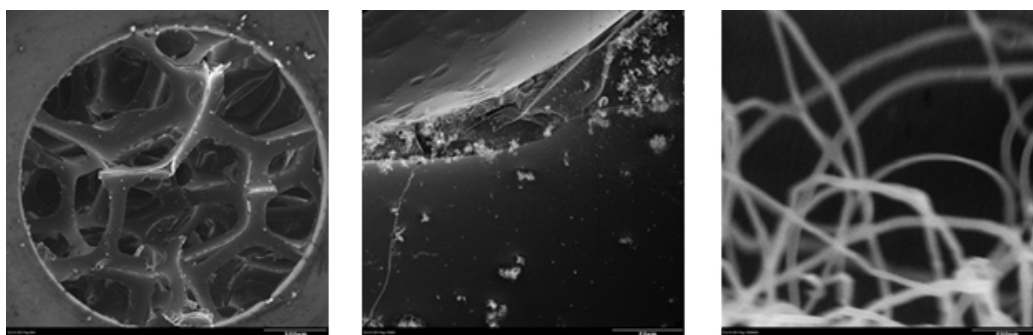


Figure 4.25. SEM image of CNTs grown on as-received carbon foam surface

Following the nitric acid treatment described early, Figure 4.26 shows CNT growth on 4 hours and 8 hours carbon foam treatment with nitric acid, respectively. The purpose of the nitric acid treatment is to functionalize the surface of the carbon foam for better CNT growth. However the image shows that there was no noticeable difference in the amount of CNTs that grew on either the 4 hour treatment or from the 8 hour treatment batch of CF samples. The overall growth is also very sparse, and similar to what is seen in the untreated sample. Carbon based materials are chemically inert, therefore the nitric acid treatment may not be adequate enough to provide the surface functionalization or modification needed for better CNT growth.

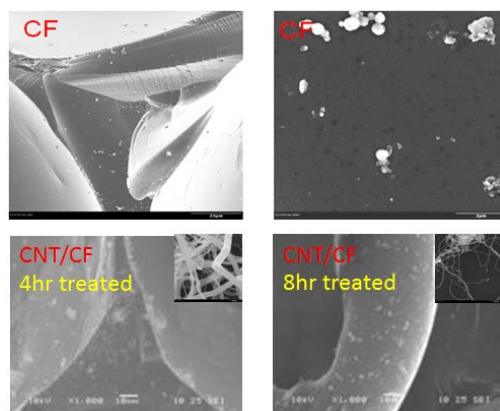


Figure 4.26. SEM image of nitric acid treated CF before (*top*) and after CNTs growth (*bottom*)

Figure 4.27 shows CNT grown on the oxygen treated carbon foam at temperatures of 350 °C, 400 °C, 450 °C and 500 °C, respectively. All treatment temperatures were carried out for an hour. Results show that there could be a correlation between the amounts of CNTs grown versus the temperature at which the carbon foam is being treated. Figure 4.27 shows the samples being treated at 450 and 500 °C have higher CNTs growth concentrations than the samples grown at 350 and 400 °C. However, this is just an initial test and preliminary results, systematic testing needs to be performed in order to verify these results. The foam samples were not treated above 500 °C, due to severe deterioration of the foam sample if treated above this temperature. It has been reported in [36] that at elevated temperatures, carbon based materials will create defects that weakens the mechanical properties. Although the images shown better yield of CNT growth on samples treated at a higher temperature, the sample mechanical properties may be loss.

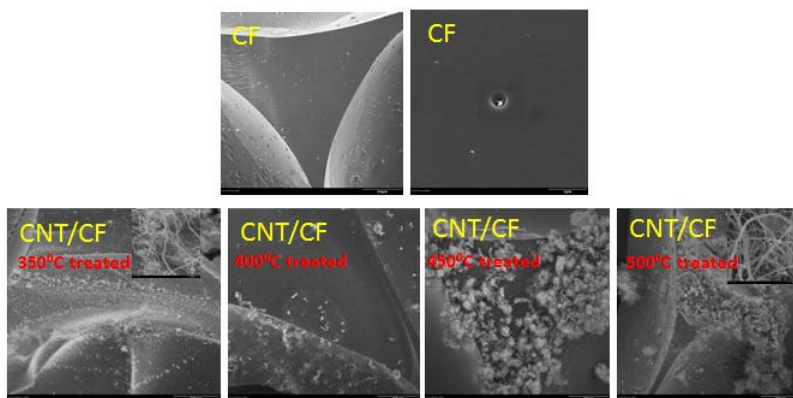


Figure 4.27. SEM image of oxygen treated CF before (*top*) and after CNTs growth (*bottom*)

HMDS is used to provide a thin layer of silica on the surface of the carbon foam. Figure 4.28 show that CNT grown on HMDS treated carbon foam. This low CNT growth result can be thought that amount of silica coated on the surface of carbon foam may not be thick enough for iron particles to nucleate and promote CNT growth.

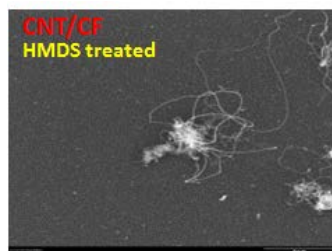


Figure 4.28. SEM image of HDS treated CF after CNTs growth

Figure 4.29 highlights the CNT growth on ALD treated carbon foam. The samples in Figure 4.29 were coated with 2 nm, 5nm, 10nm and 50nm alumina, respectively. Compared to other surface treatment, with just 2 nm of alumina, there is an increase in the density of grown CNTs. When Al_2O_3 thickness is continued to increase (to 5nm, 10 nm and 30nm), the growth of CNTs was so dense that it covered the entire surfaces of the carbon foam to in its entirety. Also, with the 10 nm and 50nm sample, we can see that highly dense and aligned CNTs are grown. This was not seen from any other surface treatments discussed above. One possible reason for this dense growth was seen here is because that alumina thin film may be provide a thick enough barrier layer between the reactive carbon surface and the metal catalyst. Thus the catalyst was able to nucleate on the surface of the alumina and provide dense CNT growth as seen in Figure 4.29.

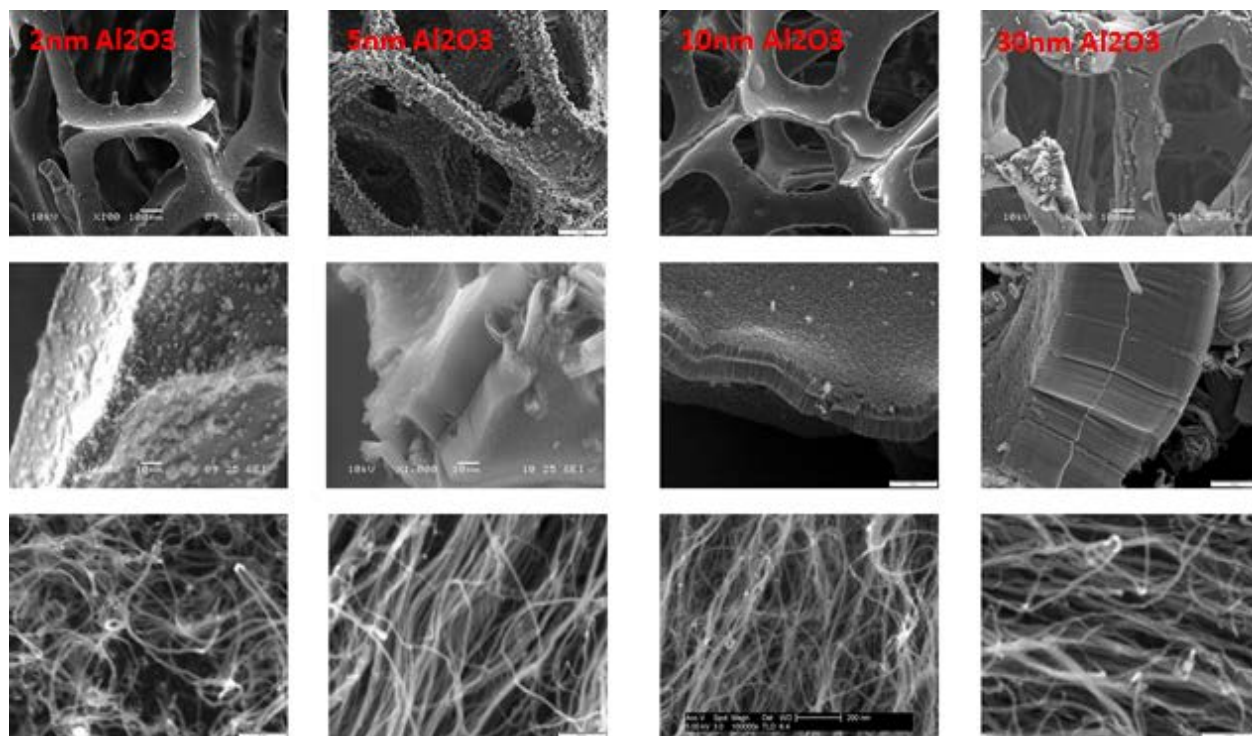


Figure 4.29. SEM image of Al_2O_3 (various thicknesses) coated CF after CNTs growth

4.4.3.2 Thermal Property Testing of CNT/CF

Initial thermal testing was conducted using a Netzsch Laser Flash 457 system available in AFRL's Materials and Manufacturing Directorate (Figure 4.30). The Laser Flash 457 has the ability to hold three samples per run. Sample size is limited to 1 cm x 1 cm x 0.2 cm. Carbon foam samples with and without CNTs was filled with epoxy (EPON 862 and curing agent W). Thermal diffusivity (α) and specific heat capacity (C_p) were measured $\kappa = \alpha * \rho * C_p$. Figure 4.31 shows the initial thermal testing results of carbon foam with CNTs made from 10 nm ALD coated alumina sample. The result shows that the sample with CNTs had higher thermal conductivity value than the samples without. However, this is just an initial testing result. To make a firm conclusion, further tests are needed.

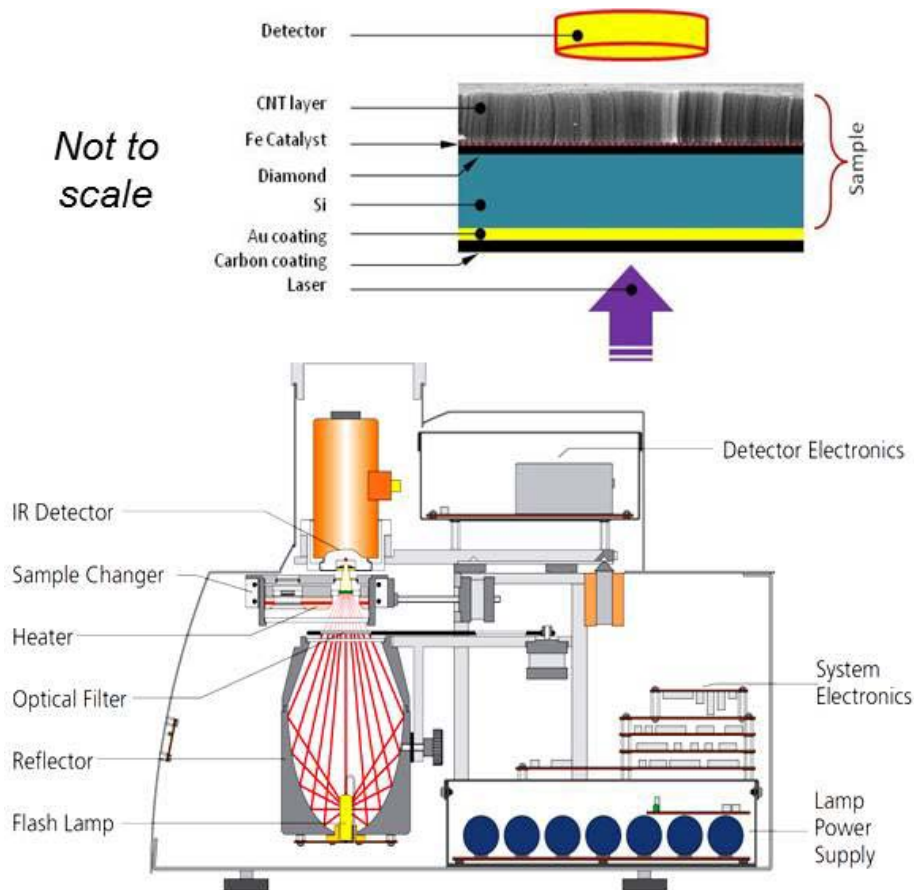


Figure 4.30. Netzsch LFA instrument schematic

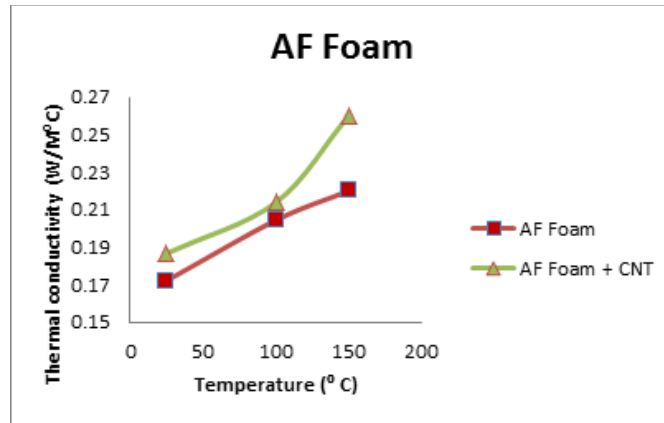


Figure 4.31. Thermal conductivity of CNT/Carbon foam substrate

4.4.3.3 Post-growth Nickel Coating

Plating CNTs/carbon foam samples with nickel provides a way for composite structure to be bound to pertinent surfaces in a package configuration. Two methods, including electroless plating and electroplating have been tried to plat Ni particles onto CNT layer. The SEM images of Ni plated CNT/CF results are shown in Figures 4.32 and 4.33. Compare two methods, the Electroless plating requires multiple chemical steps in order to coat the surface of forest grown CNTs and CNT forest seems to be disturbed by the multiple step process, resulting in web-like structures. Electroplating is a simple straight forward process that keeps the CNTs forest structure intact and has uniform nickel coverage.

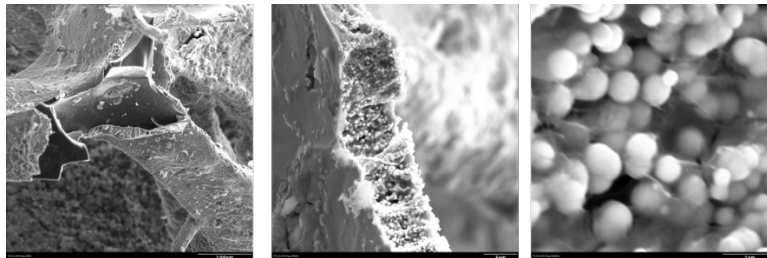


Figure 4.32. SEM image of Nickel Electroplating CNT/CF

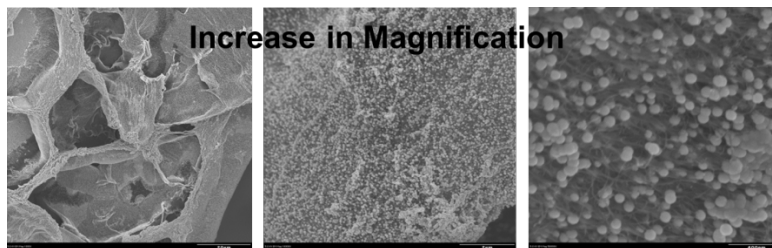


Figure 4.33. SEM image of Nickel Electroless plating CNT/CF

4.4.4 Summary

Growing CNTs onto carbon surfaces still remains as a big challenge due to reactive carbon surfaces to the metal catalysts. In order to grow dense CNTs, the carbon surface needs to be either functionalized or buffered from the catalyst. It can be seen that after the various types of surface treatments studies performed here, the one that provides the most impact to CNTs growth is the one that was treated with ALD alumina buffer layer. As it is seen from Figure 4.29, with an increase in alumina thickness, highly dense, aligned CNTs are achievable. These figures show that alumina, when used as a buffer layer on the carbon foam surface, plays an important role in the alignment and density of the CNT arrays. The result from the primary thermal testing revealed that samples with CNTs provided a higher thermal conductivity value than ones without CNTs. Comparing two methods of nickel plating CNTs, Electroplating is a simple straight forward process. It could keep the CNTs forest structure intact and also have uniform nickel coverage on CNT layer.

4.5 References

- [1] Teresa de los Arcos, M. G. Garnier, *Carbon* (42), 187-190, 2004.
- [2] S. Handuja, P. Srivastava, V.D.Vankar, *Nanoscale Res Lett* (5): 1211-1216, 2010.
- [3] A. Cao, P. M. Ajayan, G. Ramanath, *Applied Physics Letters* (84), 109-111, 2004.
- [4] W. Lin, V. R. Olivares, Q. Z. Liang., R.W. Zhang, “9th IEEE Conference on Nanotechnology, 2009.
- [5] W. Lin, K. S. Moon, C. P. Wong, *Advanced Materials*, (21), 2421-2424, 2009.
- [6] Xu J. and Fisher T. S., *International Journal of Heat and Mass Transfer*, vol. 49 (2006), pp.1658-1666.
- [7] Tong T., Zhao Y., Delzeit L., Kashani A., Meyyappan M.,and Majumdar A., *IEEE Transactions on Components and Packaging Technologies*, vol. 30 (2007), pp. 92-100.
- [8] Kordas K., Toth G., Moilanen P., Kumpumaki M., Vahakangas J., Uusimaki A., Vajtai R., and Ajayon P. M *Applied Physics Letters*, vol. 90 (2007).
- [9] Cola B. A., Xu J., Cheng C. R., Xu X. F., Fisher T. S., and Hu H. P., *Journal of Applied Physics*, vol. 101 (2007).
- [10] Huang H., Lui C. H., Wu Y., and Fan S. S., *Advanced Materials*, vol. 17 (2005), pp. 1652-1653.
- [11] Panzer M. A., Zhang G., Mann D., Hu X., Pop E., Dai H., and Goodson K. E., *Journal of Heat Transfer-Transactions of the ASME*, vol. 130 (2008).
- [12] Sihni S., Ganguli S., Roy A. K., Qu L. T., and Dai L. M., *Composites Science and Technology*, vol. 68 (2008), pp. 658-665
- [13] H. Wang, J. Y. Feng, X. J. Hu, and K. M. Ng, *Journal of Physical Chemistry C*, (111), 12617-12624, 2007. [14] X. Yin, Q. L. Wang, C. G. Lou, X. B. Zhang , *Applied Surface Science*, (254), 6633-6636, 2008.
- [15] Zhu L. B., Hess D. W., and Wong C. P., presented at *Electronic Components and Technology Conference*, 2007
- [16] Hu X. J., Padilla A. A., Xu J., Fisher T. S., and Goodson K. E., *Journal of Heat Transfer-Transactions of the ASME*, vol. 128 (2006), pp. 1109-1113.
- [17] Son Y., Pal S. K., Borca-Tasciuc T., Ajayan P. M., and Siegel R. W., *Journal of Applied Physics*, vol. 103 (2008).

- [18] B. Gan, J. Ahn, Q. Zhang, S. F. Yoon, J. Yu, Y-junction carbon nanotubes grown by in situ evaporated copper catalyst, *Chem. Phys. Lett.* (333), 23–28, 2001.
- [19] Y. Qin, Q. Zhang, Z. L. Cui, *J. Catal.* (223), 389–394, 2004
- [20] Z. Zhang, P. He, Z. Sun, T. Feng, Y. Chen, H. Li, & B. Tay, *Applied Surface Science*, (256), 4417-4422, 2010.
- [21] N. Zhao, J. Kang, *Carbon Nanotubes-Synthesis, Characterization, Applications*, 6, 99-116, 2011.
- [22] Y. Wang, B. Li, P. S. Ho, Z. Yao, L. Shi, *Applied Physics Letters* (89), 1831131-1831133, 2006.
- [23] S. Helveg, C. L-Cartes, J. Sehested, P. L. Hansen, *Nature* (427), 426, 2004.
- [24] Son Y., Pal S. K., Borca-Tasciuc T., Ajayan P. M., and Siegel R. W., *Journal of Applied Physics*, vol. 103 (2008).
- [25] Nakagawa, K. (2011) Bianco, S., *Carbon Nanotubes – from Research to Applications* (313-327). Intech
- [26] Ajayan, P., Carrillo, A., Chakrapani, N., Kane, R., and Wei, B United States Patent 7473411 B2 Jan 6, 2009
- [27] Worsley, M., Kucheyev, S., Satcher, J., Hamza, A., and Baumann, T. *APL* 94 (2009)
- [28] Chakrapani, N., Wei, B., Carrillo, A., Ajayan, P., and Kane, R. *PNAS* 101 12 (2004)
- [29] Li, K, Shi, Z., Li, H, Tian, Z, and Wang, C. *Sci Technol. Adv Mater.* 9 (2008)
- [30] Yang, et al. *J of Nano Letters* 5 11 (2005)
- [31] Lin W., Olivares V. R., Liang Q. Z., Zhang R.W., Moon K. S., Wang C.P., *9th IEEE Conference on Nanotechnology*, (2009)
- [32] Z. Konya, P. M. Vilarinho, A. Mahajan, and A. Kingon, “*Studies on the thermal decomposition of multiwall carbon nanotubes under different atmospheres*,” vol. 90, pp. 165–168, 2013.
- [33] Y. Fan, H. Yang, H. Zhu, X. Liu, M. Li, Y. Qu, N. Yang, and G. Zou, “*Metallization of Carbon Fibers with Nickel by electroless Plating Technique*,” *Metallurgical and Materials Transactions A*, vol. 38 A, p. 2148, 2007.
- [34] S. Mukhopadhyay, P. Joshi, and R. Pulikollu, “*Thin Films for Coating Nanomaterials*,” *Tsinghua Science & Technology*, vol. 10, no. 6, pp. 709–717, Dec. 2005
- [35] R. L. Puurunen, “*Surface chemistry of atomic layer deposition : A case study for the trimethylaluminum / water process*,” *Journal of Applied Physics*, vol. 97, pp. 1–53, 2005
- [36] Q. Zhang, J. Liu, R. Sager, L. Dai, and J. Baur, “*Hierarchical composites of carbon nanotubes on carbon fiber: Influence of growth condition on fiber tensile properties*,” *Composites Science and Technology*, vol. 69, no. 5, pp. 594–601, Apr. 2009.

5. Enhancement of Thermoelectric Materials to Provide Solutions for Power and Thermal Challenges

5.1 Research Objectives

The goal of this research effort is to optimize and identify highly efficient TE materials that operate in both the high and low temperature regimes through two (2) innovative research approaches. Materials are evaluated at given temperature ranges for electrical conductivity, thermal conductivity, and Seebeck coefficient behavior over a broad temperature range. The electrical conductivity of TE material candidates can be improved via doping of the material, while the thermal conductivity can be lowered by lattice modification, *e.g.*, by restricting electrons to move only in two dimensions as a result of anisotropy and layering, rattling and distortion induced by void-filling effects, and other structural modifications.

The objectives for this effort are to synthesize and characterize promising material candidates with enhanced TE performance, which will lead to efficient modules for mid-to-high temperature power generation applications. To achieve this goal, two major approaches are considered: (1) a Microstructural Self-assembly Approach to fabricate nano-dimensional materials with nano-inclusions, and (2) a High-throughput Combinatorial Approach for the identification of new materials. The *Self-assembly Approach*, which was broadened to also include doping effects, takes advantage of the materials' inherent ability to self-assemble in addition to other microstructurally induced growth mechanisms. The second thrust employs a high-throughput *Combinatorial Approach* to quickly generate binary and ternary libraries for rapid screening of compositions with optimized TE behavior. Both approaches explore novel chemistries and processes for tailoring TE responses, including the exploration and development of novel and stable doping reagents and processes, advanced combinatorial methods, and most importantly, processes originally designed outside of TEs that can be uniquely applied to this field. In addition to chemical characterization, high-resolution microscopy, along with electronic and thermal property measurements are explored to develop comprehensive processing-structure-composition-property relationships. Furthermore, a thin/thick film module development concept is also explored with a proof-of-concept demonstration.

5.2 Introduction

A fundamental understanding of the thermoelectric (TE) concept is needed for improved TE applications – a necessary strategy as the demand for alternative energy sources and technologies increases. In part, the discovery of new materials and the innovation of novel synthesis techniques, along with the exploitation of the TE concept (*i.e.*, generation of power through the utilization of underused thermal energy) for use in devices have motivated many researchers to invest in the optimization of the properties of known TE materials [1].

Thermoelectricity can be explained as a result of three reversible effects: (1) the *Seebeck* effect, or the generation of a voltage in a closed circuit due to temperature variances of the junctions between two different metal conductors/semiconductors; (2) the *Peltier* effect, induced when an electric current causes a change in temperature at the junction of two different conducting metals; and (3) the *Thomson* effect, which explains the temperature change in a metal conductor with a temperature gradient due to the flow of electric current. We, among other researchers in this field, are most interested in increasing the dimensionless figure-of-merit, zT , which is a measure for the efficiency of a TE material. zT is defined as $(\alpha^2 \sigma / \kappa) T$, where α is the

Seebeck coefficient, σ is the electrical conductivity, κ is the thermal conductivity, and T is the absolute temperature. Current state-of-the-art (SOA) TE materials are the $\text{Bi}_{2-x}\text{Sb}_x\text{Te}_{3-y}\text{Se}_y$, Bi_2Te_3 , $\text{Bi}_{1-x}\text{Sb}_x$, $\text{Si}_{1-x}\text{Ge}_x$ and PbTe-based alloys, which reach zT values between $\sim 0.8 - 1$ at various temperatures, although a zT value of one is not the highest possible value for a material to possess.

The TE properties of materials are interrelated, therefore, altering one property usually results in an adverse effect in the others. Desirable materials are those which possess a large Seebeck coefficient or thermopower (for a maximum conversion of heat to electrical power or electric power to cooling), excellent electrical conductivity (to minimize Joule heating), and poor thermal conductivity – a consequence of both lattice and electronic contributions. The numerator term, $\alpha^2\sigma$, is considered the power factor (PF); therefore, maximizing the PF while minimizing the thermal conductivity (referred to as the “ zT barrier”) increases the zT value. These strict requirements for a good TE material have resulted in a relatively small number of candidates – divided into two types, p - and n -type – which should have a large zT value (≥ 1) at operating temperature.

One benefit for utilizing TE devices for power generation and electronic refrigeration applications is no moving parts, and thus, long device lifetimes. For power generation technologies, as long as a heat differential is maintained, devices fabricated from TE modules will continue to operate. Other benefits include environmental friendliness, ability to function over a wide temperature range, precise temperature control (refrigeration) and silent, maintenance-free operation. TE modules that are currently on the market are designed from materials combined into pairs (p - and n -type) to make unicouples, which are connected electrically in series and thermally in parallel. A TE module’s figure-of-merit, ZT , is related to the individual materials’ figure-of-merit, zT , though it is generally lower than the average zT , due to the individual materials’ electrical and thermal property mismatches. Thermal expansion coefficient differences can result in mechanical instability of the modules. Therefore, it is important to ensure the compatibility of the materials used. In TE power generators, along with selecting compatible materials, increasing a device’s power output per unit weight or volume is of the utmost importance. As illustrated in Figure 5.1, increasing the temperature gradient has a profound impact on the power output. Matched TE materials with zT values greater than 1 that can operate over a wide temperature range will result in the most useful waste-heat scavenging power generators.

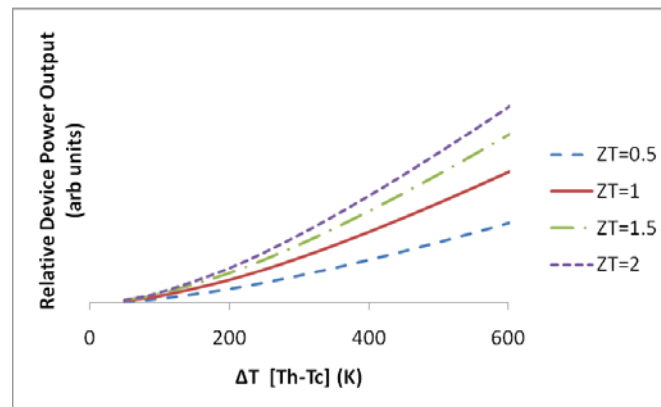


Figure 5.1. Power output dependence on both ZT and temperature differential (ΔT)

5.2.1 Thermoelectric Materials Challenges

Although the TE concept has been understood and applied since ~1821, the strenuous requirements placed on TE materials for efficient operation are not easily satisfied, and thus have prevented their widespread application. For practical applications, TE materials must first possess high conversion efficiency (zT). For TE power generators, not only must the materials possess a high energy inter-conversion efficiency, but they must also be composed of nontoxic and abundantly available elemental materials with high chemical stability in air at high temperatures. Although the energy inter-conversion efficiencies of the SOA heavy-metal-based materials are large enough for practical applications, these materials are not attractive, particularly for operation at high temperatures, because decomposition, vaporization and/or melting of the constituents can easily occur. Furthermore, the use of these heavy metals, which are expensive, mostly toxic, low in abundance as natural resources, and therefore, not environmentally benign; their use should be limited to specific isolated environments, *i.e.*, space. Another materials challenge is addressing size, weight and power (SWaP), which is driven by the needs of particular applications. With regards to military and aerospace applications, SWaP constraints are encountered in secure communications, radar, sensors, batteries and electronic warfare platforms. Since increases in performance and function have a direct impact on power output, and thus, size, weight, power supply type and thermal management requirements, it is critical to consider contributors to power reduction early in the design process.

5.2.2 Nano-structure Engineering to Achieve High TE Performance

Desirable TE materials possess a low thermal conductivity while maximizing electrical carrier transport, or behave as a so called “phonon-glass/electron-crystal” [2]. TE materials have long been thought to be too inefficient to be cost effective in most applications [3]. However, a resurgence of interest in TEs began in the mid-1990s when theoretical predictions suggested that TE efficiency could be greatly enhanced through nano-structural engineering. This then led to experimental efforts that demonstrated proof-of-principle with high efficiency materials [4, 5]. One strategy for nano-structured TE materials is to scatter phonons at interfaces, thus leading to the use of multiphase composites mixed at the nano-scale. These nano-structured materials can be formed as thin-film superlattices (multilayers) or as intimately mixed composite structures. However, the challenge for any nano-structured systems is electron scattering at interfaces and grain boundaries (GBs) between randomly oriented grains, leading to a concurrent reduction of *both* the electrical and thermal conductivities [6]. The ideal nano-structured materials should have thermodynamically stable, coherent, epitaxial-like interfaces between the constituent phases to prevent scattering of electrons at interfaces and GBs.

5.2.3 Advantages of Complex Oxide Materials for TE Applications and Current Technology Barriers for Applications

Oxide materials, such as recently discovered nontoxic *p*-type CCO-349, are particularly promising for high temperature TE applications because of their thermal stability and desirable TE performance. Layered cobalt oxides such as CCO-349 can be regarded as hybrid crystals that are composed of the periodic arrangement of nano-sheets possessing different TE functions [7]. In these oxides, the CoO_2 nano-sheets possess a strongly correlated electron system, and serve as electronic transport layers, while the Ca_2CoO_3 misfit layers serve as phonon scattering regions to

achieve low thermal conductivity. CCO-349 displays enhanced TE behavior with a zT exceeding 0.8 at 973 K [8], and is highly stable in air up to 1300 K. In regards to a suitable counterpart for unicomplex fabrication, among the promising n -type oxide-based TE candidates, Nb-doped SrTiO₃ (Nb:STO) exhibits a large Seebeck coefficient as a result of its large density of states and effective mass. Epitaxial Nb:STO films have shown zT values up to 0.4 at 1000 K [9]. STO itself has desirable electrical conductivity behavior, which is easily tuned for insulating to metallic behavior by doping with La³⁺ or Nb⁵⁺, respectively. Additionally, STO-based materials (e.g. electron-doped STO crystals) have very high melting points (~ 2350 K) and thus are highly stable at extreme temperatures. CaMnO₃ (CMO) is another promising n -type perovskite oxide TE material with Seebeck coefficient values reaching ~ 500 $\mu\text{V/K}$ at high temperatures. Applications utilizing TE oxide modules extends not only to generators for the recovery of high-temperature waste-heat emitted as exhaust by aircraft, automobiles and similar sources, but also to portable generators, and the power supplies of mobile phone chargers, personal computers, and other electronic devices. The largest hurdle to overcome in the development of oxide-based TE modules is to improve the energy inter-conversion efficiency, which is currently considerably lower than that of conventional TE materials.

5.3 Results and Discussion

5.3.1 *Approach 1: Microstructural Self-assembly to Fabricate Nano-dimensional Materials with Nano-inclusions*

5.3.1.1 Introduction

The primary aim of the *Self-assembly Approach* is to enhance the TE behavior of low-dimensional materials through quantum confinement effects, reduction of the lattice contribution to the overall thermal conductivity via lattice mismatching, and other structural modifications. Manipulation of the growth of existing TE materials at the nano-level is made possible through a controlled microstructural growth mode. On the nanometer scale, lattice-mismatched material additions to a bulk matrix material can also induce self-assembled nano-particulate additions to form nano-columns (or nano-wires of the material addition). We have successfully demonstrated this capability in-house. In Figure 5.2, it can be seen that by adding BaSnO₃ (BSO) material to YBa₂Cu₃O_{7-x} (YBCO), nano-wires of BSO form inside the YBCO matrix due to lattice mismatching of the chemically compatible material additions [10, 11]. Also, the growth of these nano-wires is at a high density, and the nano-wires extend from the substrate to the film surface. This process can also be applied to TE materials to create the desired nano-wire structure.

The advantage of creating nano-wires for TE materials is that in nano-structured materials, the electron density of states at the Fermi level is increased and the small dimensions of the nano-structures will result in boundary scattering of the phonons to reduce thermal transport [12]. Recent efforts to achieve these nano-wires often involve only the creation of the nano-wire itself that lacks a definitive matrix to isolate the nano-wire for improved boundaries. Broido and Mingo determined theoretically that the effectiveness of nano-wires as TEs is dependent on the cross-sectional size of the nano-wire-composite matrix relative to the nano-wires [13]. Documented efforts to create the nano-wires in an appropriate matrix material typically use multiple processing steps to achieve the final result, thus making for a complex and therefore costly process [14-16]. Even then, more recent attempts at this have not been fully and successfully culminated.

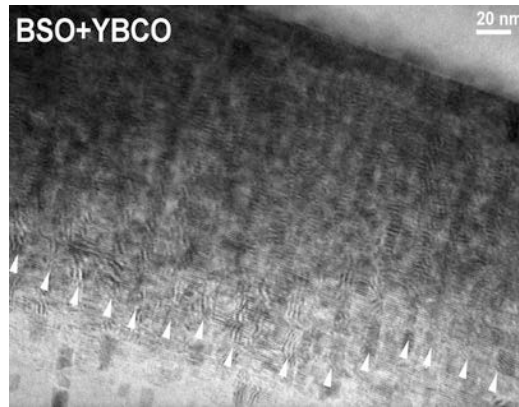


Figure 5.2. BSO nano-columns (highlighted by arrows) in YBCO matrix grown by PLD

Phonon scattering to inhibit thermal transport in TE materials can also be achieved by nano-particulate dispersions [17]. The nano-particulate additions can also increase the electron transport in the composite material. In this case, self-assembly of the microstructural additions need not be complete. However, the material's addition is not the primary TE material itself, but is now the secondary material which may or may not possess TE properties; the matrix material becomes the primary TE material. Many groups internationally have demonstrated how to achieve nano-particulate dispersions by a variety of processes. We have developed a cost-effective method in-house for controlling the microstructural growth of nano-particles in materials, and have begun to apply these techniques to the oxide-based TE material CCO-349.

For CCO-349-based materials, the potential for practical use in applications is evident from the unique combination of an extraordinarily high thermopower with metallic-like transport properties at high temperatures [7, 18]. In addition, CCO-349 is largely anisotropic. It is reported that in textured CCO-349, the *in-plane* electrical conductivity is 1.54×10^4 S/m and the *out-of-plane* electrical conductivity is 2.83×10^3 S/m [19]. For polycrystalline samples, the improved alignment of crystal grains facilitates the enhanced current transport along the *ab*-plane of the misfit-layered structure. As such, high-quality textured CCO-349 possesses a low electrical resistivity (high electrical conductivity) and a large Seebeck coefficient intrinsic to its electronic band structure.

The monoclinic structure of CCO-349, shown in Figure 5.3, is comprised of two misfit layered subsystems: a distorted rocksalt-type Ca_2CoO_3 layer sandwiched between two CdI_2 -type CoO_2 layers along the *c*-axis [20]. The lattice parameters are $a = 4.8339$ Å, $c = 10.8436$ Å, and $\beta = 98.14^\circ$. However, along the *b*-direction, the incommensurate nature of the structure results in two different *b*-axis lengths, $b_1 = 2.8238$ Å for the CoO_2 subsystem, and $b_2 = 4.5582$ Å for the Ca_2CoO_3 subsystem. The ratio between b_1/b_2 is $p = 0.6195$. Moreover, it is the alternating stacking of these substructures, which are incommensurate along the *b*-axis that leads to the “misfit” classification.

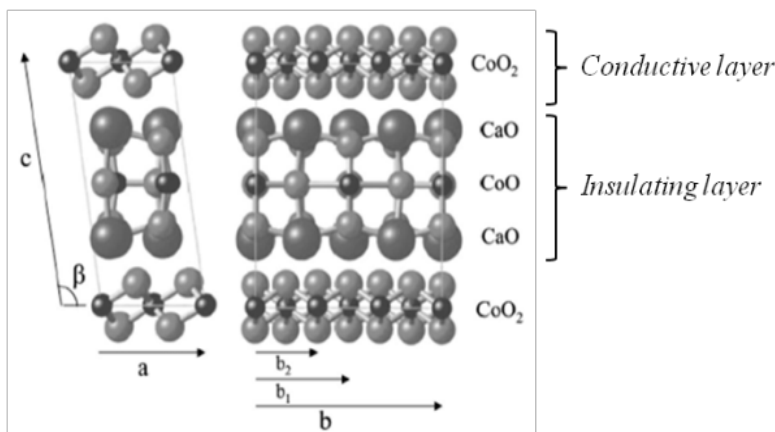


Figure 5.3. Schematic illustration of the crystal structure of $\text{Ca}_3\text{Co}_4\text{O}_9$ (CCO-349). Adapted from [18].

Due to the layered stacking of the two subsystems within the CCO-349 lattice, its structure can be further complicated by the presence of other structurally related non-CCO-349 phases called spurious phases. Spurious phases with similar crystal symmetry and structural motifs, and nearly identical c -axis lattice parameters to CCO-349, can be formed under different synthesis conditions and starting stoichiometry of the materials. In the Ca-Co-O phase diagram, there are three such phases: CaCo_2O_4 (CCO-124), $\text{Ca}_2\text{Co}_2\text{O}_5$ (CCO-225) and $\text{Ca}_3\text{Co}_2\text{O}_6$ (CCO-326).

Among the four similar cobaltite phases, CCO-349 and CCO-225 exhibit the best TE behavior, and rival the behavior of some of the conventional TE materials such as the $\text{Bi}_2\text{Te}_3/\text{Sb}_2\text{Te}_3$ alloys. Single crystal CCO-225 has a calculated $zT = 1.2 - 2.7$ above 600 K in air, making CCO-225 a suitable candidate for high-temperature TE applications [21]. CCO-326 is a decomposed phase of CCO-349 and has an enhanced Seebeck coefficient at room temperature ($450 \mu\text{V/K}$) along with high chemical stability up to 1300 K [22]. Due to its stability at high temperatures, it has potential as a more efficient TE candidate than CCO-349. However, it is not currently being considered for TE applications, as its zT is 0.15 at 1073 K, resulting from the large electrical resistivity (typically $\sim 50 \Omega\text{-cm}$). CCO-124 is yet another phase with a large Seebeck coefficient of $145 \mu\text{V/K}$ at 300 K [23]. This phase appears as a result of internal stresses, stacking faults, and localized oxygen deficiency, but when present, can be converted to CCO-349 through annealing in flowing O_2 .

5.3.1.2 Experimental

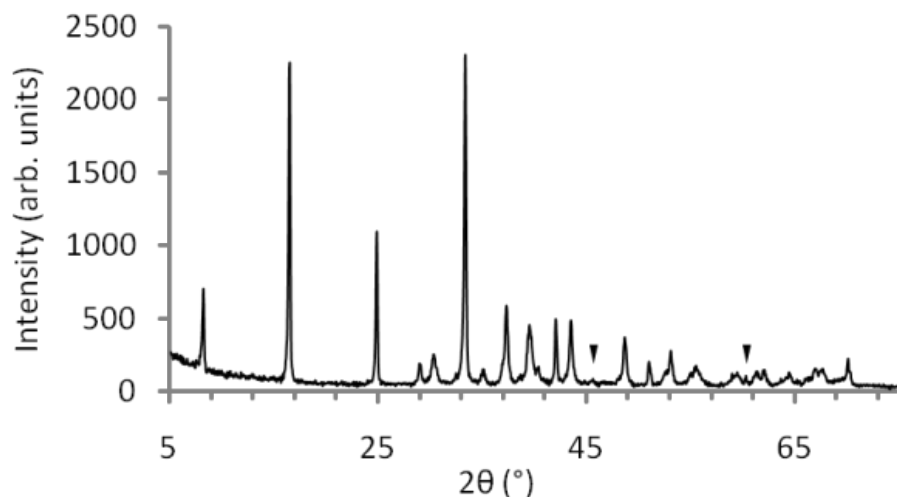
Since FY10, we have made considerable progress towards inducing nano-inclusion formation in CCO-349 using BaZrO_3 (BZO) as the initial second phase material. Although the crystal structure of CCO-349 is closely related to that of another misfit-layered oxide, $\text{Bi}_2\text{Sr}_2\text{Co}_2\text{O}_y$ —originally believed to be an isomorph to the high-temperature superconducting (HTS) material $\text{Bi}_2\text{Sr}_2\text{CaCu}_2\text{O}_8$ —the nano-inclusion formation mechanism identified in HTS YBCO is different for the two systems. Despite unsuccessful attempts to grow CCO-349-BZO nano-composites, we have successfully obtained Zr- and Ba-doped samples. In addition, we have identified an alternate material candidate for continued nano-inclusion experiments.

A 2.54 cm (1 in.) dia. CCO-349 target was prepared via solid-state reactions of stoichiometrically-combined high-purity powders of CaCO_3 and Co_3O_4 . The heating/reaction

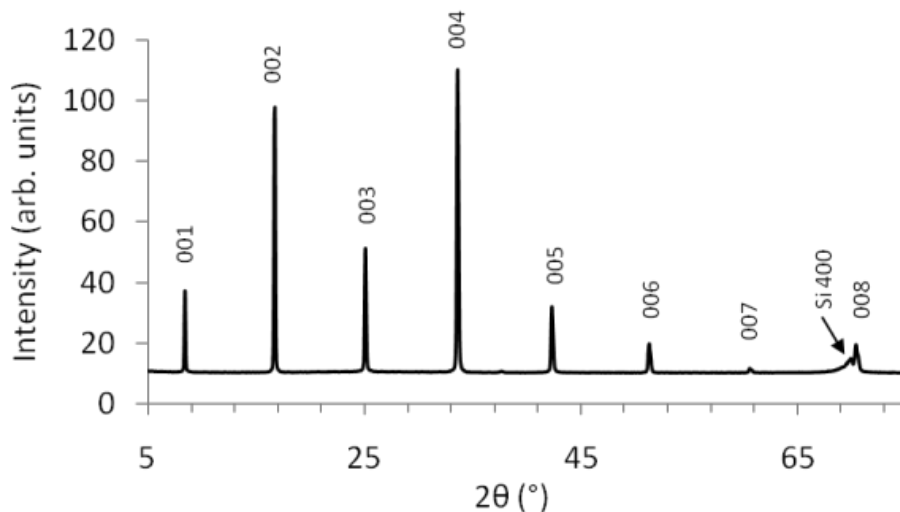
process has evolved slightly over time, but most commonly the powder mixture is heated in air at 1163 K for 12 h. The resulting mixture is then cold-pressed into a pellet and heated in air to 1163 K for 60 h, ground after cooling to room temperature, re-pressed, and reheated to 1163 K for an additional 138 h. In the final step, the pellet is ground again, re-pressed, then heated to 1073 K in flowing O₂ for 2 h. This extensive process is done to promote a complete reaction of the starting materials and formation of a single phase (CCO-349). The target's relative density was > 70 %. Our thin film samples were grown *in-situ* by pulsed laser deposition (PLD) of the prepared CCO-349 targets [24]. Single crystal Si (100), LaAlO₃ (LAO) (100), Al₂O₃ (100), and Si/SiO₂ (amorphous) substrates are cut to various dimensions, most commonly 4 mm x 4 mm and 4 mm x 8 mm. The cut substrates are ultrasonically cleansed only in acetone and isopropanol prior to depositions. Generally speaking, thin films 300 – 350 nm thick were deposited using a KrF excimer laser ($\lambda = 248$ nm) at 4 Hz (energy density ~ 1.7 J/cm²) under an O₂ partial pressure of 300 mTorr, and a substrate temperature of 973 K. Variations of this deposition procedure have also been done to identify the effect of laser repetition rate (2 – 4 Hz), substrate temperature (923 K – 1023 K), and film thickness (50 – 350 nm), on the resulting film structure and TE properties. Following deposition, the samples are generally cooled in the PLD chamber to 773 K under 1 atm O₂, annealed for 1 h, then slowly cooled to room temperature. An *ex-situ* anneal is done at 1073 K for 2 h in flowing O₂ using a tube furnace. Initial studies on the effect of the annealing processes have also been conducted, though not discussed in detail in this report. Film thickness determinations were completed using profilometry and confirmed during the scanning electron microscopy (SEM) experiments. *(For the numerous experiments conducted under this effort, the above procedures are generally similar with slight variations made where necessary.)*

5.3.1.3 Results and Discussion

After post-annealing samples, preliminary structural studies were done by XRD using a Rigaku DMAX 2500 x-ray diffractometer with Cu K α radiation ($\lambda = 0.15406$ nm) over the range $5^\circ \leq 2\theta \leq 80^\circ$. Representative XRD patterns for a bulk CCO-349 target and a pure CCO-349 thin film are shown in Figures 5.4 (a) and (b), respectively. Very minor impurities (highlighted by ▼ symbol) are present in the polycrystalline target sample, and usually correspond to un-reacted starting materials. In the thin film sample, only peaks corresponding to the (00*l*) plane family of the CCO-349 monoclinic phase are observed, suggesting that the film has a well-defined texture, *i.e.*, a preferential growth orientation along the *c*-axis. No additional phases could be detected.



(a)



(b)

Figure 5.4. XRD patterns for a (a) CCO-349 target and (b) 200 nm CCO-349 thin film on Si (100)

Electrical resistivity measurements of thin film samples were initially carried out by the van der Pauw (vdP) technique [25] using the Physical Property Measurement System (PPMS) from 10 – 390 K. The advantage of the vdP configuration versus the typical 4-probe configuration for sheet resistance (surface resistivity) measurements is that the vdP route is a more convenient method for attaching leads to arbitrarily-shaped, thin samples with uniform thickness. In addition, probe (lead) spacing becomes negligible. Figure 5.5 shows the temperature-dependant electrical resistivity data (10 – 390 K) for a film grown on Si (100). Weakly metallic behavior in the ρ - T plots is observed at higher temperatures ($T > 100$ K). At

lower temperatures ($T < 100$ K), behavior similar to that of semiconductors is observed, and can be attributed to spin density wave effect in CCO-349 [2].

Additional transport properties (α and 4-probe ρ) were measured at room temperature using the Power Factor Screening Instrument (PFSI), which is a modified version of a NIST-developed room temperature thermopower screening tool [26-28].

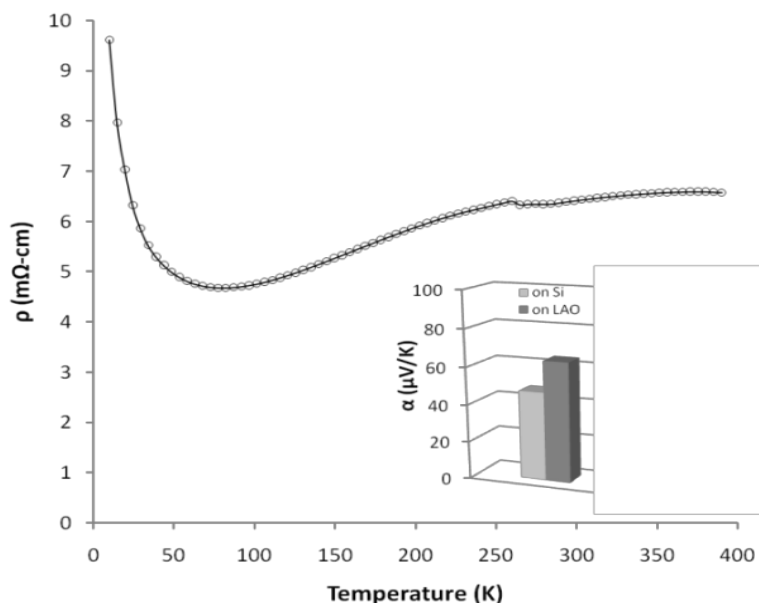


Figure 5.5. Temperature-dependent electrical resistivity (ρ) measured using the van der Pauw method for a film grown on Si (100). *Inset:* Thermopower behavior measured at room temperature using our custom thermopower screening tool. For comparison, the thermopower was measured for samples grown on Si (100) and LaAlO₃ (100).

The probing system (described later in more detail in the *Combinatorial Approach* section) is designed to measure 4-probe electrical resistivity by applying a fixed current through two outer probes and measuring the voltage drop across the inner two; and the Seebeck coefficient by heating one probe and measuring the voltage and ΔT across the two inner probes. This tool was designed to rapidly screen large (up to 4 in.) combinatorial samples, but can also be applied to bulk and smaller individual thin film samples. Samples from each deposition are currently being measured using the screening tool and checked for reproducibility. The inset of Figure 5.5 shows the α data, which is lower than expected, possibly due to measurement errors at the time of data collection. The sign of the α values indicates dominant hole carriers.

From high resolution transmission electron microscopy and scanning electron microscopy (HR-TEM and HR-SEM, respectively), five distinguishable types of diffraction rows (*A*, *B*, *C*, *D* and *E*), each with different inter-planar spacing, were taken from different areas of the film on Si (100) and are illustrated in Figure 5.6. The largest inter-planar spacing d (indicated with arrows) was measured for each diffraction pattern, and are 0.24 nm for *A*, 0.14 nm for *B*, 0.27 nm for *C*, 0.37 nm for *D* and 0.63 nm for *E*. According to the inter-planar spacing, diffraction *A* was indexed as from the [010] direction of CCO-349, diffraction *B* was indexed as from the [100] direction from CCO-349, diffraction *C* was indexed as from the [010]

direction of the CCO-225 phase, diffraction D was indexed as from the $[100]$ direction of CCO-225, and diffraction E was indexed as from the $[110]$ direction of CCO-225.

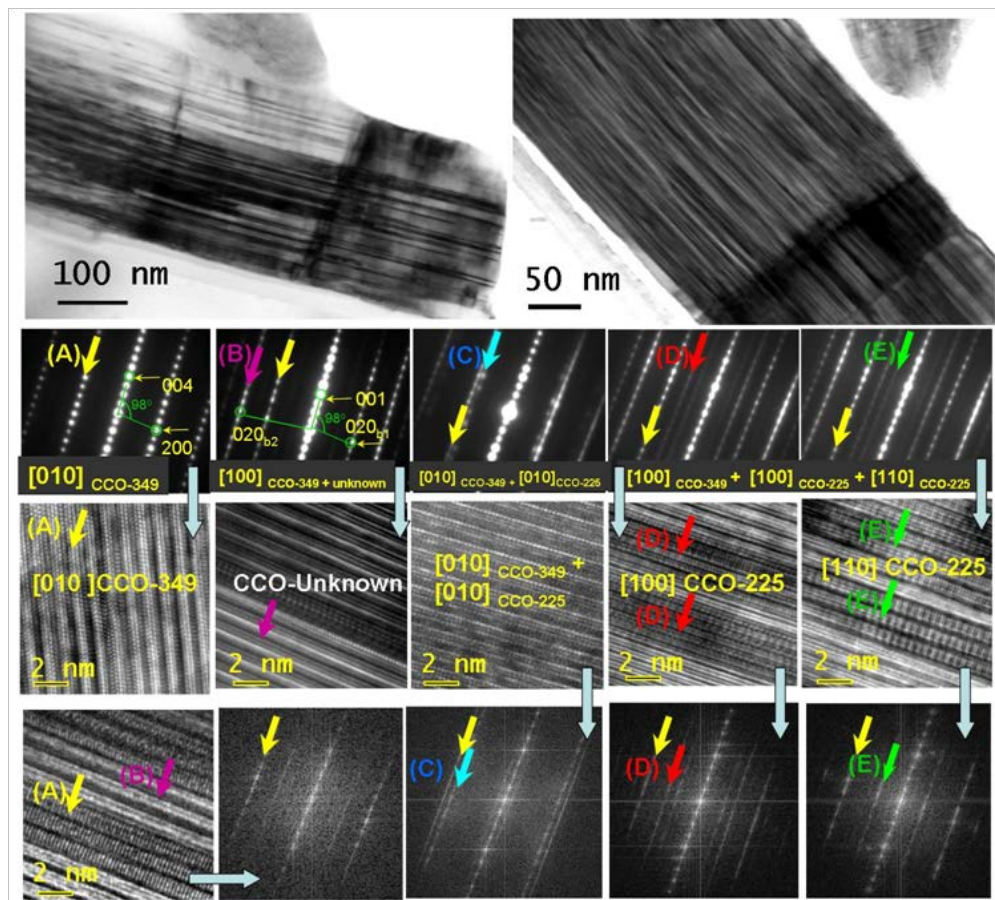


Figure 5.6. TEM and HR-TEM images of the three Ca-Co-O phases in the “pure” CCO-349 film

In addition to the CCO-349 and CCO-225 phases, there is an un-identified phase present, indicated as CCO-unknown, with a d -spacing of 0.14 nm, which is identical to (020) d -spacing CoO_2 sub-system. Because the d -spacing of the un-identified phase is 0.14 nm, smaller than the spatial resolution of 0.23 nm for the TEM instrument used, the 2D lattice image is not fully resolved, and only the lines parallel to the film plane are observable in the high-resolution transmission electron microscopy (HR-TEM) images. It is suspected that the un-identified phase may be related to CCO-349, possibly by mis-orientation. Each of the co-existing CCO phases share the same *out-of-plane* or c -axis lattice parameter as that of CCO-349 phase (~ 10.8 Å). However, the CCO-225 and CCO-unknown phases have very different *in-plane* lattice parameters from that of the CCO-349 phase. The phases have a nano-lamellar relationship (alternating stacking of different compositions) and are $\sim 5 - 10$ nm thick along the film normal.

The local chemical composition and additional details on the crystalline structure of the CCO-349 films were obtained from scanning transmission electron microscopy (STEM) equipped with High Angle Annual Dark Field Detector (HAADF) for Z-contrast imaging and Energy Dispersive Spectroscopy (EDS) for compositional mapping under STEM mode. EDS

mapping illustrates that all 3 phases consist of Ca, Co and O. In comparison with the CCO-349 phase, the CCO-225 and CCO-unknown have less Ca, as shown in Figure 5.7.

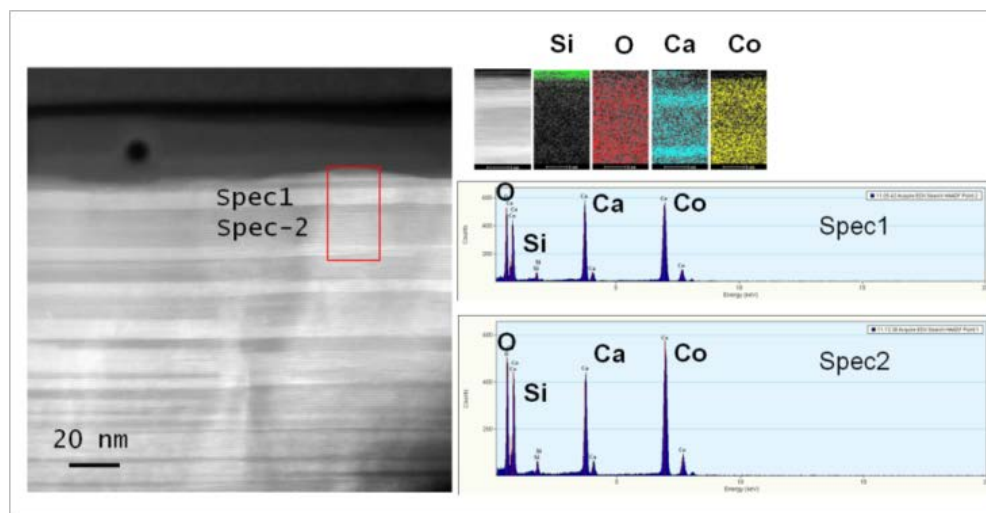


Figure 5.7 STEM Z-contrast images, EDS spectrum and EDS elemental mapping of CCO-349 (Spec 1) and CCO-225 (Spec 2)

As stated earlier, among the Ca-Co-O phases, CCO-349 and CCO-225 have the most enhanced TE properties. However, for CCO-225, film synthesis and the relationship of its structure and electronic and thermal properties to its TE behavior remains largely unexplored, as it has been discovered more recently. During the course of this study, we became interested in synthesizing textured Ca-Co-O films with various portions of CCO-349 and CCO-225 as multilayers. The TE properties of the different phases are still being explored to determine the influence of the co-existent nature of the various phases, which may enhance interfacial phonon scattering. The specifics of the task approach are outlined below:

1. Control of target stoichiometry: Current PLD films consist of ~ 70 – 80 % CCO-349 and CCO-225 phase, and ~ 20 – 30 % of the un-identified *B* phase. The presence of the nano-lamellar phases with slightly different Ca-concentration offers the unique opportunity of controlling the abundance and distribution of the compositions through controlling film growth conditions and stoichiometry of the target materials.
2. PLD growth temperature and oxygen partial pressure control: It was found that for Ca-Co-O phases such as CCO-326, O₂ pressure could have significant influence on the film's texture [29]. We currently deposit our films at an O₂ pressure of 300 mTorr, after which, the pressure is increased to 1 atm during cooling. We will conduct experiments at various pressures.

The concentration of charge carriers, and thus the electrical conductivity and TE properties of a semiconducting material, can be tuned by suitable substitution reactions. Several dopants have been reported to increase the TE properties of CCO-349. For example, it is reported that partial substitution of Fe⁺² for Co⁺³ can decrease the electrical resistivity and increase the thermopower simultaneously. At room temperature, the figure-of-merit of Ca₃Co₄.

$x\text{Fe}_x\text{O}_{9+\delta}$ ($x = 0.05$) is $zT = 0.017$ [30], which is significantly higher than that of pure CCO-349 ($zT = 0.009$ at 300 K).

We have conducted a similar doping approach by doping CCO-349 with BaZrO_3 (BZO) [24]. A composite target containing a mixture of pure CCO-349 and 3 wt% addition of BZO (hereafter, CCO+BZO), was prepared by mixing the two phases in a mortar and pestle, and compressing the materials into a pellet. Thin film samples were deposited using identical growth conditions as detailed earlier for the pure CCO-349 samples. Indexing of the (00 l) XRD peaks (not shown) reveal that the samples are hetero-epitaxially grown with strong c -axis texture. From the eight (00 l) peaks, the c -axis parameters were calculated and are 10.83 Å and 10.86 Å for pure CCO-349 and CCO+BZO, respectively. Although slight, this increase in the c -axis parameter suggested diffusion of Ba and Zr into the CCO-349 lattice. These data are within reasonable agreement with values from previous thin film studies and comparable to bulk CCO-349.

Electrical resistivity and Seebeck coefficient data for the samples grown from the composite target were measured and are shown in Figure 5.8. Majority carriers in CCO-349 are holes, so a decrease in ρ by doping with BZO may be attributed to substitutions on the Ca^{2+} site, which introduces more hole carriers, although further investigation is necessary. In other composite studies done with CCO-349, secondary additions facilitate well connections between cobaltite grains, which reduces carrier scattering at the grain boundary. This phenomenon considerably reduces the resistance at the grain boundary and, thus, decreases ρ . Thermopower behavior for all samples is metallic and typical for CCO-349-based materials, albeit with values much lower than expected, possibly a result of band structure changes due to cation substitution for Ca^{2+} . This behavior has been also observed for Ag-added samples versus Ag-doped samples [31]. Other possible explanations include the increase in carrier concentration and/or the resulting decrease of the effective mass of the hole, and also the spin-states of the Co ions. With the addition of 3wt% BZO, preliminary power factor ($PF = \alpha^2/\rho$) values increased by 7 % for the samples grown on Si and 27 % for LAO (Figure 5.8). Further studies such as photoemission or Seebeck suppression in a magnetic field may be necessary to reveal the ratio of $\text{Co}^{3+}/\text{Co}^{4+}$ to determine the spin-states in our samples.

The TEM analysis, STEM Z-contrast imaging and EDS mapping for the CCO+BZO samples is shown below in Figures 5.9 – 5.11. It was found that BZO doping has the following effects on the microstructure of CCO-349 films:

1. Increases the mis-orientation of nano-lamellae and induces low angle GBs perpendicular to the film plane (highlighted in Figure 5.9)
2. Stabilizes CCO-349 phase formation, although the film still consists of three (3) phases, CCO-349, CCO-225 and CCO-unknown (Figure 5.10)
3. Distributes Zr uniformly throughout the film (Figure 5.11)
4. Segregates Ba into the Ca-deficient regions of CCO-225, CCO-unknown, and also into the low-angle GBs (Figure 5.11).

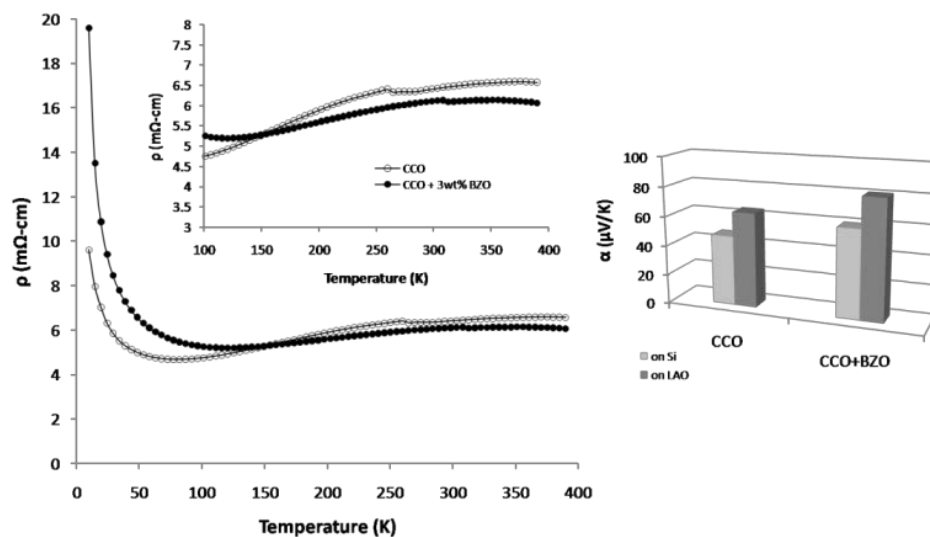


Figure 5.8. *Left panel:* Temperature-dependent electrical resistivity (ρ) measured using the van der Pauw method for films grown on Si (100). *Inset:* Blow-up of high temperature data. *Right panel:* Thermopower behavior measured at room temperature using the PFSL. For comparison, the thermopower was measured for samples grown on Si (100) and LaAlO₃ (100).

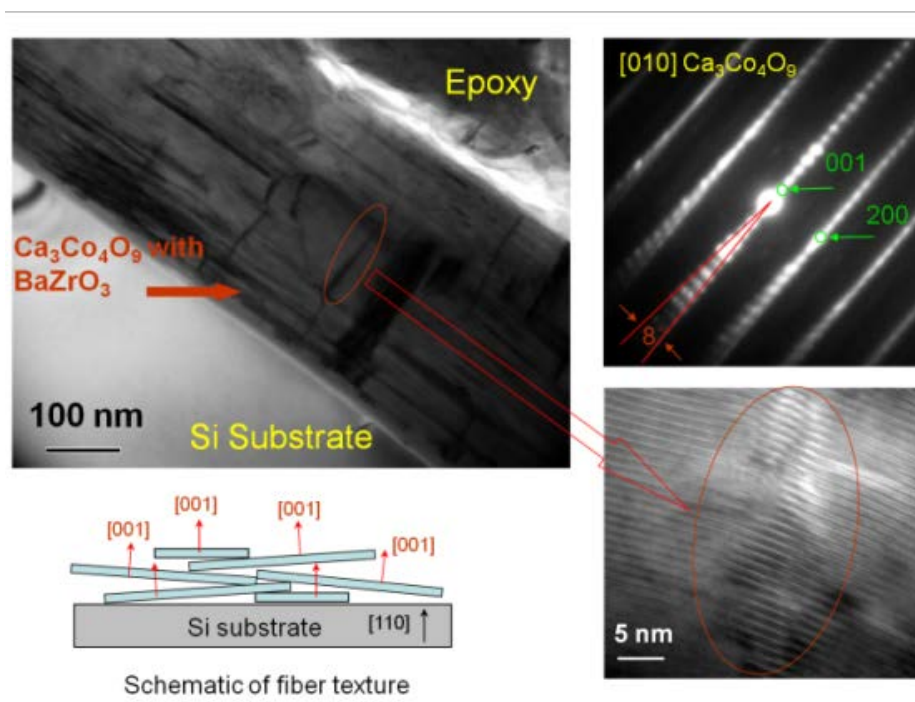


Figure 5.9. BZO-doped CCO film with increased mis-orientation and low angle grain boundaries perpendicular to the film plane

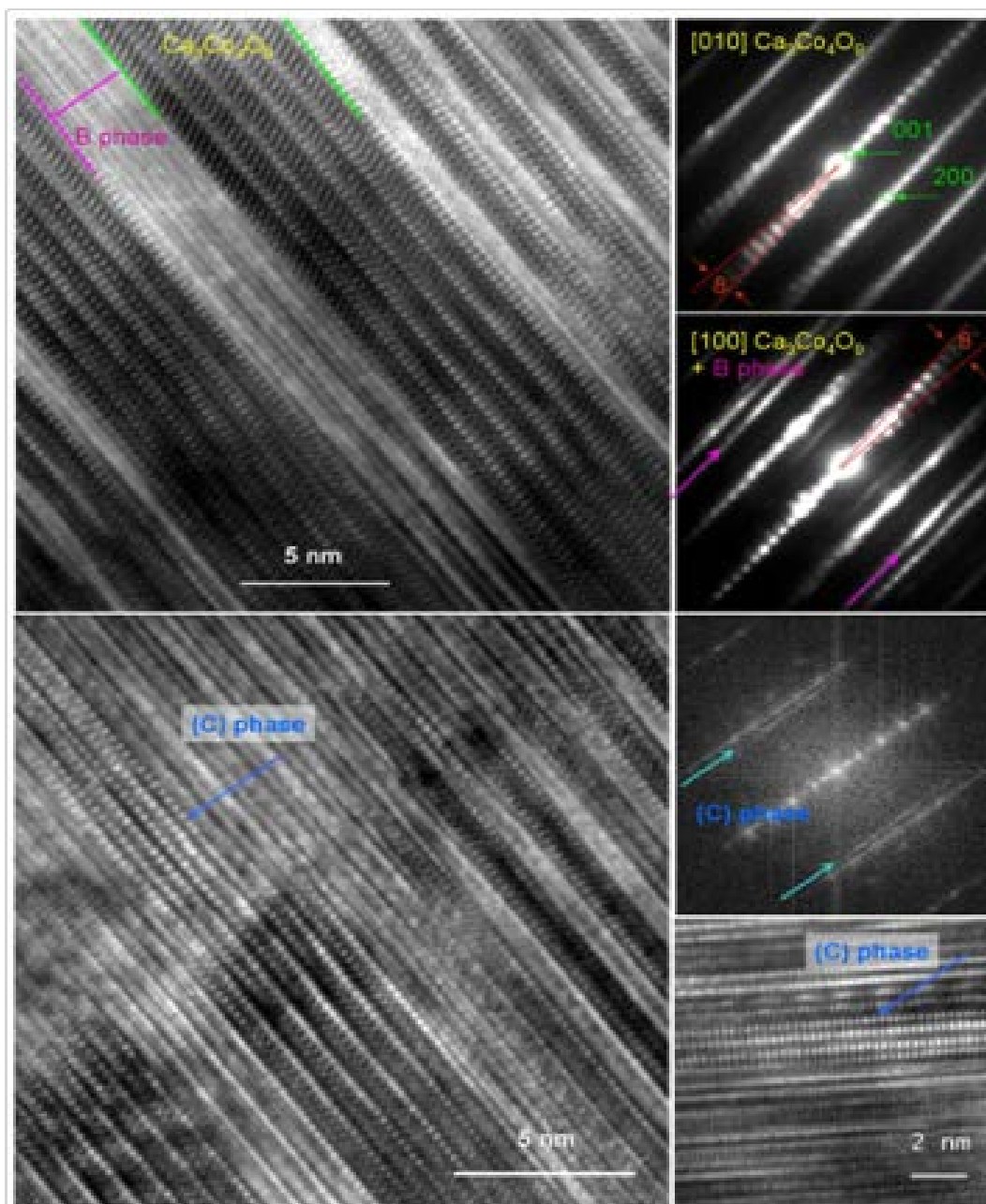


Figure 5.10. BZO-doped film with CCO-349 as the main phase and nano-lamellar CCO-225 (*B*) and CCO-unknown (*C*) phases

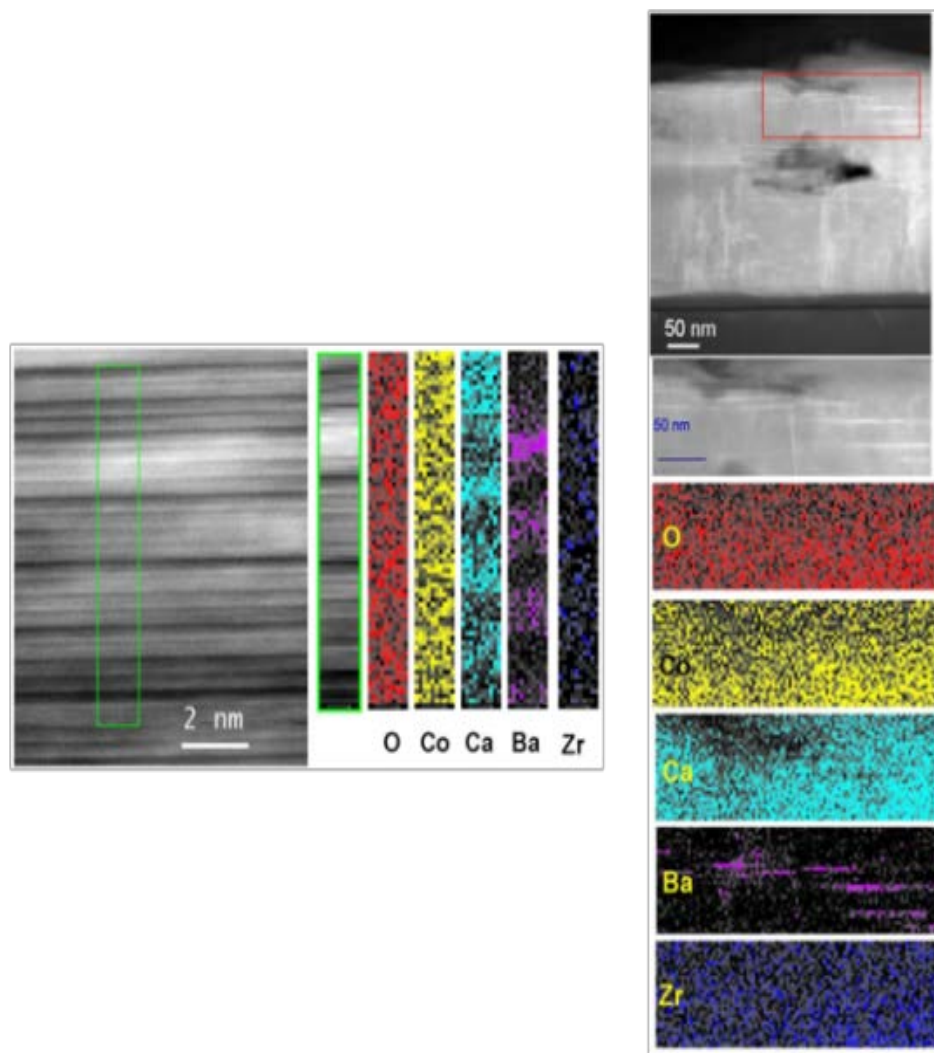


Figure 5.11. Zr is uniformly distributed throughout the film, while Ba segregates into Ca-deficient phases and GBs

The above results from the BZO-doped film clearly indicate that the formation of the low angle GBs and the chemistries of each phase can be controlled through doping. In order to obtain an enhanced figure-of-merit, the following doping approaches were attempted:

1. Optimization of BZO doping by adjusting weight fractions or volume percentages
2. Selection of other dopants such as Fe, Gd and Bi.

For the initial series of Ca-Co-O films grown on Si (100), we conclusively discovered that there is a reaction at the interface, with the stacking sequence: Si (100) / amorphous Si-Ca-O / crystalline Co_3O_4 / crystalline Ca-Co-O. The amorphous Si-Ca-O layer is likely due to the migration (diffusion) of Ca atoms into the thin SiO_2 layer on the surface in the Si substrate. This is highlighted in Figure 5.12. From the HR-TEM micrograph shown in Figure 5.13, it appears that the Ca-Co-O film spontaneously grows epitaxially on the crystalline Co_3O_4 layer. The

crystal orientation relationship between the Co_3O_4 phase and the Ca-Co-O phase is: $[110] \text{Co}_3\text{O}_4 // [010] \text{Ca-Co-O}$ and $(110) \text{Co}_3\text{O}_4 // (001) \text{Ca-Co-O}$.

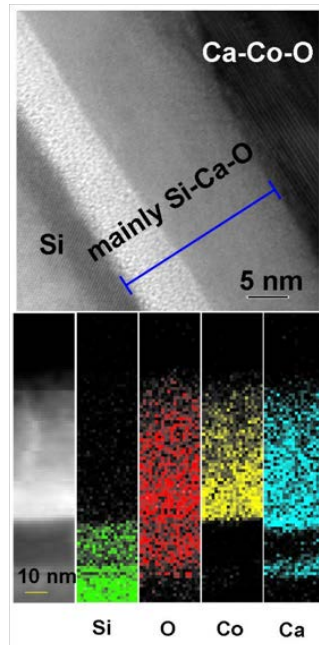


Figure 5.12. (Top) Ca-Co-O film with interface reaction layer highlighted. (Bottom) Element distribution at interface reaction layer (note scale)

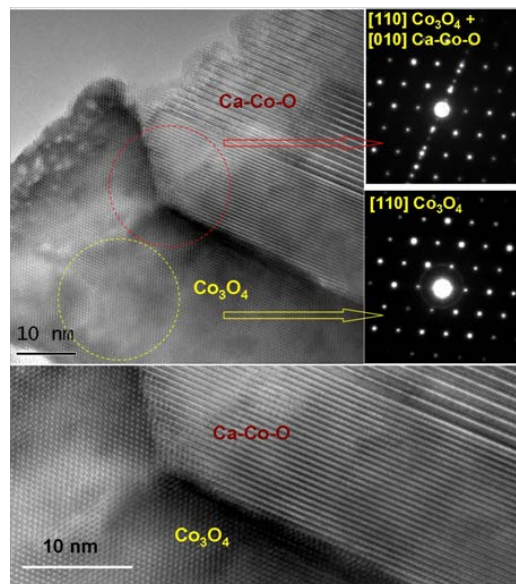


Figure 5.13. HR-TEM micrograph revealing the epitaxial growth of the Ca-Co-O phases on the interface reaction layer of crystalline Co_3O_4 (note scale)

5.3.1.4 Ca-Co-O/Co₃O₄ nano-composite

The addition of nano-inclusions into bulk-scale TE materials such as SiGe- and Bi_{2-x}Sb_xTe₃-based systems for use in high-temperature power generation and cooling applications, respectively, has proven to be very effective in enhancing the phonon scattering and the figure-of-merit. Recently, particular emphasis on nano-structured engineering has been towards systems based on PbTe, AgPb_mSbTe_{2+m}, NaPb_mSbTe_{2+m}, Bi₂Te₃, and Si. To date, the dramatic zT enhancements seen in bulk nano-structured materials have come from very large reductions in lattice thermal conductivity rather than from improvements in power factors ($PF = \alpha^2 \sigma$). The addition of nano-inclusions into oxide materials for TE property enhancement is largely unexplored. As mentioned in the Introduction of this chapter, the challenge for any nano-structured system is charge carrier scattering at interfaces and GBs between randomly oriented grains, thus leading to a concurrent reduction of *both* the thermal and electrical conductivities [6]. The ideal nano-structured materials should have *thermodynamically stable, coherent, epitaxial-like* interfaces between the constituent phases to prevent scattering of electrons at interfaces and GBs.

The objective here is to develop high performance Ca-Co-O films with designed nano-defects, including nano-inclusions with appropriate *size* and appropriate *interval spacing*, for enhanced phonon scattering. The evidence for epitaxial growth of the Ca-Co-O phases on the Co₃O₄ phase that we discovered earlier offers the opportunity of growing a Ca-Co-O film with Co₃O₄ nano-inclusions, or alternately, nano-layered Co₃O₄, uniformly distributed inside the Ca-Co-O film. We continued to explore the method for incorporating secondary oxide phases into textured Ca-Co-O films, by starting with the new candidate Co₃O₄, since Co₃O₄ is chemically compatible with Ca-Co-O and is also stable at high temperature. By satisfying the interface requirements with Ca-Co-O to prevent scattering of electrons at interfaces and GBs, Co₃O₄ is an ideal candidate for serving as nano-dispersions (inclusions) inside the Ca-Co-O films. In addition, the electrical conductivity behavior of *p*-type semiconducting Co₃O₄ [32] is expected to simultaneously increase the electron conductivity and decrease the thermal conductivity when incorporated as nano-inclusions, due to migration of vacancies.

An in-house grown Ca-Co-O/Co₃O₄ nano-composite sample is shown in Figure 5.14. Here, a multilayer structure is formed from the two material compositions; however, the notion that the two phases are insoluble is confirmed. In following depositions, nano-inclusion concentration was controlled at various levels ranging from ~ 1 – 5 mol%. This was made possible by using a bulk CCO-349 target with a 30° sector (slice) of Co₃O₄ affixed to the top surface. As the target rotates during the laser ablation deposition process, minute amounts of the second phase are trapped inside of the bulk matrix. Additions were easily controlled by alternating targets during deposition or by varying the dimensions of the sectorized material. In addition to Co₃O₄, the use of other compatible oxide candidates for nano-inclusion incorporation into the film(s) is being considered as well.

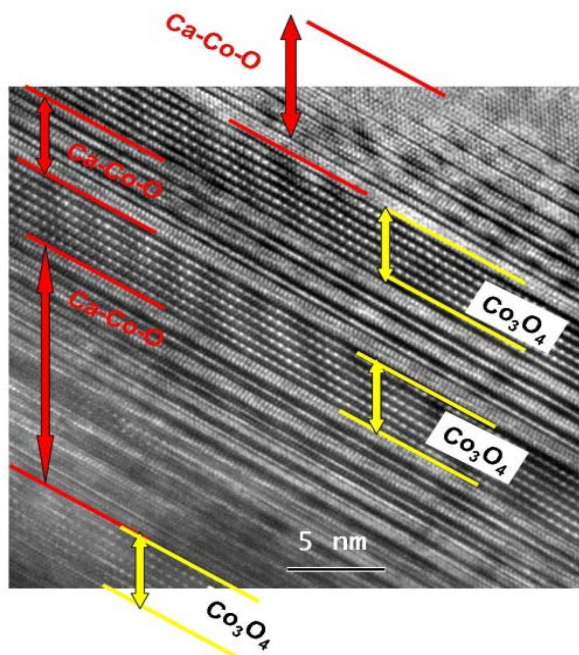


Figure 5.14. Nano-layer Co_3O_4 alternating with Ca-Co-O deposited using a sectored target PLD approach

5.3.1.5 Physical Property Measurement System Upgrades and Data Collections

Early in FY11, the Physical Property Measurement System (PPMS) was upgraded with the Thermal Transport Option (TTO) for TE property measurements from 10 K – 390 K (-263 – 127 °C). The TTO measures the electrical resistivity ρ , thermal conductivity κ , and Seebeck coefficient α , to calculate the figure-of-merit (zT). Both thin film and bulk TE samples can be measured, however, the thermal conductivity for thin films cannot be decoupled from the supporting substrate and therefore figure-of-merit determinations would be inaccurate. With this being the case, typically only PF (α^2/ρ) behavior is observed and reported for film samples. Furthermore, our samples are deposited onto insulating substrates, to avoid electrical shorting during measurement. By combining the PPMS/TTO data with data from the internally-developed PFSI, and also with data collected externally using a high temperature Linseis Seebeck and electrical resistivity measurement system (WVU collaboration), the PF s of our materials can be evaluated from -263 – 1000 °C.

Since its installation, the TTO has been used to evaluate the low temperature performance of 200+ thin film and bulk samples in-house. Figure 5.15 shows a sampling of the PF data collected for a variety of thin film samples deposited at different rates (2, 3 and 4 Hz), on different substrates (Al_2O_3 and LAO), and using different targets (2 pure CCO-349 and 1 BZO-doped CCO-349 target). Beneath the plot in Figure 5.15 is a schematic of the electrical lead configuration adapted for TTO transport measurements of thin film samples.

One of the challenges encountered when comparing TE property data reported by different research groups is the large variation of metrology. Many groups routinely measure α on one sample, and ρ on a different sample, then combine the data from the two independent property measurements to determine the performance characteristics. Also, many studies may report data collected for a single sample using separate measurement techniques. While these

data from the same sample may be considered more accurate, data collection in this manner is very time-consuming. The method of thin film sample preparation developed in-house allows for *simultaneous* measurement of both electrical resistivity and Seebeck coefficient on the *same* samples using the PPMS/TTO. Several samples of CCO-349 on LAO or sapphire (Al_2O_3) have shown Seebeck coefficients of 140 – 145 $\mu\text{V/K}$ at 300 K (*not shown*), which is comparable to the highest values reported in literature for pure CCO-349 single crystals and epitaxial films. A reference curve [33] from the study of an optimized, textured CCO-349 epitaxial film grown on Al_2O_3 , and tested in a manner similar to ours, is superimposed in the *PF* plot in Figure 5.15 for comparison.

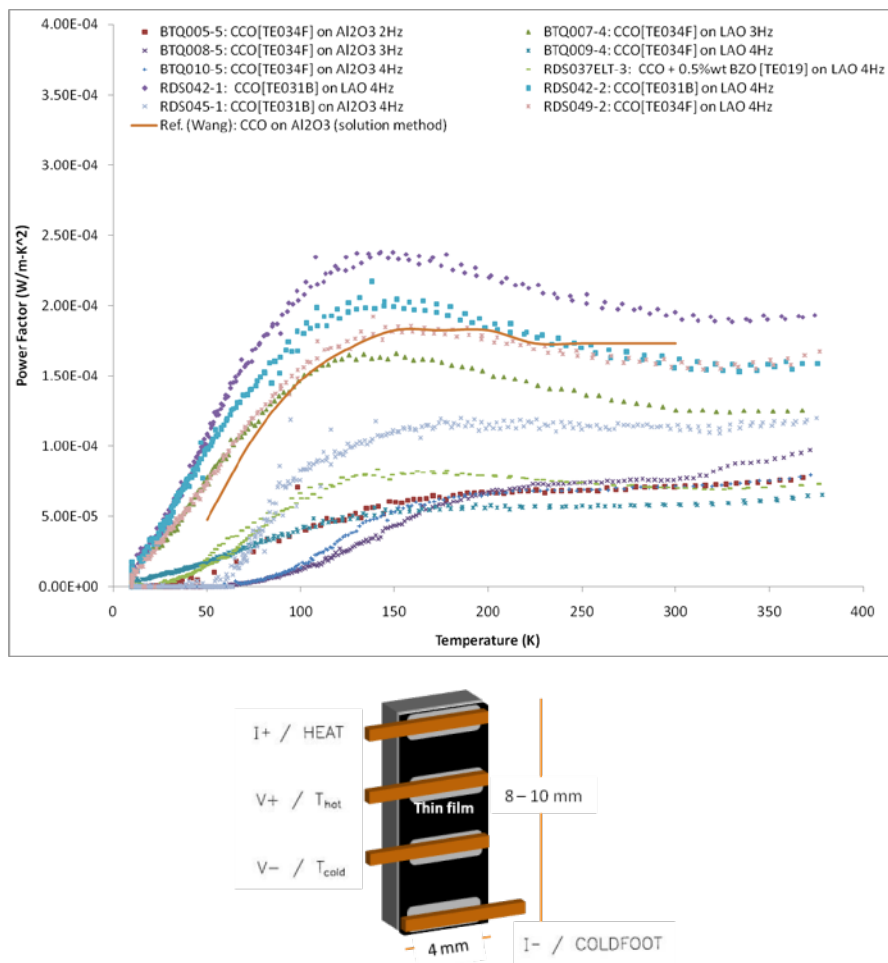


Figure 5.15. (top) Temperature-dependent Power Factor data for Ca-Co-O-based thin film samples deposited on insulating substrates. A reference curve (Wang, et al.) is shown for comparison. (bottom) 4-probe configuration for thin film measurement using the PPMS/TTO.

Figure 5.16 displays a sampling of the zT data collected for a variety of pure CCO-349 and BZO-doped CCO-349 bulk samples grown in-house. These tests have revealed two noticeable trends: (1) the oxygenation of bulk samples after cutting for property measurements reduced the electrical resistivity by nearly an order of magnitude, and (2) the addition of BZO lead to a pronounced reduction of the zT . The oxygenation procedure (annealing in flowing O_2

at $500 \leq T \leq 800$ °C) ensured that the samples' surfaces were not oxygen deficient, which lead to better electrical conduction, and therefore higher zT values. The addition of BZO results in a reduction in both the electrical conductivity and Seebeck coefficient, likely due to localized phase dispersion within the CCO-349 bulk material. Moreover, if a chemical reaction between the two phases occurs during the composite target synthesis, then substitution of Zr for Co would alter the Co spin-states, facilitating the behavior observed. The very different segregation behavior of the Zr and Ba atoms in our thin film samples has been presented earlier and illustrated in Figure 5.11. Ba occupies Ca-deficient regions within the film, and being larger than Ca, also introduces strain, thus adversely affecting the carrier transport. Though yet to be seen, this phenomenon may also play a role in the bulk materials. As the concentration of BZO increases, the zT decreases further. To accurately determine the cause of the reduction in zT due to BZO addition, we began additional studies, which included iodometric titration to determine O_2 content, photoemission, and Seebeck suppression in a magnetic field via the PPMS/TTO to determine the Co^{3+}/Co^{4+} ratio.

With very few references reporting zT behavior of CCO-349-based materials at low temperatures, the reference curves [34] in Figure 5.16 were calculated from the reported PF values by Kenfau, et al. Since the thermal conductivities for nearly all of our bulk samples of CCO-349 fall between 1 – 2 W/m-K, we used the reported PF values to estimate a likely range of zT values for the reported data (assuming that the thermal conductivity behavior is similar to ours). Based on this assumption and subsequent calculations, we find that our CCO-349 samples are within range of values reported by other research groups at $T < 300$ K.

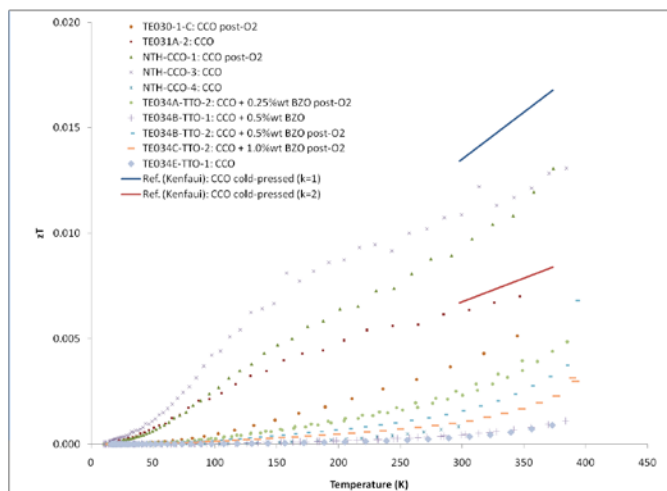


Figure 5.16. zT data for bulk Ca-Co-O-based samples measured using the PPMS/TTO (note temperature range). The reference curves were calculated from reported data by Kenfau, et al.

1.1.1.1 Fe Doping Study Summary

Bulk Fe-doped CCO-349 ($Ca_3Co_{4-x}Fe_xO_{9+\delta}$) samples and pulsed laser deposition (PLD) targets were made using standard solid state ceramic processing methods. Stoichiometric amounts of Co_3O_4 , $CaCO_3$ and Fe_2O_3 were mixed to form samples with various Fe content. The synthesis approach was developed experimentally using the $CaO-Co_3O_4$ phase diagram and iterative powder XRD results. These experiments showed that Fe could be used to increase the

electrical conductivity and Seebeck coefficient while simultaneously decreasing the thermal conductivity in doped CCO-349 bulk samples.

Thin film samples were deposited on various substrates using PLD. A KrF excimer laser was used ($\lambda = 248$ nm) at a repetition rate of 4 Hz and pulse energy of ~ 348 mJ (~ 1.7 J/cm). 350 nm thick films were deposited at 973 K (700 °C) in 300 mTorr O₂. After deposition, the films were cooled to room temperature in 1 atm O₂ with a 1 hour *in-situ* anneal at 773 K (500 °C).

Initially, elemental (Ca, Fe, Co) analysis of the Fe-doped CCO-349 bulk samples was done using energy dispersive spectroscopy. The actual content of Co and Fe was very close to the expected value throughout the range of Fe contents.

Powder x-ray diffraction of the Fe-doped CCO-349 bulk materials revealed the formation of secondary phases with increasing Fe content. Below $x = 0.5$, Fe appeared to be incorporated into the CCO-349 crystal structure as the *c*-axis parameter varies with Fe content. In addition, below $x = 0.5$ there is no evidence of secondary phases in the diffraction patterns. As the Fe-content increases above $x = 0.5$, the amount of CCO-349 decreases and two secondary phases begin to appear: an Fe-rich phase (Ca₂Fe₂O₅) and an Fe-poor phase (Co₃O₄). At $x = 2.0$, these two phases are the only phases present; there was no evidence of CCO-349.

Several samples have been analyzed via XPS in AFRL's Materials Directorate. Initially, 3 thin film samples with varying Fe content were analyzed. These samples were tested both as-received and after sputtering for 60 seconds to probe the composition of sample about 50-100 nm below the initial surface. There was a substantial amount of carbon, C (~ 35 at%), in the as-received samples. Even after sputtering, the C content of the film was ~ 20 at%, although it was suggested that this could be due to mixing of the surface contamination with the film during sputtering. Interestingly, the most Fe-rich sample showed evidence of C atoms existing as FeC within the depth of the film, which was not seen in XRD analysis of thin film samples from this target. This lends evidence to the theory that mixing may be occurring during sputtering. For lower loadings (~ 1.5 at%) of Fe, there was no evidence of Fe in the sample through XPS. There could be several reasons for this. First, the large amount of C contamination reduces the sensitivity of the technique and the low Fe content is near the detection limit for the technique. Also, the peaks for Fe and Co are fairly close together with the Fe 2p doublet overlapping with the Co auger peak making identification more difficult. These results are still under investigation.

The TE properties of our Fe-doped CCO-349 bulk samples have been compared to values found in literature. In all cases, electrical resistivity decreases with small additions of Fe ($x \leq 0.5$) as expected. The Seebeck coefficient remains constant for most datasets. Regardless of the magnitude of effect on Seebeck, all of our samples show a notable increase in the Power Factors (combination of electrical resistivity and Seebeck coefficient) at Fe contents below $x = 0.5$. Our samples show a significantly lower thermal conductivity – three to six times – than reference samples, and suggests a weak relationship to Fe content, unlike that of reference samples. These measurements will be re-evaluated for accuracy.

In our samples, however, overall, zT increases up to 200-300% with increasing Fe content below $x = 0.5$ have been observed. Similar analyses have been performed on thin film samples. These samples also did not display a strong relationship between Seebeck coefficient and Fe content, with neither improvements nor reductions in Seebeck coefficient. These samples do however show a strong increase in electrical conductivity (significant reduction in electrical resistivity) over bulk samples due to increased density and sample texturing due to structural

changes as a result of Fe-doping. The Power Factor of these samples was increased by 300-400% as compared to the bulk samples.

5.3.2 Approach 2: High-throughput Combinatorial Approach for Rapid Identification of Novel TE Materials

5.3.2.1 Overview

Combinatorial science was first demonstrated in the medical industry for drug discovery, and with considerable advances in methodology, has now been successfully applied to materials science. For materials research, this approach has been effective in allowing a small number of precursor chemical reagents (solid or solution-based) to be merged into all possible combinations in a given reaction scheme for direct comparisons (crystal structures, performance properties, *etc.*) [35]. In addition, combinatorial screening methods have allowed for multidimensional chemical composition exploration at an unprecedented level of detail, and have led to the discovery of a wide variety of technologically important materials ranging from high temperature superconductors, magnetic, dielectric, ferroelectric, and structural materials to catalysts, polymeric coatings and advances in thin-films. Although the combinatorial processing and high-throughput screening is readily becoming more accepted in the materials science community, similar capabilities to those at AFRL are restricted to a severely limited number of research facilities, one of which being the National Institute of Standards and Technology (NIST). NIST uses these capabilities primarily for standard certification or for metrology and methodology advances and not for the purposes of materials enhancement. This makes our custom combinatorial deposition and screening apparatus a near one-of-a-kind asset.

5.3.2.2 Introduction

A variety of novel synthesis and processing techniques for tailoring TE responses have been employed in the study of new TEs, however, a disadvantage associated with many of these methods is the time-effort involved in the processes. The combinatorial approach has been a prevalent technique in the pharmaceutical and biotechnology industries in which various combinations of materials are evaluated for specific physical properties. The combinatorial method can eliminate some of the effort associated with the trial-and-error syntheses of inorganic solid-state materials such as intermetallics and ceramics, and can quickly and cost-effectively produce libraries of binaries, ternaries, quaternaries, *etc.*, in the investigation for compounds with interesting electronic, magnetic, optical or mechanical properties [35]. Using this technique, precursors are deposited successively through physical masks to vary the elemental compositions, after which, physical property measurements of the fabricated films may be screened. Since materials previously synthesized by bulk methods may exhibit different electronic behavior than their thin film and nanostructured counterparts, the combinatorial method will likely lead to a facile measurement of the *PF*, which may be the most valuable property to evaluate for potential TE materials by serving as a preliminary *zT*. In this regard however, a reliable identification of materials most suitable for TE applications depends largely upon innovative methods designed to rapidly scan thin films for compositions with enhanced TE properties, which are currently lacking. The combinatorial approach to the research and development of TE materials may further advance and improve the materials needs of the U.S.

government and industries. Otani, et al. [26, 27] studied the $(\text{Ca}_{1-x-y}\text{Sr}_x\text{La}_y)\text{Co}_4\text{O}_9$ system and found that substituting La for Ca results in an increase in resistance and Seebeck coefficient, whereas Sr substitution decreases resistance. This effort was instrumental in testing the effectiveness of a high-throughput screening tool, although measurements were limited to room temperature. In order to identify efficient ($zT > 1$) materials compositions and the effects of doping on TE behavior, it is of key interest to measure performance over a range of operating temperatures.

In FY10, we designed a method in which to rapidly identify novel TE materials and determine compositions with optimized TE behavior by applying a high-throughput *Combinatorial Approach*. Combinatorial mapping is a state-of-the-art screening technique, and is an effective method for accelerating the selection and introduction of TE materials into the manufacturing process. It allows for rapid identification and characterization of materials as well as for concise descriptions of composition-structure-property relationships. TE property enhancements have been achieved in different materials systems through various approaches, including nano-structuring, texturing, and other structural modifications. Additionally, TE materials can often be further improved through doping and void-filling effects. However, a major disadvantage associated with many of the conventional synthetic techniques that have shown success in improving TEs, is the extensive time and manpower involved in single material processing (synthesis and characterization). The combinatorial method eliminates much of the effort associated with the trial-and-error syntheses of inorganic solid-state materials, such as intermetallics and ceramics, and can quickly and cost-effectively produce libraries of binaries, ternaries, quaternaries, *etc.*, in the search for compounds with enhanced electronic, magnetic, optical or mechanical properties. Using this technique coupled with pulsed laser deposition (PLD) for the fabrication of solid-solution thin-films, precursors are deposited successively either through physical masks to vary the elemental compositions, or by the natural-spread method, after which, physical property measurements of the fabricated films may be screened. Figure 5.17 shows the general combinatorial PLD method for fabricating thin film libraries on 3 to 4 in diameter substrates at high temperatures. Since materials previously synthesized by bulk methods often exhibit different electronic behavior than their thin film and nano-structured counterparts, the combinatorial method will likely lead to a facile measurement of the power factor. In this regard however, a reliable identification of materials most suitable for TE applications depends largely upon innovative methods designed to rapidly scan thin-films for compositions with enhanced TE properties, which are currently lacking. The combinatorial approach to the research and development of TE materials stands to further advance and improve the materials needs of the TE industry.

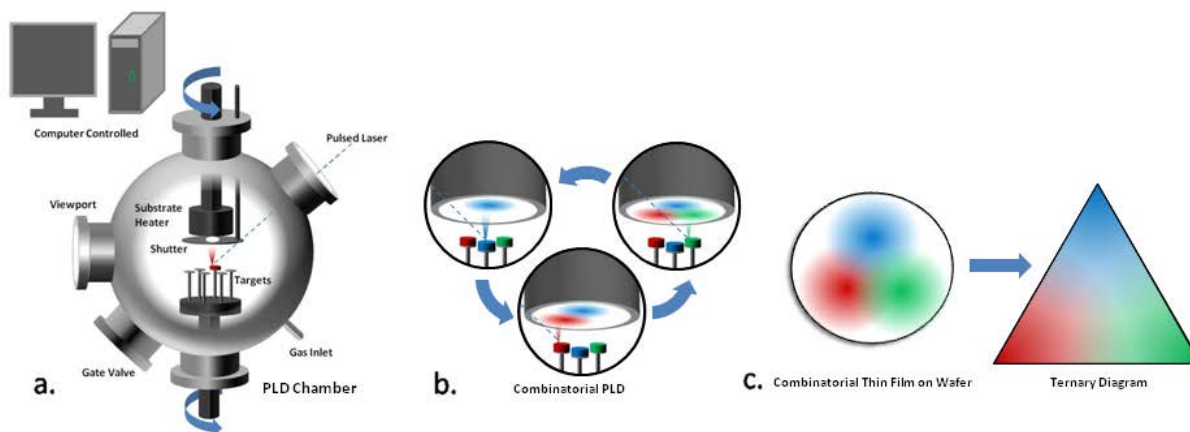


Figure 5.17. Fully-automated combinatorial deposition process. (a) Depiction of PLD chamber components with laser entry and rotating targets and substrate. (b) Alternating targets are ablated to deposit single layers at various substrate positions. (c) After reaching desired thickness based on material calibrations, a ternary diagram is achieved where the three materials overlap.

One of the greatest hurdles to overcome in this *Combinatorial Approach* is to reliably conduct rapid yet accurate screening of continuous composition sample libraries. Typically, thin film research samples are small (4 mm x 8 mm), and consist of a single composition, which is evaluated initially on the basis of crystal structure, sample morphology and TE properties. This requires structure and homogeneity analyses via XRD (~10 min scans) and TE property measurements by PPMS/TTO (~1 h for a 300 K measurement or 8+ h for a 10 – 390 K sweep). These techniques can be labor intensive as each sample must be prepared and tested individually. Through the *Combinatorial Approach*, the number of sample compositions on a 4 in wafer grows substantially to over 200 for patterned samples, and up to 1000+ for natural-spread samples. An additional challenge using this approach occurs with the introduction of gradients, which adds two more variables to be analyzed for each sample: elemental composition and film thickness. Even with effective complementary measurement techniques, the sample compositions contained on a single combinatorial sample would take several months to analyze by conventional methods, and unfortunately, no COTS combinatorial-specific analysis equipment is currently available.

There are several analyses that are crucial to evaluating combinatorial libraries in search of promising TE compositions, including crystal structure determinations and morphology analysis, composition studies, film thickness determination, and electrical and thermal property measurements. Crystal structure and material morphology are typically evaluated via XRD and microscopy techniques, respectively. The importance of these techniques is two-fold. First, one is provided an initial glimpse at the multi-phase structure (substitutional dopant, secondary phase, *etc.*). Second, since individual sample compositions on a substrate may not crystallize at the same temperature, crystallinity mapping allows us to identify crystalline regions of a combinatorial library and observe any deposition/anneal temperature effects for eventual structure-property correlations. (Ideally composition-spread samples are solid-solutions and thus have similar structural properties.) The Division Bruker D8 XRD system allows for fully automated, high precision structure determinations of the different compositions that make up the combinatorial libraries. These analyses ensure a greater accuracy when evaluating various compositions for enhanced TE behavior. Elemental composition analyses ensure that the

structures and TE property data is being assigned to the proper compositions, and can be determined via x-ray fluorescence (XRF), x-ray photoelectron spectroscopy (XPS), or wavelength dispersive spectroscopy (WDS).

Electrical resistivity in low-dimensional materials is a function of the materials' thickness (specifically, inversely proportional), thereby making film thickness measurements vital for accurate TE property measurements. While it would be ideal to assume a constant film thickness gradient following deposition, our large combinatorial film samples typically contain thickness variations depending on each material's ablation profile. Due to the nanometer scale thickness of our thin film samples, even minor variations in the film thickness could result in large variations of the measured electrical resistivity and could drastically alter the TE property maps if left unaccounted for. We have carefully considered these aspects (discussed later) in our sample processing and analysis procedures, which are designed to be conducted both quickly and cost-effectively.

5.3.2.3 *Experimental*

Aside from the TE property measurement methods mentioned earlier, in general, reliable means for adequate high temperature measurements of thin-films are still deficient. The methods discussed are sufficient for *PF* determinations for individual thin film samples, but are impractical for measurements of large, composition-spread samples. We have designed and built a Power Factor Screening Instrument (PFSI), with the capability to measure these large samples. This state-of-the-art tool, shown in Figure 5.18, is a high temperature adaptation of a measurement system developed by our collaborators at the National Institute of Standards and Technology (NIST). It consists of five main parts: the sample stage, the measurement head, the vacuum chamber, the instrumentation rack and the computer. The wiring diagram is provided for completeness in Figure 5.18 (d). This fully automated device is equipped with two linear translation stages and one vertical translation stage from Newport Corp. These control the movement of the sample to the different measurement positions. A water-cooled 3" dia. heater is mounted on the translation stages and can heat the sample up to 500 °C. The measurement head (highlighted in Figure 5.18 (b)) consists of a ceramic arm on an aluminum vertical support, and attached to the bottom of the ceramic arm are two copper blocks which are designed to measure electrical conductivity (resistivity) and Seebeck coefficient ($\Delta V/\Delta T$) using four (4) Au-plated BeCu spring probes as sample contacts. Each Cu block (detailed in Figure 5.18 (c)) has embedded within it a small resistive cartridge heater to establish and maintain a small temperature gradient (ΔT). The heads also contain two Pt resistance temperature detectors (RTDs) within the Cu blocks, one for feedback to the controller and the other directly on the spring probe to measure the temperature precisely at the location of the ΔV measurements. The spring probes and thermocouples are electrically isolated from the copper blocks and each other by a thin layer of high temperature epoxy. The spring probes are arranged in a straight line and used to make 4 probe resistivity and Seebeck voltage measurements.

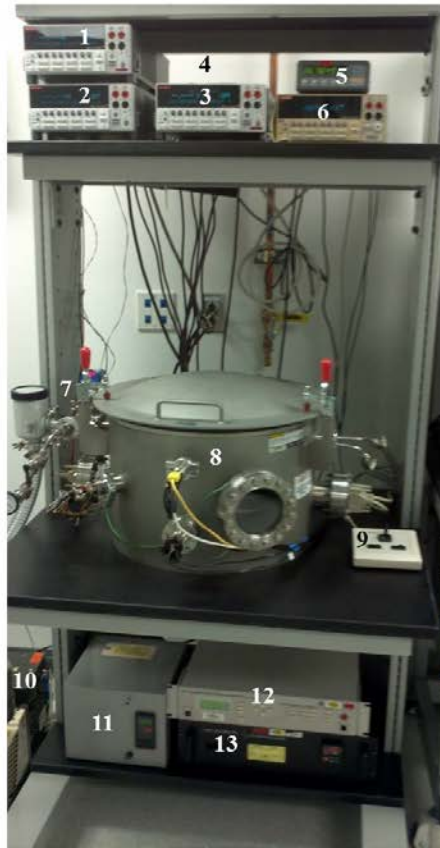
By collecting data at a rate of over 150 sample points per hour, it becomes evident that this is an extremely effective method for the rapid identification and characterization of materials, as well as for reliable descriptions of composition-structure-property relationships at different temperatures. Several other screening tools have been reported, however, many can only be used for bulk samples, or up to ten thin film samples, and/or are limited by temperature.

The sample is manually positioned with the center of the sample under the measurement head. The custom-designed software program is then used to input the sample dimensions and

the spacing between the sample locations. The program then automatically generates a field of sample locations to be measured. The stages move the sample to those locations and take the measurements. Figure 5.19 illustrates the front panel of the LabVIEW program designed to input data collection parameters. This program employs necessary algorithms and correction factors, and applies them to the measurement process in real-time.

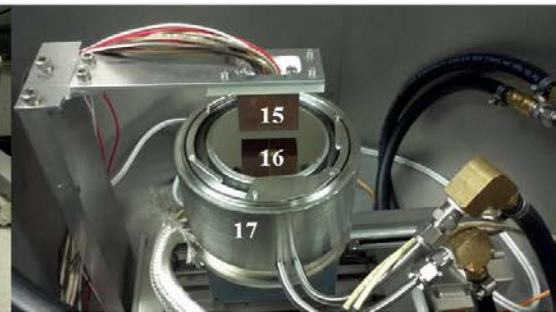
The cartridge heaters are controlled by an Omega CN616 heater controller. Each heater is controlled separately to allow for a large variety of temperatures and temperature gradients (ΔT). The cartridge heaters in the measurement head are controlled to a user specified ΔT . The sample is then moved into contact with the spring probes and a ΔT is allowed to develop across the sample. After a user specified delay time, the Seebeck voltage is measured for a user specified time and the values averaged to yield the thermopower.

$$\alpha = \frac{\Delta V}{\Delta T} \quad (1)$$

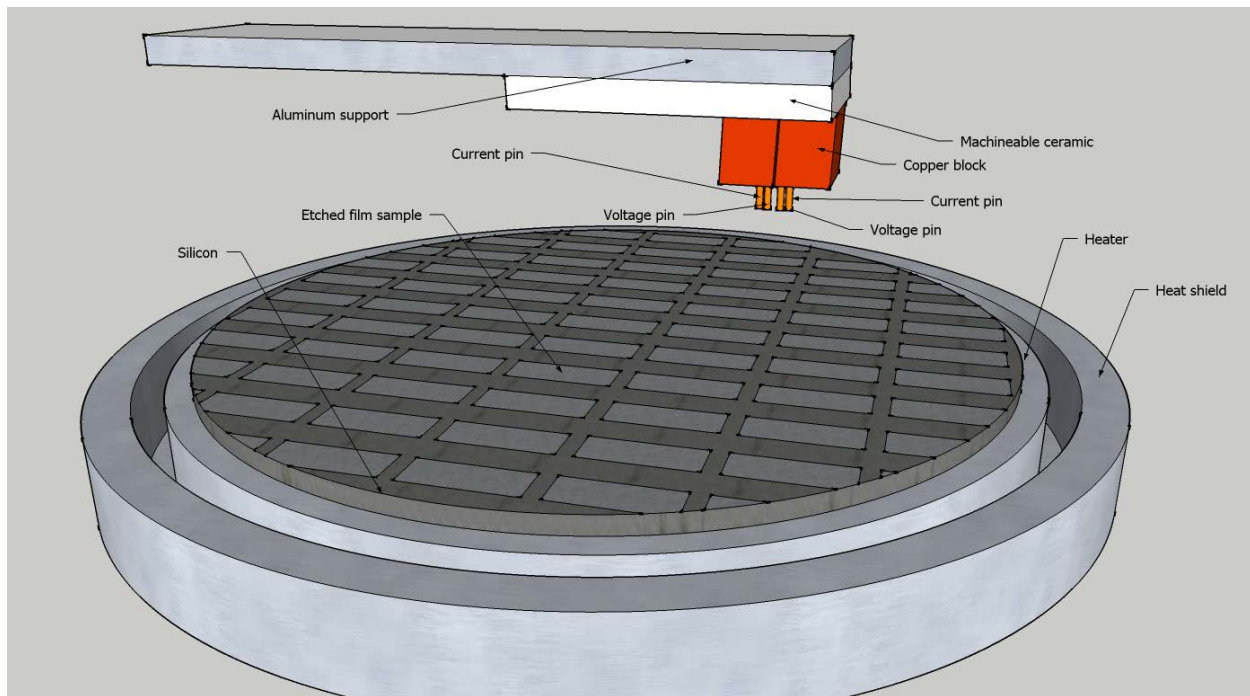


PFSI Components

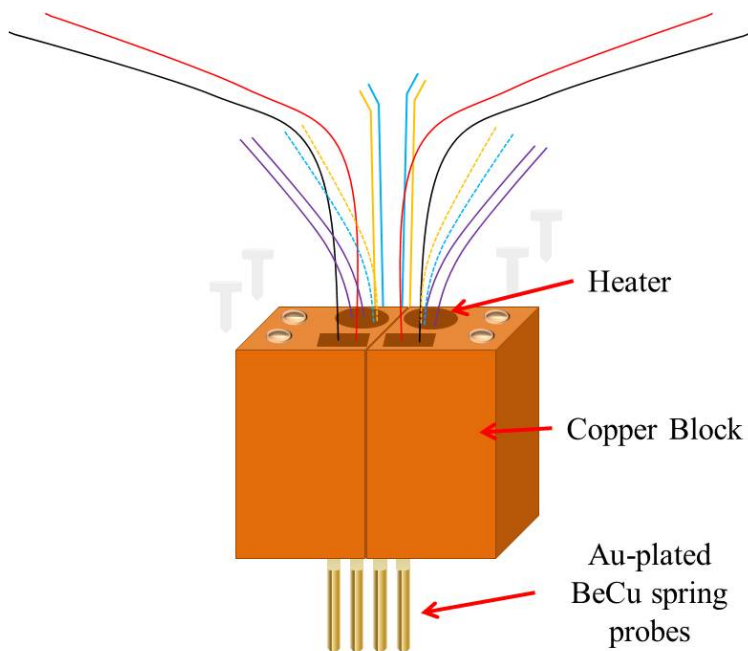
1. Keithley 2400 Sourcemeter (J23544)
2. Keithley 2400 Sourcemeter (J23545)
3. Keithley 2400 Sourcemeter (J25341)
4. Keithley 2181A Nanovoltmeter (J25324)
5. Fluke Thermometer Readout (J27323)
6. Keithley 2000 Multimeter (J1136)
7. Kurt J, Lesker Pressure Gauge (J23693)
8. Vacuum Chamber
9. Newport Motion Controller Joystick
10. Vacuum Pump
11. HA400 Temperature Controller (J23758)
12. Newport Universal Motion Controller/Driver Model ESP 300 (J18708)
13. HeatWave Labs, Inc. Model 101303 Temperature Controller (J23458)
14. PolyScience Water Chiller/Circulator (J27218)
15. Probe Head
16. Sample
17. Sample Stage



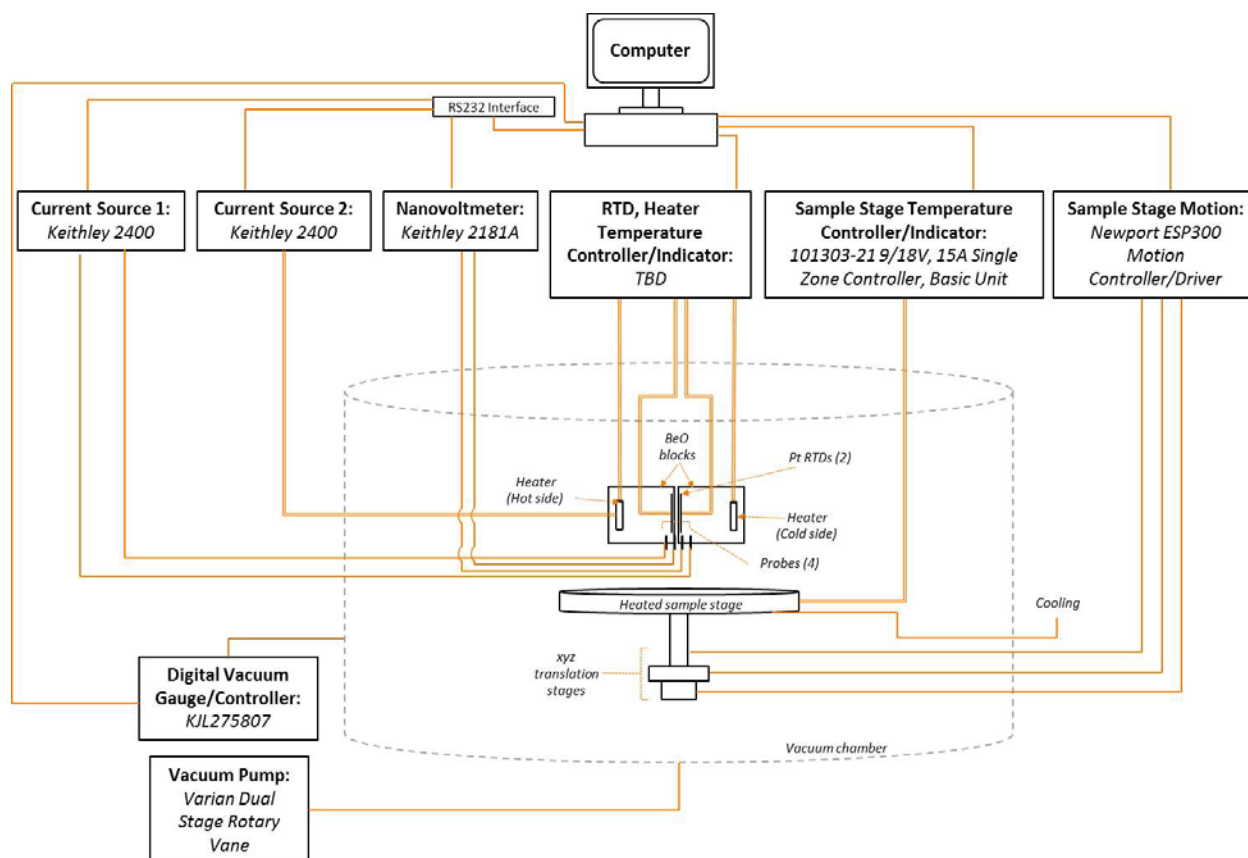
(a)



(b)



(c)



(d)

Figure 5.18. (a) Custom Power Factor Screening Instrument (PFSI) and components. (b) Close-up of sample stage and measurement head. (c) Detail of measurement head components. (d) PFSI wiring diagram

The system then waits the user specified time delay and measures the resistance of the sample. The resistance of the sample is measured by DC current reversing method. This sends a constant DC current thru the sample and the voltage developed is recorded. The current polarity is then reversed and the voltage recorded. These voltages are then averaged to remove any voltage contribution for the resistance of the voltage leads. The resistivity is then calculated from resistance with a user specified thickness value (t) and a correction factor is applied (CF).

$$\rho = \frac{V}{I} \times t \times CF \quad (2)$$

The correction factor that is applied to the resistivity values accounts for the thickness of the film being measured, probe spacing and misalignment, probe placement, and sample size and geometry. The correction factor is then determined using two steps. First, the film thickness correction factor is determined assuming an insulating substrate. Then, the remaining correction factors are determined using the method of images. Ideally, measured films are deposited on substrates that form insulating boundaries. That is either the resistivity of the film is much lower than the substrate ($\rho_{sub} \gg \rho_{film}$) or the film and substrate are of opposite carrier types (p -/ n -).

Since the films are very thin (~ 300 nm) when compared to the probe spacing (~ 1.5 mm), the correction factor due to film thickness is 1, as shown in Equation 3.

$$CF = CF_{thickness} \times CF_{probe\ misalignment} \times CF_{probe\ placement} \times CF_{sample\ size/geometry} \quad (3)$$

$$CF_{thickness} = \frac{\ln(2)}{\ln\left(\frac{\sinh(t/s)}{\sinh(t/2s)}\right)} \quad (4)$$

when $t/s \ll 1$, $CF_{thickness} = 1$

The remaining correction factors (probe geometry, probe placement, sample size and geometry) are grouped together as shown in Equation 5. They can be simultaneously determined using the method of images.

$$CF_{geo} = CF_{probe\ misalignment} \times CF_{probe\ placement} \times CF_{sample\ size/geometry} \quad (5)$$

For samples with a circular radius R , the method of images derived by Buehler and Pearson (shown in Equation 6) was used.

$$CF_{geo} = 2\pi \left[\ln \left(\frac{r_{35}r_{45}r_{26}r_{16}}{r_{25}r_{15}r_{36}r_{46}} \right) \right]^{-1} \quad (6)$$

$$r_{12} = \sqrt{r_1^2 + r_2^2 - 2r_1r_2\cos(\theta_1 - \theta_2)}$$

Pin/image coordinates:

$$I^+ image \left(r_1 = \frac{R^2}{r_2}, \theta_1 = \theta_2 \right)$$

$$I^+ source (r_2, \theta_2)$$

$$I^- sink (r_3, \theta_3)$$

$$I^- image \left(r_4 = \frac{R^2}{r_3}, \theta_4 = \theta_3 \right)$$

$$V^+ (r_5, \theta_5)$$

$$V^- (r_6, \theta_6)$$

For samples with rectangular geometry, the method of images derived by Perloff (shown in Equation 7) was used in conjunction with elliptical functions found in Abramowitz and Stegun.

$$CF_{geo} = 4\pi \left[\ln \left(\frac{\alpha_1\alpha_2}{\alpha_3\alpha_4} \right) + \ln \left(\frac{\beta_1\beta_2}{\beta_3\beta_4} \right) \right]^{-1} \quad (7)$$

$$\alpha_1 = (v_2 - v_4)^2 + (u_2 - u_4)^2$$

$$\alpha_2 = (v_2 + v_4)^2 + (u_2 - u_4)^2$$

$$\alpha_3 = (v_2 - v_1)^2 + (u_2 - u_1)^2$$

$$\alpha_4 = (v_2 + v_1)^2 + (u_2 - u_1)^2$$

$$\beta_1 = (v_3 - v_1)^2 + (u_3 - u_1)^2$$

$$\beta_2 = (v_3 + v_1)^2 + (u_3 - u_1)^2$$

$$\beta_3 = (v_3 - v_4)^2 + (u_3 - u_4)^2$$

$$\beta_4 = (v_3 + v_4)^2 + (u_3 - u_4)^2$$

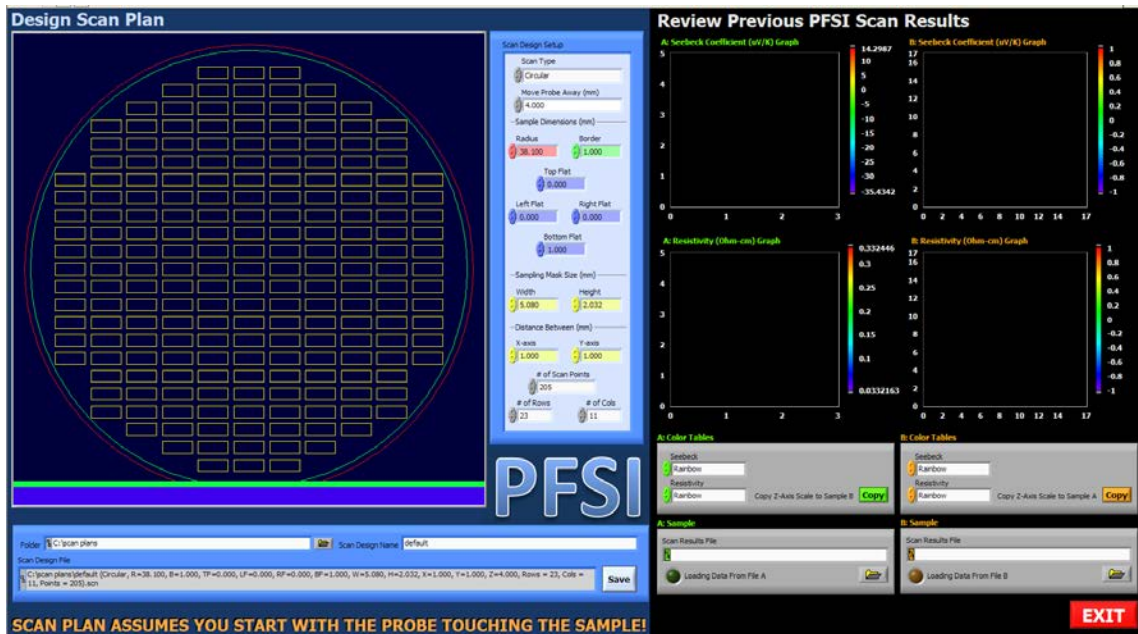
Pin/Images Coordinates:

$$I^+ source (u_1 + iv_1)$$

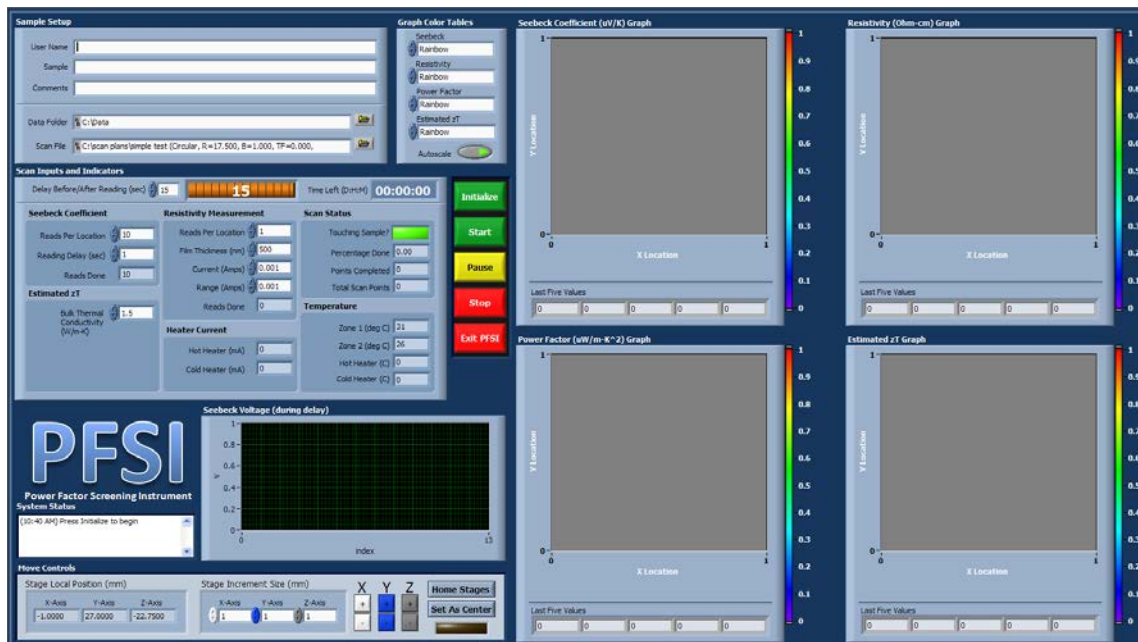
$$V^+ (u_2 + iv_2)$$

$$V^- (u_3 + iv_3)$$

$$I^- sink (u_4 + iv_4)$$



(a)



(b)

Figure 5.19. Custom LabVIEW-generated interface for (a) designing the wafer scan and (b) physical property data collection

Following film deposition (via PLD or rf magnetron sputtering), to prevent unwanted interference from neighboring compositions, the samples are sometimes patterned into discreet units using standard photolithography techniques. Patterned Ni and Au films, shown below in Figure 5.20, were used as standards to calibration the PFSI. The use of gold allows for

identification of the lower limits of the PFSI measurement capabilities. Sample scan data is shown in Figures 5.21 – 5.23. Since the move to building 23 at WPAFB, the PFSI has undergone a few modifications and new standard data will be collected along with data from newly generated combinatorial samples.

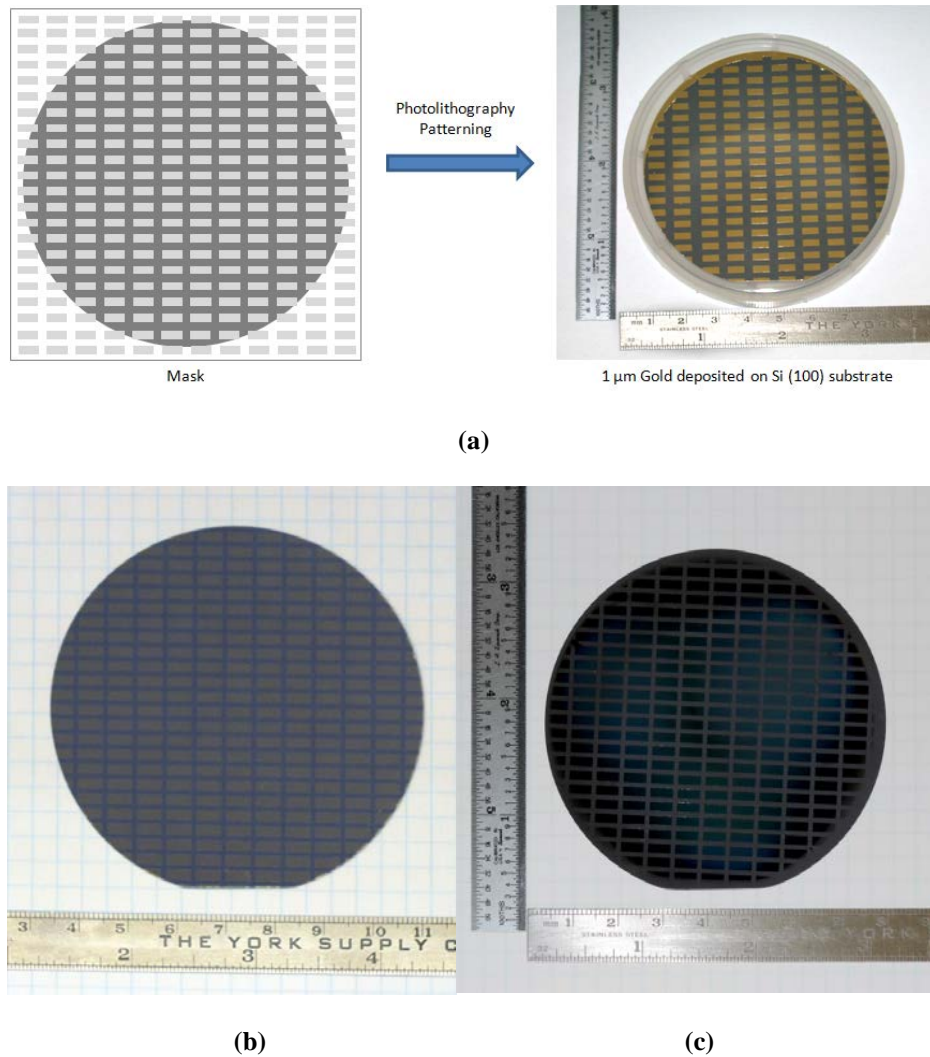
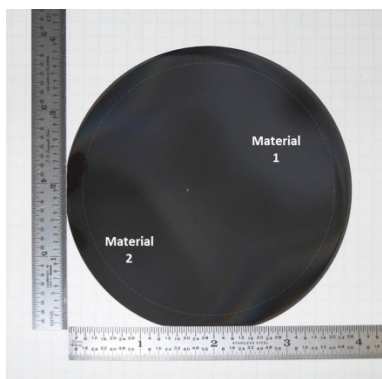
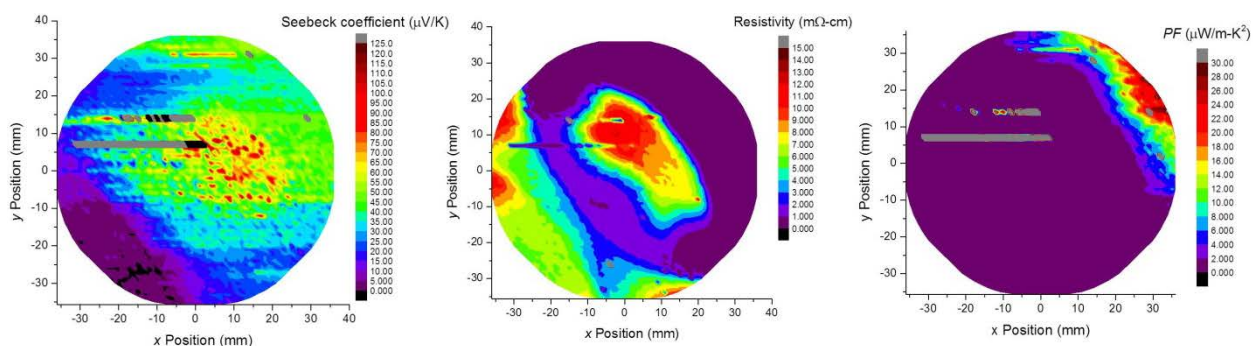


Figure 5.20. (a) Post-deposition processing via standard photolithography techniques (negative resist NR71-3000) followed by 1 μm Au sputtering and removal of Au with RR41 photoresist remover to generate discrete composition units in the calibration sample. The same process was followed for the (b) Ni standard sample and the (c) $\text{Ca}_3(\text{Fe,Ni,Co})_4\text{O}_9$ combinatorial ternary sample (with HCl etchant).

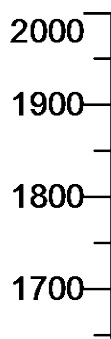


(a)



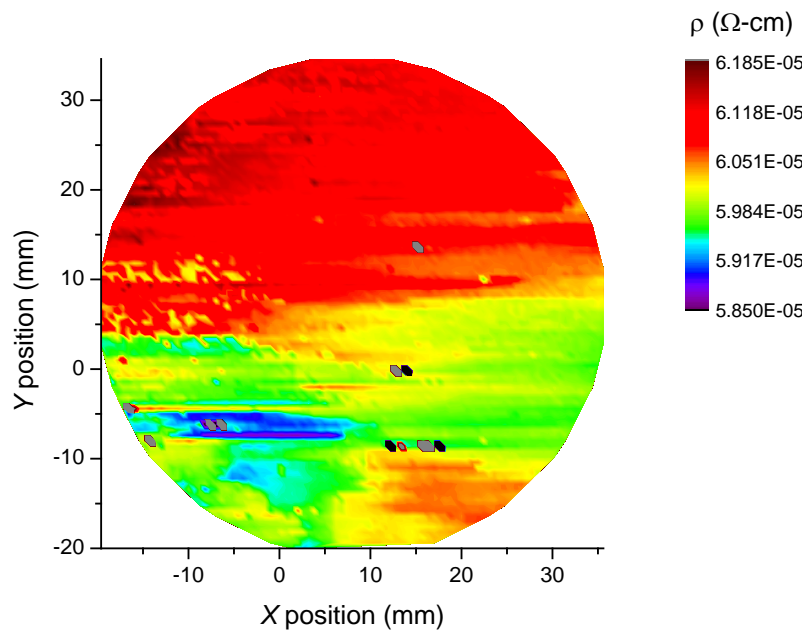
(b)

PSFI-006 (Fe-CCO/LMO Binary)

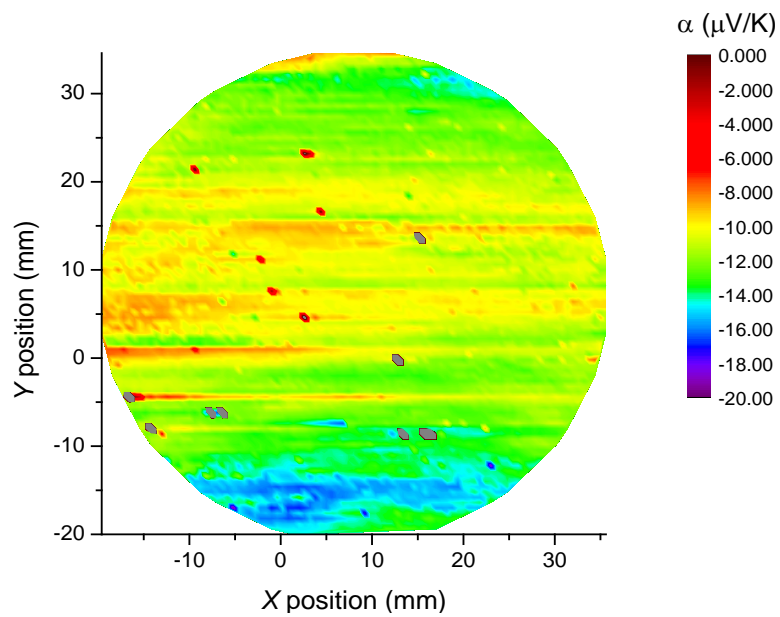


(c)

Figure 5.21. (a) $\text{Ca}_3\text{Co}_4\text{O}_9$ (Material 1) – CaMnO_3 (Material 3) Binary combinatorial sample. (b) Electrical property data collected using PFSI. (c) XRD data from diagonal line scan from Material 1 to Material 2

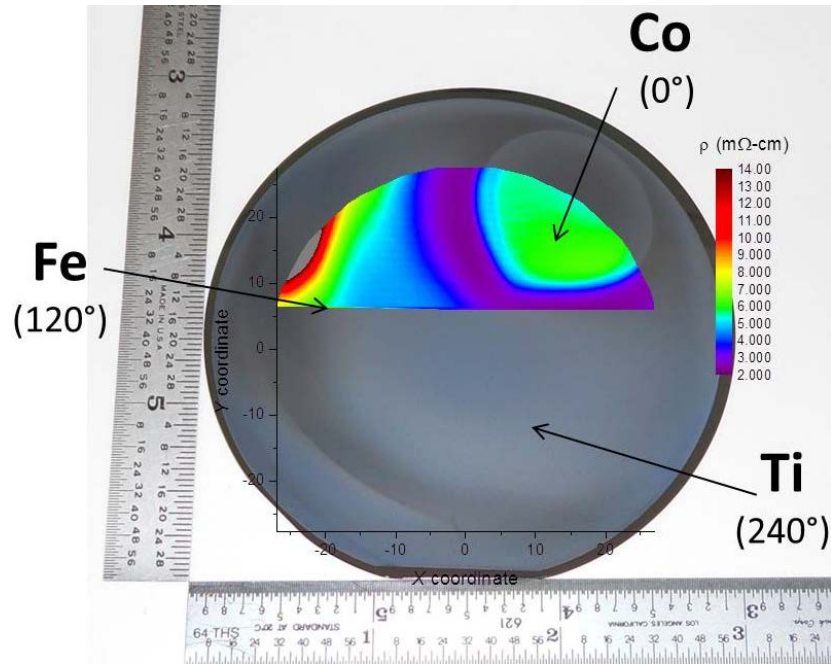


(a)



(b)

Figure 5.22. Electrical property data collected using PFSI of a 500 μm Nickel standard film (non-patterned)



- **Sample:** (Ti-Fe-Co) CCO on Si/SiO₂
- **Deposition Parameters:** 100 K Laser shots (10 Hz) at each position; 850 °C (700 °C); 300 mTorr/1 atm
- **Total Deposition Time:** 8 h 22 m
- **Room Temperature Resistance:** $R_{2p} \sim 500 \Omega$
- **PFSI Parameters:**
 - 20 s delay for S
 - $T_H \sim 36 \text{ }^\circ\text{C}$, $T_C \sim 30 \text{ }^\circ\text{C}$
 - 1 Seebeck and ρ measurement per location
 - 6793 data pts

Figure 5.23. Overlay of electrical resistivity short scan data from PFSI on optical image of a 3 in dia. Ca₃(Ti, Fe, Co)₄O₉ sample grown on Si/SiO₂. Experiment parameters are shown below the figure.

5.3.3 Thick and Thin Film TE Device Fabricated from Oxide-based Materials: Design and Synthesis of Textured Ca-Co-O Films

5.3.3.1 Introduction

Despite many new materials discoveries in the past decade, the development of large-scale TE waste-heat recovery technologies remains extremely challenging. There are major challenges in the areas of materials, processes and integration. We have discovered a method to exploit the superior *in-plane* properties of textured materials for TE device integration. At present, this invention to produce thin and thick film TE modules has been conceptualized and is now in the development phase. *Proof-of-concept* evaluations have been conducted, and with further design improvements and testing, this invention could potentially be available for commercial purposes within several years.

Many studies on low-dimensional, high-quality thin film structures, such as superlattices based on Bi₂Te₃ and PbTe, have shown that a significant increase in zT could be achieved by

reducing dimensionality. While some of these structures exhibit enhancements in their electrical properties, most of the gains were attributed to scattering of phonons at interfaces leading to large reductions in lattice thermal conductivity values. Such low-dimensional thin film structures are, however, ill-suited to the demands of high-temperature power generation applications that require long term thermal and mechanical stability as well as efficient coupling with existing heat sources. Compared to bulk materials, *cross-plane* thin film devices would require very high heat flux densities to generate significant temperature differentials, while *in-plane* thin film devices are extremely sensitive to thermal shunts from supporting substrates and insulation packaging.

5.3.3.2 Results and Discussion

As highlighted earlier in this chapter, in films grown on Si (100), despite the perfect texture of Ca-Co-O, there is an interface reaction layer, including an amorphous region ~ 15 nm thick, between the Si/Co₃O₄ layer and subsequent Ca-Co-O film (refer to Figure 5.12). In order to demonstrate the versatile nature of the Ca-Co-O film growth mechanism, we purposely deposited a 2 μ m thick amorphous layer of SiO₂ on a Si substrate by sputtering, then, using PLD, deposited a 200 nm Ca-Co-O film. The growth of a perfectly textured Ca-Co-O film on the amorphous SiO₂ was still observed. Furthermore, the SiO₂ layer remained amorphous even after the high-temperature film deposition and post-annealing. HR-TEM for this sample is shown in Figure 5.24. The versatility of a textured Ca-Co-O thin film grown on the amorphous buffer layer will be incorporated into the *in-plane* TE device design. Because amorphous SiO₂ is a perfect insulator, it will be used as the separator between the *p*-type and *n*-type oxide materials.

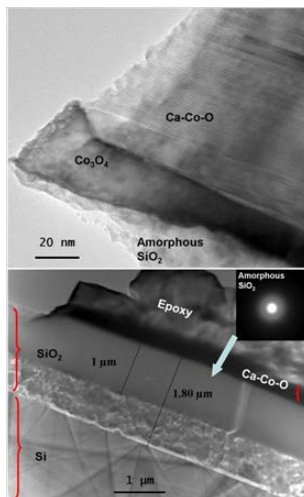


Figure 5.24. Textured Ca-Co-O film grown on 2 μ m thick layer of amorphous SiO₂

The objective here was to design an all-oxide TE device with textured *p*-type Ca-Co-O grown on amorphous SiO₂ buffered *n*-type CMO or Nb:STO substrates. The designed TE power generator was built to significantly and simultaneously increase the power output and decrease the size, weight of the entire device. A schematic of the fabricated TE device is shown below in Figure 5.25.

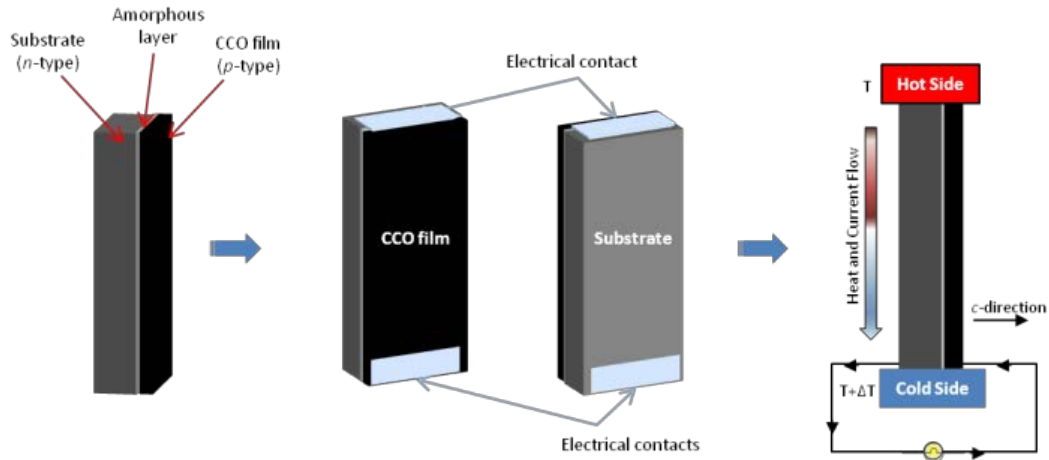


Figure 5.25. In-plane thin film TE device schematic (not to scale)

The conceived design of the *in-plane* textured film-based device has a configuration similar to that of a bulk TE module shown in Figure 5.26, albeit with significantly longer legs and dramatically reduced leg cross sections, and a miniscule amorphous insulating separator. The designed device shown above in Figure 5.25 has several key advantages over the conventional design, which are detailed later in this section.

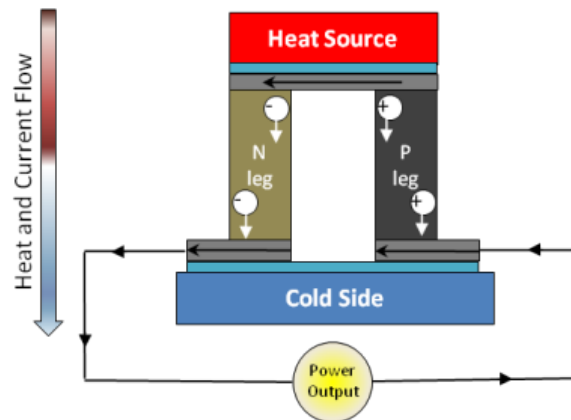


Figure 5.26. Ordinary design for TE power generation module

For TE superlattice films, such as V–VI-based superlattices, the zT values of V–VI-based superlattices can be measured in either the *in-plane* or *cross-plane* directions. Nevertheless, the largest enhancement is found in the *cross-plane* direction, with the major gain coming from the thermal conductivity reduction induced by interface phonon scattering. Cross-plane devices from superlattice films are mostly used for sensors [36, 37].

In regards to the oxide CCO-349, it was reported that the electrical conductivity in the *in-plane* direction of CCO is about 5 – 10 times larger than that of the *out-of-plane* electrical conductivity. Our *in-plane* device design takes advantage of this by promoting electronic transport along the strongly textured Ca-Co-O film plane to maximize the TE performance.

The growth of the textured Ca-Co-O films on amorphous SiO₂ inspired the TE device design with SiO₂ used as separator between the *p*- and *n*-legs. SiO₂ combines a very low thermal expansion coefficient, a low thermal conductivity and electrical insulation, all of which is desirable for application in TE devices. It has remarkable thermal insulating properties, with thermal conductivity values ranging from 0.03 W/m•K down to 0.004 W/m•K [41], which correspond to *R*-values of 14 to 105 for 3.5 in thickness. By comparison, typical wall insulation is 13 for 3.5 in thickness. Additionally, the melting point of SiO₂ is high, at 1473 K (~1750 °C).

For any conventional thin-film device, the most daunting task encountered in the incorporation of nano-structured thin films is the necessity for metallic interconnections between the different TE components. Therefore, the substrate must be insulated to prevent short circuits. In our case, the device comprised of textured Ca-Co-O grown directly onto the *n*-type substrate with SiO₂ as buffer, easily overcomes this issue. In contrast to the conventional design of having the *p*-type leg and *n*-type leg fabricated separately, to be later combined to form a device, our design allows for the *p*-type material to be grown directly onto *n*-type material, with a minuscule amorphous (such as SiO₂) insulating layer deposited in between the *p*-type and *n*-type materials. This provides for greater simplicity in the device fabrication.

For *in-plane* super-lattice-based device applications, such as V–VI-based superlattices, thermal bypass through the substrate must be minimized by removing the substrate, then transferring the superlattice film to another low thermal-conductivity substrate, or depositing the film directly on a low-thermal-conductivity substrate. We used a thin SiO₂ layer to address this issue, as it is electrically insulating and has an extremely low thermal conductivity. Thus, thermal shunts from supporting substrates and insulation packaging is easily managed for the device with insulating glass silica (SiO₂) as the separator.

Another significant challenge is the thermal management at both the hot and the cold sides, as the heat flux through each leg can be as large as 1000 W/cm². Heat spreading by using sparsely spaced elements or advanced thermal management methods will be necessary. Closely packed *p*-type and *n*-type oxides will prevent radiated heating from the sides of the *p*-type and *n*-type legs, and enhance the temperature gradient in our design.

Conventional TE devices have various specifications for various applications. The dimensions can vary from ~ 3 mm² by 4 mm thick to ~ 60 mm² by 5 mm thick; the maximum heat-pumping rate ranging from 1 to 125 W. Such devices may contain several to over 100 thermocouples. Typically in bulk-scale TE devices, the thermocouples are separated by a distance of ~ 4 mm to ~ 4 cm. In some innovative designs, the empty spaces between the thermoelectric legs would be subsequently backfilled with thermal insulation Aerogel.

In one of our early experiments for *proof-of-concept*, the 2 μm thick SiO₂ buffer served as a good insulating separator between the *p*-type Ca-Co-O thin film (300 nm) and *n*-type Si substrate, and preliminary results (*unpublished data*) from a single TE unicouple (4 mm x 8 mm), using the homemade measurement system depicted in Figure 5.27, show that the unicouple can generate up to ~ 180 mV and ~ 1 μW by heating one side to a temperature of 673 K and maintaining the opposite water-cooled side at ~320 K. These data are presented in Figure 5.28.

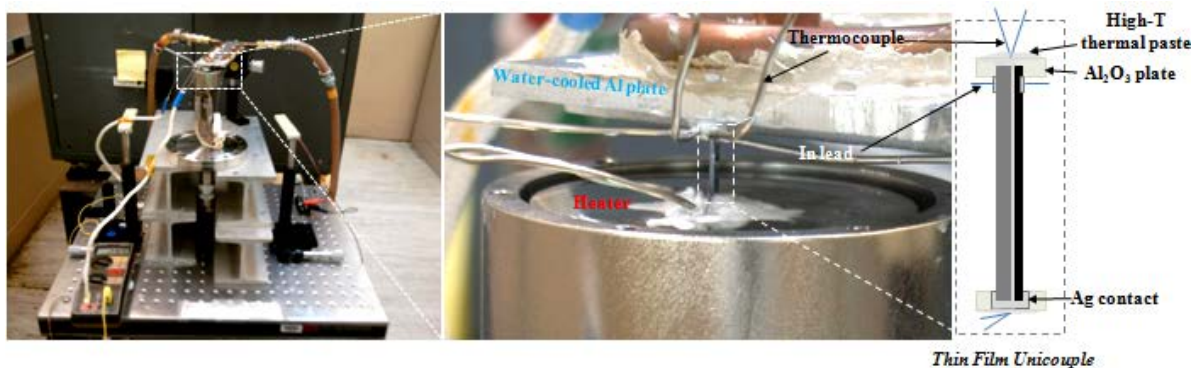


Figure 5.27. Custom-built water-cooled power generation measurement system. (Right panel) Close-up of thin film uncouple mounting schematic

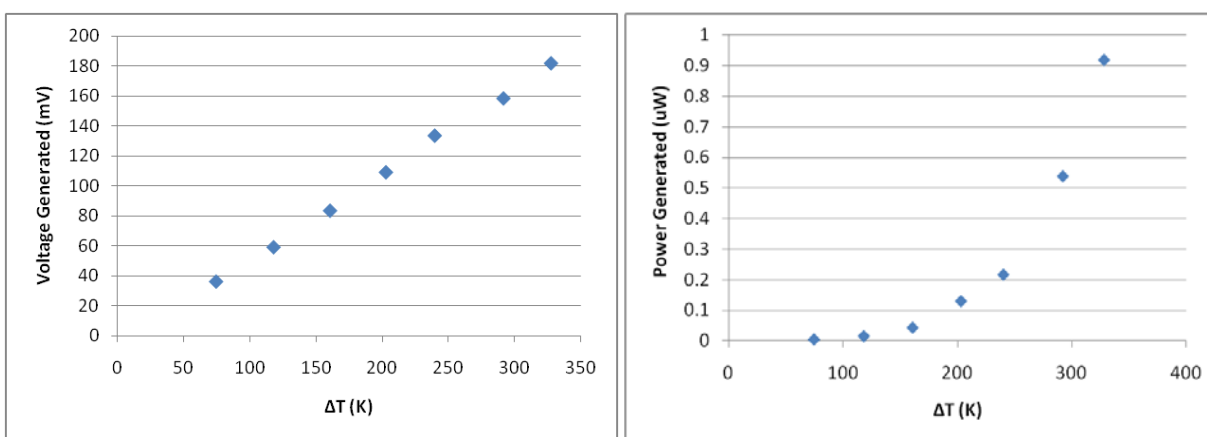


Figure 5.28. (Left panel) Voltage output and (Right panel) Power generated from a thin film uncouple as a function of the temperature gradient across the sample

We anticipate that a slightly thicker 4 μm silica glass separator would easily satisfy the requirements for electrical insulation and thermal management, although the ideal thickness of SiO_2 is subject to study as well. This concept alone will increase the power-per-area and dramatically decrease the size of the TE device.

The close-packing of the thermocouples will significantly reduce the length of the interconnecting materials, and thus reduce the weight of the entire device. The joins between the TE materials and the cold-side and hot-side interconnect materials are exposed to stress during fabrication, and the choice of interconnect materials is critical to achieving a mechanically stable thermocouple. TE materials with lower coefficients of thermal expansion tend to be more suitable for device integration, as most refractory metals often used as interconnect materials tend to have relatively low thermal expansion coefficients. Instead of using 4 cm interconnect materials, the 4 μm thick glass silica will allow for the minimum size of interconnect refractory materials, significantly reducing the weight of the entire device.

In short, our thin/thick film design has the following novel aspects that will significantly increase the power and decrease the size, weight of the entire device:

1. *In-plane* transport device with strongly textured *p*-type Ca-Co-O film for enhanced energy inter-conversion efficiency

2. Integrated design composed of strongly textured *p*-type materials grown directly onto *n*-type materials for simplicity of device fabrication
3. Micron-sized and closely-packed insulating separator for better thermal management and dramatic reduction of the overall-size and weight of the device.

5.3.3.3 *n*-type CaMnO_3 -based Materials

We acknowledge that there are other potential oxide-based TE candidates for high temperature applications, and we extended consideration to these systems as well, particularly with the goal being to identify a suitable *n*-type material for TE module considerations. While simultaneously pursuing enhancements to CCO-349, our plan was to continue optimizing other candidates through doping via the combinatorial approach. One such candidate was CaMnO_3 (CMO). CMO is promising *n*-type perovskite oxide for TE power generators. Similar to LCO, it also crystallizes with the well-known perovskite-type structure. We have made numerous references throughout this chapter to researchers' attempts to control the nano-structures of bulk and low-dimensional materials to introduce phonon-scattering nano-interfaces and, hence, reduce κ while suppressing a reduction in the PF for zT increases. Phase separation, such as spinodal decomposition and exsolution to form thermodynamic nano-structures or nano-composites, has also been shown effective in improving the TE performance of SOA non-oxide materials. On the other hand, *multiphase* nano-composite systems generally result in a concurrent reduction of both the thermal conductivity and electrical conductivity, and thus exhibit poor efficiency at operation temperature. However, $\text{Ca}_{0.9}\text{Yb}_{0.1}\text{MnO}_3$ ceramics with nanometer-sized grains have shown reductions in thermal conductivity with decreasing grain size due to enhanced grain boundary (GB) scattering, while maintaining the intrinsic CMO electrical conductivity behavior.

To begin exploring the feasibility of nano-grain approaches to synthesize bulk CMO, we started with the fabrication of a nearly 100% dense CMO polycrystalline sample with large grain size. The Seebeck coefficient of our *n*-type CMO bulk sample is nearly $-560 \mu\text{V/K}$ at room temperature (*unpublished data*), and the high temperature behavior is further illustrated in Figure 5.29. Our data is consistent with data reported from other CMO bulk studies. This sample was a first attempt at making the bulk pure phase CMO without any post-annealing under flowing oxygen, and without any optimization of doping and grain refinement. The properties of CMO are expected to be enhanced upon further treatment and composition/structure optimization. Preliminary TEM results are shown in Figure 5.30, and suggest that the grain boundaries in this as-sintered CMO sample are free of amorphous or secondary phases. Interestingly, it was also shown that the Ca:Mn ratio varies from one local region to another. In the Mn deficient region, our preliminary results show the distribution of nano-sized domains. Once optimized through solid-state processing methods, dense CMO targets will be prepared for combinatorial PLD experiments and solid-solution thin film libraries will be generated to determine the optimal dopant concentrations of Y, Ba and Yb.

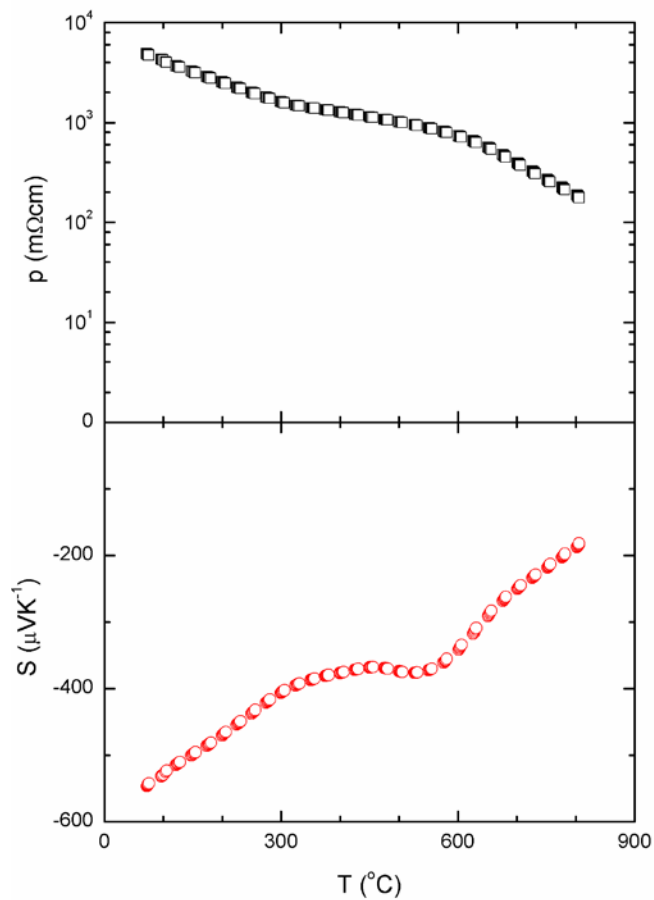


Figure 5.29. Temperature dependence of electrical resistivity ρ (*top*) and Seebeck coefficient S (*bottom*) for CMO bulk sample

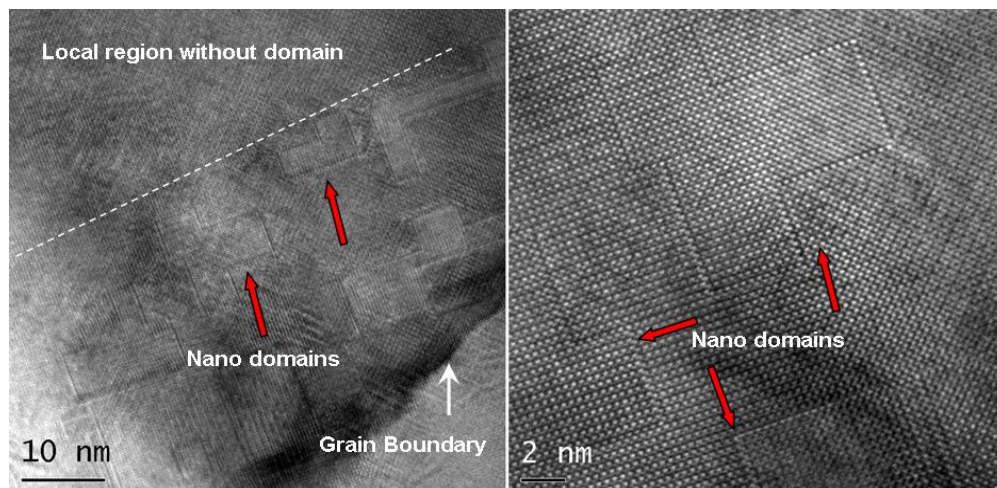


Figure 5.30. Morphology of clean GBs and nano-domains within the grains of an as-sintered CMO sample

5.3.3.4 In-plane Film Device: Solution-based Synthesis of Large Scale Textured Ca-Co-O on the *n*-type Oxide Substrate:

The featured film device, fabricated by growing textured Ca-Co-O on amorphous SiO₂, could prove to be a very significant challenge to scale up to meet the potential needs of terrestrial waste-heat recovery applications [39]. To address this challenge and improve the power of the entire device, it will be necessary to conduct large scale synthesis of textured Ca-Co-O on the amorphous-buffered *n*-type oxide substrate using sol-gel spin-coating and subsequent heat-treatments (experiments are currently being designed). The chemical solution sol-gel spin-coating, which has the advantage of low fabrication cost, easy stoichiometry control and high deposition rate, is one of the more promising fabrication methods of oxide films. Depending on the application requirements, the thickness of the sol-gel coatings can be adjusted in a wide range from less than 1 to several tens of microns. It has been reported that sol-gel-processed *c*-axis oriented Ca-Co-O-based thick-films up to 650 nm were successfully grown on sapphire (0001) substrates [40-42]. We will coat the *n*-type oxide with an amorphous SiO₂ layer 2 – 4 μm thick. Study of textured thick films on the amorphous-buffered *n*-type substrate will proceed by considering the following aspects:

1. Effect of the sintering temperature, (ranging from 650 – 800 °C), on the crystal structure, film morphology and TE properties. The nominal composition of the thick-film will be the same as that from the optimized PLD thin film, including pure Ca-Co-O, doped Ca-Co-O and Ca-Co-O with nano-inclusions
2. Synthesis of textured thick sol-gel film with thicknesses up to several tens of microns. Single spin-coating and multiple-step coating processes will be attempted to achieve a thick layer of up to 100 microns. (It is reported that, depending on the solvent content in the coating solution, coating thickness can be varied from 3 μm up to more than 25 μm in a single spin coating step. Thicker layers of up to 100 μm can be realized using the multi-step coating process.)
3. The sol-gel thick films will first be grown on commercial *n*-type single crystal substrates to optimize the synthesis conditions of Ca-Co-O. The textured thick-films, grown under optimized growth conditions will then be grown on the SiO₂-buffered *n*-type oxide substrate (CMO or Nb:STO) to produce the all-oxide TE device prototype.

Ultimately, evaluations of power generation and durability of the devices and modules fabricated under this effort will be carried out through the use of the custom-designed measurement system recently built for dynamic testing of commercial TE modules. Various leg dimensions and film thicknesses will be considered to determine optimum device dimensions. As it will be of high importance to maintain separation of the *p*- and *n*-legs, the outer edges of all devices will be polished prior to measurements to ensure electrical insulation.

We must also at this stage consider additional physical property measurements. Internal resistance measurements will be carried out using the standard 4-probe and van der Pauw testing methods. To minimize contact resistance, Ag and Au will be sputtered and annealed prior to measurements. As our design concept calls for the unicouples to be stood on edge, it may be necessary to determine the mechanical strength by conducting three-point bending tests at room temperature and at maximum operating temperature. Ultimately, the *n*-type substrate will provide the largest contribution to the device's mechanical strength. Linear thermal expansion coefficients will also be measured during operation.

5.4 Summary

We have been able to identify the unique dopant segregation behavior in $\text{Ca}_3\text{Co}_4\text{O}_9$ (CCO-349) and determine film growth initiators and solubility limits as a path to enhancing other oxide-based high-temperature TE materials. With 200+ bulk and film samples synthesized using various processes, we have made considerable progress in elucidating structure-property relationships in Ca-Co-O-based materials, and have substantially improved the TE properties of CCO-349 through doping effects.

We have designed and built a SOA Power Factor Screening Instrument (PFSI), with the capability to measure the Seebeck coefficient and electrical resistivity simultaneously up to $\sim 500^\circ\text{C}$ for thin film samples. Useful demonstrations of the effectiveness of the PFSI, have been carried out by first exploring the oxide-based $p\text{-Ca}_3\text{Co}_4\text{O}_9/n\text{-CaMnO}_3$ system. Although zT values for alloys and semiconductors are typically higher than those for oxide-based materials, oxides are more desirable for use in high-temperature power generation applications for their high thermal stability in air, low toxicity, affordability and raw material abundance. Perovskite ceramics are appealing functional materials that are utilized in numerous energy conversion processes due to their flexible structure and a variety of properties. The very attractive physical-chemical properties of perovskite-type phases can be modified in a controlled way by changing the composition and crystallographic structure in chemistry synthesis processes.

After discovering the self-assembling behavior of CCO-349 on an amorphous substrate, we exploited this behavior to optimize the energy inter-conversion properties of oxide-based materials by developing and successfully demonstrating an innovative all-oxide TE device for mid-to-high temperature power generation applications. It is intended that this invention generates TE devices, which are easy to fabricate and thus facilitate mass production, with a high potential for use in large-scale operations. We specifically target materials for mid- to high-temperature power generation applications that overcome the traditional barriers faced by low dimensional materials during scale-up productions, and possess the ability to enhance the efficiency of other systems by waste-heat scavenging.

With continued investment in this project, the payoffs remain high. Existing SOA TE material compositions present several issues such as low efficiency, poor stability at high temperatures in air, high reactivity, and are generally comprised of rare and/or costly materials. There is a great need for newer TE material compositions that have higher efficiency and are economical. Success has been realized in low-dimensional material studies, but very few transitional demonstrations with oxide-based TE thin films exist. Through the approaches presented in this report, our team continues to address the obstacles faced in the development of high efficiency TE materials.

5.5 References

- [1] Tritt, T. M.; Subramanian, M. A. *MRS Bull.* **2006**, *31*, 188 (and references therein).
- [2] Slack, G. A.; CRC Press, Boca Raton, FL, 1995.
- [3] Rowe, D. M., Ed.; *CRC Handbook of Thermoelectrics: Macro to Nano*; CRC, Boca Raton, FL, 2005.
- [4] Chen, G.; Dresselhaus, M. S.; Dresselhaus, G.; Fleurial, J. P.; Caillat, T. *Int. Mater. Rev.* **2003**, *48*, 45.
- [5] Dresselhaus, M. S.; Chen, G.; Tang, M. Y.; Yang, R. G.; Lee, H.; Wang, D. Z.; Ren, Z. F.; Fleurial, J. P.; Gogna, P. *Adv. Mater.* **2007**, *19*, 1043.

- [6] Bhandari, C. M., Ed., *CRC Handbook of Thermoelectrics*; CRC, Boca Raton, FL, 2005.
- [7] Masset, A. C.; Michel, C.; Maignan, A.; Hervieu, M.; Toulemonde, O.; Studer, F.; Raveau, B.; Hejtmanek, J. *Phys. Rev. B* **2000**, 62, 166.
- [8] Shikano, M.; Funahashi, R. *Appl. Phys. Lett.* **2003**, 82, 1851.
- [9] Ohta, S.; Nomura, T.; Ohta, H.; Hirano, M.; Hosono, H.; Koumoto, K. *Appl. Phys. Lett.* **2005**, 87, 092108.
- [10] Varanasi, C. V.; Burke, J.; Brunke, L.; Wang, H.; Sumption, M.; Barnes, P. N. *J. Appl. Phys.* **2007**, 102, 063909.
- [11] Varanasi, C. V.; Burke, J.; Wang, H.; Lee, J. H.; Barnes, P. N. *Appl. Phys. Lett.* **2008**, 93, 092501.
- [12] Rao, A. M.; Ji, X. H.; Tritt, T. M. *MRS Bull.* **2006**, 31, 218.
- [13] Broido, D. A.; Mingo, N. *Phys. Rev. B* **2006**, 74, 195325.
- [14] A. R. Abramson, W. C. K., S. T. Huxtable, H. Yan, Y. Wu, A. Majumdar, C.-L. Tien and P. Yang *J. Microelectromech. Sys.* **2004**, 13, 505.
- [15] Huber, T. E.; Celestine, K.; Nikolaeva, A.; Gitsu, A.; Konopko, D.; Huang, J.; Graf, M. J. In *Thermoelectrics, 2003 Twenty-Second Int. Conf. Thermoelect.* p 359.
- [16] Lin, Y. M.; Cronin, S. B.; Rabin, O.; Ying, J. Y.; Dresselhaus, M. S. In *Thermoelectric Materials 2001-Research and Applications*; Nolas, G. S., Johnson, D. C., Mandrus, D. G., Eds. 2001; Vol. 691, p 377.
- [17] Zide, J. M.; Klenov, D. O.; Stemmer, S.; Gossard, A. C.; Zeng, G.; Bowers, J. E.; Vashaee, D.; Shakouri, A. *Appl. Phys. Lett.* **2005**, 87, 112102.
- [18] Li, S. W.; Funahashi, R.; Matsubara, I.; Ueno, K.; Sodeoka, S.; Yamada, H. *Chem. Mater.* **2000**, 12, 2424.
- [19] Itahara, H.; Tani, T. *R&D Review of Toyota CRDL* 39.
- [20] Asahi, R.; Sugiyama, J.; Tani, T. *Phys. Rev. B* **2002**, 66, 155103.
- [21] Li, S., Funahashi, R., Matsubara, I., Ueno, K., Sodeoka, S., Yamada, H. *J. Mater. Sci. Lett.* **2000**, 19, 1339.
- [22] Mikami, M.; Funahashi, R.; Yoshimura, M.; Mori, Y.; Sasaki, T. *J. Appl. Phys.* **2003**, 94, 6579.
- [23] Miyazaki, Y.; Huang, X. Y.; Kajiwar, T.; Yamane, H.; Kajitani, T. *J. Ceram. Soc. Jpn.* **2009**, 117, 42.
- [24] Thomas, E. L.; Song, X.; Yan, Y.; Martin, J.; Wong-Ng, W.; Ratcliff, M.; Barnes, P. N. *Mat. Res. Soc. Symp. Proc.* **2010**, 1267, 1267.
- [25] van der Pauw, L. J. *Phillips Res. Rep.* **1958**, 13, 1.
- [26] Otani, M.; Itaka, K.; Wong-Ng, W.; Schenck, P. K.; Koinuma, H. *Appl. Surf. Sci.* **2007**, 254, 765.
- [27] Otani, M.; Lowhorn, N. D.; Schenck, P. K.; Wong-Ng, W.; Green, M. L.; Itaka, K.; Koinuma, H. *Appl. Phys. Lett.* **2007**, 91.
- [28] Otani, M.; Thomas, E. L.; Wong-Ng, W.; Schenck, P. K.; Chang, K. S.; Lowhorn, N. D.; Green, M. L.; Ohguchi, H. *Jpn. J. Appl. Phys.* **2009**, 48.
- [29] Moubah, R.; Colis, S.; Schmerber, G.; Petersen, J.; Dinia, A. *Appl. Phys. Lett.* **2009**, 94.
- [30] Wang, Y.; Sui, Y.; Ren, P.; Wang, L.; Wang, X. J.; Su, W. H.; Fan, H. J. *Chem. Mater.* **2010**, 22, 1155.
- [31] Wang, Y.; Sui, Y.; Cheng, J. G.; Wang, X. J.; Su, W. H. *J. Alloy. Compd.* **2009**, 477, 817.
- [32] Brabers, V. A. M.; Broemme, A. D. D. *J. Magn. Magn. Mater.* **1992**, 104, 405.

- [33] Wang, S. F.; Chen, M. J.; He, L. P.; Zheng, J.; Yu, W.; Fu, G. S. *J. Phys. D Appl. Phys.* **2009**, *42*.
- [34] Kenfaui, D.; Bonnefont, G.; Chateigner, D.; Fantozzi, G.; Gomina, M.; Noudem, J. G. *Mater. Res. Bull.* **2010**, *45*, 1240.
- [35] X.-D. Xiang and I. Takeuchi, *Combinatorial Materials Synthesis*, New York: Marcel Dekker, Inc., 2003.
- [36] Nurnus, J.; Bottner, H.; Kunzel, C.; Vetter, U.; Lambrecht, A.; Schumann, J.; Volklein, F.; Ieee, I. 2002 *Int. Conf. Thermoelect. XXI*, p 523.
- [37] Völklein, F.; Blumers, M.; Schmitt, L. *Int. Conf. Thermoelect.* **1999**, 285.
- [38] <http://www.reade.com/products/35-oxides-metallic-powders/684-sio2-silicon-dioxide-crystalline-silica-microcrystalline-silica-amorphous-silica-amorphous-fused-silica-silica-aerogels-food-grade-silica-hydrophobic-fumed-silica-treated-fumed-silica-precipitated-amorphous-silica-hydrated-precipitated-silica-filter-sand->.
- [39] Fleurial, J. P. *JOM* **2009**, *61*, 79.
- [40] Liu, C. J.; Nayak, P. K.; Lin, Z. R.; Jeng, K. Y. *Thin Solid Films* **2008**, *516*, 8564.
- [41] Zhu, X. B.; Chou, S. L.; Wang, L.; Li, Q.; Shi, D. Q.; Wang, J. Z.; Chen, Z. X.; Sun, Y. P.; Liu, H. K.; Dou, S. X. *Electrochem. Solid St.* **2009**, *12*, A176.
- [42] Zhu, X. B.; Shi, D. Q.; Dou, S. X.; Sun, Y. P.; Li, Q.; Wang, L.; Li, W. X.; Yeoh, W. K.; Zheng, R. K.; Chen, Z. X.; Kong, C. X. *Acta Mater.* **2010**, *58*, 4281.

6. Magnetically Hard/Soft Nanocomposite Magnets

6.1 Introduction

Permanent magnet materials with room-temperature magnetic performance superior to the best $\text{Nd}_2\text{Fe}_{14}\text{B}$ -based magnets and with high-temperature magnetic performance superior to the best $\text{Sm}_2\text{Co}_{17}$ -based magnets are needed. Since the magnetic properties of both magnets have been pushed very close to their limitation, the maximum energy product $[(\text{BH})_{\text{max}}]$ of 59 MGOe (theoretical value of 64 MGOe) and 31 MGOe (theoretical value of 39 MGOe) for $\text{Nd}_2\text{Fe}_{14}\text{B}$ and $\text{Sm}_2\text{Co}_{17}$ -based magnets, respectively, new classes of materials have to be studied and developed to meet the higher performance requirement.

Nanoscale hard magnetic materials, especially exchange-coupled nanocomposite magnets, have demonstrated new opportunities for development of future generations of permanent magnets [1]. Exchange-coupled nanocomposite magnets consisting of a hard magnetic phase that provides high coercivity and a soft magnetic phase that provides high magnetization have the potential for achieving significant enhancements in energy product. In order to take advantage of the outstanding specific magnetic characteristics of each component and to obtain high energy product nanocomposite magnets, the hard and soft phases should be coupled through intergranular magnetic exchange interactions [2-4]. In order to obtain high-energy-density magnetic materials, the bulk magnetically hard/soft nanocomposite magnets must be the following status: a) nanoscale soft phase; b) right crystal structure; c) anisotropic bulk; d) full density. To date, most hard/soft composite systems have been based on hard phase components such as $\text{Nd}(\text{Pr})\text{-Fe-B}$, Sm-Co and soft phase components such as Fe and Fe-Co . Bulk composite magnets have been prepared using compaction techniques such as hot pressing/deformation, dynamic shock compaction, spark plasma sintering, and warm compaction [5-10]. In this study, we focused on investigation of Sm-Co/Fe nanocomposite magnets. Bulk Sm-Co/Fe nanocomposite magnets were fabricated by high energy ball milling and subsequent hot pressing techniques. Anisotropic Sm-Co/Fe composite nanoparticles are prepared by surfactant-assisted high energy ball milling.

6.2 Experimental

In order to obtain SmCo_5 hard magnetic phase and Fe soft magnetic phase composite in nanoscale, the DM-HP process was utilized. The DM procedure is used to prepare composite powder consisted of SmCo_5 amorphous powder and Fe nanoscale crystalline particles. The HP procedure is used to compact the milled composite powder to a composite bulk which consists of crystallized Sm-Co hard phase and Fe soft phase. DM means dry high energy ball milling which is to mill SmCo_5 and Fe powders to prepare the mixed powders. HP means hot pressing which is to compact the milled mixture to fabricate Sm-Co/Fe bulks. The process is shown in Figure 6.1.

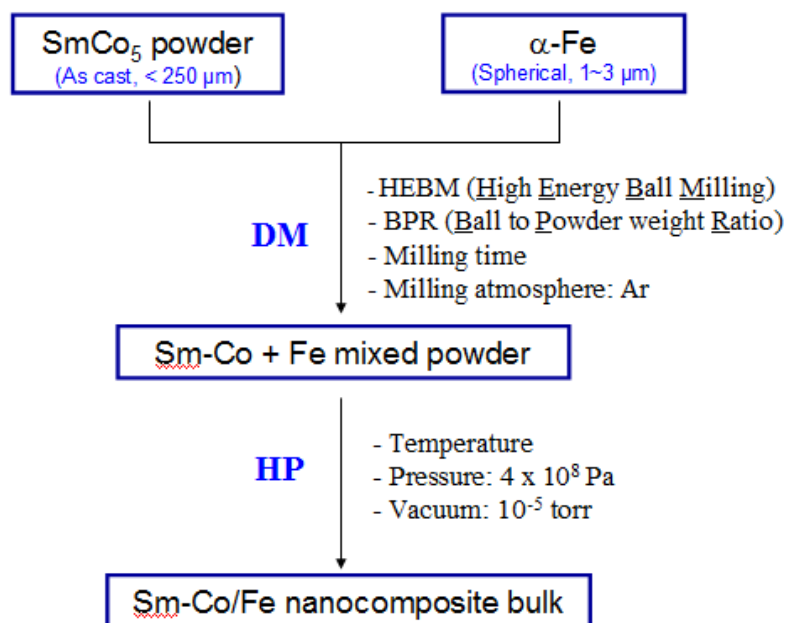


Figure 6.1. DM-HP process for preparation of bulk Sm-Co/Fe nanocomposite magnets

The SmCo₅ alloy was prepared by arc-melting. The ingots were crushed and ground down to less than 250 μm for starting powders. The soft phase Fe was a commercial spherical α-Fe powder (Alfa Aersa) with particle size of 1~3 μm. The SmCo₅ powders were mixed with a certain amount of α-Fe powder, and then the mixtures of 8 g were milled in a hardened stainless steel ball vial using a SPEX 8000 mill. The hardened steel milling balls had diameters of 4.8 – 12.7 mm. The milling parameters such as powder to ball weight ratio (BPR) and milling time were varied, which will be described in the following sections. The milled mixture powders of 5 g were loaded into a WC die with diameter of 0.315'' in glove box. Then the powders were heated to the pressing temperature in an RF inductive furnace under vacuum of 10⁻⁵ torr and meanwhile compacted under a pressure of 400 MPa. The finished bulk samples were in the form of rods with diameter of 8 mm and length of 12 mm.

6.3 Results and Discussion

6.3.1 Isotropic Sm-Co/Fe Nanocomposite Bulks

6.3.1.1 Microstructures and Magnetic Properties

The crystal structure, phase fractions, and microstructure of bulk samples were characterized by x-ray diffraction (XRD) with CuK_α radiation, scanning electron microscopy (SEM), and energy dispersive spectroscopy (EDS). The magnetic properties at room temperature were measured by a closed-circuit hysteresisgraph (model HG-700, KJS Associates Inc.).

Figure 6.2 shows the XRD patterns of the starting powder mixture of SmCo₅ + 10 wt % Fe before milling, after milling for 4 hours, and the bulk sample pressed at 600 °C with the 4 h milled powder. For the starting powder, XRD study shows that a single 1:5 type structure is developed in the as-cast SmCo₅ alloy. After milling the SmCo₅ powder and Fe powder mixture

for 4 hours, the original crystalline SmCo_5 phase became amorphous, but the Fe phase maintained its crystalline structure. Thus, the final milled composite mixture consisted of amorphous Sm-Co and crystalline Fe powder. After compacting at 600°C , the amorphous Sm-Co phase crystallized into the nanocrystalline CaCu_5 type SmCo_5 phase (1:5H) and TbCu_7 type SmCo_7 phase (1:7H). The appearance of the 1:7 phase should be related to compositional changes which may be a result of both milling and pressing procedures. Part of the Fe could be mechanically alloyed with the Sm-Co during high energy ball milling, in addition thermal diffusion between Fe and Sm-Co could take place during hot compaction. The mechanical alloying and thermal diffusion result in compositional changes in Sm-Co phase. The bulk magnets had densities around $8.3 \sim 8.5 \text{ g/cm}^3$, corresponding to more than 97% of the theoretical density.

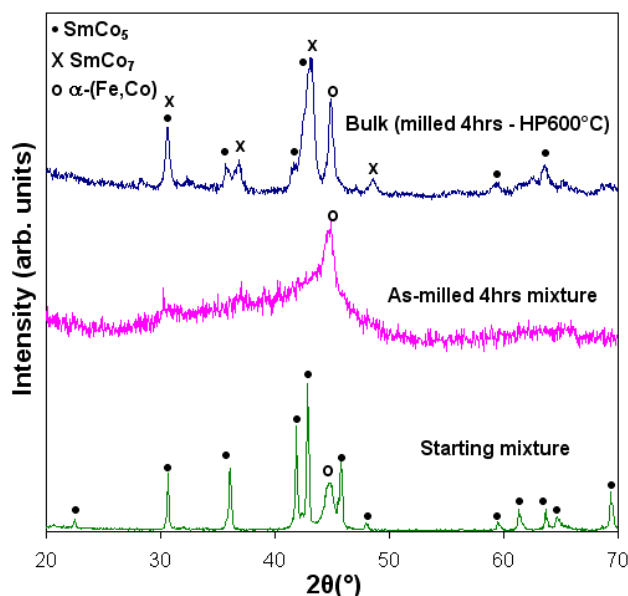


Figure 6.2. XRD patterns for $\text{SmCo}_5 + 10 \text{ wt } \%$ Fe starting mixture, after 4 hours of milling, and the bulk sample after subsequent compaction at 600°C

Figure 6.3 shows the SEM back-scattered electron (SEM/BSE) images of the polished bulk sample with different magnifications. The images show that the Fe particles (black dots) are distributed uniformly in the Sm-Co matrix (Figures 6.3 (a) and 6.3 (b)). Most of the starting spherical Fe particles of $1\sim 3 \mu\text{m}$ were milled down to particles of a few hundred nanometers with irregular shapes after milling 8 hours. However, several larger Fe particles with a few micrometers in diameter were distributed randomly within the Sm-Co matrix, shown in Figure 6.3 (c). They have been deformed but not broken into smaller pieces. Figure 6.3 (d) shows that the Sm-Co matrix forms a cellular structure. The cell size is around 400 nm . SEM/EDS investigation on bulk Sm-Co/Fe sample is shown in Figure 6.4. Fe exists in the Sm-Co matrix, and Co is found within the unbroken larger Fe particles. It is also observed that there is more Co at the edge of the Fe particle (the area marked as C) compared to the center (the area marked as B). Thus, the soft phase within the matrix is not pure Fe, but alloyed with Co. When Fe enters the Sm-Co phase, the ratio of 3d-elements to Sm (3d/Sm) increases, which leads to the formation of the Sm-(Co,Fe) 1:7 phase. The results of EDS analysis coincide with the results of XRD analysis.

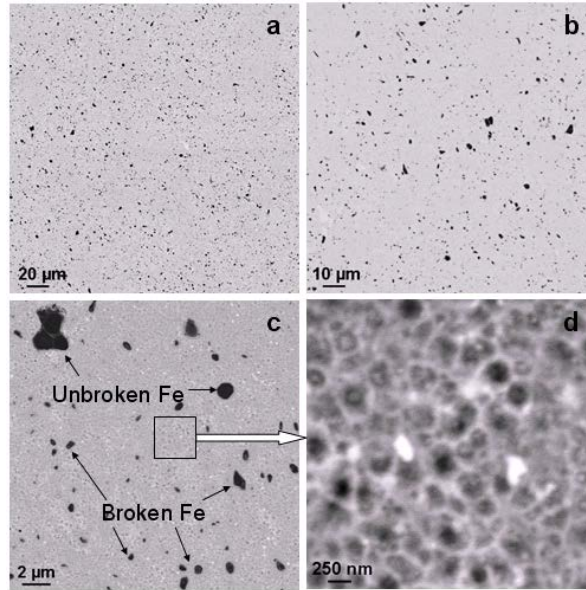


Figure 6.3. SEM/BSE images of bulk Sm-Co/Fe compacted at 600 °C using 8 h milled powder with a starting composition of $\text{SmCo}_5 + 10 \text{ wt } \% \text{ Fe}$

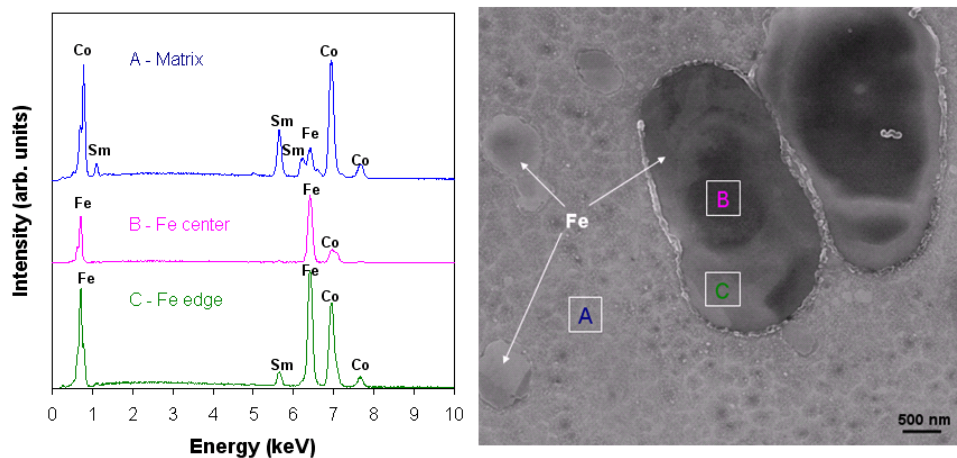


Figure 6.4. SEM/BSE image and corresponding EDS patterns for the bulk Sm-Co/Fe sample compacted at 600 °C using 8 hour milled powder

Figure 6.5 shows the demagnetization curves for the bulk samples. SmCo_5 and Sm-Co/Fe samples were prepared by hot pressing SmCo_5 DM12h powder and $\text{SmCo}_5 + 10 \text{ wt } \% \text{ Fe}$ DM12h powder, respectively. Adding 10 wt % Fe into SmCo_5 , the magnetization $4\pi M$ at 10 kOe, remanence B_r and maximum energy product $(BH)_{\text{max}}$ are 8.9 KG, 7.79 kG, and 12.46 MGOe, increased 50%, 36%, and 58% in comparison to bulk SmCo_5 single phase nanocrystalline magnet, respectively. However, the coercivity H_{ci} is 11.15 kOe, decreased more than 45% compared to SmCo_5 magnet. The smooth curve (no kink or shoulder) and enhanced magnetization of the composite magnet indicates the existence of the exchange coupling between the hard and soft phases, which demonstrates the Sm-Co/Fe composite has a good exchange coupling behavior.

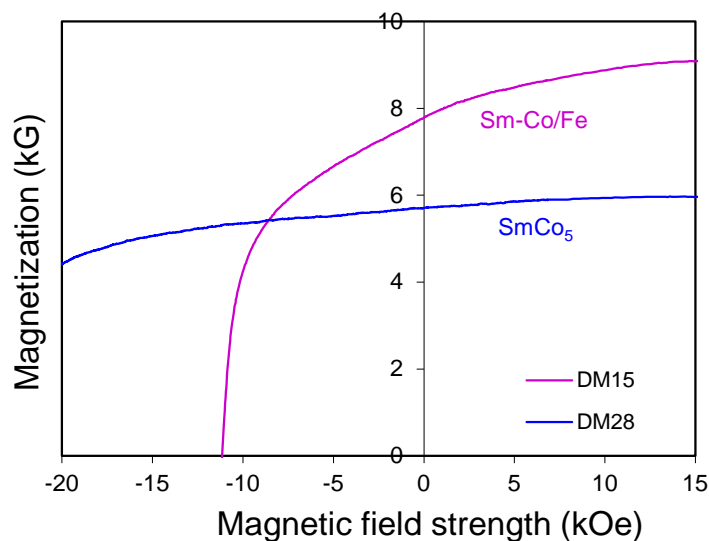


Figure 6.5. Demagnetization curves of bulk SmCo_5 and Sm-Co/Fe samples compacted at 600°C using 12 h milled powder for starting composition of SmCo_5 and $\text{SmCo}_5 + 10 \text{ wt } \% \text{ Fe}$

6.3.1.2 Optimization of Processing Parameters

For DM procedure, the milling parameters such as milling time and ball to powder weight ratio (BPR) will affect the milled powder characters (SmCo_5 amorphous status, Fe particle size, and milling diffusion degree between Sm-Co and Fe, etc.), and further affect the magnetic properties of the composite bulks. For HP procedure, the suitable pressing temperature and pressure are important to obtain full dense and higher magnetic property composite bulks. In this study, we focused on investigating milling time, BPR, and HP temperature, and meanwhile the milling and pressing parameters were optimized.

6.3.1.3 Milling Time

To obtain effective exchange coupling of magnetically hard and soft phases, the size of the soft magnetic grains should be of the order of 10 nm [3]. Milling time is one of the important milling parameters to reduce the Fe particle size. In this series of experiment, the starting composition was $\text{SmCo}_5 + 10 \text{ wt } \% \text{ Fe}$; the BPR was fixed at 5, and the milling time verified from 2 hours to 20 hours. The milled powders were hot pressed at the temperatures of 600°C under a pressure of 400 MPa.

The bulk Sm-Co/Fe composite samples were tested by KJS hysteresisgraph, and the magnetic properties are shown in Table 6.1. Figure 6.6 shows demagnetization curves of bulk Sm-Co/Fe magnets pressed at 600°C with the milling time from 2 hours to 20 hours. The demagnetization curve shape showed obvious changes as the milling time continued. When the milling time is less than 8 hours, each curve shows the shape of a downward curved shoulder, which indicated that big soft phase particles existed in the composites due to the weak exchange coupling. The best squareness of the demagnetization curve corresponds to the milling time of 12 hours, which presented a single phase magnetic behavior owing to strong exchange coupling. The magnetic properties exhibited a strong dependence on the milling time, shown as in Figure 6.7. As the milling time increasing, the $4\pi M$ at 10 kOe and the B_r increase, 9.6 kG and 8.32 kG

corresponding to milling time of 20 hours, respectively. The H_{ci} arrives biggest of 16.18 kOe corresponding to the milling time of 4 hours and then starts to decrease. The maximum energy product $(BH)_{max}$ obtains the highest value of 13.01 MGOe corresponding to the milling time of 16 hours.

Table 6-1. Magnetic properties of Sm-Co/Fe bulk samples with different milling time

ID	DM time (h)	4pM at 10 kOe (kG)	Br (kG)	Hci (kOe)	Hk (kOe)	(BH)max (MGOe)
DM8	2	7.7	5.59	14.21	0.89	4.86
DM9	4	8.1	6.28	16.18	1.24	6.62
DM11	8	8.6	7.25	14.5	2.17	9.89
DM15	12	8.9	7.79	11.15	3.54	12.46
DM19	16	9.3	8.26	8.45	2.67	13.01
DM20	20	9.6	8.32	6.2	1.69	11.65

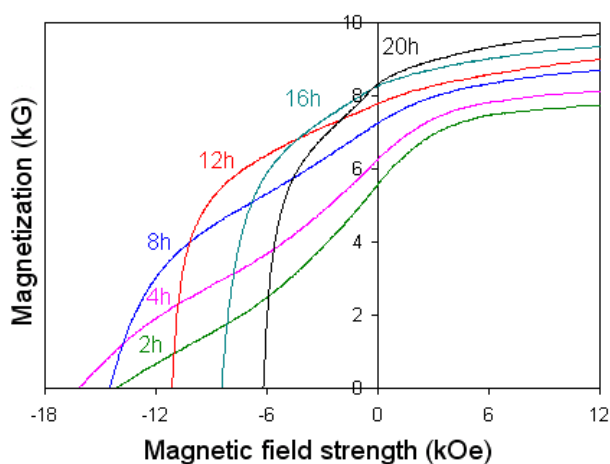


Figure 6.6. Demagnetization curves of bulk Sm-Co/Fe magnets as a function of milling time

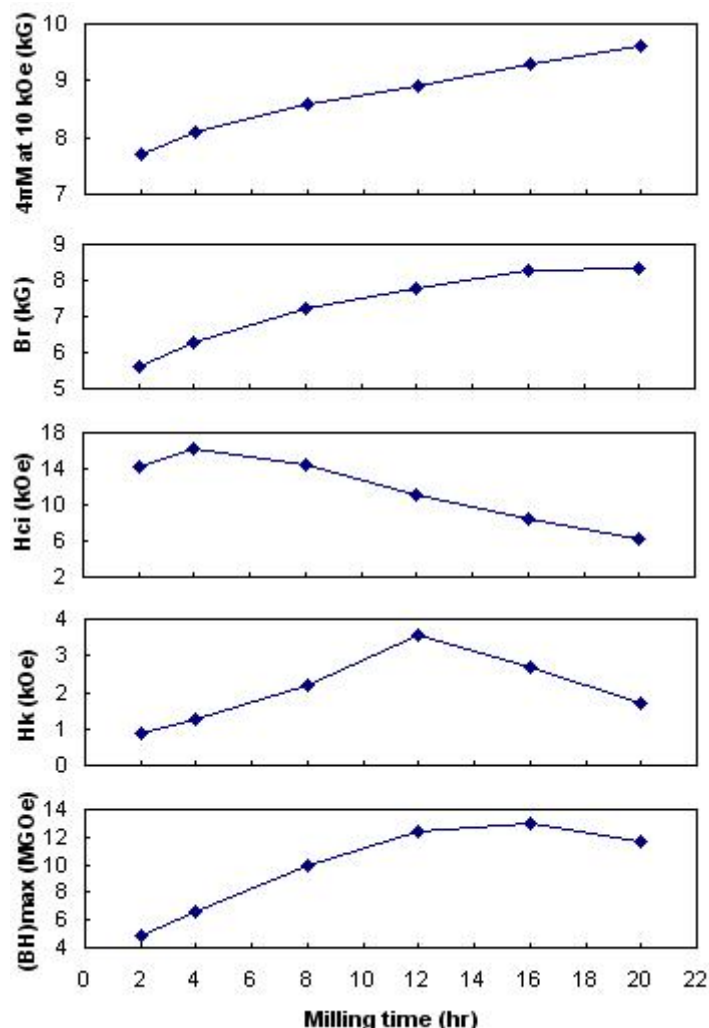


Figure 6.7. Magnetic properties of bulk Sm-Co/Fe magnets vs. milling time

X-ray diffraction (XRD) analyses further revealed the dependence of magnetic properties on the milling time. Figure 6.8 shows the XRD patterns of bulk Sm-Co/Fe magnets with different milling time. The bulk magnet made from 4 hour milled powder is consisted of SmCo_5 phase, SmCo_7 phase, and Fe phase. As milling time increasing, the content of 1:5 phase is decreasing, and the content of 1:7 phase is increasing, and meanwhile Fe (110) peak turns to lower and lower. In comparison of SmCo_5 phase and SmCo_7 phase, SmCo_5 has higher magnetic anisotropy field ($H_A \approx 210\text{-}290$ kOe) and lower saturation magnetization ($4\pi M_s \approx 9.65$ kG) [11], and SmCo_7 has lower magnetic anisotropy field ($H_A \approx 105$ kOe) and higher saturation magnetization ($4\pi M_s \approx 11.67$ kG) [12]. Thus, as milling time increased, less phase fraction of SmCo_5 and more phase fraction of SmCo_7 in the matrix led to the decrease of the coercivity and the increase of the magnetization. The content ratio of SmCo_5 phase and SmCo_7 phase in the bulk magnets is the determinant of magnetic properties changes.

As milling time longer, more Fe alloyed into Sm-Co phase, soft phase left less and more SmCo_7 phase formed in the bulk. On the other hand, Fe particles will break to smaller pieces as milling time increases, which is expected. However, Fe particle size decreasing led to the specific surface area of soft phase increasing, which resulted in more Fe diffusing into the Sm-

Co matrix during hot pressing. It is noticed that Sm_2O_3 appeared in the bulk made from 20 hours milled powder according to XRD results, which further resulted in 3d/Sm ratio increasing and H_{ci} decreasing.

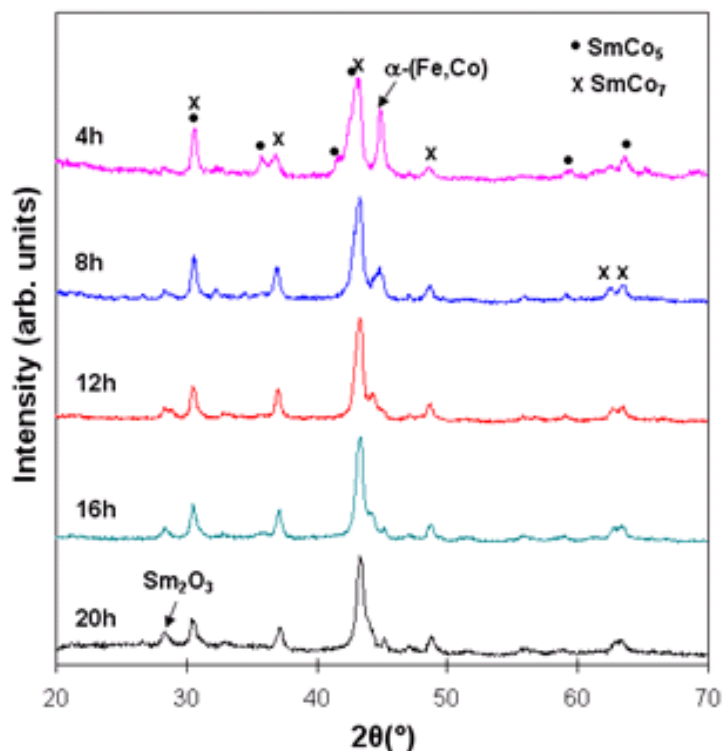


Figure 6.8. XRD patterns for bulk Sm-Co/Fe magnets with different milling time

The microstructures of bulk samples with different milling time were observed by SEM, shown in Figure 6.9. For the bulk of 4 hours milling, there were different sizes of Fe particles: a) unbroken but deformed micron scale; b) broken submicron scale (a few hundred nanometers); c) nanoscale (< a few hundred nanometers). When milling time increased to 8 hours, the micron size Fe particles still existed, but the amount became less. For the sample of milling 12 hours, micron size Fe particles could not be observed, only submicron/nanoscale Fe particles existed. The demagnetization curve revealed a good shape and squareness shown earlier in Figure 6.6. This result demonstrated when the Fe particle size is down to submicron scale, the composite bulk presents a single phase behavior in the demagnetization curve and the exchange coupling is markedly improved. However, the milling time increased to 16 hours, Fe particles showed a little amount. The SEM results are consistent with the former XRD analyses.

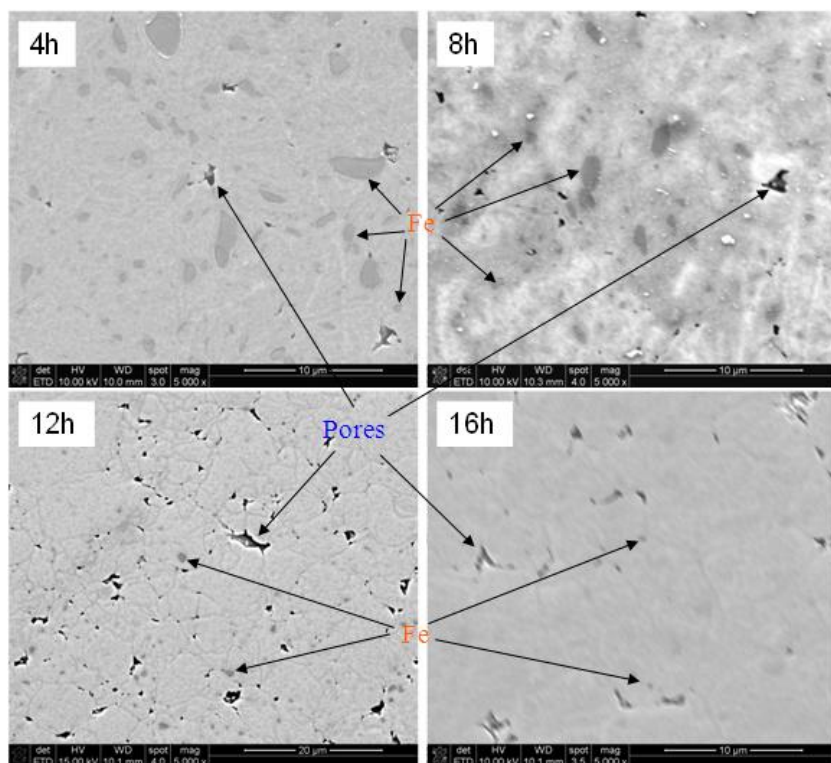


Figure 6.9. SEM images of bulk Sm-Co/Fe samples pressed at 600 °C using the powders milled 4, 8, 12, and 16 hours with starting composition of $\text{SmCo}_5 + 10 \text{ wt}\% \text{ Fe}$ (Magnification 5000 x)

In summary, milling time plays an important role in preparation of bulk Sm-Co/Fe nanocomposite magnets by DM-HP process. It obviously affects the magnetic properties and crystalline structures of the bulk magnets. Owing to milling diffusion (mechanical alloying) in the milling procedure and thermal diffusion in the hot pressing procedure, increasing milling time led to decrease of the soft phase, a decrease of the amount of SmCo_5 phase, and an increase in the phase fraction of the SmCo_7 phase, which resulted in the coercivity decreasing and the magnetization increasing. Considering the demagnetization curve shape and magnetic properties, the best milling time should be 12 hours in the present study.

6.3.1.4 Ball to Powder Weight Ratio (BPR)

For the high energy ball milling procedure, the milling balls impact against the powder sample in the vial with unusually great force, which results in the Sm-Co (brittle material) powders become the amorphous status from the starting crystalline status. And meanwhile, the balls and the powder sample grind and press each other, which results in the Fe (ductile material) particles break down to submicron/nanoscale size from the starting micron-scale size. During the processing, the milling ball size and BPR are very important parameters.

In the aforementioned study, two size of ball were used – diameter of $\frac{1}{2}$ " and $\frac{1}{4}$ ", and the BPR was 5. In order to obtain smaller and more uniform Fe particles, smaller size balls were used to replace the part of the bigger balls. And same time BPR was increased to 10 and 20, in order to shorten the milling time due to milling energy increase. Three type of milling ball (A, D, E) were utilized, shown in Table 6.2. The starting composition was $\text{SmCo}_5 + 10 \text{ wt}\% \text{ Fe}$; the

milling time was fixed at 8 hours. The milled powders were hot pressed at the temperatures of 600 °C under a pressure of 400 MPa.

Figures 6.10 and 6.11 show the demagnetization curves of the bulk magnets with different BPR. Each curve of 4 h milling has a shoulder, which indicated there are still un-broken micron sized soft phases. For samples of 8 h milling, the curves of both higher BPR of 10 and 20 have smooth and better squareness shape, and the curve of BPR of 5 still has a shoulder. This result indicates when BPR is 10 and bigger, 8 h milling could be enough to break down the soft phase particles size from starting 1~3 micron to the submicron/nanoscale. This demonstrated that increasing BPR will strengthen the milling effect and shorten the milling time. Figure 6.12 shows the magnetic properties versus BPR. It is noticed that the different BPR could not obviously affect the B_r and $4\pi M$ at 10 kG. The highest values for H_{ci} and $(BH)_{max}$ were obtained at the BPR of 10. Considering all the properties and milling time, the best BPR should be 10 (Ball-D) corresponding to 8 h milling.

Table 6-2. Milling ball type

Ball size	Type		
	A (pcs)	D (pcs)	E (pcs)
½" (12.7 mm)	2	2	2
3/8" (9.5 mm)			10
¼" (6.4 mm)	23	46	68
3/16" (4.8 mm)		38	88
Total weight (g)	40	80	160
BPR	5	10	20

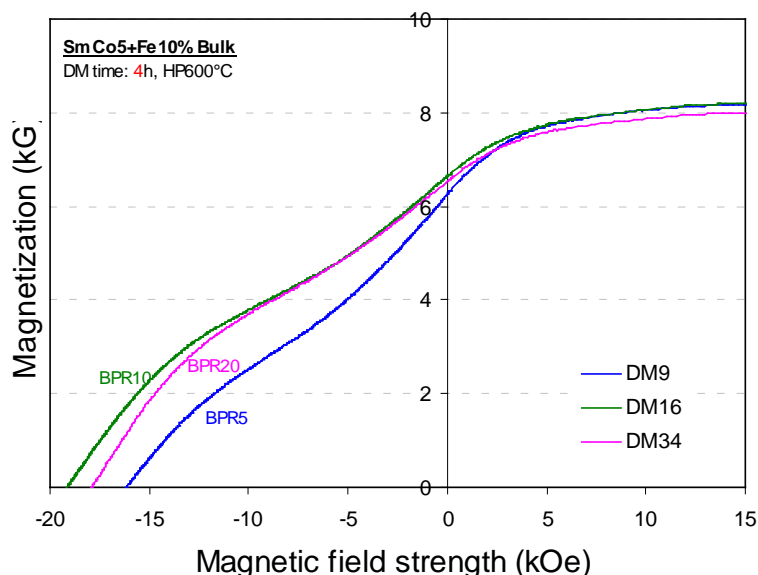


Figure 6.10. Demagnetization curves of Sm-Co/Fe bulk magnets pressed at 600 °C using the powders milled 4h with BPR of 5, 10, and 20

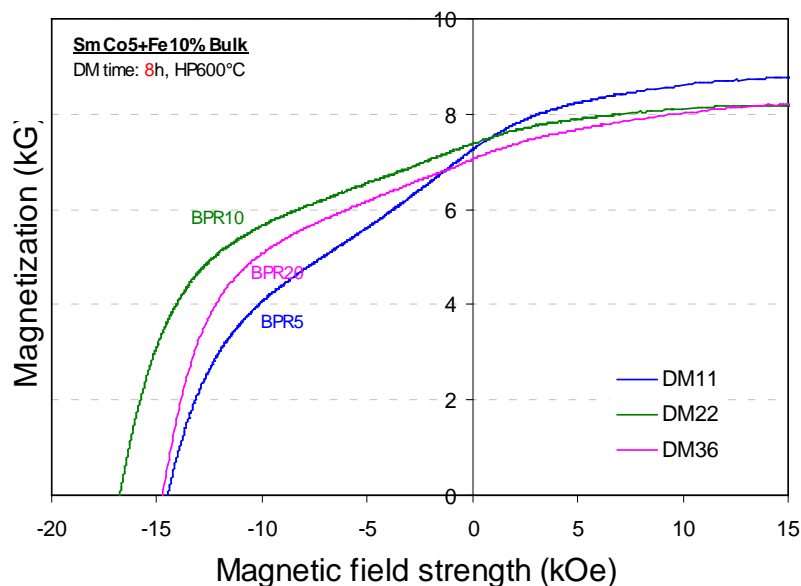


Figure 6.11. Demagnetization curves of Sm-Co/Fe bulk magnets pressed at 600 °C using the powders milled 8h with BPR of 5, 10, and 20

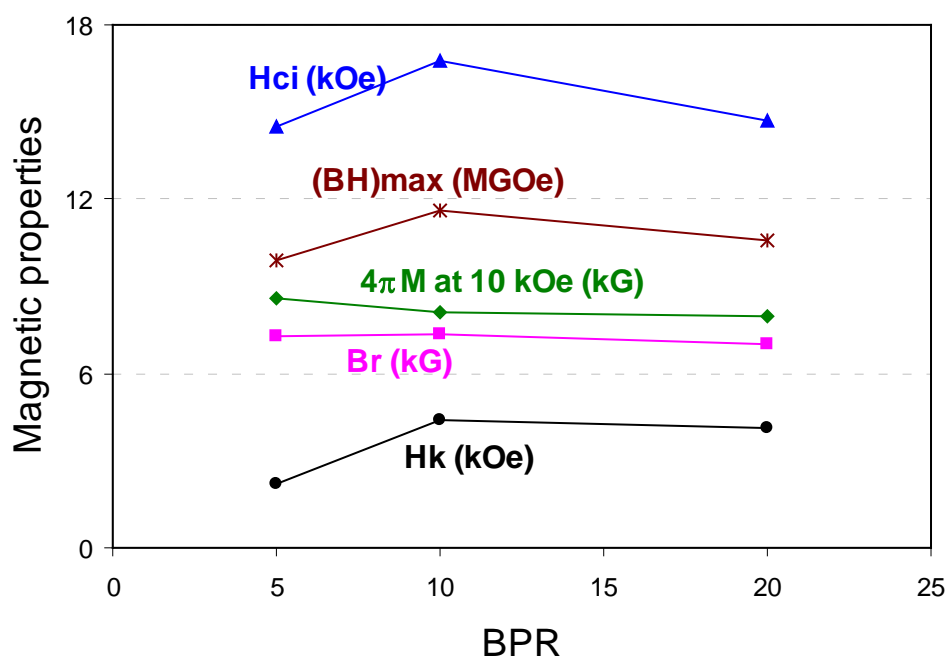


Figure 6.12. Magnetic properties vs. BPR for Sm-Co/Fe bulk samples pressed at 600 °C with milling of 8 h

6.3.1.5 Pressing Temperature

The pressing temperature is an important parameter in HP procedure. If the temperature is lower, the Sm-Co amorphous cannot crystallize totally and it is hard to obtain dense bulks; if

the temperature is higher, the diffusion between soft phase (Fe) and hard phase (Sm-Co) is easy to take place. The best HP temperature should be as lower as possible in the premise of the Sm-Co crystallization conditions. In this experiment, the starting composition of SmCo₅ + Fe 10wt% was selected. The powders were milled 8 hours with BPR of 5 (Ball-A). The pressing temperatures were 600 °C, 700 °C, and 800 °C.

The results of hysteresisgraph measurement for the composite bulk samples are shown in Table 6.3 and Figures 6.13 and 6.14. Magnetic properties became worse as the temperature increased. The coercivity reduced significantly from 600 °C to 800 °C, and the value was only 7.41 kOe at 800 °C, decreased ~ 50%. The sample pressed at 600 °C possessed the largest values of H_{ci}, Br, and (BH)_{max}. For the three samples, they had the same starting composition and were milled with same conditions, which means the milled powders should have same composition and structural status before pressing. However, after hot pressing, the value of 4πM at 10 kOe was different for the bulk samples, and it decreased as the temperature increased. This indicated the composition or phase constitution for bulk magnets should be changed due to different pressing temperature.

In order to reveal the effect of the pressing temperature on magnetic properties, the bulk samples were characterized by SEM and XRD analyses. The SEM/BSE images of the polished bulk samples are shown in Figure 6.15. The soft phase Fe (black) became less as the pressing temperature increased. The small size Fe particles almost disappeared at HP 800 °C. XRD analysis obtained the same results. Figure 6.16 shows the Fe (110) peak reduced as the HP temperature increased. Owing to soft phase Fe loss at higher temperature compaction, the magnetization of the bulk decreased as previously mentioned. For the bulks pressed at 600 and 700 °C, both hard phase (matrix) is 1:7 phase shown in Figure 6.16 (A) and 6.16 (B). For the bulk pressed at 800 °C, the matrix consisted of 1:7 and 2:17 phases shown in Figure 6.16 (C). When the pressing temperature increased, the interdiffusion between the Fe and Sm-Co was easier to take place. After Fe diffused into the Sm-Co matrix, the z value of Sm(Co, Fe)_z increased. This resulted in 2:17 phase formed for the bulk pressed at 800°C. Due to 2:17 phase with lower anisotropic field, the coercivity H_{ci} decreased obviously for the sample pressed at 800 °C shown in Figure 6.13. Thus, 600 °C is the best pressing temperature in the present conditions.

Table 6-3. Magnetic properties of Sm-Co/Fe bulk samples pressed at different temperature

ID	HP Temp (°C)	4pM at 10 kOe (kG)	Br (kG)	H _{ci} (kOe)	H _k (kOe)	(BH) _{max} (MGOe)
DM4	600	8.5	7.28	14.61	2.21	9.96
DM5	700	8.1	6.92	13.22	2.95	9.7
DM6	800	7.5	6.43	7.41	3.45	8.8

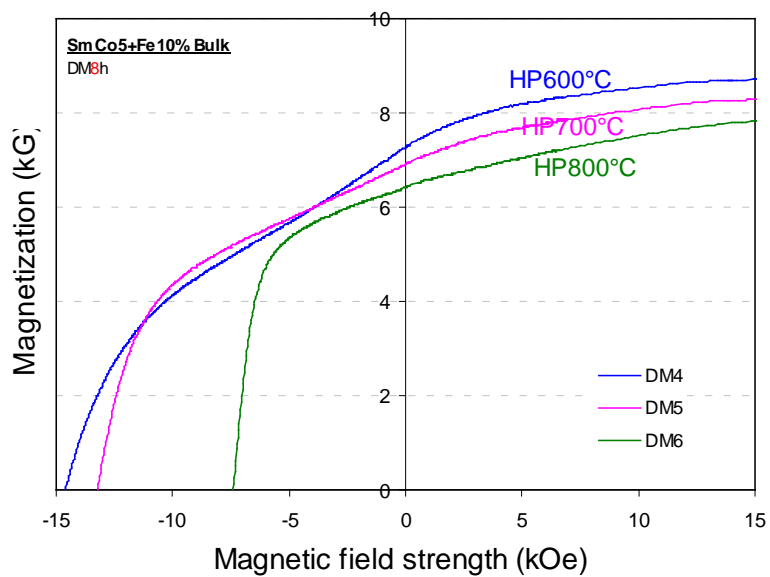


Figure 6.13. Demagnetization curves of Sm-Co/Fe bulk samples pressed at different temperatures

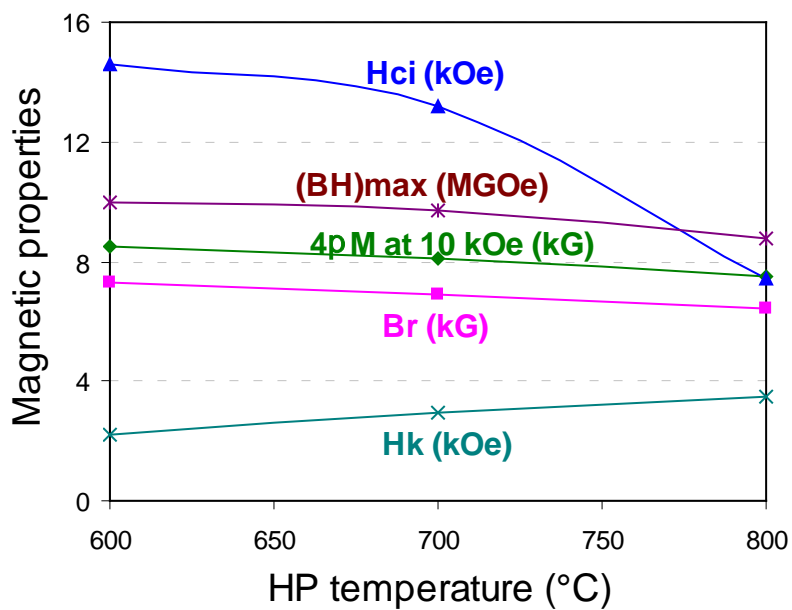


Figure 6.14. Magnetic properties of Sm-Co/Fe bulk samples vs. HP temperature

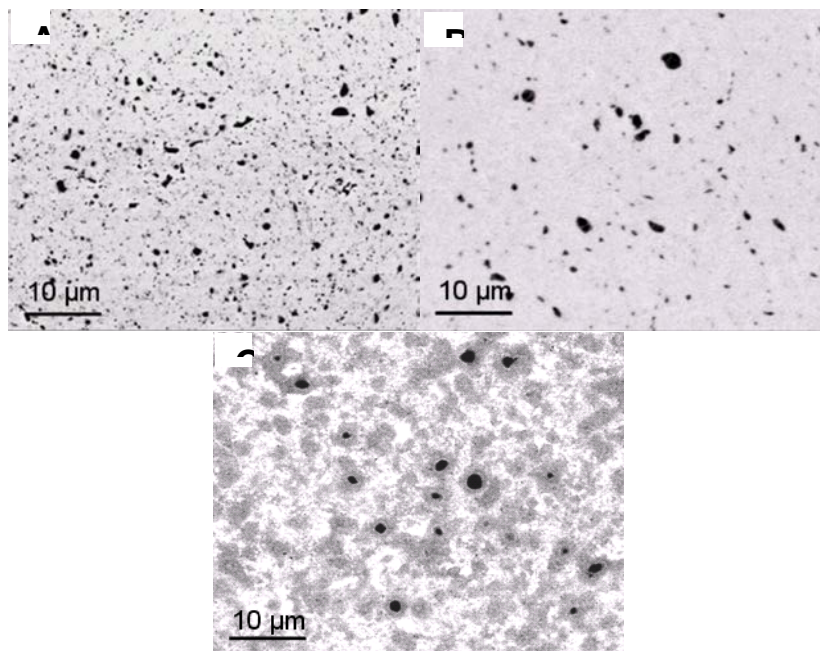


Figure 6.15. SEM/BSE images of Sm-Co/Fe bulk samples with pressing temperature of: A -HP600°C; B - HP700°C; C - HP800°C

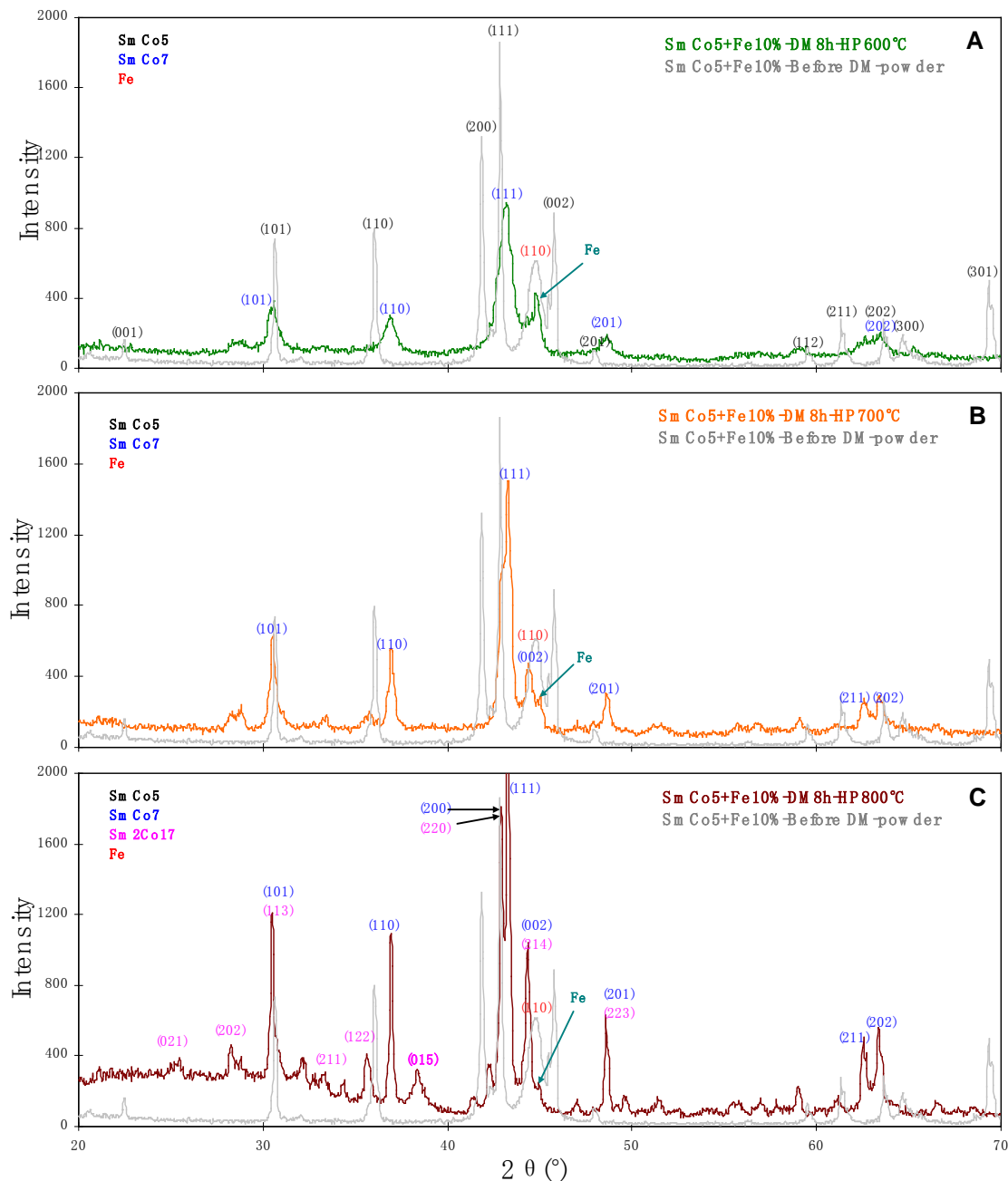


Figure 6.16. XRD patterns of the starting powder and Sm-Co/Fe bulk samples pressed at different temperatures: A – HP 600 °C; B – HP 700 °C; C – HP 800 °C

6.3.1.6 Effect of Soft Phases on Magnetic Properties

Magnetically hard/soft nanocomposite magnets consist of a hard component with high magnetocrystalline anisotropy and a soft component with high saturation magnetization. The magnetic properties of nanocomposite magnets derive not only from the intrinsic properties of the magnetic phases (hard and soft), but also from the type, dimensions, content, and distribution

of the soft phase. In this section, we will discuss the effect of soft phase content, type on magnetic properties.

The starting soft phase precursors were three type powders: micron Fe – Fe(M), nano Fe – Fe(N), and micron FeCo powders. Their composition and particle size are shown in Table 6.4. In previous study, only micron Fe powder was used. The objective to use nano Fe as precursor is to obtain more uniform and nano sized soft phase. $\text{Fe}_{49}\text{Co}_{49}\text{V}_2$ as a soft phase is because it has a higher saturation magnetization. In this serious experiment, the DM-HP process parameters are following: BPR (10, Ball-D); Milling time (8 h); pressing temperature (600 °C).

Table 6-4. Soft phase precursors

Soft phase	Composition	Particle size
Fe(M)	Pure Fe	1-3 μm
Fe(N)	Pure Fe	< 300 nm
FeCo	$\text{Fe}_{49}\text{Co}_{49}\text{V}_2$	<10 μm

The effect of Fe content on the magnetic properties of Sm-Co/Fe magnets was examined. Figure 6.17 shows demagnetization curves of the nanocomposite magnets with different amounts of Fe (M) soft phase. As the Fe content increased, the magnetization at the first quadrant significantly increased and the coercivity decreased. The opposite trends in the magnetization and the coercivity led to a peak in $(\text{BH})_{\text{max}}$ value at 15 wt% Fe addition, as shown in the inset of Figure 6.17. For the sample with 20 wt% Fe addition, magnetization at 10 kOe increased by 88% and H_{ci} decreased by ~ 82% in comparison to the values of single phase SmCo_5 (the sample without the Fe addition), which resulted in the lower $(\text{BH})_{\text{max}}$ of 8.64 MGOe. The optimal soft phase Fe addition was determined to be 15 wt% which results in remanence B_r of 8.1 kG, coercivity H_{ci} of 10.3 kOe, and $(\text{BH})_{\text{max}}$ of 12.3 MGOe.

Figure 6.18 shows demagnetization curves of the bulk magnets with Fe(M), Fe(N), and FeCo addition. The same amount of soft phase, 15 wt%, was added into the starting powders. The sample with FeCo soft phase obtained highest H_{ci} and a good squareness curve. The saturation magnetization of $\text{Fe}_{49}\text{Co}_{49}\text{V}_2$ (24.5 kG) is higher than that of pure Fe (21.6 kG). However, the magnetization at the first quadrant of the sample with FeCo addition is lower than that with Fe addition. It is noticed that nano Fe (Fe(N)) addition did not make a significant improvement for the demagnetization curve shape and properties compared to micron Fe (Fe(M)) addition.

The microstructure of the bulk samples was observed by backscattered electron (BSE) imaging in SEM, shown in Figure 6.19. For the bulk sample with the precursor of micron Fe (Figure 6.19 (a)), lots of Fe particles uniformly distributed in the matrix with separate particles. Most particle size was less than a few hundred nanometers. However, a few microscale particles still existed because they have not totally broken into small pieces during the milling. For the sample with nanoscale Fe as precursor (Figure 6.19 (b)), only a few Fe particles (< 100 nm) scattered in the matrix. For the bulk sample with microscale FeCo precursor (Figure 6.19 (c)), it was hard to find any FeCo particles within the entirety of sample. XRD analysis for the milled powders and the bulk samples are shown in Figure 6.20. For the bulk sample with Fe(M) addition, the diffraction peaks indicated TbCu_7 type Sm-Co 1:7 and Fe phases exist. For the bulk samples with Fe(N) and FeCo addition, all of the diffraction peaks were determined to be Sm-Co 1:7 phase, and there was no soft phase peak, which matches with the SEM results. Even there were a few tiny Fe particles according to SEM observation for Fe(N) addition, the Fe content in

the Sm-Co/Fe bulk should be lower than 5 wt%. XRD patterns for the milled powder of Fe(N) addition showed Fe peak existence (Figure 6.20 (a)), the most amount of Fe loss should carry out in the procedure of hot compaction owing to thermal diffusion. For the starting composition of $\text{SmCo}_5 + 15 \text{ wt\% FeCo}$, the soft phase peak was not present for the as-milled powder, which indicates that the FeCo soft phase did not exist in the milled powder before compaction and it should be mechanically alloyed into the hard phase after milling of 8 hours. Figure 6.21 shows XRD patterns of as-milled powders with different milling time. The soft phase FeCo diffraction peak was present up to only 4 hours of milling. The results indicate that FeCo powder is more readily mechanically alloyed with the Sm-Co phase during the milling procedure. Although the $\text{Fe}_{49}\text{Co}_{49}\text{V}_2$ soft phase has a higher saturation magnetization, it is not suitable as a soft phase in the present process.

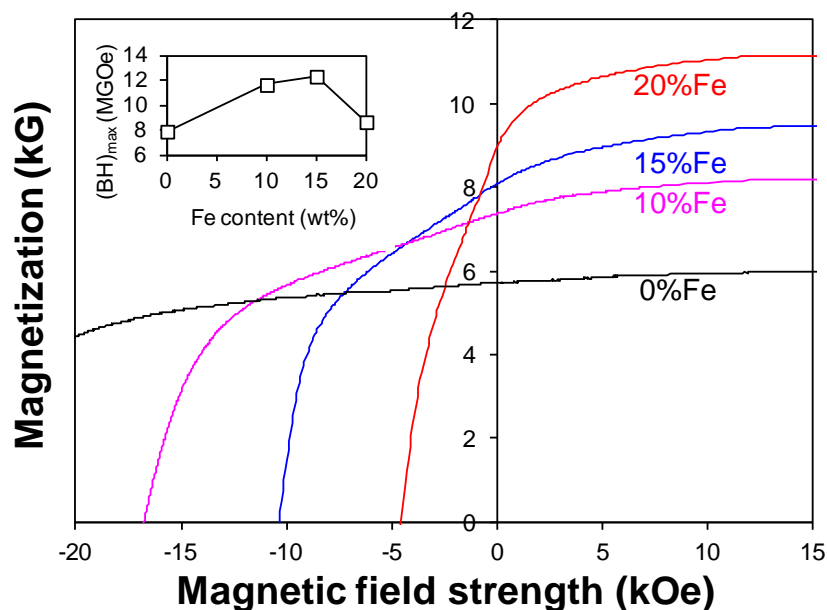


Figure 6.17. Demagnetization curves of bulk Sm-Co/Fe magnets with different amount of Fe(M) addition and maximum energy product vs. Fe content (inset)

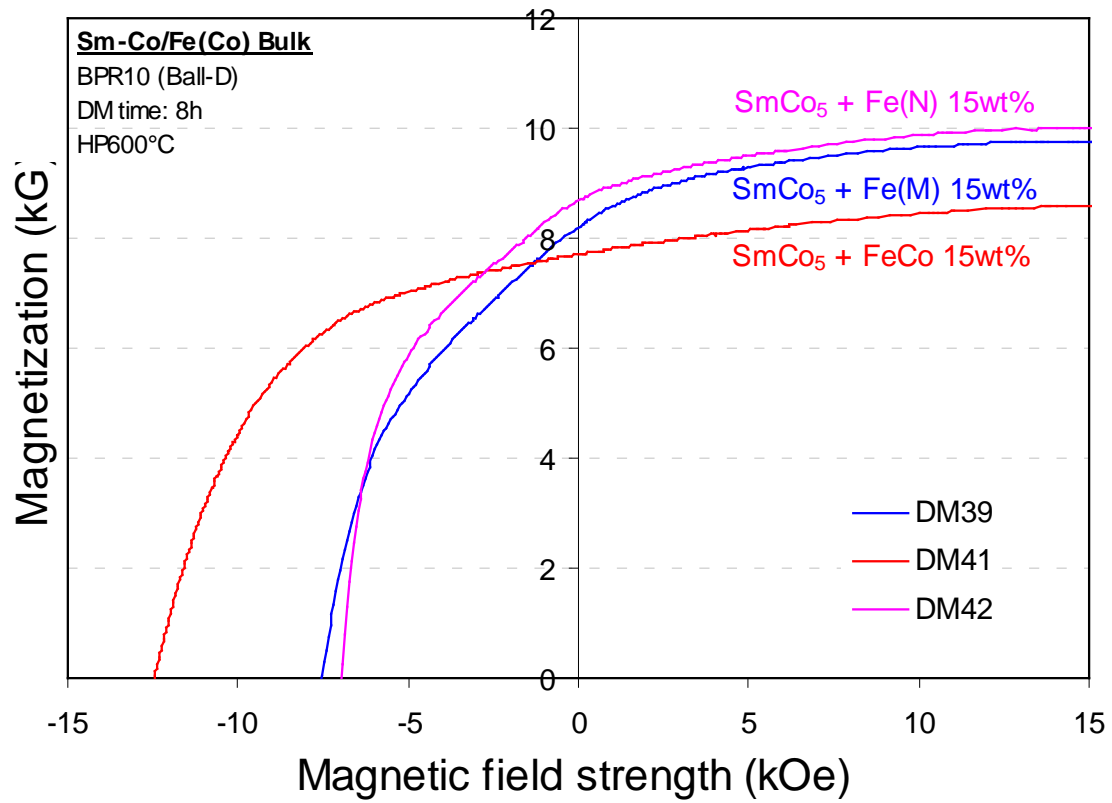
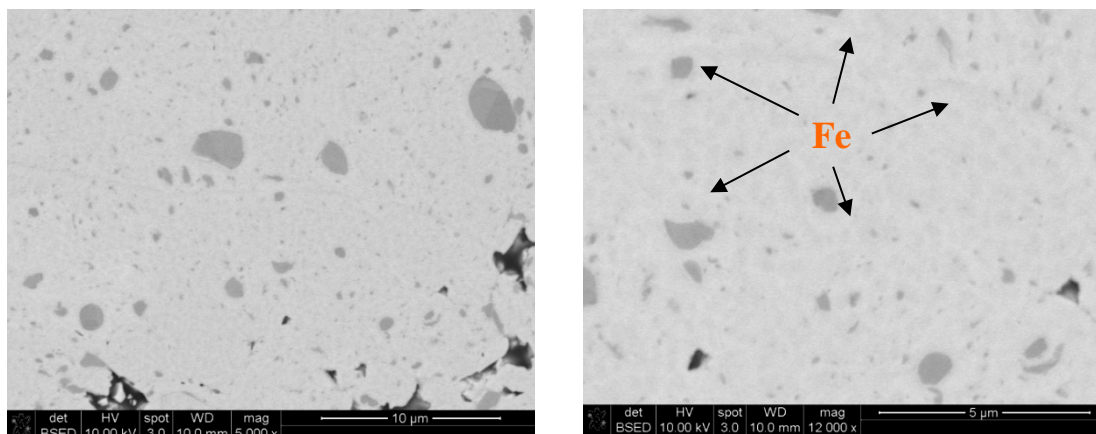
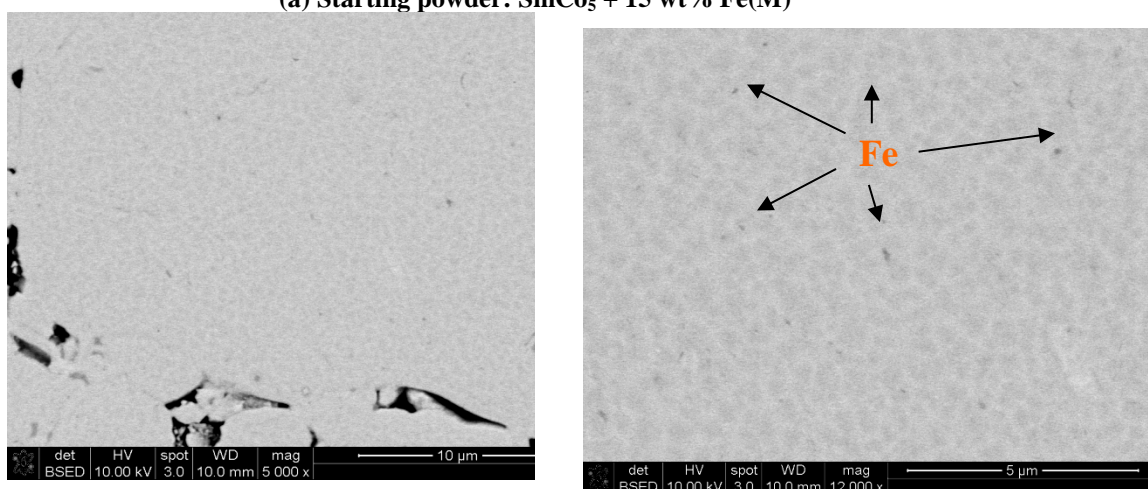


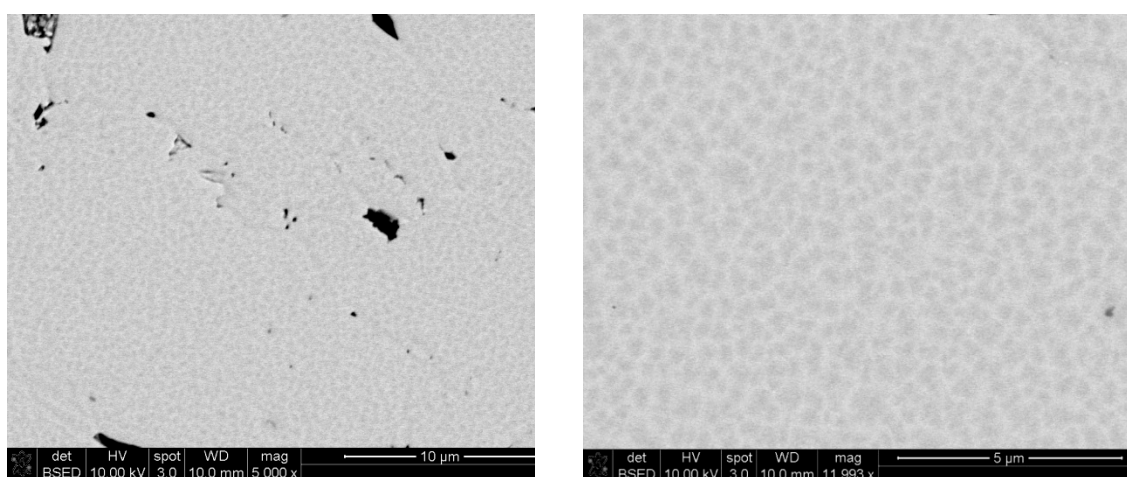
Figure 6.18. Demagnetization curves of Sm-Co/Fe bulk magnets with starting composition of SmCo₅ + 15 wt% soft phase (Fe(M), Fe(N), and FeCo)



(a) Starting powder: $\text{SmCo}_5 + 15 \text{ wt\% Fe(M)}$



(b) Starting powder: $\text{SmCo}_5 + 15 \text{ wt\% Fe(N)}$



(c) Starting powder: $\text{SmCo}_5 + 15 \text{ wt\% FeCo}$

Figure 6.19. SEM/BSE images for Sm-Co/Fe bulk samples with different soft phase precursor

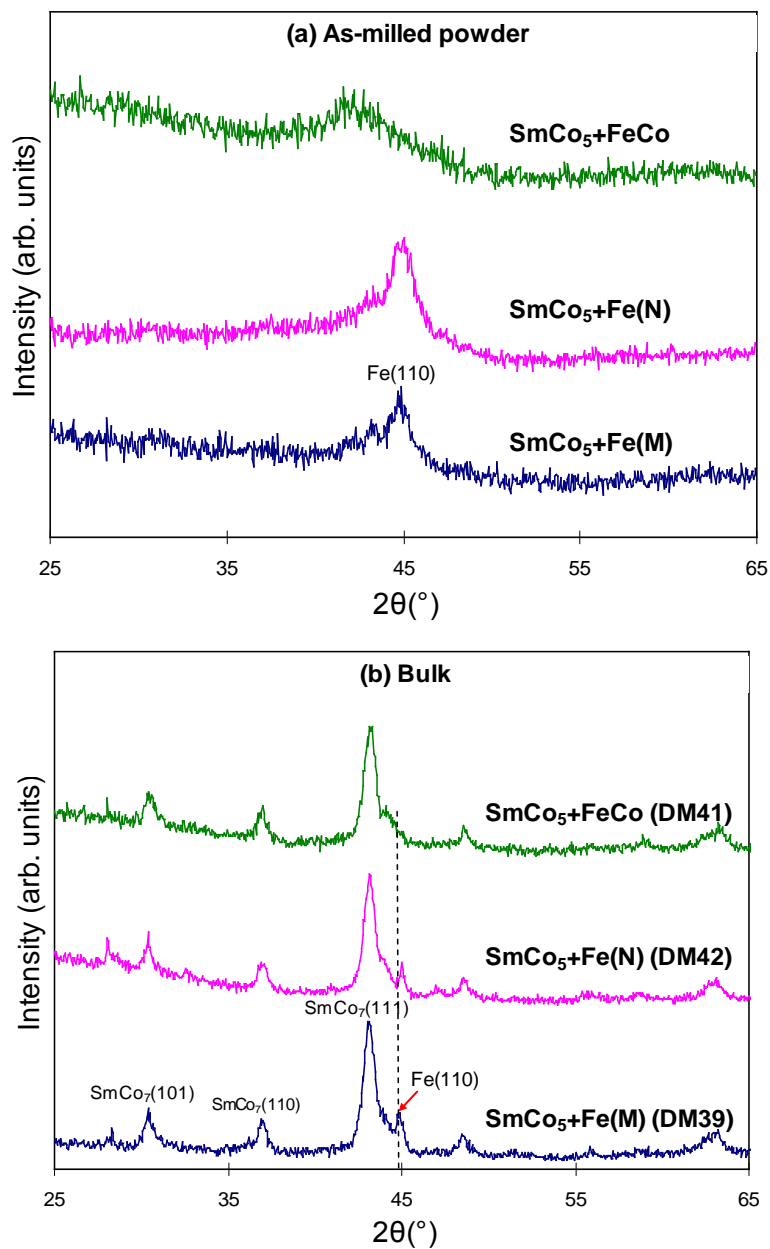


Figure 6.20. XRD patterns for as-milled powders (a) and bulk samples (b) with starting composition of SmCo₅ + 15 wt% Fe(M), Fe(N), and FeCo

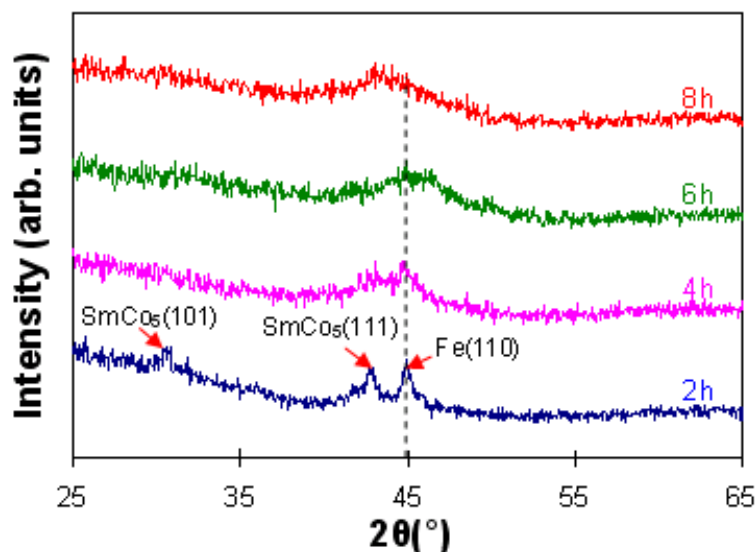


Figure 6.21. XRD patterns for as-milled powders with the starting composition of $\text{SmCo}_5 + 15 \text{ wt\% FeCo}$ after milling for 2, 4, 6, and 8 hours

6.3.2 Anisotropic Sm-Co/Fe Nanocomposite Particles

In our previous research, bulk Sm-Co/Fe nanocomposite magnets were obtained by using DM-HP process. The nanoscale soft phase Fe distributed uniformly in the nanograin hard phase Sm-Co matrix and the magnetic properties of composite bulk magnets improved significantly compared to the single hard phase bulk magnets. However the magnetically hard/soft nanocomposite bulks are isotropic magnets, which could not reach the higher magnetization value. To develop nanocomposite magnets with high energy product, nanocomposite magnets should possess high degree of anisotropy. Using wet high energy ball milling with surfactant-assistance (WM) process, anisotropic single phase SmCo_5 nanoflake powders were successfully prepared in recent years [13, 14]. In this study the WM technique was utilized to prepare magnetically anisotropic Sm-Co/Fe composite particles in order to develop high performance composite magnets.

The starting alloys for WM were isotropic Sm-Co/Fe composite bulk precursors. Precursor A was a nano-structural composite of nano-crystallite Sm-Co (1:5 and 1:7 phases) matrix and submicron and nanoscale Fe particles. Precursor B was a micro-structural composite of micro-crystallite SmCo_5 matrix and micron Fe particles. The former was prepared by dry high energy ball milling (DM) of SmCo_5 and Fe powders, and the latter was prepared by low energy ball milling (BM) of SmCo_5 and Fe powders. Both milled mixtures of Sm-Co and Fe were hot pressed to form the composite bulks and subsequently crushed to a powder form as the starting materials for WM.

6.3.2.1 Sm-Co/Fe Nanocomposite Particles Prepared by Precursor A

The Precursor A for WM was obtained by using dry high energy ball milling (DM) and subsequent hot pressing (HP) the milled powder. So the composite particle preparation process was named DM-WM process, which is shown in Figure 6.22. The SmCo_5 powders were mixed

with 15 wt % α -Fe powder, and then the mixtures were milled by DM with ball to powder weight ratio of 10 and milling time of 8 hours using a SPEX 8000 mill. Then the milled Sm-Co + Fe powders were hot pressed with a pressure of 400 MPa. In order to obtain composite bulks with different size grain, the pressing temperature varied from 650 to 940°C. And another method to obtain large grain bulk was used as heat treatment (HT), which process was the bulk samples pressed at 650°C were hold at 650, 750, 850, and 950 for 10 minutes. The bulk precursors were crushed into coarse powders under 250 μ m for WM starting powders. This WM was carried out for 1 hour in a hardened stainless steel vial using SPEX 8000 mill. Ball to powder weight ratio was 0.8. The size of milling ball was 3/32'' (2.38 mm). Heptane and oleic acid was used as the solvent and the surfactant with 60 wt% and 30 wt% of the starting powders (4.5 g), respectively. After milling, the slurry powder was rinsed with acetone and vacuum dried for further material characterizations. Epoxy samples were fabricated by mixing the milled powder with an epoxy binder and then magnetically aligning using 10 T pulse field before curing.

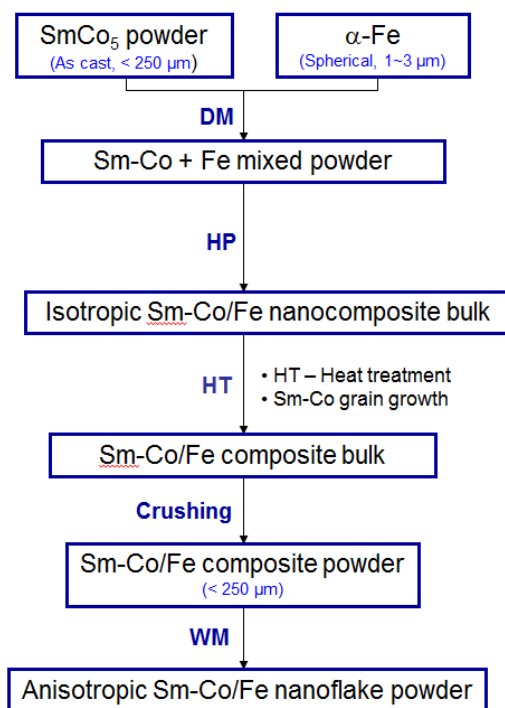


Figure 6.22. DM-WM process

For the composite bulks pressed at 650 ~ 940 °C, their demagnetization curves are shown in Figure 6.23. As HP temperature increased, $4\pi M$ at 10 kOe and Br decreased, which was resulted in soft phase Fe loss due to interdiffusion between Fe and Sm-Co under the higher temperature. The H_{ci} obtained the largest value at 700 °C, and then it went down as temperature increased, which should be related with grain growth and Sm₂Co₁₇ phase formation. Four bulk samples with pressing temperature of 650, 750, 850, and 940 °C were selected as WM precursors. Figure 6.24 shows the SEM images for the as-milled powders. The particles presented plate-like shape with size of 1 – 2 μ m in thickness and 1 – 5 μ m in width. The

magnetically aligned epoxy samples of milled composite powders were measured by the KJS Hysteresis graph along both parallel (//) and perpendicular (⊥) to the magnetic aligning direction. Figure 6.25 shows the demagnetization curves with hard and easy directions. For the precursor with HP at 650 °C, the easy direction remanence $B_{r\parallel}$ is close to the hard direction remanence $B_{r\perp}$; for the precursor with HP at 850 °C, the difference of two remanence values became larger, which indicated the powders had anisotropic magnetic behavior.

The degree of anisotropy (DOA) is described by the following equation: $DOA = (B_{r\parallel} - B_{r\perp}) / B_{r\parallel}$. For the isotropic magnet, $DOA = 0$ with $B_{r\parallel} = B_{r\perp}$; for the ideal anisotropic magnet, $DOA = 1$ with $B_{r\perp} = 0$. Figure 4.26 shows the DOA versus pressing temperature. DOA obtained the maximum value of 0.23 at HP temperature of 850 °C. But the lower value indicated the anisotropic behavior of the particles was still weak.

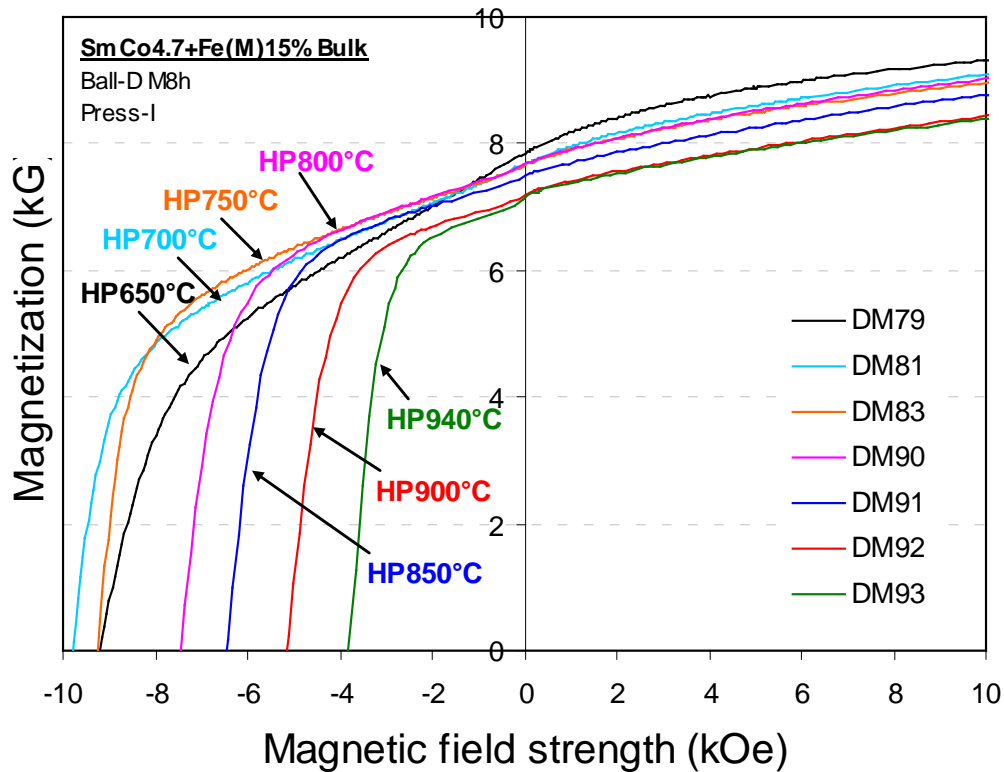
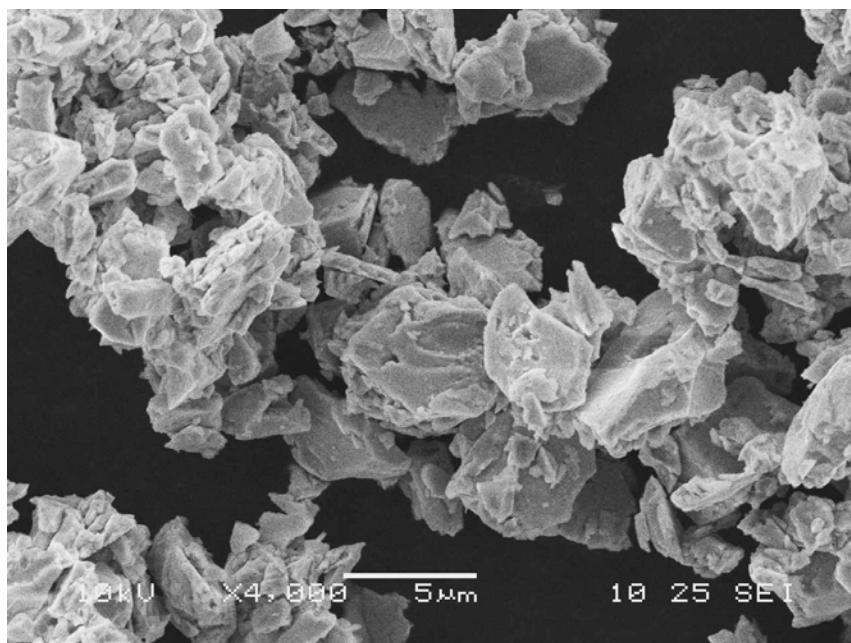
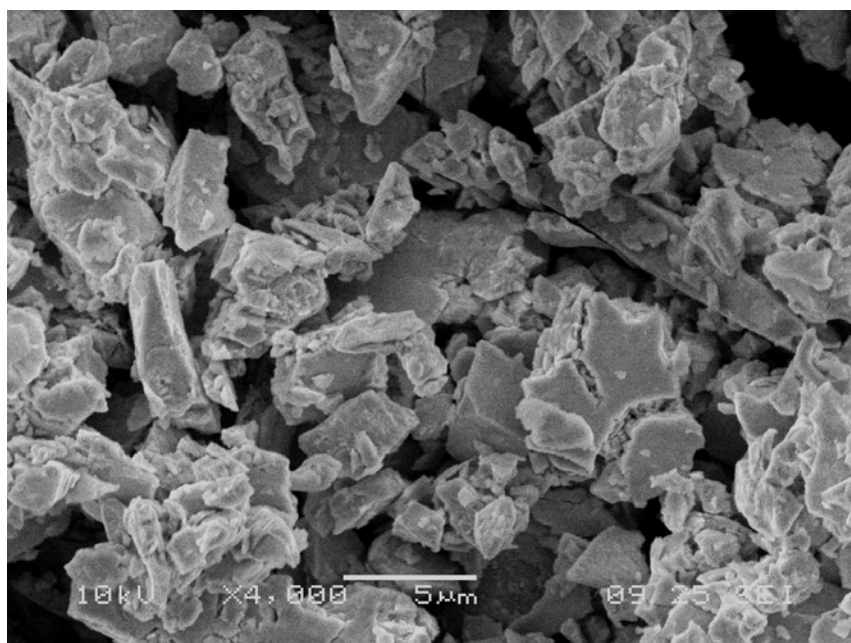


Figure 6.23. Demagnetization curves of bulk Sm-Co/Fe magnets pressed at different temperature

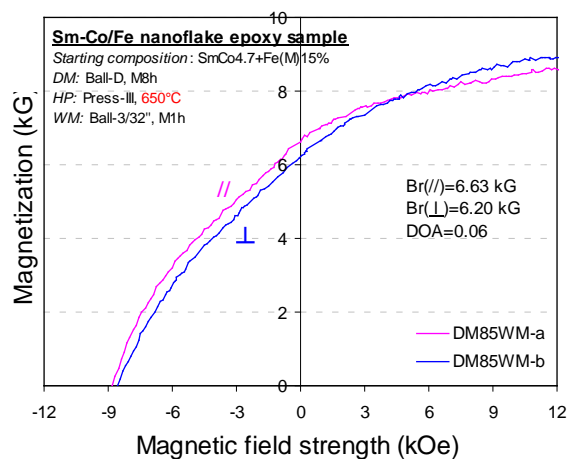


(a) Precursor pressed at 650 °C

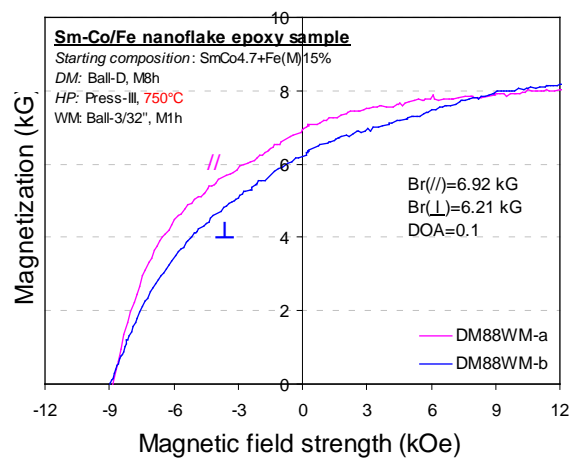


(b) Precursor pressed at 850 °C

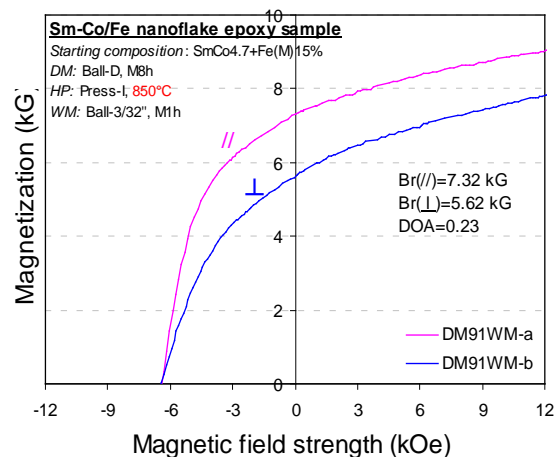
Figure 6.24. SEM images of the milled Sm-Co/Fe particles prepared with precursors pressed at 650 °C (a) and 850 °C (b)



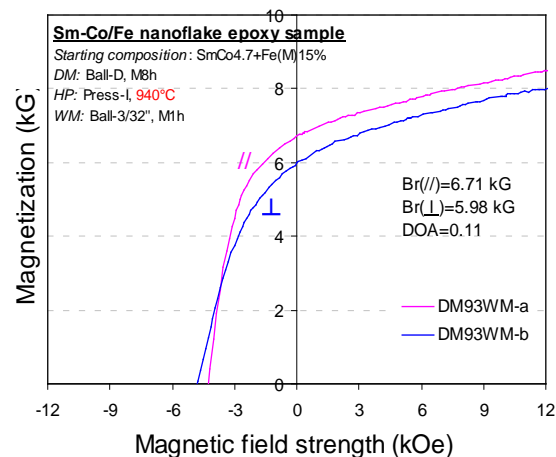
(a) Precursor pressed at 650°C



(b) Precursor pressed at 750°C



(c) Precursor pressed at 850°C



(d) Precursor pressed at 940°C

Figure 6.25. Demagnetization curves of Sm-Co/Fe particle epoxy samples tested along both parallel (//) and perpendicular (⊥) to the magnetic aligning direction

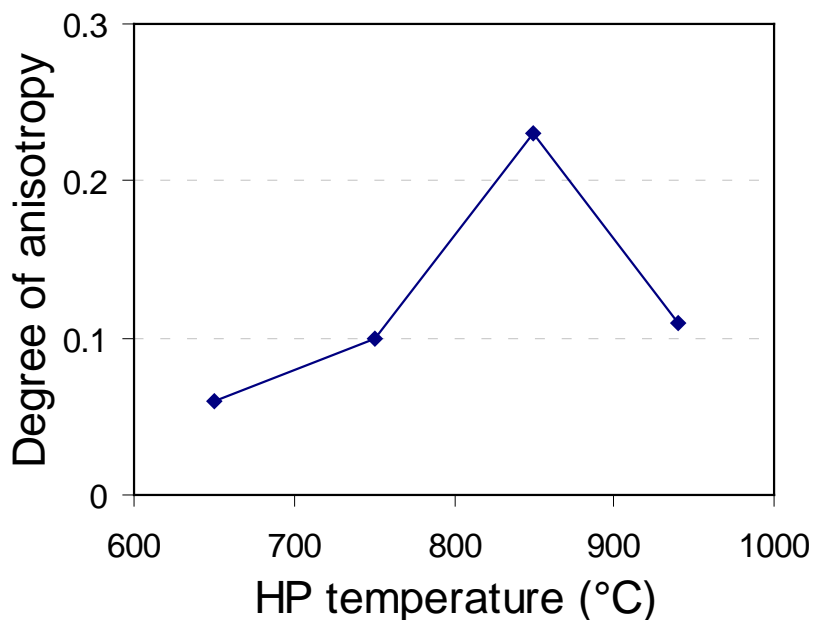


Figure 6.26. Degree of anisotropy vs. pressing temperature

For the composite bulks pressed at 650 °C and subsequently heat treated, their demagnetization curves are shown in Figure 6.27. The magnetic properties reduced for higher HT temperature, which results are same as that of pressing at higher temperature. After the bulk precursors were milled to composite particles by WM, the magnetically aligned powder epoxy samples were prepared. KJS test results are shown in Figure 6.28. The demagnetization curves for two directions (easy - parallel and hard – perpendicular) presented a little difference. Figure 6.29 shows the DOA depending on heat treatment temperature. DOA value was verified from 0.14 a 650 °C to 0.19 at 850 °C, which indicated the powders had weaker anisotropic behavior.

According to our previous studies, the bulk Sm-Co/Fe precursor had polycrystalline structure with a nanoscale grain size. As-milled particles with particle size of 1 – 5 μm were multigrain particles, which is hard to be aligned in a magnetic field. So the milled composite powders presented a weak anisotropic behavior. Increasing HP temperature and HT temperature intended to make Sm-Co grain growth to obtain larger grain precursors, however the effect was insignificant. And meanwhile, increased temperature resulted in lower magnetic properties of the composite precursors. XRD results, shown in Figure 6.30, demonstrated the soft phase Fe decreased and Sm₂Co₁₇ existed and increased for higher HP and HT temperature. Thus, isotropic Sm-Co/Fe composite bulks prepared by DM-HP are not suitable for WM precursors to prepare anisotropic composite particles.

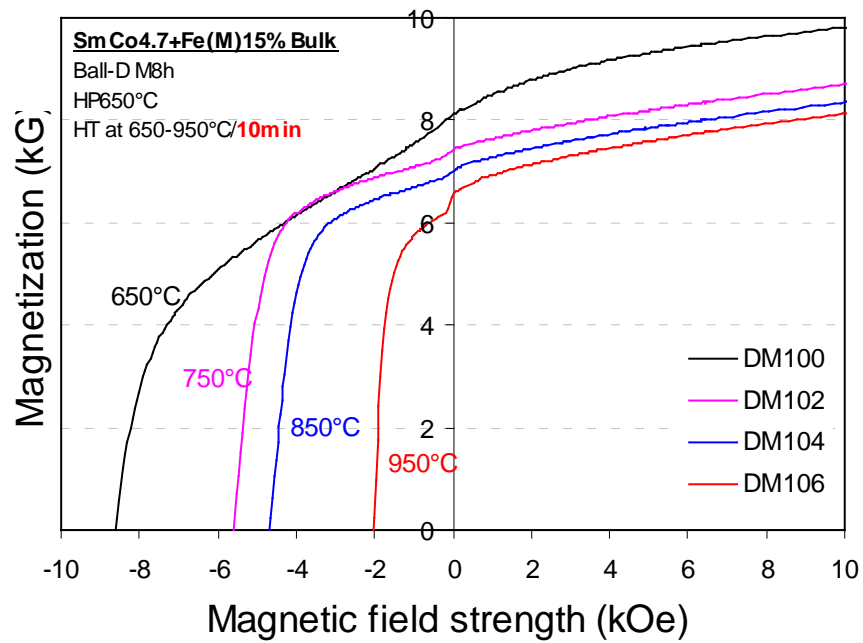
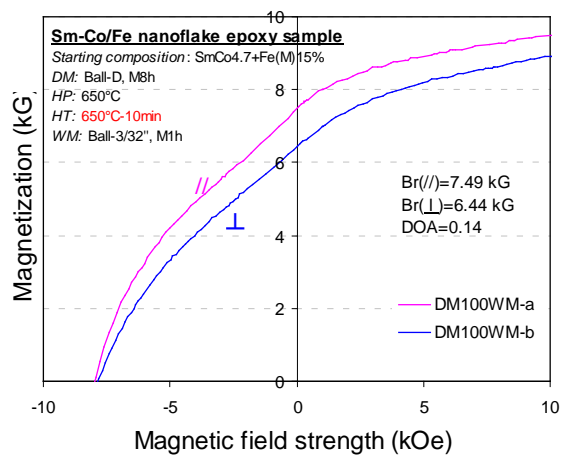
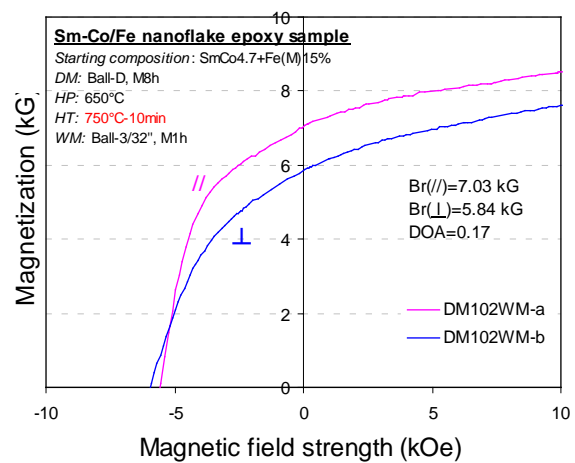


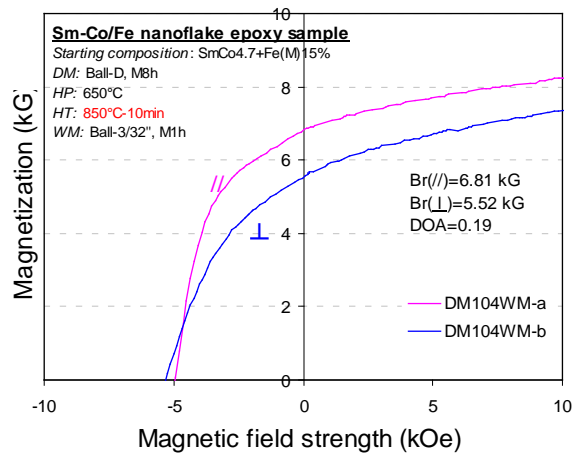
Figure 6.27. Demagnetization curves of bulk Sm-Co/Fe magnets pressed at 650 °C with different heat treatment (HT) temperature for 10 min



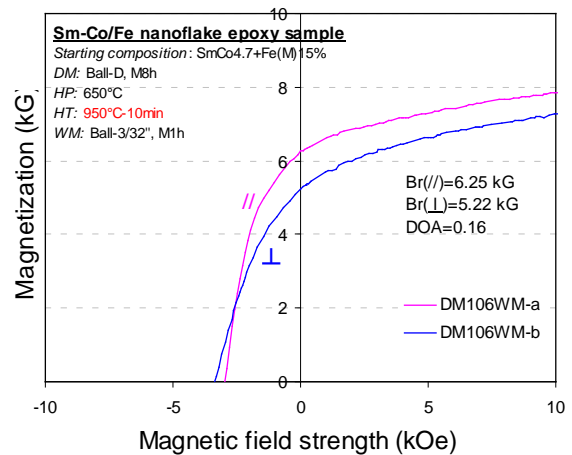
(a) Precursor HT at 650 °C



(b) Precursor HT at 750 °C



(c) Precursor HT at 850 °C.



(d) Precursor HT at 950 °C.

Figure 6.28. Demagnetization curves of Sm-Co/Fe particles epoxy samples tested along both parallel (//) and perpendicular (⊥) to the magnetic aligning direction

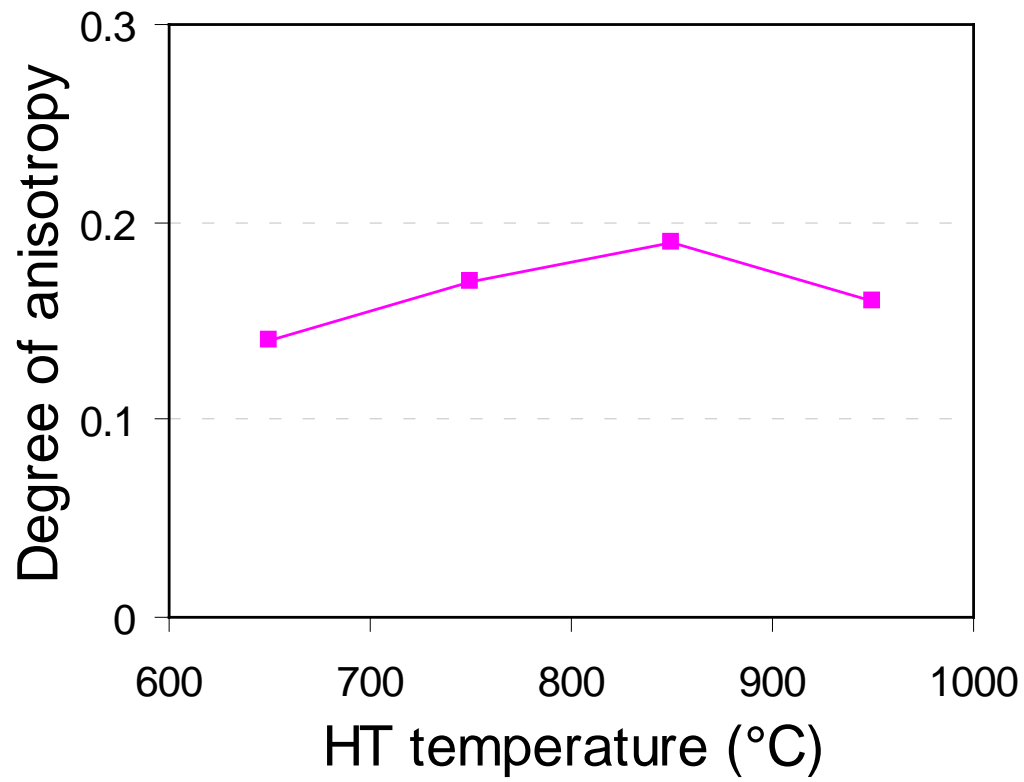
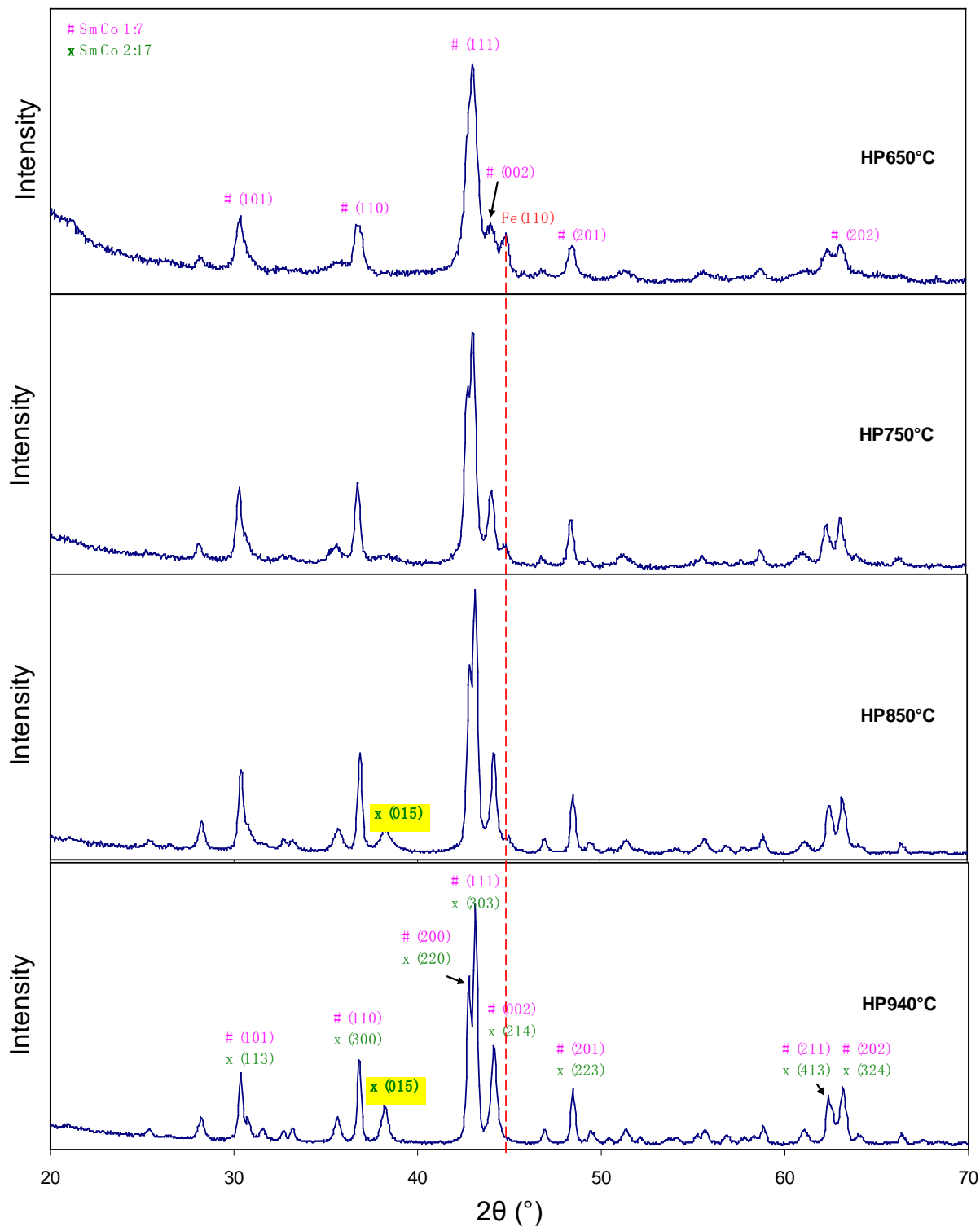
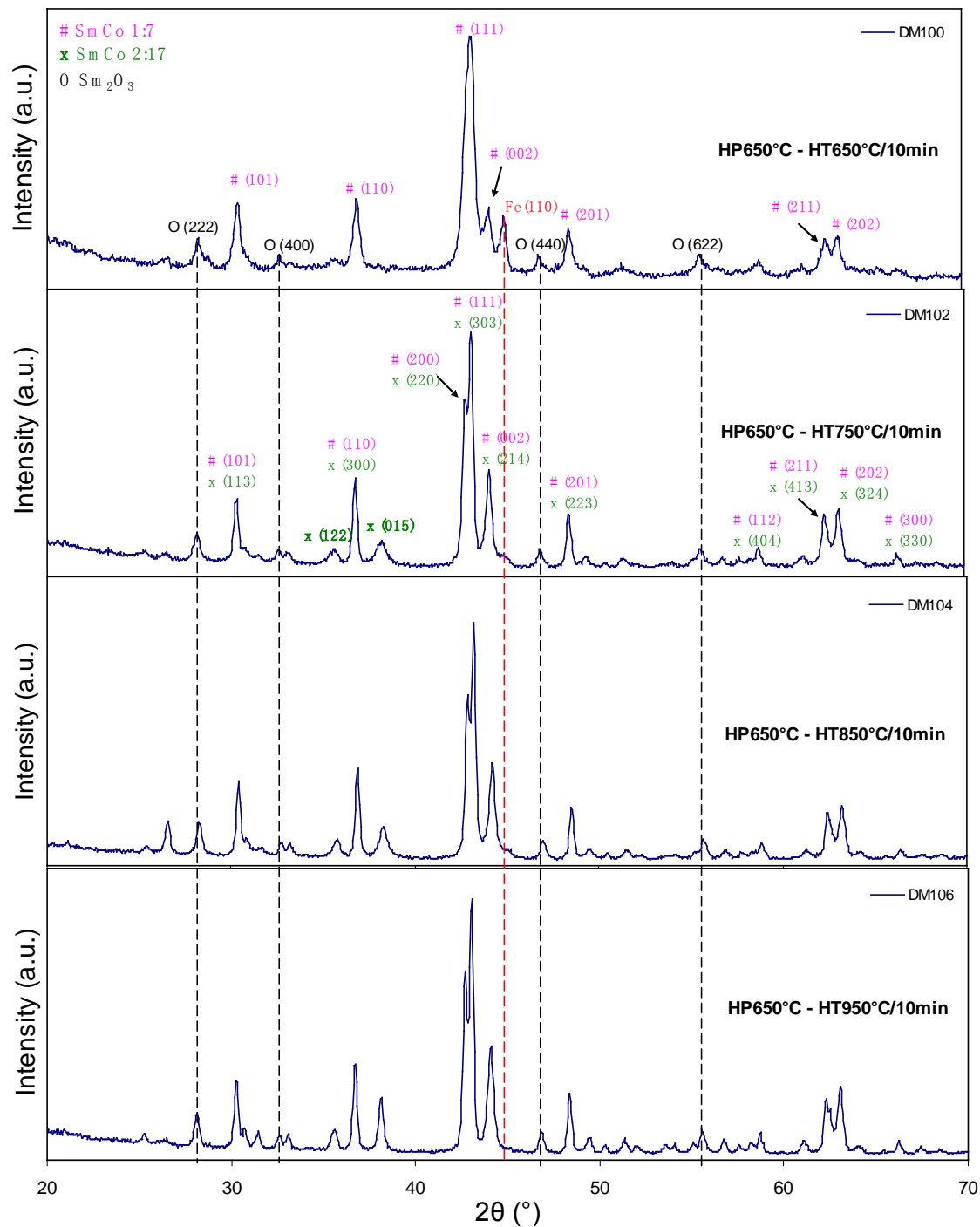


Figure 6.29. Degree of anisotropy vs. heat treatment temperature



(a) Precursor pressed at different temperatures



(b) Precursors pressed at 650 °C and HT at different temperatures

Figure 6.30. XRD patterns for Sm-Co/Fe composite bulk precursors prepared by DM-HP process: (a) Pressed at 650-940 °C; (b) Pressed at 650 °C and HT at 650-950 °C

6.3.2.2 Sm-Co/Fe Nanocomposite Particles Prepared by Precursor B

As mentioned above, nanograin composite precursor produced the composite particles with a weak anisotropy. The effort was made to prepare micrograin Sm-Co/Fe precursors (B) in this study. The Precursor B for WM was prepared by using low energy ball milling (BM) and subsequent hot pressing (HP) the milled powder. This process was named BM-WM process, which is shown in Figure 6.31. The SmCo_5 powders were mixed with 15 wt % α -Fe powder, and then the mixtures were milled by low energy ball milling with BPR of 20, acetone medium, and milling time of 4 hours using a roller ball mill. Then the milled Sm-Co + Fe powders were hot pressed at 650 °C with a pressure of 400 MPa. The bulk precursors were crushed into coarse powders under 250 μm for WM starting powders. This WM was carried out for 1 hour in a hardened stainless steel vial using SPEX 8000 mill. Ball to powder weight ratio varied from 0.8 to 10. The size of milling ball was 3/32'' (2.38 mm) for BPR of 0.8 – 4, and bigger balls 3/8'' (9.5 mm) and 1/4'' (6.4 mm) were used for BPR of 10. Heptane and oleic acid was used as the solvent and the surfactant with 60 wt% and 30 wt% of the starting powders (4.5 grams), respectively. After milling, the slurry powder was rinsed with acetone and vacuum dried for further material characterizations. Epoxy samples were fabricated by mixing the milled powder with an epoxy binder and then magnetically aligning using 10 T pulse field before curing, which were used for hysteresisgraph measurement and XRD analysis.

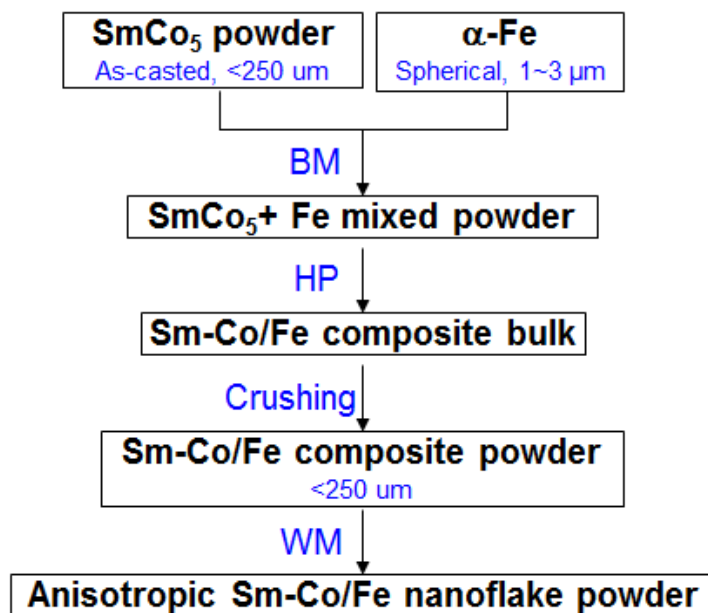


Figure 6.31. BM-WM process

Figure 6.32 shows the morphology of the BM mixed powder before compaction, which revealed that SmCo_5 was irregular shapes with the size of 1-10 μm and Fe was still kept the starting spherical shape and the size of 1-3 μm and uniformly distributed in the SmCo_5 particles. Bulk SmCo_5 ingot has a polycrystalline structure with a grain size in the range of 40 – 100 μm [15]. The as-milled SmCo_5 powder was composed of single crystal microparticles since it was milled by low energy ball milling. Thus, Precursor B bulk should be consisted of micrograin

SmCo₅ matrix and micron scale Fe particles, and it is a microcrystalline structure. The demagnetization curves of Sm-Co/Fe composite bulk (Precursor B) and Sm-Co bulks are shown in Figure 6.33. Adding soft phase obviously increased magnetic moment. Both bulks had lower coercivity (2.3 kOe for SmCo₅ and 2.06 kOe for Sm-Co/Fe) due to the micron size grain. After crushing the composite bulk and wet milling, Sm-Co/Fe composite powders were fabricated.

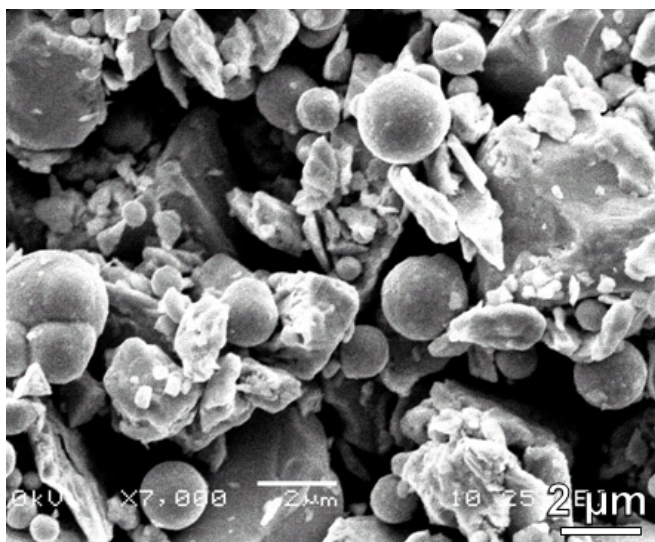


Figure 6.32. SEM images of Sm-Co + Fe mixed powders milled 4h by BM

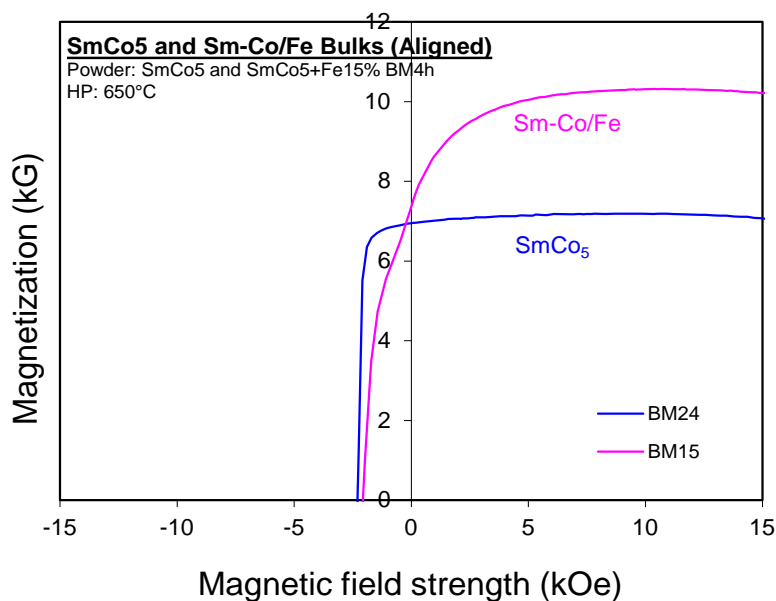


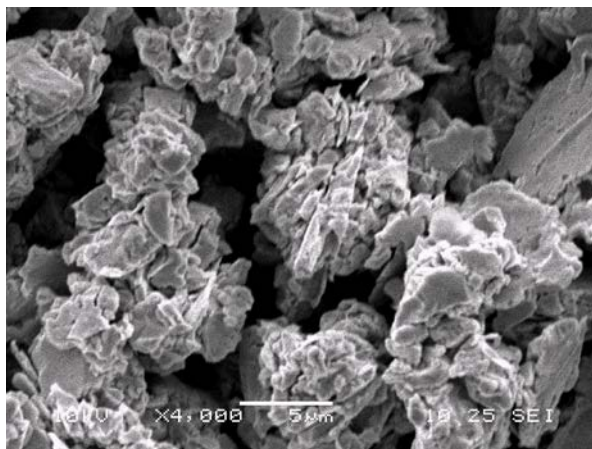
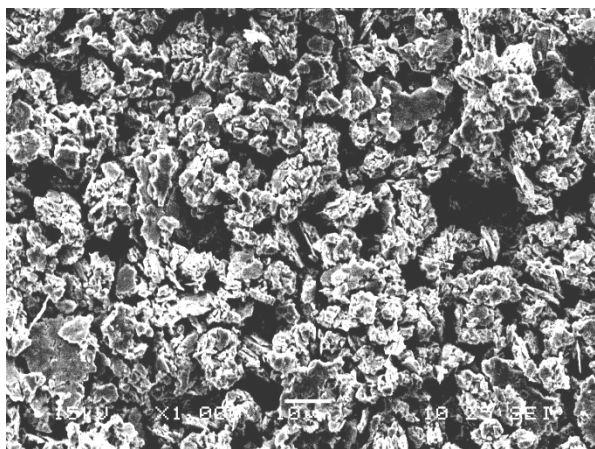
Figure 6.33. Demagnetization curves of Sm-Co and composite Sm-Co/Fe bulk magnets pressed at 650 °C

Figure 6.34 shows the morphology of Sm-Co/Fe composite particles milled with ball to BPR of 0.8, 1, 2, 4, and 10. For all the powders, the particles agglomerated to around 10 μm cluster, which could minimize their surface energy. The shape of single particle presented from

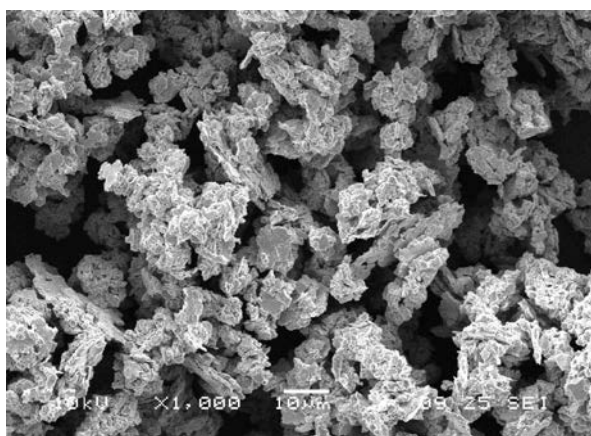
plate-like to flake-like as BPR increased. The thickness of the particle varied from around 1 micron to tens nanometer. For the powders milled with BPR of 0.8 and 1 (Figures 6.34 (a) and 6.34 (b)), the single particle presented plate shape with thickness of $\sim 1 \mu\text{m}$. For the powders milled with BPR of 2 (Figure 6.34 (c)), the powders were consisted of plate and flake particles with the thickness of 500 – 800 nm. For the powders milled with BPR of 4 and 10, all the particles showed flake shape with the thickness of 200 - 400 nm and tens – 100 nm, respectively. As the BPR increased, the particle thickness varied from micron scale to nanoscale, however the width for all particles still kept almost same size of around 1 ~ 5 μm , which means the ratio of width (length) / thickness increased. Since the grain size of the precursor was 1 - 10 μm , the milled particles (tens nm – 1 μm in thickness and 1 - 5 μm in length) should be single crystal or multigrain crystal with two or several grains.

Figure 6.35 shows the demagnetization curves for epoxy samples of Sm-Co/Fe powders prepared with different BPR, tested along both parallel (//) and perpendicular (\perp) to the magnetic aligning direction. The two curves for sample prepared with BPR of 0.8 revealed a big difference (Figure 6.35 (a)), and the DOA value was 0.64, which demonstrated the powders had a good anisotropic behavior. For the pure SmCo_5 powders milled with same WM parameters which precursor was prepared with same process (BM-HP), the demagnetization curves were showed in Figure 6.35 (a) insert, and the DOA value was 0.63. This indicated that the soft phase existence in Sm-Co/Fe composite could not obviously affect the anisotropic behavior. However, the downward shoulder curve (//) revealed bad exchange coupling between hard phase and soft phase due to micron size of soft phase. As BPR increased, the two direction curves tended to close, and the DOA value dropped to 0.41 for the BPR of 10. Figure 6.36 shows the degree of alignment versus BPR. The value of degree of alignment decreased as BPR increased, which indicated the anisotropic behavior became weaker.

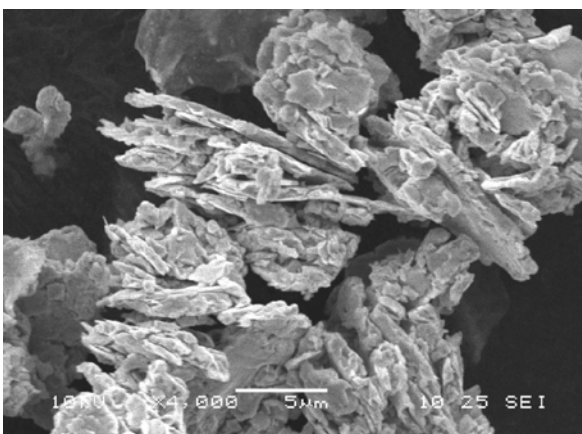
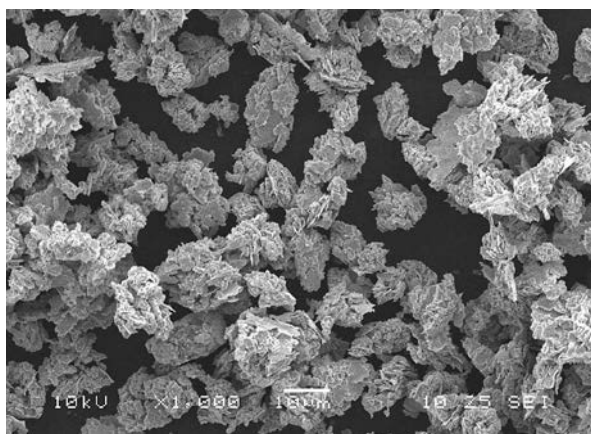
Figure 6.37 shows XRD patterns for Sm-Co/Fe composite powders milled with BPR of 0.8 along perpendicular and parallel to magnetically aligning direction (SmCo_5 patterns as reference). For the patterns along the direction perpendicular to the alignment field, peaks (001) and (002) increased and peak (111) decreased, which revealed the powder with a strong [001] out-of-plane texture. For the patterns along the parallel direction, peaks (110) and (200) increased and peak (111) decreased, and meanwhile, Fe peak (110) changed to relatively higher. The results demonstrated the particles show a strong anisotropic behavior. Figure 38 shows XRD patterns of Sm-Co/Fe particles milled with different BPR along the direction perpendicular to the alignment field. With increasing the ball to powder weight ratio from 0.8 to 10, the relative intensity of peak (002) decreased obviously. The I_{002}/I_{111} values are 5.28, 3.67, 1.94, and 1.82 for the BPR of 0.8, 1, 4, and 10, respectively. This indicated a decreased degree of structural anisotropy as the BPR increased. The results should be related with SmCo_5 crystalline changes in milling. For high energy ball milling, some defects such as dislocations can form during milling procedure [16, 17], and dislocation density increases with longer milling time or higher milling energy. As BPR increased, the finer particles (or thinner flakes) could form polycrystalline structure [18]. The polycrystalline nanoflakes will not carry out perfect rotation during magnetic alignment. So nanoscale powders milled with larger BPR had weaker anisotropy. Similar results were obtained for single phase SmCo_5 flakes [19].



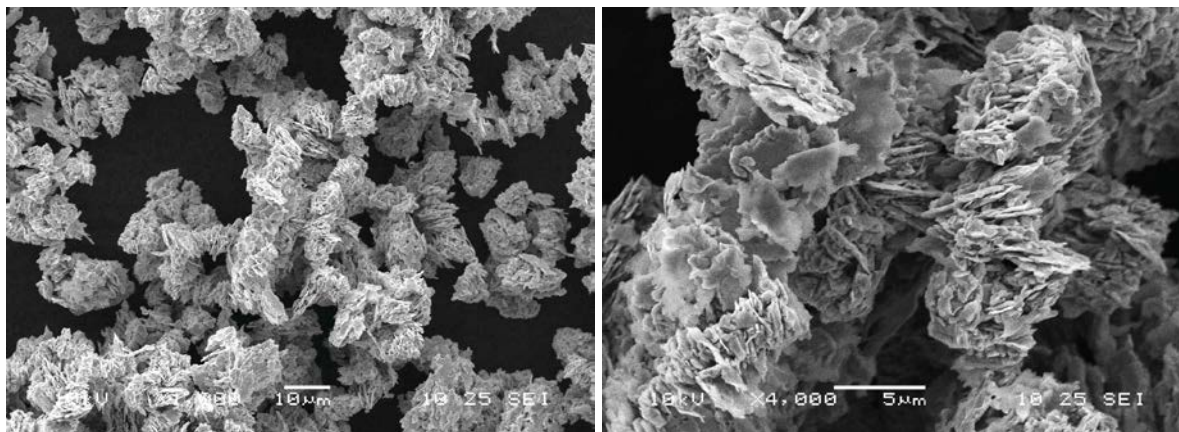
(a) BPR-0.8



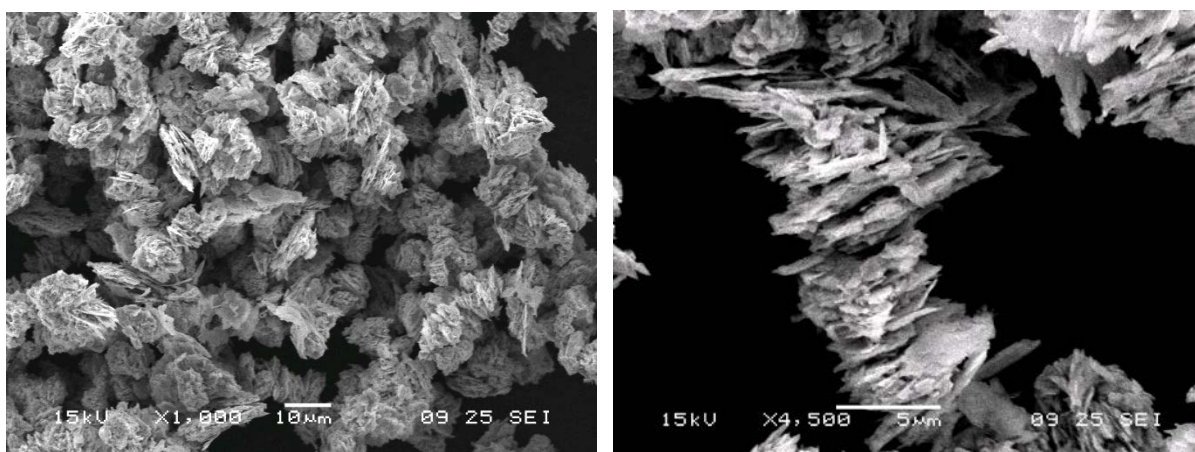
(b) BPR-1



(c) BPR-2

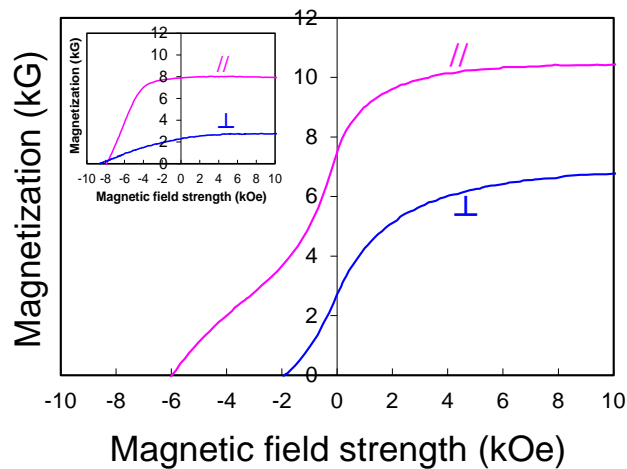


(d) BPR-4

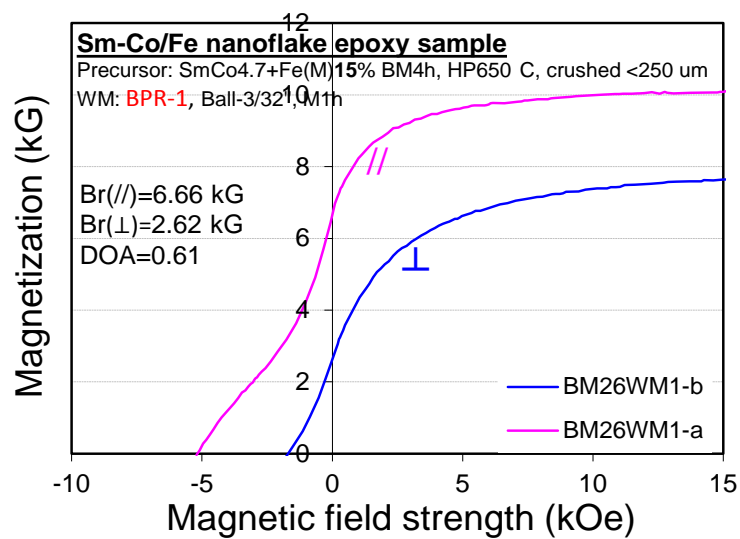


(a) BPR-10

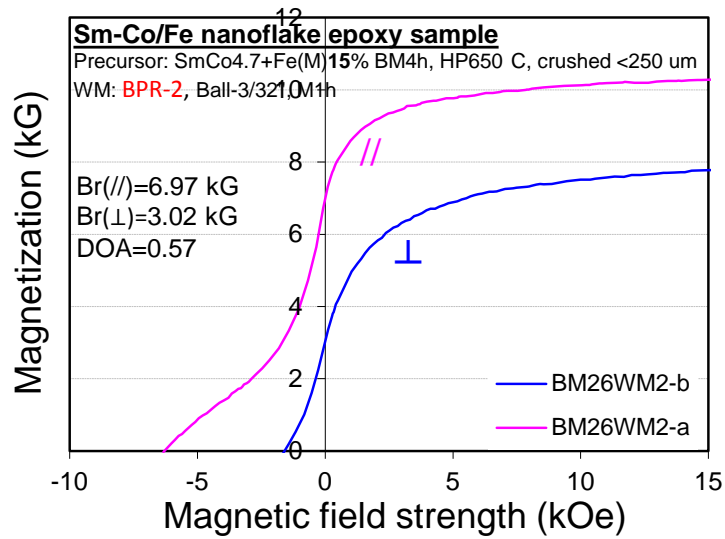
Figure 6.34. SEM images for Sm-Co/Fe composite particles milled 1h with different BPR by WM



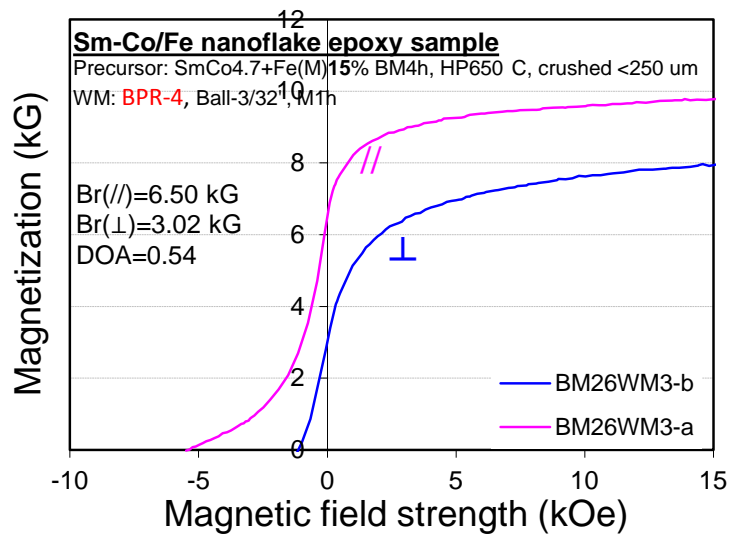
(a) BPR-0.8



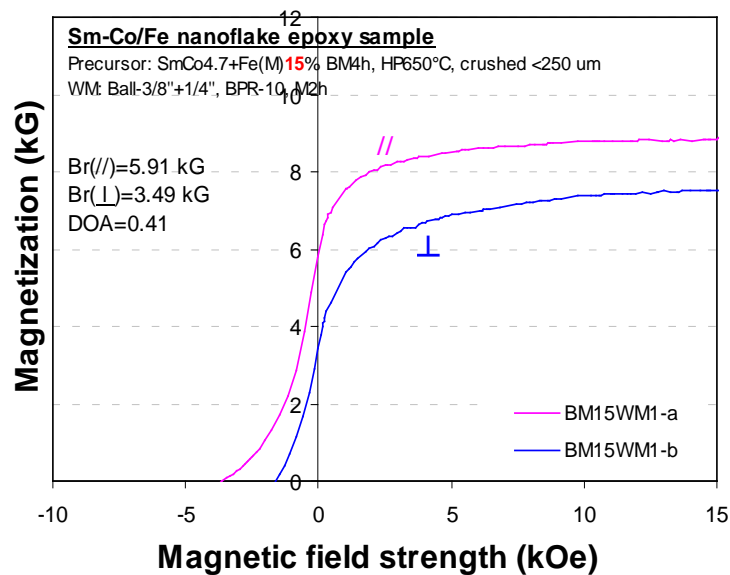
(b) BPR-1



(c) BPR-2



(d) BPR-4



(e) BPR-10

Figure 6.35. Demagnetization curves of Sm-Co/Fe powder epoxy samples tested along parallel (//) and perpendicular (⊥) to the magnetic aligning direction. (Insert is demagnetization curves of SmCo_5 particles prepared with same process)

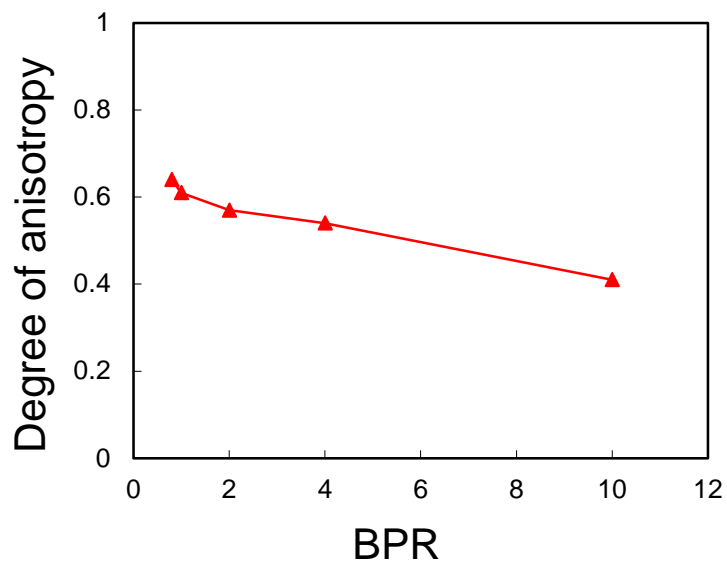


Figure 6.36. Dependence of degree of anisotropy of Sm-Co/Fe particles on BPR

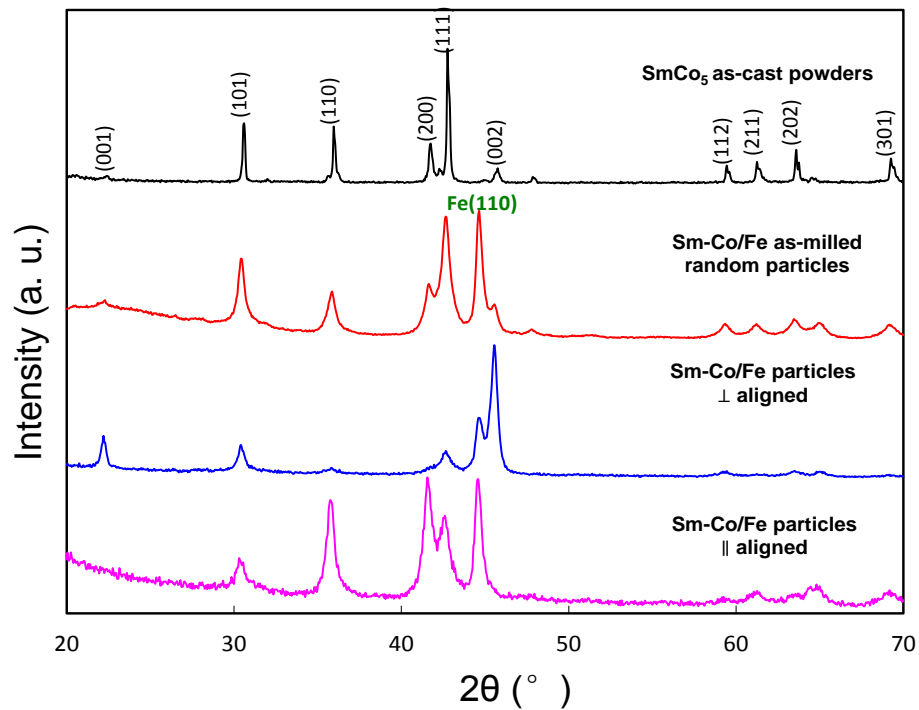


Figure 6.37. XRD patterns of SmCo₅ as-cast random powders, Sm-Co/Fe as-milled random powders and aligned powders prepared with BPR of 0.8 (\perp aligned – X-ray detected surface perpendicular to magnetic aligning direction; \parallel aligned – X-ray detected surface parallel to the magnetic aligning direction during epoxy sample preparation)

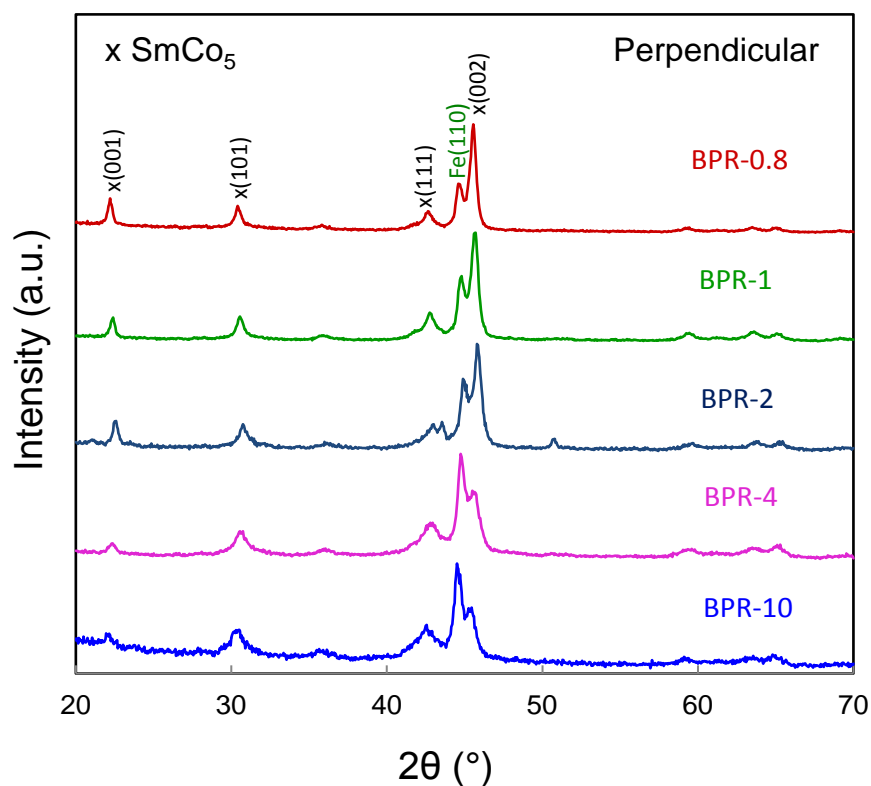


Figure 6.38. XRD patterns of Sm-Co/Fe powder (milled with different BPR) epoxy samples (X-ray detected surface perpendicular to magnetic aligning direction in epoxy sample preparation)

In summary, anisotropic Sm-Co/Fe composite particles were prepared by using isotropic bulk Sm-Co/Fe composite magnets as precursor and WM process. The crystalline structure and grain size of the starting composite (precursor) is the dominating factor for the attainable degree of anisotropy in milled composite particles. The nano-structured Sm-Co/Fe composite precursor resulted in particles with stronger exchange coupling and lower anisotropy, and the micron size composite precursor produced particles with higher magnetic anisotropy and weaker exchange coupling.

6.4 Summary

Bulk Sm-Co/Fe nanocomposite magnets were fabricated by hot pressing composite powders prepared by high energy ball milling of SmCo_5 powder and Fe powder. The bulk magnets had a nanocomposite structure consisting of Sm-Co matrix (1:5H and 1:7H phases) and Fe phases, and the soft phase particles were distributed uniformly in the Sm-Co matrix. This nanocomposite magnet increased 58% in maximum energy product compared to that of bulk single phase nanocrystalline SmCo_5 magnet prepared by the same process.

Anisotropic Sm-Co/Fe composite particles were prepared by surfactant-assisted high energy ball milling using isotropic Sm-Co/Fe bulks as precursors. The resulted composite particles had plate-like or flake-like shapes with the size of tens nm – 1 μm in thickness and 1 - 5 μm in width, depending on the precursor type and milling parameters. The nano-structured Sm-

Co/Fe precursor resulted in composite particles with lower anisotropy, and the micron size composite precursor produced particles with higher magnetic anisotropy.

6.5 References

- [1] S. D. Bader, *Rev. Mod. Phys.*, 78, 1 (2006).
- [2] R. Coehoorn, D. B. de Mooij, and C. de Waard, *J. Magn. Magn. Mater.*, 80, 101 (1989)
- [3] E. F. Kneller and R. Hawig, *IEEE Trans. Magn.*, 27, 3588 (1991).
- [4] R. Skomski and J. M. D. Coey, *Phys. Rev. B*, 48, 15812 (1993).
- [5] D. Lee, S. Bauser, A. Higgins, C. Chen, S. Liu, M. Q. Huang, Y. G. Peng, and D. E. Laughlin, *J. Appl. Phys.*, 99, 08B516 (2006).
- [6] A.M. Gabay, Y. Zhang, and G.C. Hadjipanayis, *J. Magn. Magn. Mater.*, 302, 244 (2006).
- [7] K. H. Chen, Z. Q. Jin, J. Li, G. Kennedy, Z. L. Wang, N. N. Thadhani, H. Zeng, S. F. Cheng, and J. P. Liu, *J. Appl. Phys.*, 96, 1276 (2004).
- [8] Q. Zeng, Y. Zhang, M. J. Bonder, G. C. Hadjipanayis, and R. Radhakrishnan, *IEEE Trans. Magn.*, 39, 2974 (2003).
- [9] T. Saito and H. Miyoshi, *J. Appl. Phys.*, 111, 07B534 (2012).
- [10] C. B. Rong, Y. Zhang, N. Poudyal, X. Xiong, M. J. Kramer, and J.P. Liu, *Appl. Phys. Lett.*, 96, 102513 (2010).
- [11] E. A. Nesbitt and J. H. Wernick, *Rear Earth Permanent Magnets*, Academic Press, Inc. (1973).
- [12] H. Saito, M Takahashi, T. Wakiyama, G. Kido, and H. Nakagawa, *J. Magn. Magn. Mater.* 82, 322 (1989).
- [13] B. Z. Cui, A. M. Gabay, W. F. Li, J. F. Liu, and G. C. Hadjipanayis, *J. Appl. Phys.*, 107, 09A721 (2010).
- [14] S. J. Knutson, Y. Shen, J. C. Horwath, P. Barnes, and C. H. Chen, *J. Appl. Phys.*, 109, 07A762 (2011).
- [15] E. P. Wohlfarth, K. H. J. Buschow, *Ferromagnetic materials: a handbook on the properties of magnetically ordered substances*, vol. 4. Amsterdam: Elsevier Science Publishers B. V. (1988).
- [16] H. J. Fecht, *Nanostruct. Mater.*, 6, 33 (1995).
- [17] L. S. Vasil'ev, S. F. Lomayeva, *J. Mater. Sci.*, 39, 5411 (2004).
- [18] B. Z. Cui, W. F. Li, G. C. Hadjipanayis, *Acta Mater.*, 59, 563 (2011).
- [19] C. H. Chen, S. J. Knutson, Y. Shen, R. A. Wheeler, J. C. Horwath, *Appl. Phys. Lett.*, 99, 012504 (2011).

7. Development of Hard-Soft Bulk Nanocomposite Magnets

7.1 Introduction

Uprising need for higher performance and improved reliability of future air and space vehicles for the AF mission requires development of new more efficient and lightweight mechanical and electrical components able to function well at adverse conditions such as elevated temperatures and high mechanical stresses. Permanent magnets play the key role in design of power conversion and energy generating units used in military aircraft, therefore magnetic materials with superior properties to the current state-of-art magnets are required.

Performance of a permanent magnet is characterized by its maximum energy product $(BH)_{\max}$, which depends on the magnetic coercivity and saturation magnetization of the material. Development of a magnet with higher BH_{\max} product will lead to the increased performance as well as reduced size and weight of the essential aircraft components. Magnetic materials retain their properties within certain temperature range limited by the Curie temperature T_C , which is specific for each material composition. Expanding the working temperature range by engineering new materials exhibiting higher T_C will result in prolonged lifetime and improved reliability of the magnetic components of the aircraft. In addition, such materials with better temperature stability will require less power and service equipment used for the component cooling.

In the past several decades the primary materials for permanent magnet manufacturing were $\text{Sm}_2\text{Co}_{17}$ -based and $\text{Nd}_2\text{Fe}_{14}\text{B}$ -based alloys owing to their superior magnetic strength originating from intrinsic anisotropy of the crystal lattice. Maximum energy products $(BH)_{\max}$ of 31 MgOe and 59 MGOe have been achieved in $\text{Sm}_2\text{Co}_{17}$ and $\text{Nd}_2\text{Fe}_{14}\text{B}$ systems respectively by optimization of the chemical composition and metal grain structure. However, these numbers are approaching the corresponding theoretical energy product limits of 39 and 64 MGOe for $\text{Sm}_2\text{Co}_{17}$ and $\text{Nd}_2\text{Fe}_{14}\text{B}$, therefore in order to meet the higher performance requirements new classes of permanent magnet materials have to be studied and developed.

A promising new class of permanent magnets is an exchange-coupled nanocomposite material, which consists of two ‘hard’ (high coercivity) and ‘soft’ (large saturation moment) magnetic phases suitably dispersed on the scale of tens of nanometers. Such composite material will benefit from both high magnetocrystalline anisotropy of the hard phase and large magnetic saturation of the soft phase leading to significant enhancement of the $(BH)_{\max}$ energy product compared to the individual phases. Since the soft phase is usually a FeCo-based composition an additional advantage is the reduces overall amount of rare-earth metal, and therefore cost, needed to prepare the composite material due to smaller volume fraction of the RE-rich hard phase. Theoretical calculations on nanograin exchange-coupled magnets predict values of $(BH)_{\max}$ up to 94 MGOe, 75 MGOe and 65 MGOe for $\text{Nd}_2\text{Fe}_{14}\text{B}/\text{Fe}_{65}\text{Co}_{35}$, $\text{Sm}_2\text{Co}_{17}/\text{Fe}_{65}\text{Co}_{35}$ and $\text{SmCo}_5/\text{Fe}_{65}\text{Co}_{35}$ nanocomposite magnets with 40 wt% of the $\text{Fe}_{65}\text{Co}_{35}$ soft phase, which indicate a 1.5-2 times increase in $(BH)_{\max}$ compared to single phase $\text{Nd}_2\text{Fe}_{14}\text{B}$ or Sm-Co alloys.

7.2 Experimental

In order to obtain high energy product material the bulk magnetically hard/soft nanocomposite magnet should meet a number of requirements: (1) the nanocomposite phases homogenously distributed with the grain size on order of 10 nm; (2) both the hard and soft phases crystallographically coherent as a necessary condition for mutual exchange coupling; (3) anisotropic bulk magnet structure; and (4) full bulk density.

In recent years, magnetic powder with anisotropic flake particle morphology and flake thickness on order of few tens nanometers were made by surfactant-assisted high energy ball milling (HEBM) of magnetic alloys prepared by melt-spinning or arc melting techniques. Flake shape and thickness can be controlled by varying the milling process parameters such as weight ratio between powder, surfactant and ball media, milling time etc. The main difficulty with this process is the surfactant removal from the milled powder, which requires heat treatment at temperatures above the surfactant boiling point. At elevated temperature interdiffusion can occur between powder particles leading to larger particle size. In order to avoid unwanted grain growth during the heat treatment surfactants with lower molecular weight, and therefore lower boiling point, can be used. Alternative methods such as CO₂-assisted leaching can also be employed.

Nanoflake appearance of the milled powder is highly beneficial for fabrication of anisotropic bulk magnets using the powder magnetic alignment techniques. High energy ball milling carried out in a constant magnetic field created by permanent magnets placed around the milling jar as well as pulse magnetizing immediately prior to powder compaction will result in better grain alignment and anisotropic properties of the final bulk magnet.

Nanopowder compaction is another challenge since in conventional hot isostatic pressing (HIP) prolonged heat treatments at high temperatures will result in the grain growth and loss of nanoscale microstructure, while compaction at lower temperatures may not produce the full density bulk. An alternative method of shockwave metal powder consolidation resulting in nearly 100% dense bulk and minimum grain growth has been practiced in the past. In this method a powder sample is confined inside a metal capsule, which is impacted by a high-velocity projectile. The impact-generated shockwave delivers energy to the powder plastically deforming the particles and compacting it into a bulk sample. The shockwave propagation time is on order of nanoseconds, which is insufficient for interdiffusion and grain growth to take place, therefore the nanostructure of the magnetic material is preserved.

Exchange-coupled nanocomposite magnetic materials are a promising new class for development of high energy bulk permanent magnets. Nanoscale combination of magnetically hard phase (Nd₂Fe₁₄B, SmCo₅, Sm₂Co₁₇) with high coercivity and magnetically soft phase (Fe, FeCo) with large saturation moment will produce a composite material superior to the current state-of-art magnets in terms of maximum energy product (BH)_{max}.

Fabrication of such material requires preparation of nanoscale powder, its magnetic alignment and subsequent consolidation. Powder preparation will be realized by arc melting of the necessary alloy ingots, crushing the ingots into microscale coarse powder followed by surfactant-assisted high energy ball milling in order to achieve nanoscale particle size. Low molecular weight valeric acid will be used as a surfactant to reduce temperature needed for the surfactant removal. Hypervelocity impact powder compaction technique will be developed in collaboration with a local research facility. Powder capsule, projectile, target will be designed and machined for the impaction experiment. Crystal structure and grain morphology characterization will be carried out on the compacted bulk magnets using x-ray diffraction, transmission and scanning electron microscopy (SEM). Magnetic properties such as coercive field, remnant and saturation magnetic moments, maximum energy product will be measured and compared to the corresponding single phase materials.

7.3 Results and Discussion

7.3.1 *SmCo₅ Nano-flake Powder Preparation via Wet Milling Route using Oleic Acid Surfactant*

7.3.1.1 Objectives

The objective for this project were to (1) Prepare nano-scale SmCo₅ powder via surfactant assisted wet milling technique; and to (2) Characterize powder morphology using SEM and compare it between powders obtained at different milling conditions.

7.3.1.2 Experiments and Results

SmCo₅ powder batches were prepared using the following parameters: powder mass 5g, milling balls 3/32" 4g, solvent heptanes 2.75g, surfactant oleic acid 1.5g. Different milling times of 1, 2, 4 and 8 hours were used for batches #2-2, #2-4, #2-3 and #2-5, respectively, as depicted in Figure 7.1. After milling, powders were washed in acetone and vacuum-dried for 1 hour. Figure 7.2 (a-d) shows the SEM micrographs collected on the Quanta 1 and Quanta 2 instruments at 10kV and 30μm aperture.

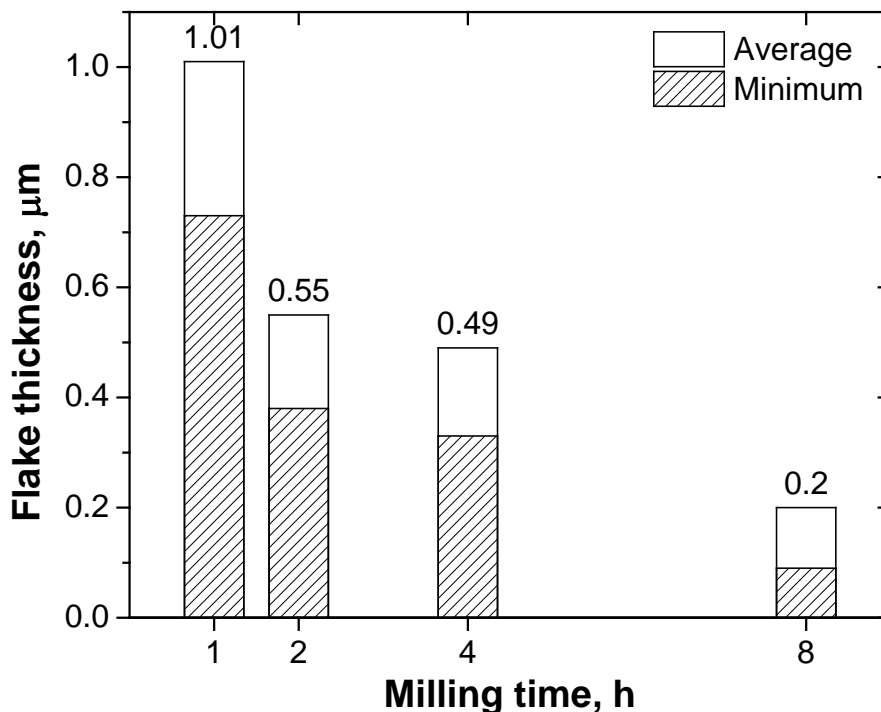
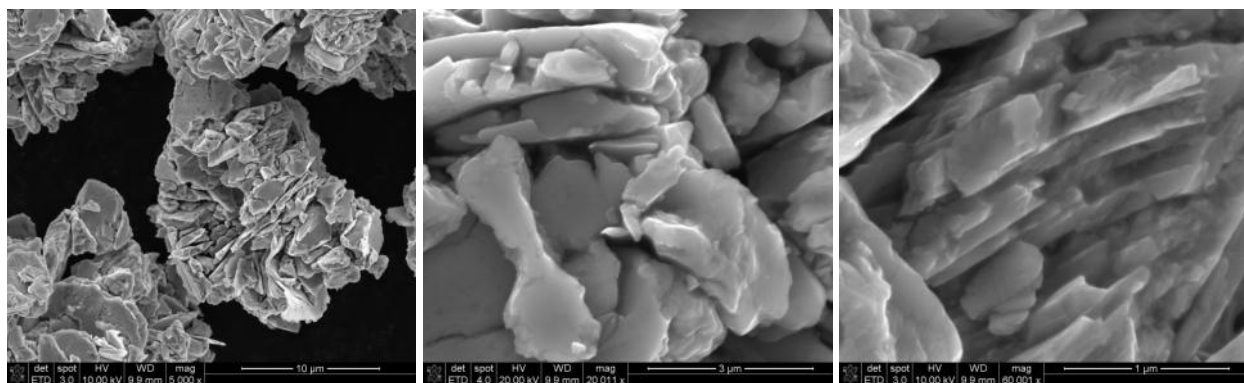
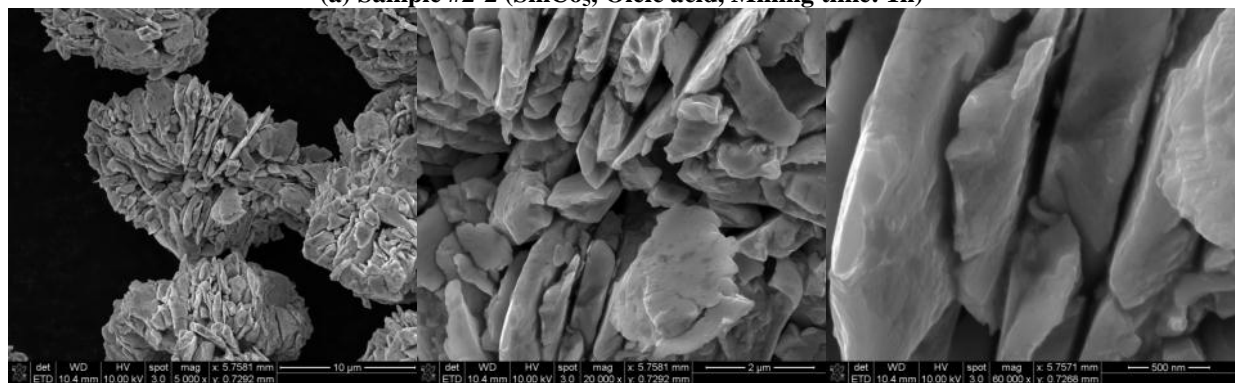


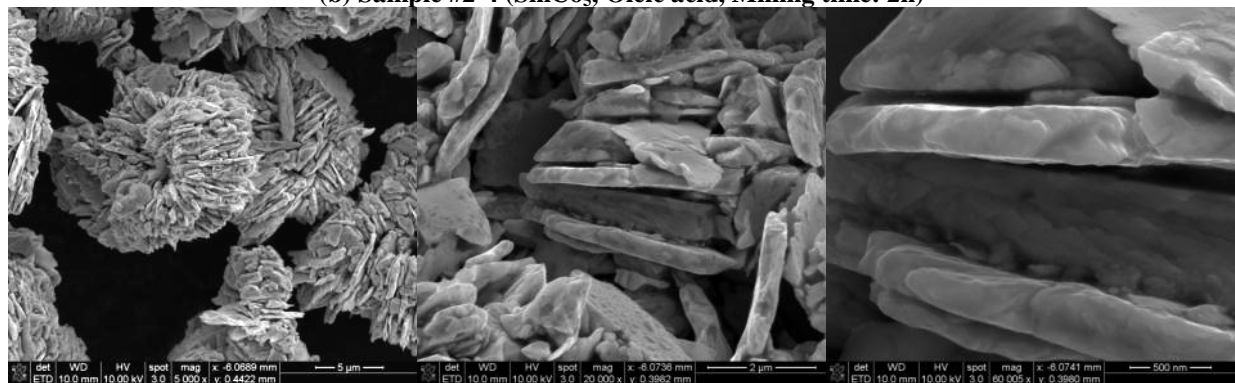
Figure 7.1. Powder flake thickness dependence on the milling time



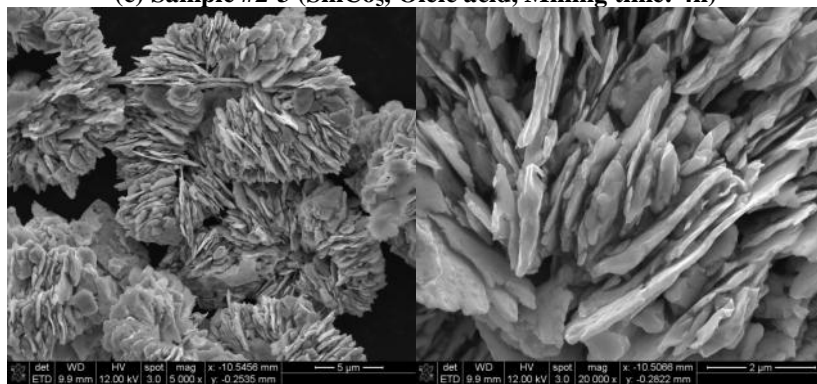
(a) Sample #2-2 (SmCo₅, Oleic acid, Milling time: 1h)



(b) Sample #2-4 (SmCo₅, Oleic acid, Milling time: 2h)



(c) Sample #2-3 (SmCo₅, Oleic acid, Milling time: 4h)



(d) Sample #2-5 (SmCo₅, Oleic acid, Milling time: 8h)

Figure 7.2. SEM micrographs for SmCo₅ powder batches

7.3.1.3 Summary

SEM imaging showed flake-like morphology of the milled powder. Flake thickness strongly depends on the milling time, ranging from 1010 nm (1h) to 200 nm (8h). Flake lateral dimensions are on order of 1-3 μ m and decrease slightly with longer milling times.

7.3.2 *SmCo₅ Nano-flake Powder Preparation via Wet Milling Route using Valeric Acid Surfactant*

7.3.2.1 Objectives

The objectives for this study were to: (1) Prepare nano-scale SmCo₅ powder via surfactant assisted wet milling technique using Valeric acid; (2) Study the differential scanning calorimetry (DSC) response and estimate a temperature range for surfactant removal heat treatment; and (3) Characterize powder morphology using SEM and compare between powders obtained at different milling times.

7.3.2.2 Experiments and Results

SmCo₅ powder batches were prepared using the following parameters: powder mass 5g, milling balls 1/8" 20g, solvent heptanes 2.75g, surfactant valeric acid 1.5g. Different milling times of 1, 2, 4 and 8 hours were used for batches #3-2, #3-3, #3-1 and #3-4, respectively. After milling, powders were washed in acetone and vacuum-dried for 20 minutes.

DSC data, shown in Figure 7.3 (left panel) was collected on the dried powder in the range 30-600 °C at a heat rate of 20 °C/sec. For comparison, the powder flake thickness dependence on the milling time is shown in the right panel of Figure 7.3. Samples before and after DSC (held at 600 °C for 5 minutes) were imaged with SEM on Quanta 2 instrument at 10kV and 30 μ m aperture, and are shown in Figures 7.4 (a-d).

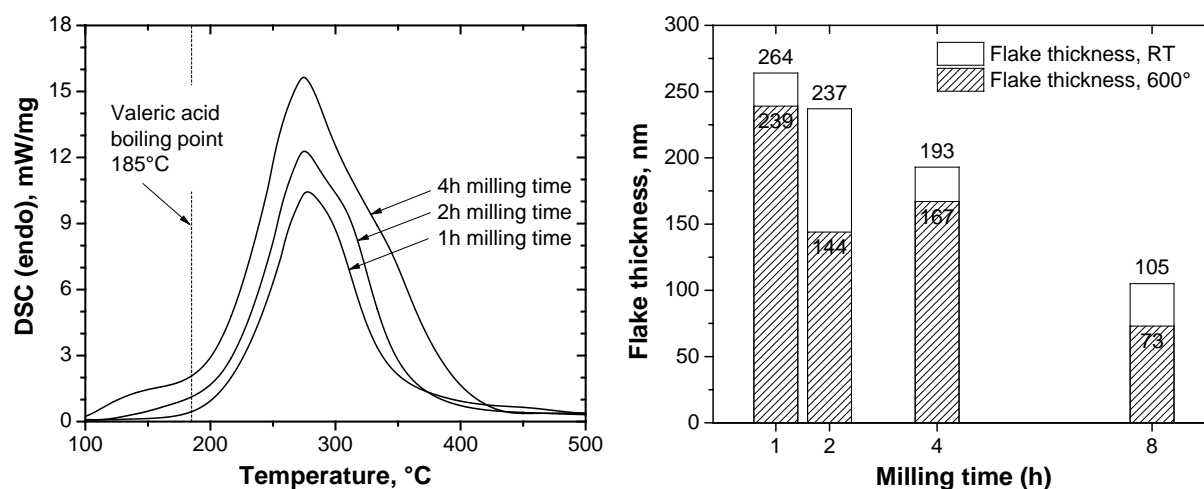
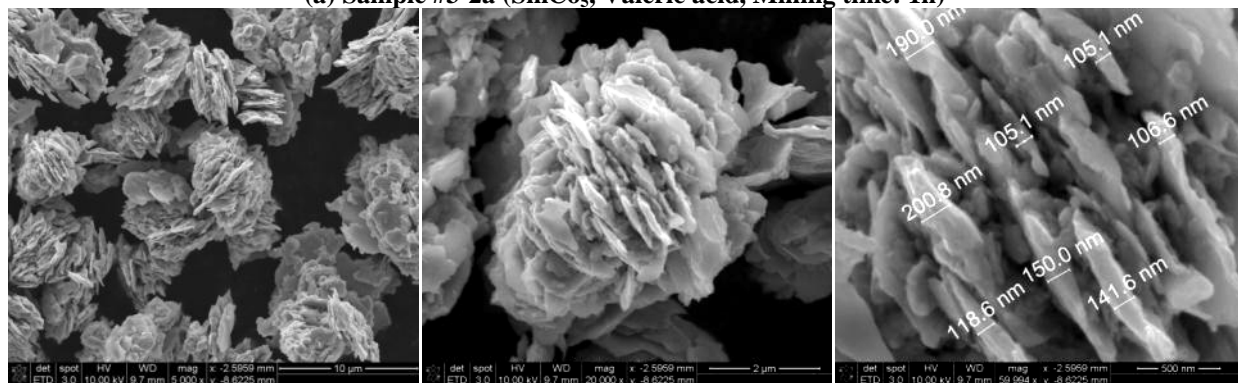


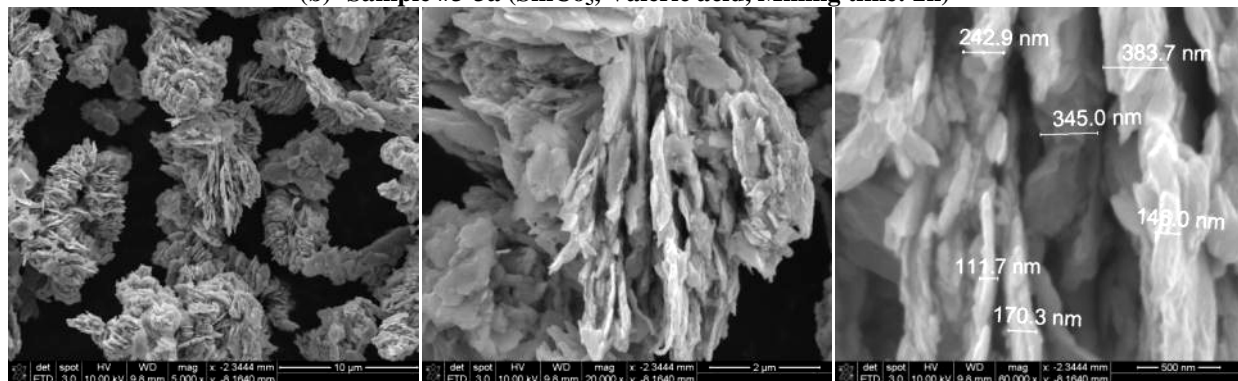
Figure 7.3. (Left) DSC data. (Right) Powder flake thickness dependence on the milling time



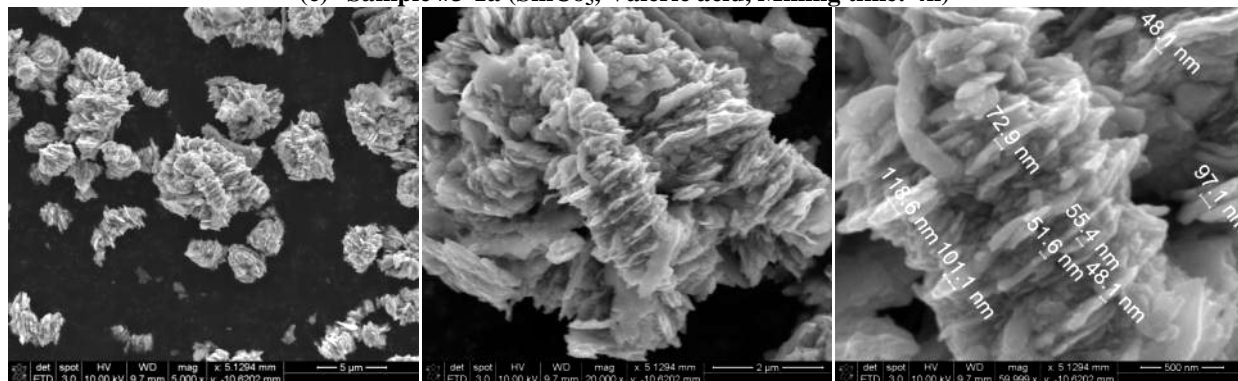
(a) Sample #3-2a (SmCo_5 , Valeric acid, Milling time: 1h)



(b) Sample #3-3a (SmCo_5 , Valeric acid, Milling time: 2h)



(c) Sample #3-1a (SmCo_5 , Valeric acid, Milling time: 4h)



(d) Sample #3-4a (SmCo_5 , Valeric acid, Milling time: 8h)

Figure 7.4. SEM micrographs for SmCo_5 powder batches before and after DSC tests

7.3.2.3 Summary

DSC showed evaporation of Valeric acid starting at 200 °C, stronger heat flow for longer milling time samples is due to larger surface area of the powder. Sample milled for 8h needs more investigation. SEM imaging showed flake-like morphology of the milled powder. Flake thickness depends on the milling time, ranging from 260 nm (1h) to 100 nm (8h). Flake lateral dimensions are on order of 1-3µm and decrease slightly with longer milling times. After heat treatment no significant particle sintering was observed. Sample for 8h became cleaner (mass loss 6%), while other samples look similar to untreated (mass loss ~0.5%).

7.3.3 *Surfactant Removal Study for Nanoscale SmCo₅ Powder Prepared by High Energy Ball Milling*

7.3.3.1 Introduction

Surfactant-assisted high energy ball milling (HEBM) has become a viable tool for production of various micro- and nano-scale powders used in a wide range of materials science applications. For magnetic alloys, HEBM is employed as a method for preparation of nano-scale anisotropic rare-earth magnetic powders with controlled particle size and morphology [1]-[7]. Final powder particle properties depend on the milling process parameters such as milling time, ball-to-powder mass ratio, and, most critically, choice and the relative amount of the surfactant [8]-[10]. During the milling process surfactant molecules adhere to the freshly exposed particle surface creating a thin organic layer. This layer protects the particles from mechanical alloying when they come in contact with each other further in the milling process. Organic fatty acids are typically used as surfactants; their molecules contain carboxylic functional components which form carboxylate bonds with the metal surface and long molecular chains which create an electrostatic barrier for the surrounding powder particles. Recently, surfactant-assisted HEBM has been used in preparation of nanostructured SmCo₅ magnetic powders with anisotropic flake-like morphology and particle thickness below 100 nm [4], [6], [11], [12].

Surfactants play an essential role in HEBM process, however, they often need to be removed after milling and prior to a powder consolidation step. The presence of surfactant during powder sintering or hot pressing may result in organic material decomposition or reaction with the base metal alloy producing impurities in the final product. Typically surfactant removal is achieved through a vacuum annealing process which requires relatively high temperatures and long dwelling times. Such thermal conditions are undesirable for treatment of nanostructured powders, since exposure to elevated temperatures results in grain growth and oxidation [9], [13]. A recent study has shown that heat treatment temperature depends on surfactant molecular weight (MW) and it can be reduced by using surfactants with shorter molecular chains. Oleic acid (OA) is the most commonly used surfactant reported in the literature for preparation of SmCo₅ nano-flake powders [6], [7], [9], [12]. Due to its chemical interaction with the metal, temperatures above 500°C under atmospheric conditions are required for OA removal (OA boiling point is 360°C, MW = 282 g/mol). A lower molecular weight surfactant such as valeric acid (VA, boiling point 185°C, MW = 102 g/mol) would require a less aggressive heat treatment and may be more suitable for SmCo₅ alloy powder processing [10].

In the present work SmCo₅ nano-flake magnetic powder were prepared by HEBM using valeric acid. Different annealing conditions for surfactant removal were investigated. The effect

of the heat treatment has been evaluated by estimation of residual surfactant content and magnetic property comparison between the as-milled and treated SmCo_5 .

7.3.3.2 Experimental

Pure Sm and pure Co were combined in a 1:5 atomic ratio and arc melted into a SmCo_5 alloy button in Ar atmosphere. The button was mechanically crushed into coarse powder (particle size under $250\text{ }\mu\text{m}$) which was used as the starting material for high energy ball milling. For HEBM the SmCo_5 powder (5 g), milling balls ($1/8''$ diameter, hardened stainless steel, 20 g, 152 balls), vehicle (heptane, 2.75 g, Acros Organics) and surfactant (valeric acid, 1.5 g, Aldrich) were combined and sealed under Ar atmosphere in a stainless steel jar and milled in a SPEX 8000D vibratory mill for 1 hour. After milling the powders were rinsed with acetone, vacuum dried and separated from the ball media.

The as-milled SmCo_5 powders were heat treated at two different temperatures: 200°C and 400°C . In order to avoid oxidation an argon atmosphere was used at a pressure slightly above atmospheric (800 Torr); treatment in air was also conducted (at pressure ~ 1 Torr) for comparison. Relative contents of residual surfactant were compared by DSC analysis, Perkin Elmer DSC 8000, temperature range $30\text{--}600^\circ\text{C}$, heat rate $20^\circ/\text{min}$, in flowing high-purity Ar. The presence of metal oxides and primary SmCo_5 phase were evaluated by X-ray diffraction data collected on beamline 33-BM-C [14] at the Advanced Photon Source of Argonne National Laboratory, using x-ray radiation with wavelength $\lambda=0.0589605\text{ nm}$. Measurements were performed on powder samples mounted in quartz capillaries and using a curved image plate detector in the 2θ angular range $3.5\text{--}35.5^\circ$; additional procedure details are described in [15]. Powder morphology before and after heat treatment was investigated with SEM, FEI Quanta ESEM. For magnetic property measurements SmCo_5 powders were combined with an epoxy resin (80% powder, 20% epoxy by mass), pulse magnetized in a 10 T magnetic field, and set for curing between permanent magnets in a field $\sim 1\text{ T}$ for 24 hours. A KJS Associates closed-loop hysteresisgraph (model MG-700) was used to measure magnetic behavior of the cured samples and determine magnetic coercivity H_{ci} , remanence B_r and maximum energy product $(BH)_{\text{max}}$.

7.3.3.3 Results and Discussion

SEM imaging of the as-milled and heat treated SmCo_5 powders prepared by HEBM using valeric acid, shown in Figure 7.5, revealed a highly anisotropic flake-like morphology with flake sizes in the range $1\text{--}5\text{ }\mu\text{m}$ wide and $200\text{--}600\text{ nm}$ thick. Formation of flake-shaped particles is consistent with previous experiments [4]–[7] and is facilitated by the presence of the surfactant during HEBM. A preliminary study has also been conducted to determine effect of milling time on the SmCo_5 nano-flake thickness. The selected time of 1h produced $200\text{--}600\text{ nm}$ flakes which according to [7] results in relatively high energy product $(BH)_{\text{max}}$. The flake dimensions are also in agreement with previous reports using oleic acid as a surfactant. However, no study of relation between milling parameters and final powder morphology for the case of valeric acid has been done.

Comparisons between SEM images of the untreated powders and treated at 200°C and 400°C (both in Ar and Air atmospheres) did not show any visible differences in the powder morphology, even though an onset of particle coagulation was expected after the heat treatment. Presence of the organic surfactant in the as-milled powder was indirectly evidenced by minor charging during SEM raster due to lower powder surface conductivity. TEM imaging would be

more suitable for a detailed particle surface analysis and estimation of the surfactant layer thickness.

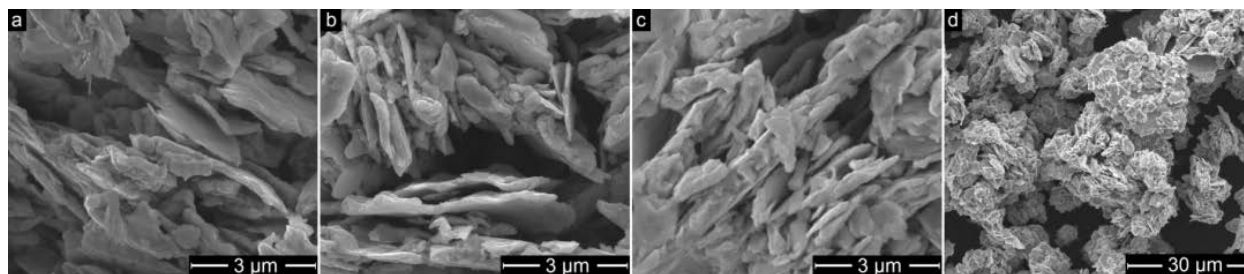


Figure 7.5. SEM images of as-milled (a), heat treated in argon at 200 °C (b) and 400 °C (c) SmCo₅ nano-flake powders prepared by HEBM using valeric acid; clusters of SmCo₅ nano-flakes (d)

Residual surfactant content was estimated from DSC analysis with the data shown in Figure 7.6. For the as-milled powder a large endothermic peak with an onset near the valeric acid boiling temperature (185°C) indicated the presence of the surfactant. Powders heat treated in Ar exhibit similar peaks but with the peak area decreasing for higher dwell temperatures, which is evidence of a reduced amount of the surfactant. In addition, the peak onset temperature shifts toward higher values suggesting stronger bonding of the valeric acid to the metal particles as the surfactant layer becomes thinner. Detailed peak area comparison showed partial (58%) and nearly complete (96%) surfactant removal after treatment in Ar at 200°C and 400°C respectively. Treatment in air at reduced pressure resulted in full surfactant removal; no DSC peak from valeric acid was observed after either dwell temperatures. This can be attributed to the reduced boiling point of the surfactant due to lower air pressure (1 torr) than Ar (800 torr) during annealing. Also the presence of oxygen facilitates organic surfactant decomposition in addition to evaporation.

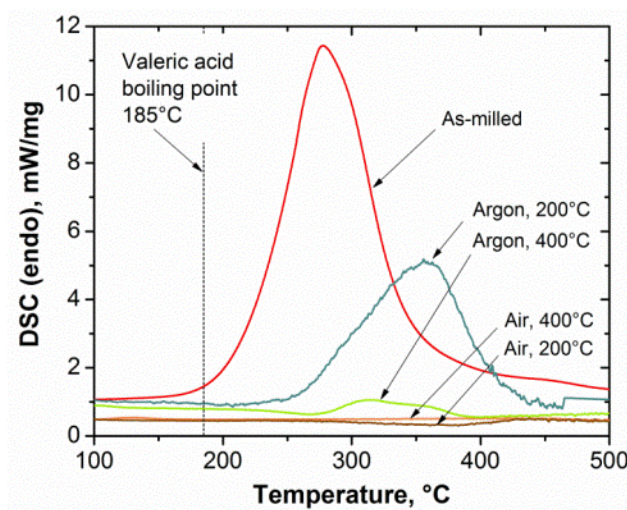


Figure 7.6. DSC heat flow (heating) for as-milled and heat treated SmCo₅ nano-powders

Exposing SmCo_5 powder to air at elevated temperatures resulted in oxidation as indicated by CoO , Co_3O_4 and Sm_2O_3 oxide XRD peaks as shown in Figure 7.7. The oxide peaks progressively become sharper and more pronounced corresponding to larger metal oxide volume fraction and crystallite size formed after annealing at higher temperature. Note that the initial SmCo_5 phase was not detected among the metal oxides, which is discussed later in the text. On the other hand, no oxide formation was observed after treatment in Ar, which confirms that excess Ar pressure is highly effective in preventing oxygen access to the powder and avoiding alloy oxidation.

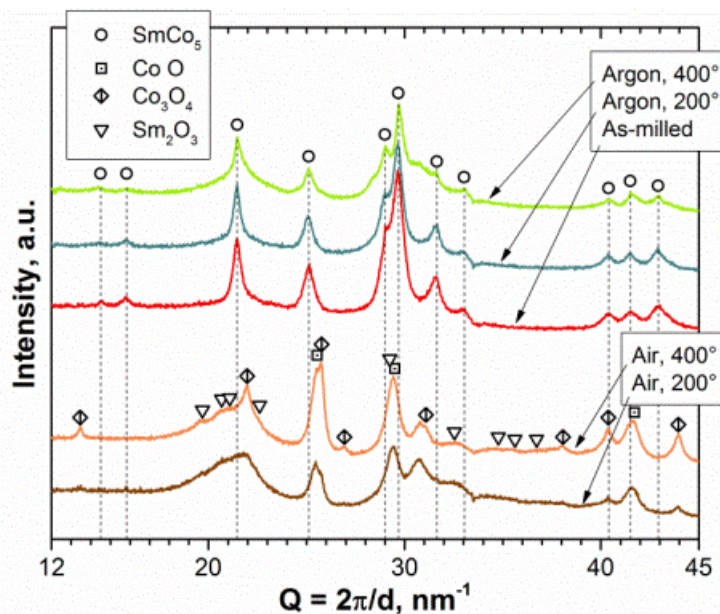


Figure 7.7. Powder x-ray diffraction data for as-milled and heat treated SmCo_5 nano-scale powder

Demagnetization data for all heat treated and as-milled SmCo_5 powders are shown in Figure 7.8. The heat treatment at 200°C results in significant reduction of the maximum energy product $(\text{BH})_{\text{max}}$ to 1.7 MGOe down from 5.3 MGOe (see Figure 7.8 inset table), which is further degraded after treatment at 400°C to 0.3 MGOe. Strong suppression of the $M(H)$ curve squareness and appearance of a slope change around $H \sim 3$ kOe after annealing at 200°C suggests gradual development of a SmCo_5 volume fraction with much lower coercivity H_{ci} than the initial untreated SmCo_5 . This fraction is further expanded to the full SmCo_5 volume after 400°C treatment leading to overall deterioration of H_{ci} and $(\text{BH})_{\text{max}}$. As shown in previous reports the coercivity of SmCo_5 nano-flake powders strongly depends on the particle thickness [7], [16] reaching its maximum of 20 kOe for 180 nm flakes. In the present study the average thickness of SmCo_5 flakes is around 300 nm and measured coercivity for the untreated samples $H_{\text{ci}} = 18$ kOe agrees well with the above reference. Particle growth would be the first choice to explain the decrease in magnetic coercivity, however, according to SEM no significant particle sintering or merging were observed. Moreover, even micron thick flakes produced by HEBM still exhibit H_{ci} around 10 kOe [16], while a decrease in H_{ci} by a factor of 15-20 is observed after the heat treatment in the present 300 nm powder. Therefore it was assumed that the coercivity

mechanism is strongly related to the specifics of the ball milling process and structural dynamics within individual particles during annealing.

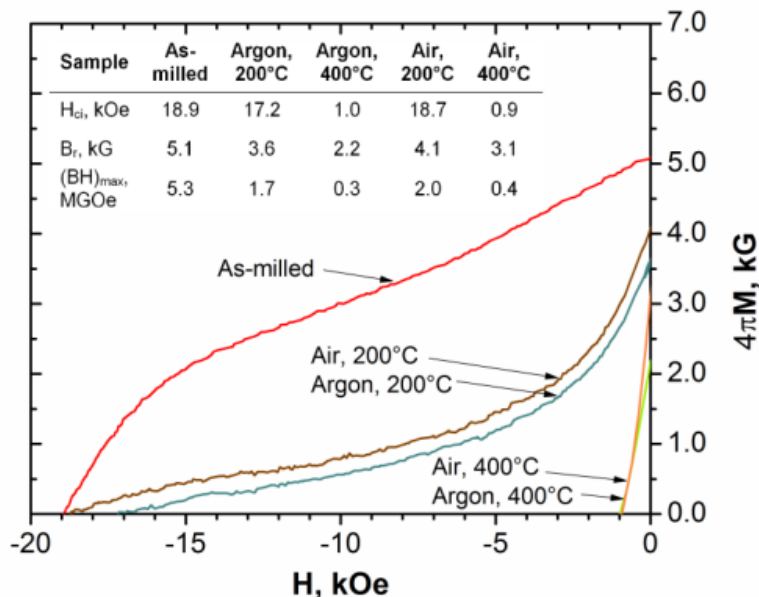


Figure 7.8. Demagnetization data for epoxy bound as-milled and heat treated SmCo₅ nano-powders. Inset table: coercivity H_{ci} , remanence B_r and maximum energy product $(BH)_{max}$

There are several factors affecting the coercivity in SmCo₅ powders. Magnetization reversal process is strongly related to the magnetic domain nucleation and domain wall motion. In a defect-free single domain particle magnetization reversal would require cooperative rotation of all magnetic spin moments producing the highest coercivity due to strong magnetocrystalline anisotropy of SmCo₅ [17]. However, the coercivity decreases dramatically with the presence of domain nucleation sites such as structural defects, chemical impurities, surface edges etc. most of which concentrate close to the particle surface. On the other hand, similar defects within the bulk of the particles serve as domain wall pinning centers inhibiting domain wall propagation through the particle thus enhancing its coercivity [18]-[20]. As a result of the ball milling process large amounts of both surface and bulk defects are produced in SmCo₅ powder giving the resultant H_{ci} values.

It has been shown in literature that lower coercivities in SmCo₅ powders were observed with aging or annealing due to decrease in concentration of bulk domain wall pinning centers [18]. Additionally, surfactant reacting with SmCo₅ at elevated temperatures creates chemical uniformities on particle surfaces thus increasing domain nucleation site concentration and further degrading the coercivity. It is believed both above mechanisms contribute to the strong suppression of $(BH)_{max}$ in the present heat treated SmCo₅ nano-powders.

An attempt was made to estimate SmCo₅ average grain size from the XRD peak geometry using Scherrer's equation [21]:

$$Size = \frac{k \cdot \lambda}{\cos(\theta) * (FWHM)},$$

where λ is the x-ray wavelength, k is a shape factor, 2θ is the peak center position, and $FWHM$ is peak width. Gaussian and Lorentzian equations were used to fit several peaks and the average grain size was calculated as 10.3 ± 1.7 nm, 11.2 ± 1.5 nm and 9.5 ± 3.4 nm for untreated, treated at 200 °C and 400 °C powders respectively. These results do not show a trend in grain growth.

Interestingly enough, the difference between magnetic response, namely in $(BH)_{\max}$ energy product, for SmCo_5 samples treated in Ar and air is relatively small (around 20%) compared to the effect of the annealing temperature (by a factor of 3-4) despite heavy oxidation in air-treated SmCo_5 (Figure 7.7). Taking into account that slight variation in measured remanence B_r and coercivity H_{ci} between samples is expected due to some inconsistency in sample preparation steps we assumed $M(H)$ data (Figure 7.8) for air and Ar-treated SmCo_5 are approximately the same with no significant atmosphere effect.

Such a result indicates a contradiction: the SmCo_5 phase was not observed in the air-treated powder, but its magnetic response is very close to the unoxidized SmCo_5 annealed in Ar at the corresponding temperature. Initially we assumed only an insignificant fraction of SmCo_5 transformed into an oxide forming a thin layer on particle surfaces without affecting magnetic response but masking the underlying non-oxidized phase from detection by XRD. The x-ray attenuation length in SmCo_5 is under 10 μm for the beamline photon energy (21 keV) and incidence angles ($2\theta = 3.5\text{-}25^\circ$) used in this study [22] and the information depth is on the order of several microns. This depth is much larger than average powder flake thickness (~ 300 nm) and is comparable with the flake lateral dimensions (1-5 μm). In this case absence of the initial SmCo_5 phase peaks would imply complete particle oxidation without a remaining SmCo_5 core, which contradicts the magnetic response data. Alternatively it is suggested that flake agglomeration into clusters (Figure 7.5 (d)) due to magnetostatic interaction results in a large amount of the SmCo_5 protected from exposure to oxygen at the cost of oxidation of a few outer cluster flake layers. For the observed cluster size of 5-30 μm this assumption qualitatively agrees with the XRD and demagnetization results, however, additional investigations such as neutron diffraction and TEM are needed for better understanding of the metal oxide presence in the heat treated SmCo_5 powders.

7.3.3.4 Summary

Nano-flake SmCo_5 powders were prepared by surfactant-assisted high energy ball milling using a low molecular weight valeric acid surfactant. Final powder morphology showed flake shape and dimensions (width 1-5 μm and thickness 200-600 nm) similar to previously prepared powders using conventional oleic acid. A heat treatment approach for the surfactant removal was investigated. Annealing at 200°C and 400°C in argon resulted in partial (58%) and nearly complete (96%) valeric acid removal and avoided powder oxidation. However, the magnetic energy product $(BH)_{\max}$ strongly degraded from 5.3 (as-milled) to 1.7 (200°C) and 0.3 MGOe (400°C) after the heat treatment, which was attributed to suppressed coercivity due to generation of domain nucleation sites (surface defects) and reduced concentration of domain wall pinning centers (bulk defects) within individual flakes. Annealing in air has led to complete surfactant removal but also thin surface oxide layer formation, which did not significantly affect the magnetic properties.

In summary, the results of the present study indicate that even a modest heat treatment of SmCo_5 nano-powder prepared by HEBM severely degrades its magnetic properties regardless of the atmosphere. The heat treatment process is not suitable for surfactant removal and either

alternative methods must be considered, or the surfactant must remain during further powder processing.

7.3.4 UDRI Gas Gun Target Fixture Design

7.3.4.1 Introduction

The objective for this task was to design a target assembly for hypervelocity powder compaction experiment at UDRI's gas gun facility. In order to assembly our own target fixture a few existing similar designs from other research groups have been first reviewed.

A research group at Georgia Tech has employed a single-stage gas gun with 80 mm bore diameter to launch a cylindrical sabot with a metal flyer plate at a target containing three sealed powder capsules embedded into a metal disc. The capsule disc and the surrounding ring were backed by a mounted momentum trap plate. As the flyer plate impacts the target surface a plane shockwave propagates through the metal encasement and the sample powder, and with a proper set of initial parameters the delivered shockwave energy will consolidate the powder to nearly 100% density.

The point of such design is the use of three samples at once, which can be allowed with 80 mm wide flyer plate and is time and cost efficient. Another important aspect is the construction of powder capsules, which are threaded and are sealed by a plug and epoxy. The plug prevents air access to the powder to avoid oxidation and keeps the powder partially compressed. All the metal components in this design are made of general purpose 304 stainless steel as illustrated below in Figure 7.9.

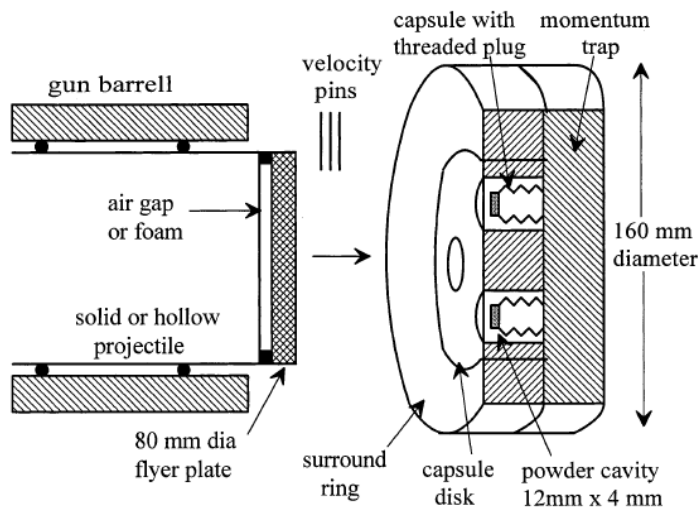


Figure 7.9. Schematic of three-capsule palte-impact recovery fixture used with the 80 mm diameter gas-gun for dynamic densification experiments

An alternative setup was used by a group at California Tech, which had a 35mm wide sabot and flyer plate impacting a target containing one powder capsule, is shown in Figure 7.10. On the contrary to the previous design, the powder sample only and not the surround ring is impacted. In this case less energy is wasted and the experiment is more cost efficient. The capsule design is also simpler. The powder is contained inside a sleeve (cylindrical tubing) and

plugged from both sides by press fitted cylindrical plugs. There is less control on air access to the powder inside the sleeve compared to the threaded capsule but the construction is much easier to machine. The design used hardened stainless steel for the target ring and the sleeve, while the back plug and the momentum trap were made of 6061 Al alloy.

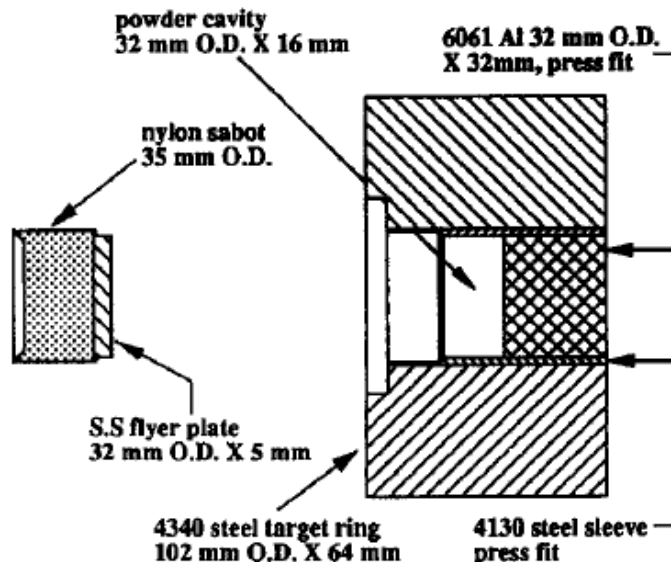


Figure 7.10. Target fixture and flyer plate assembly used in the shock consolidation. Note that only the sample, and not the containment assembly, is impacted

7.3.4.2 Proposed Design

Based on the review of previously employed powder impact compaction designs, schematics of a target fixture for the present SmCo_5 compaction experiment is proposed. The key points of the fixture design are:

- This is the first trial experiment therefore the fixture should be simple and low cost. The design with one sample capsule will be used.
- The sample capsule will be similar to the CalTech design – a cylindrical sleeve with press fitted plugs at both sides.
- Two different modifications of the plug-sleeve arrangement will be tried (rigid and compressive capsule, see below).
- Target ring, sleeve, front plug and flyer plate made of multipurpose 304 and extra corrosion resistant 316 stainless steel. Back plug and momentum trap made of 6061 Al alloy.
- The fixture will be assumed for one-time use and a new one will be used for each shot.

The sketch of the target fixture is shown below in Figure 7.11. The powder capsule is pressed into a surround ring, which is attached to the momentum trap plate. The momentum trap plate is wider than the surround ring to allow space for mounting to the base of the catch-tank.

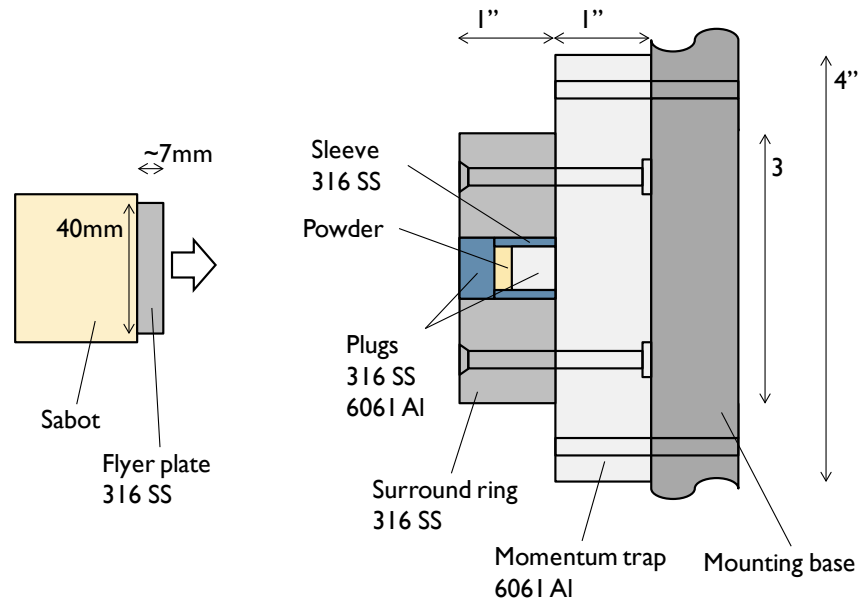


Figure 7.11. Preliminary target fixture design

Two modifications of the powder capsule will be tried and are presented in Figure 7.12. The rigid capsule design will have the front plug diameter equal to the outside sleeve diameter so that the plug rests on the sleeve edge thus providing good rigidity through the thickness of the surround ring. This arrangement is equivalent to the ones used in both groups reviewed earlier and is expected to transport the shockwave front equally through the surround ring and the capsule casing.

In addition to the rigid a compressive capsule design is proposed. In this case the front plug is placed inside the sleeve similarly to the back plug and the sleeve length is equal to the thickness of the surround ring. This model will be less rigid since the front plug can slide inside the sleeve and the shockwave profile may be distorted compared to the rigid capsule. However, the displacement of the front plug may aid in the powder compaction.

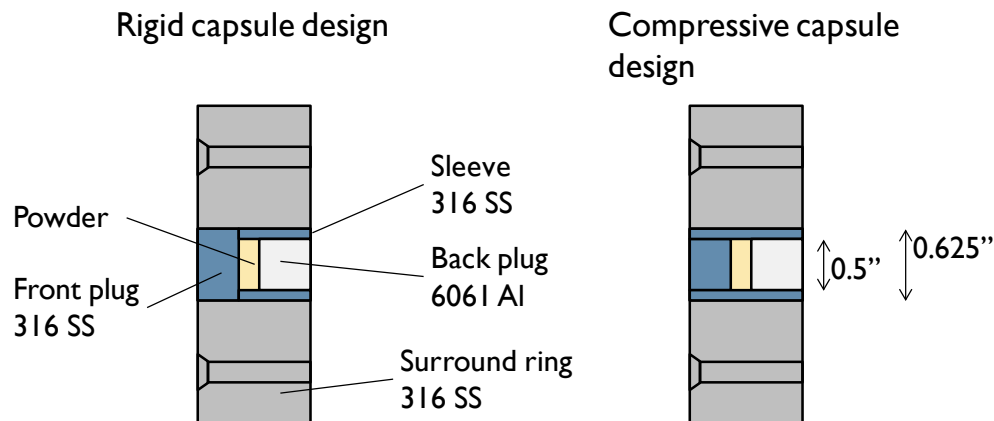


Figure 7.12. Powder capsule modifications

7.3.4.3 Summary

The proposed target fixture design is relatively simple to implement, the 304 and 316 steels are not hardened and the machining required is boring through holes for the powder capsule and mounting screws, slightly reducing plug rod diameter to fit into the sleeve, cutting tubing and rods to the required length. The sabot, flyer plate and the tank mounting stage parts will be machined at UDRI.

For the target to be assembled properly, the powder capsule front and back surfaces should be leveled flat with the surface of the surround ring. Part of it can be achieved by accurate cutting and fine grinding of the sleeve and the front plug. Additionally, since the size of the powder cavity depends on the powder mass the length of the back plug can be adjusted by fine grinding to make it flat with the outside surface for each target individually.

7.3.5 UDRI Gas Gun Powder Compaction Experiment

7.3.5.1 Objectives

The objectives of this experiment were to (1) Design sample and target capsule based on literature review; (2) Design and machining of target fixtures, projectiles and targets; (3) Conduct experiments at different impaction speeds; and (4) Sample property characterization.

7.3.5.2 Experimental and Discussion

Two types of target assemblies were machined in house – rigid and compressive capsule design (see drawings in Figures 7.11 and 7.12). Two identical targets were made of each type (four targets total).



Figure 7.13 Target assembly

Experimental nano-scale SmCo_5 alloy powder was prepared by surfactant-assisted high energy ball milling using Valeric acid surfactant. Preparation steps are summarized in the diagram in Figure 7.14. Final powder, including remaining surfactant, was loaded into target capsules and pre-compacted in hydraulic hand press.

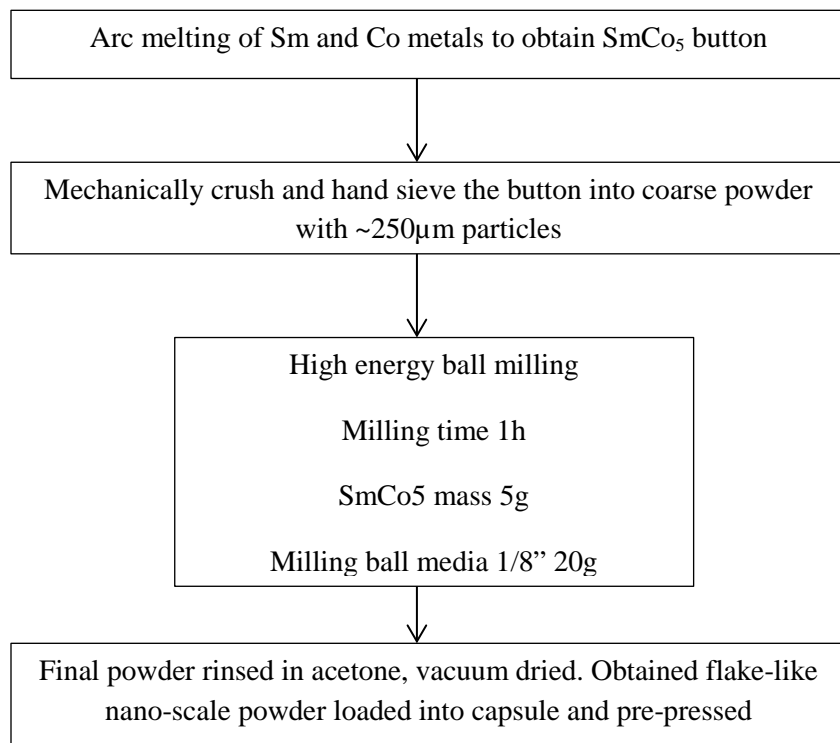


Figure 7.13. SmCo_5 experimental powder preparation flowchart

For target fixtures, cold rolled steel plates were cut to size according to the drawings in Figure 7.15. All fixture parts (front plate, base and gussets) were welded together as shown in Figure 7.16. Excessive heat from welding caused the bottom plate to warp, which was fixed later by level milling. Two fixtures were made and the target assemblies were mounted onto the front plates. The same fixtures were planned to use for up to two shot experiments.

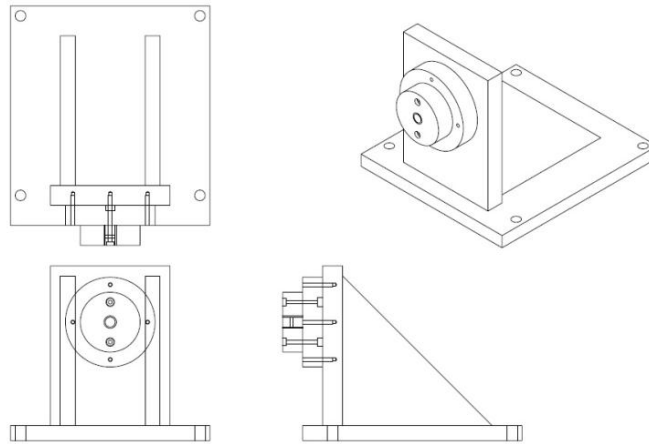
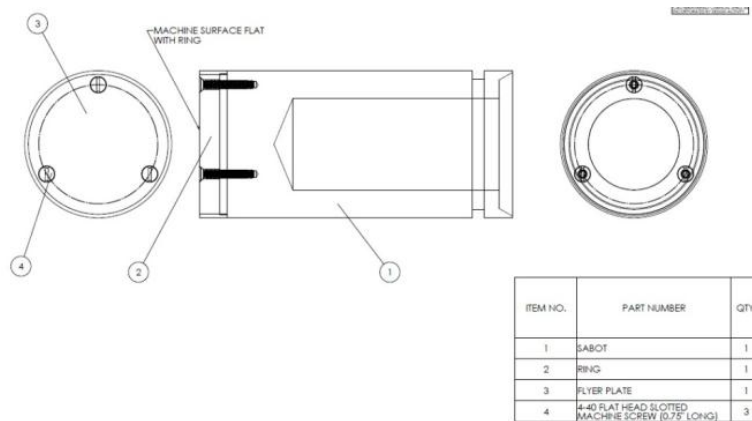


Figure 7.14. Target fixture drawing



Figure 7.15. Machined and welded target fixture with and without the target assembly mounted

For the projectiles, two sets were machined (4 pieces for velocity calibration and 4 pieces for the actual powder compaction). As shown in Figure 7.17, the body of a projectile was made from Lexan plastic cylinder, a flyer stainless steel plate was mounted on the front of the projectile and surrounded by aluminum ring.



(a)



(b)

Figure 7.16. (a) Projectile schematic. (b) Set of 4 machined projectiles

The powder compaction experiments consisted of four shots at two different projectile speeds (300 and 1000m/s) for each of the two types of powder capsule (rigid and compressive designs). The 300m/s shots were conducted using compressed Helium as the projectile propulsion medium, the 1000m/s shots were performed using gun powder charges. In all cases the sample chamber was evacuated to 17mmHg pressure to improve the velocity of the projectiles.

- Shot 1:
 - Velocity 303m/s
 - Propulsion: compressed He at 300psi
 - Target: rigid capsule
 - SmCo_5 powder and capsule top plug scattered after the shot, a sample piece was recovered.
- Shot 2:
 - Velocity 304m/s
 - Propulsion: compressed He at 300psi
 - Target: compressive capsule
 - SmCo_5 powder was contained after the shot (successful)

- Shot 3:
 - Velocity 990m/s
 - Propulsion: gun powder charge
 - Target: rigid capsule
 - Impact caused too much damage to the target assembly, no samples were recovered
- Shot 4:
 - Velocity 645m/s
 - Propulsion: gun powder charge
 - Target: compressive capsule
 - Impact caused no damage to the target assembly, but no samples were recovered

UNIVERSITY OF DAYTON RESEARCH INSTITUTE
IMPACT PHYSICS LABORATORY
 DAYTON, OHIO 45469-0116 937/229-3546

BALLISTIC TEST REPORT

Prepared For: UDRI Magnetics Materials Group

Test Date: February 4, 2013 Contract/Order No.: K50L21

Ambient Temperature: 70 °F Relative Humidity: Not recorded %

Test Article Description: Powder Compaction Targets

Projectile Description: 7 mm thick x 48.51 mm diameter 316 SS plate mounted on Lexan sabot

Propellant Type: Helium/WC895 powder Gun I.D.: Range 7 – 50 mm smoothbore

Witness Plate Material: None

Impact Obliquity: 0 degrees File Name: PowderCompaction 2-4-13BTR.doc

Shot Number	Target ID	Projectile Weight (g)	Impact Velocity (m/s)	Comments
7-1931	#1	269.49	303	Front piston plug found on tank floor. Pieces of compressed powder recovered from tank floor. Tank floor debris collected.
7-1932	#3	266.90	304	Target assembly remained intact.
7-1933	#2	278.48	990	Substantial damage to target and mounting frame. Surround ring was broken and found on tank floor. Aluminum base plate was deformed with clamping bolts bent/broken. Piston plugs found on tank floor. No recognizable compacted powder was initially recovered. Tank floor debris collected and bagged.
7-1934	#4	269.78	641	Front piston plug found on tank floor. Tank floor debris collected and bagged.

Comments: Projectile weight was the total package impacting the target. Flyer plate weight was not measured.

Characterization of only one sample obtained in Shot #2 experiment was conducted since no other samples were recovered. The SEM image in Figure 7.18 revealed a microstructure indicating partial powder compaction with significant amount of porosity and low particle bonding. This can be attributed to insufficient shock energy as well as low green-body density during initial powder pre-pressing. However, the particles are much denser packed compared to as-milled powder. The sample is isotropic, no degree of flake alignment was observed. Particle size remained unchanged after the compaction experiment (at 300m/s impact velocity).

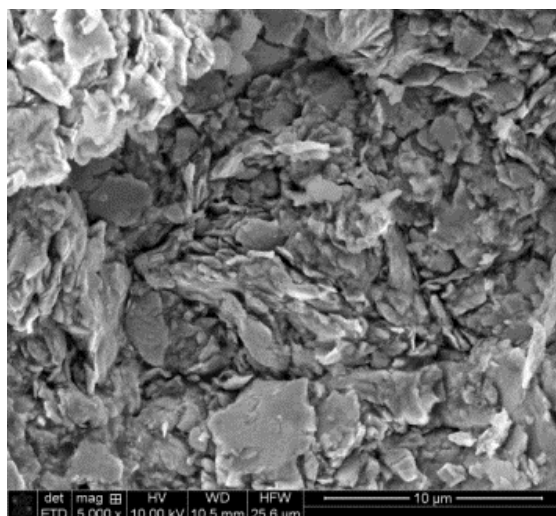


Figure 7.17. SEM imaging of shock compacted SmCo₅ nano-scale powder

Vibrating sample magnetometry (VSM) measurements were carried out to collect magnetic hysteresis $M(H)$ data, shown in Figure 7.19, on the as-milled SmCo₅ loose powder and the two recovered compacted samples. As-milled powder showed H_{ci} values very close to the closed loop KJS $B(H)$ measurements. The magnetic hysteresis measurements revealed slight (~15%) coercive field decrease in compacted material compared to lightly packed as-milled powder. According to the previous results, the lower H_{ci} values may be the result of sample heating during the shock experiment. It is hard to estimate the temperature of this local heating, however, it did not significantly deteriorate the magnetic properties. Remnant magnetization as well as saturation are approximately the same for all three samples, since magnetization M is measured in emu/g and sample density is not important.

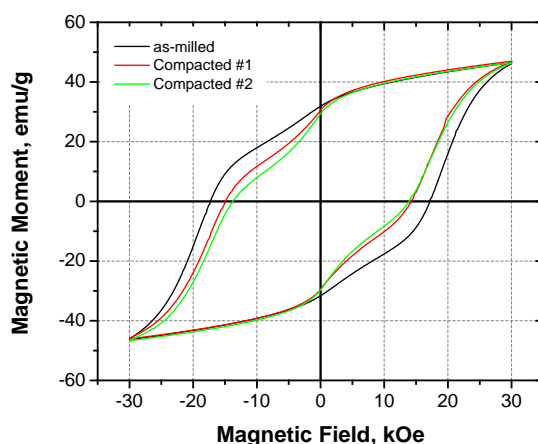


Figure 7.18. Magnetic hysteresis data for shock compacted and as-milled SmCo₅ nano-scale powder

7.3.5.3 Summary

The gas gun powder compaction technique tried was not successful in sintering SmCo_5 nano-powder. The 300m/s velocity is not enough to compact the powders onto bulk, while higher velocity (600-1000m/s) requires more advanced powder capsule design and target configuration

7.3.6 SmCo_5 Powder Microwave Sintering

Based on the microstructure analysis of the shock compacted SmCo_5 powders a new approach was planned in order to achieve better bulk SmCo_5 density. A microwave (MW) sintering process was chosen as a next experimental step based on the existing reports in literature on successful sintering of various metal alloy powders into fully dense final products. Additionally the experimental arrangements have been made at a local UDRI research facility which has suitable microwave sintering equipment readily available.

7.3.6.1 Experimental and Characterization

Starting powder was prepared by standard high energy ball milling process: combined in a steel jar under Ar 5g SmCo_5 coarse powder, 20g stainless steel milling ball media 1/8" diameter, 2.75g heptane (60 wt%) and 0.15g valeric acid surfactant (3 wt%). After 1h milling time powders were rinsed in acetone and vacuum dried. The nano-scale SmCo_5 powders were be magnetized in order to align the nano-flake particles and pressed in the cold isostatic press (CIP) at 30 kpsi for 30 min as a preparation for microwave sintering powder. Compacted powder samples were sintered in a microwave furnace (UDRI) at 300, 450 and 600°C for 5-15 min in forming gas atmosphere (95% N_2 and 5% H_2).

Microstructures of the sintered and compacted as-milled SmCo_5 samples are shown in Figure 7.20. An onset of particle coagulation is visible after MW sintering, however, no major densification or reduced porosity was observed. In order to obtain highly dense bulk higher sintering temperatures and longer dwelling times need to be employed.

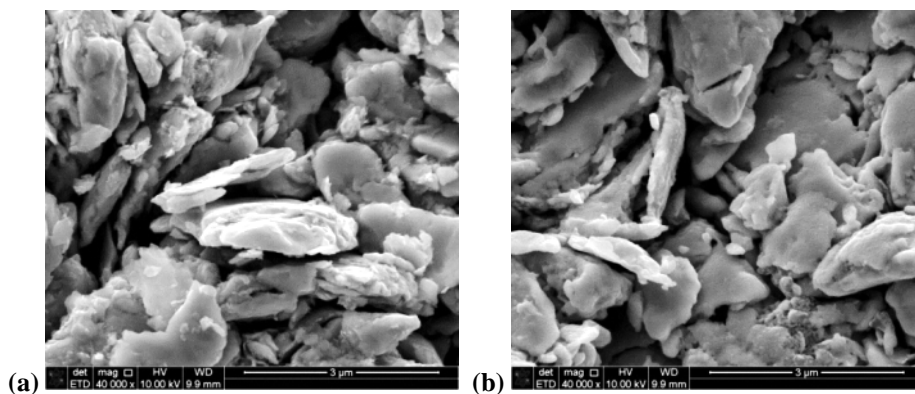


Figure 7.19. SEM images of CIP compacted as-milled SmCo_5 nanopowder (a) and microwave sintered sample at 600°C for 15 min (b)

The as-milled and MW sintered samples have been investigated using magnetic hysteresis measurements on a VSM instrument. The magnetic moment as a function of applied magnetic field $M(H)$ data are shown in Figure 7.21. The M_R and H_{ci} for as-milled powder are consistent with previous measurements, the CIP compacted powder has slightly better loop squareness due to higher sample density. Magnetic response of the MW treated SmCo_5 is similar for all treatment temperatures showing greatly reduced coercivity and remanence. Such a substantial difference could be attributed to sample structure change due to oxidation or recrystallization, which can be clarified by XRD investigation.

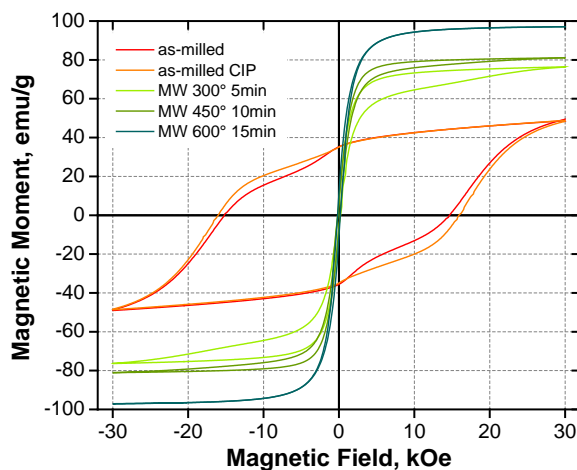


Figure 7.20. Magnetic hysteresis data for as-milled and microwave sintered nano-scale SmCo_5

Continued characterization of microwave sintered SmCo_5 nanopowders by x-ray diffraction has been carried out on samples sintered at 300 °C for 5 min, 450 °C for 10 min and 600 °C for 15 min using Cu $K\alpha$ radiation. XRD scans in the 2θ range 25-65° are shown in Figure 7.22. Pattern analysis and phase identification done with Diffrac.Eva software revealed presence of the original SmCo_5 and secondary phases (Sm oxide and Co) for the 300 °C treated sample. As the sintering temperature increases Sm oxides and Co become dominant and more pronounced while SmCo_5 is no longer detectable. These results indicate preferential oxidation of Sm during the heat treatment and growth of SmO, Sm_2O_3 phases and formation of Co phase. Since the sintering was done in forming gas atmosphere (95% N_2 and 5% H_2) the source of oxygen is believed to be the residual surfactant on powder particle surface. This structural analysis is in agreement with magnetic property $M(H)$ data: decomposition of hard SmCo_5 and growth of soft Co phases at progressively higher sintering temperatures.

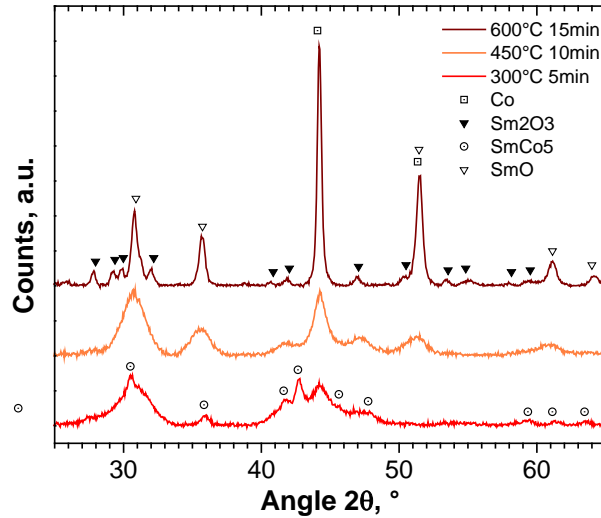


Figure 7.21. XRD data for SmCo_5 samples sintered at 300, 450 and 600 °C

7.3.6.2 Summary

The microwave sintering approach for producing dense SmCo_5 bulk alloy from nano-scale powder was attempted. Microstructure analysis indicated that the experimental temperature range 300–450 °C was not high enough to result in sintered body, only slight particle coagulation was observed. However, treatment temperatures above 300 °C were detrimental to the material composition and magnetic properties as heavy oxidation of Sm and precipitation of Co occurred.

7.3.7 Computer Simulation of Magnetic Inductor Components using FEM

7.3.7.1 Eddy Loss Calculation in Laminated Magnetic Inductor Core using Computer Modeling

Computer modeling is a viable technique for estimation of properties and behavior of different electro-magnetic systems. Such an approach can provide useful data for design of an electro-magnetic device or a component without the need for physically manufacturing a large set of test parts.

Within the current project a Maxwell 3D software package was used for simulating a laminated inductor core made of amorphous magnetic alloy tape. The material of interest was FeCoTaB-based alloy. In the amorphous state it has low electrical conductivity and high magnetic permeability, which are the required qualities for a high performance inductor material. The alloy can be cast as tape of various thicknesses (20–30 μm) then the tape is wound into a shape of an inductor core producing fine laminated structure. The goal of the numerical simulation was to optimize lamination thickness of such core in order to achieve low estimated power losses (Eddy loss, hysteresis loss) at different operating frequencies prior to manufacturing of the alloy tape.

A digital model of the inductor core has been created using standard dimensions in Maxwell 3D environment (Figure 7.23). By taking advantage of scripting language the model size, lamination layer quantity, excitation current and all other parameters were made easily

adjustable. This model can be used for Eddy power loss calculation inside the core volume at given frequency.

Full-scale simulation of the inductor core requires an excessive amount of computer memory; therefore first the Eddy loss was calculated in a small section in a simplified single layer model. This simulated power loss (P_e) is shown as a function of frequency in Figure 7.24, and excellent agreement with the theoretical values was achieved.

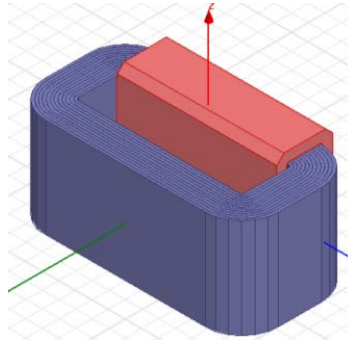


Figure 7.22. Model of a laminated inductor core in Maxwell 3D software

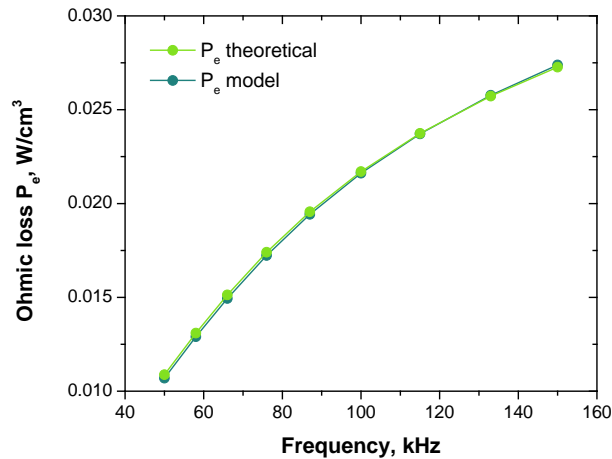


Figure 7.23. Simulated and theoretical Eddy loss frequency dependence

7.3.8 Magnetic Field Comparison for Solid and Wound Coil in Maxwell 3D

7.3.8.1 Objectives

The main objective of this effort is to calculate magnetic field distribution created by a wound coil with constant current, and compare it to the field of a solid coil of equivalent dimensions and current density using Maxwell 3D software. A second objective was to determine if the solid coil model could be used in order to simplify the model and reduce computation time.

7.3.8.2 Experimental

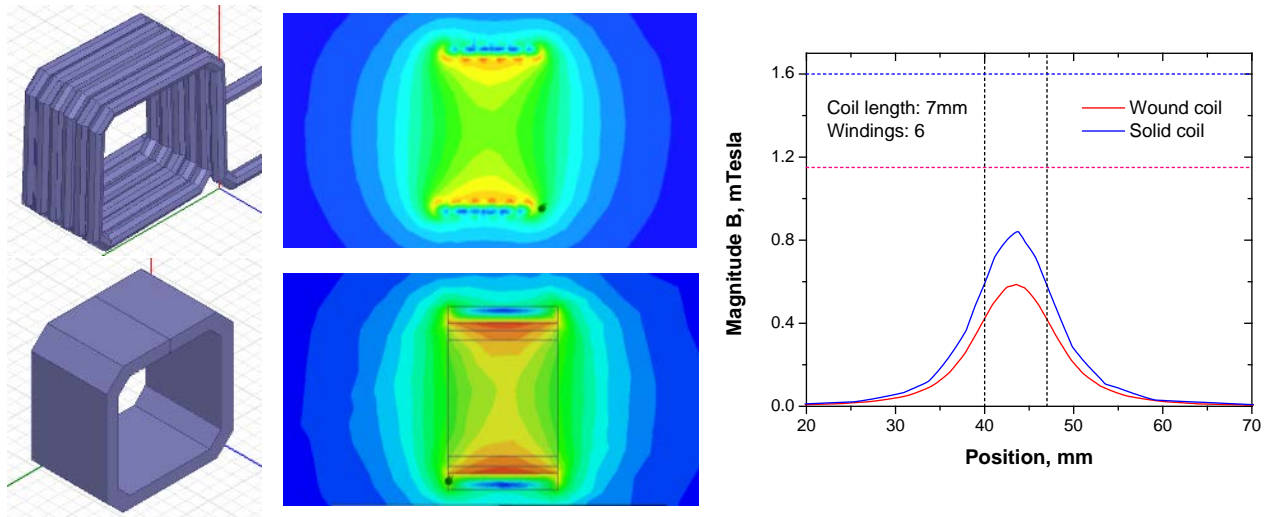
A 3D model of a wound coil was created with an aid of scripting language in Maxwell 3D environment. The following model parameters were used: coil size 10x10mm, wire diameter 1mm, winding pitch 1.1mm, number of windings 6, 11, 21 and 51, coil material Cu, current 1A. The solid coil had corresponding dimensions (length = number of turns x pitch, inside and outside dimensions = 9.5x9.5 mm and 10.5x10.5 mm, material Cu) and the same current density ($1A/\pi R^2$). Magnitude of the magnetic field B was calculated in two crosssectional planes as well as along the central axis of the coil.

7.3.8.3 Results

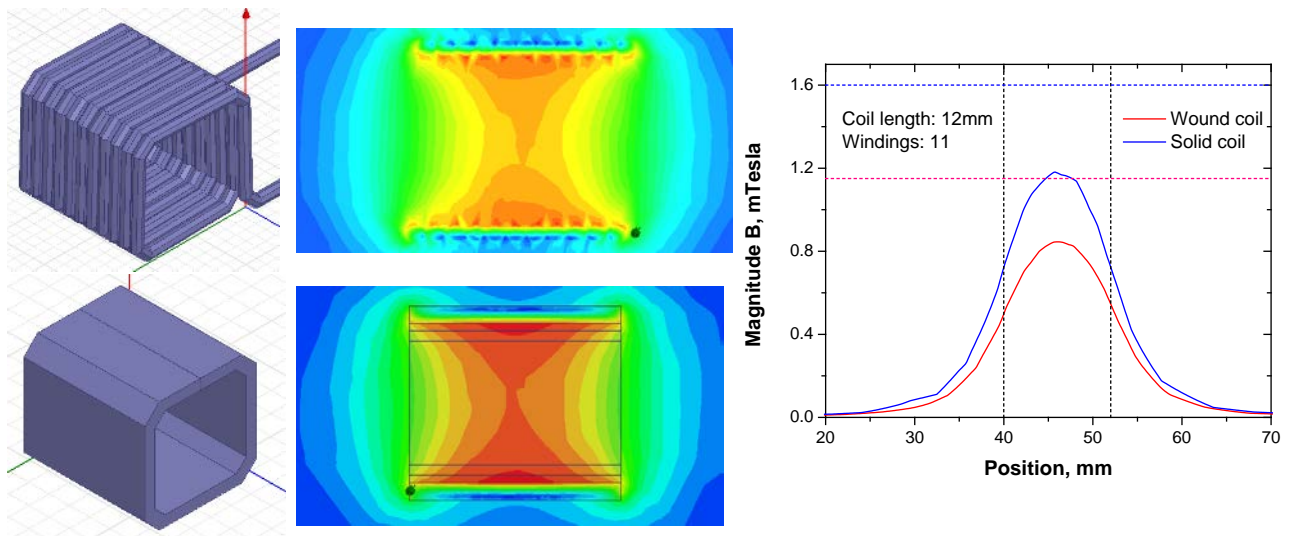
Magnitude of the magnetic field B along the central axis of the coil. Dashed horizontal lines correspond to the field inside an infinite coil:

- Wound coil: $B = \mu_0 I n$, where I is current, n is number of turns per unit length
- Solid coil: $B = \mu_0 d j$, where d is the coil thickness, j is the current density

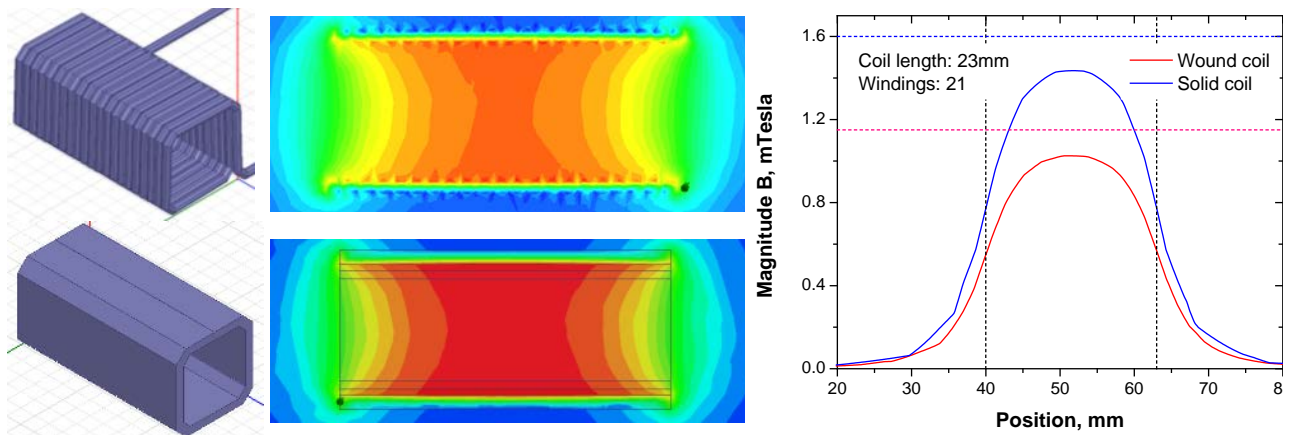
N = 6 turns coil and equivalent solid coil



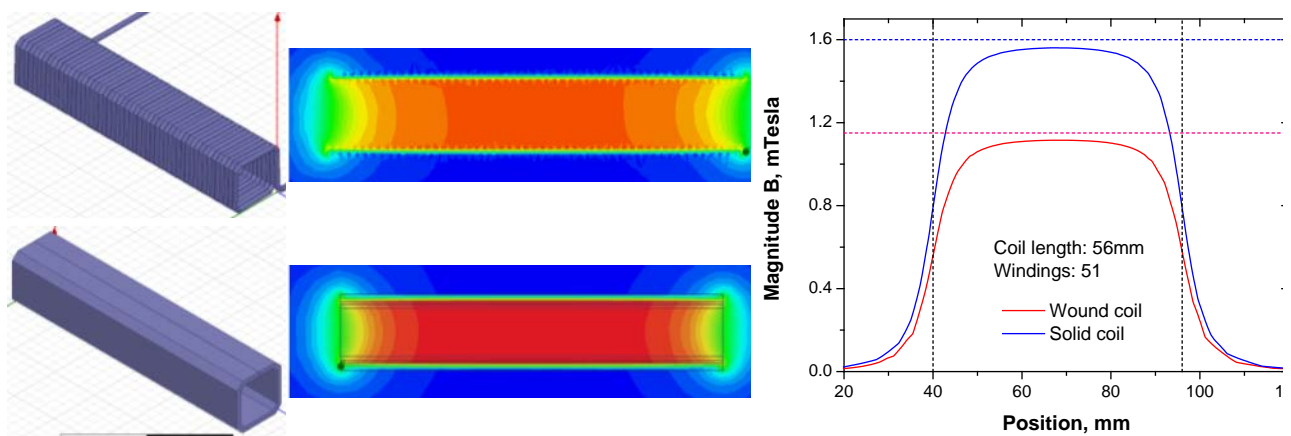
N = 11 turns coil and equivalent solid coil



N = 21 turns coil and equivalent solid coil



N = 51 turns coil and equivalent solid coil



7.3.8.4 Summary

Based on the model calculations both the wound and the equivalent solid coils produce similar profiles of the magnetic field B along the coil central axis for all considered geometric configurations (number of turns ranging from 6 to 51). At a high ratio of the coil length to its diameter (>5) the field in the center of the coil approaches its theoretical value of an infinite solenoid, both for wound and solid coils. Lower field strength produced by a wound coil compared to the equivalent solid coil (carrying the same current density) can be related to the presence of gaps between individual turns in the wound coil.

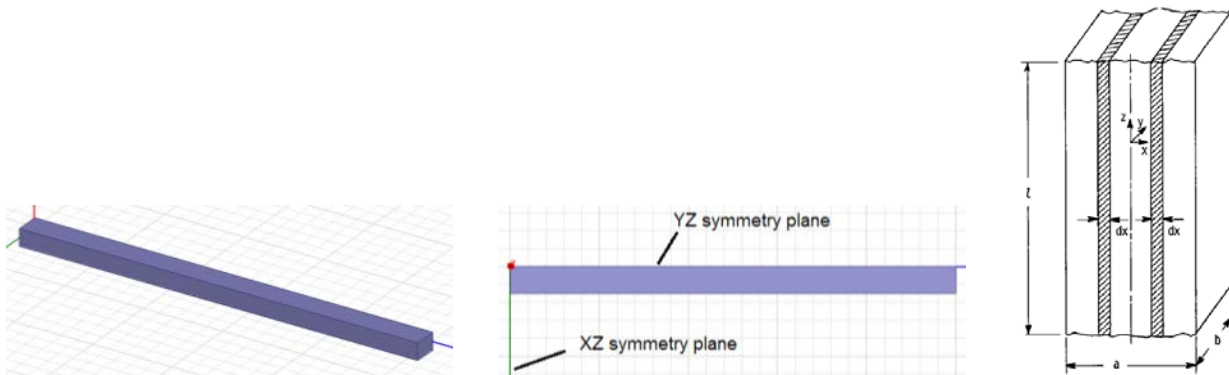
7.3.9 Eddy Current Power Loss Test in Maxwell 3D: Single Bar Model

7.3.9.1 Objectives

- Create a basic model of a single metal inductor core layer in AC magnetic field taking advantage of model symmetry planes.
- Calculate Eddy current and magnetic field distribution inside the layer, estimate power loss and compare the calculated values to theoretical ones at various AC frequencies.

7.3.9.2 Model Description

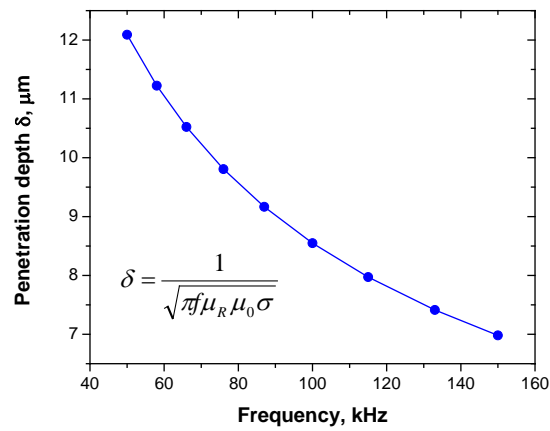
- Core layer material: Metglas 2605SA1, $\mu_R = 45000$, $\sigma = 7.7 \times 10^5 \text{ 1/}\Omega\text{m}$.
- Bar dimensions: $a = 23 \text{ }\mu\text{m}$ (lamination thickness), $l = 600 \text{ }\mu\text{m}$ (bar length), $b = 10 \text{ }\mu\text{m}$ (bar height).
- Applied magnetic field: $H_{\max} = 1.76 \text{ A/m}$ ($B_{\max} = 0.1 \text{ T}$), frequency 50-150 kHz.
- Symmetry consideration: odd (flux tangential) symmetry boundary conditions in XZ and YZ planes.



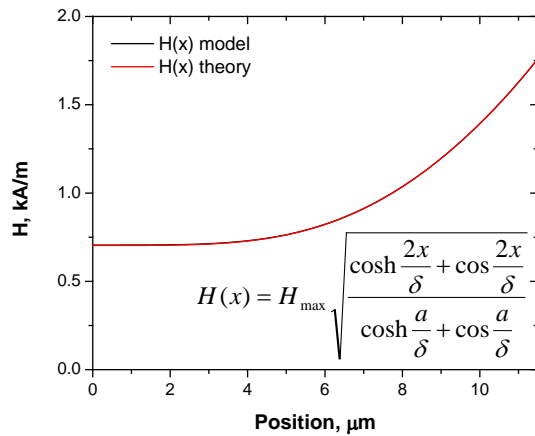
The model was run at several setup conditions (mesh size, frequency) and the Eddy power loss (p_e) was calculated as the integrated ohmic loss divided by the volume of the bar. Complex magnitudes of the Eddy current density $J(x)$ and field $H(x)$ were also measured as functions of position across the bar and compared to the theoretical values (from Kazimierzczuk, 2009).

7.3.9.3 Results

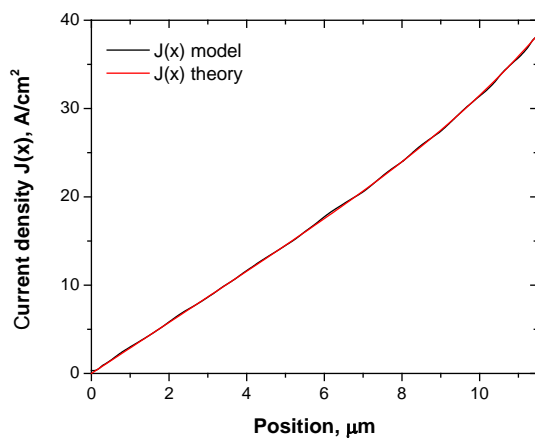
Field depth of penetration



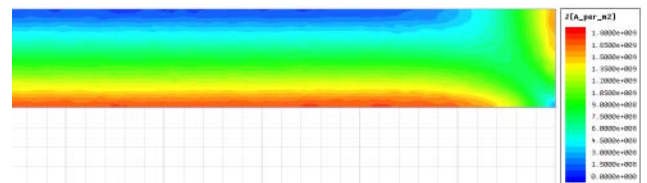
Magnetic field distribution $H(x)$ at 150 kHz



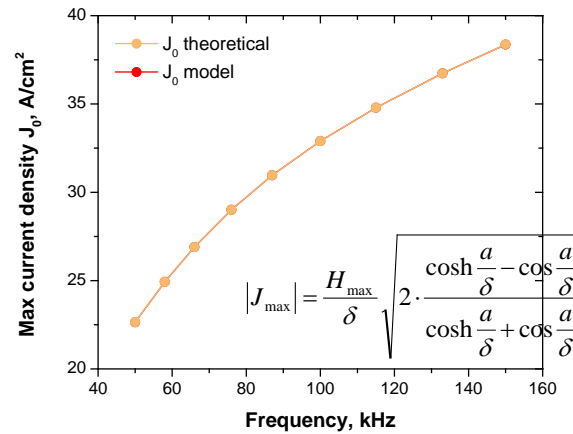
Eddy current density distribution $J(x)$ at 150 kHz



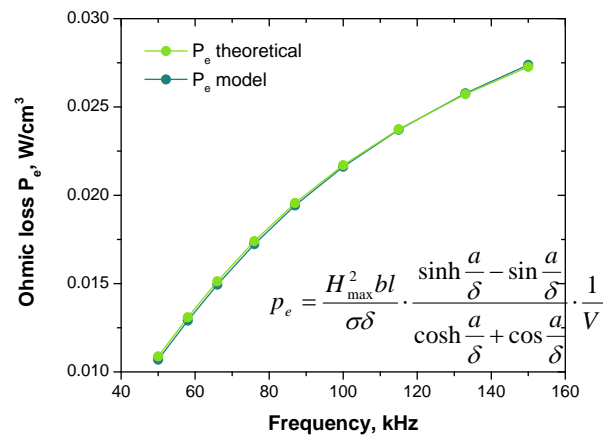
$$|J(x)| = \frac{H_{\max}}{\delta} \sqrt{2 \cdot \frac{\cosh \frac{2x}{\delta} - \cos \frac{2x}{\delta}}{\cosh \frac{a}{\delta} + \cos \frac{a}{\delta}}}$$



Surface current density frequency dependence $J_{\max}(f)$



Eddy loss per unit volume frequency dependence $P_e(f)$



7.3.9.4 Summary

Depth of penetration δ is comparable with the lamination layer thickness: $\delta = 7 \mu\text{m}$, $a = 23 \mu\text{m}$ (at 150 kHz). Skin effect observed, $H(x)$ and $J(x)$ are in excellent agreement with theory. Surface current density J_{\max} and Eddy power loss per unit volume p_e increase with higher frequency and are also in excellent agreement with theory.

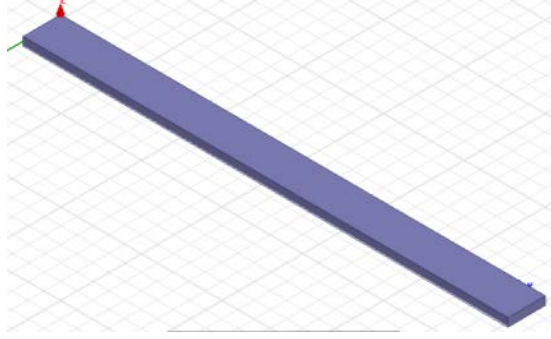
7.3.10 Eddy Current Single Bar Model in Maxwell 3D: Mesh Size Optimization

7.3.10.1 Objectives

- Use the existing single bar model of an inductor core lamination layer.
- Estimate most suitable model mesh element size in order to achieve good Eddy power loss calculation accuracy and low PC memory requirements.

7.3.10.2 Model Description

- Core layer material: Metglas 2605SA1, $\mu_R = 45000$, $\sigma = 7.7 \times 10^5$ 1/ Ω m.
- Bar dimensions: $a = 23$ μ m (lamination thickness), $l = 300$ μ m (bar length), $b = 5$ μ m (bar height).
- Applied magnetic field: $H_{\max} = 1.76$ A/m ($B_{\max} = 0.1$ T), frequency 150 kHz.



The model was run at several initial mesh setup conditions, specifically, the size of a mesh element was set to a value ranging from 3 to 30 μ m. This results in a finer or coarser mesh leading, respectively, to higher (more memory and time required) or lower (less memory and time) Eddy loss calculation accuracy.

Eddy power loss (p_e) was calculated as the integrated ohmic loss divided by the volume of the bar and compared to the theoretical value as shown in Equation (1) below (from Kazimierczuk, 2009).

$$p_e = \frac{H_{\max}^2 b l}{\sigma \delta} \cdot \frac{\sinh \frac{a}{\delta} - \sin \frac{a}{\delta}}{\cosh \frac{a}{\delta} + \cos \frac{a}{\delta}} \cdot \frac{1}{V} \quad (1)$$

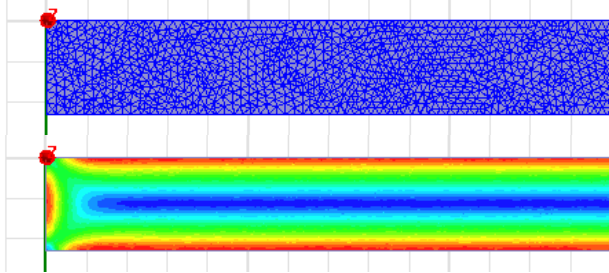
$$\delta = \frac{1}{\sqrt{\pi f \mu_R \mu_0 \sigma}}$$

Complex magnitudes of the Eddy current density $J(x)$ was also mapped in the bar cross section plane together with the model mesh wireframe for different mesh settings.

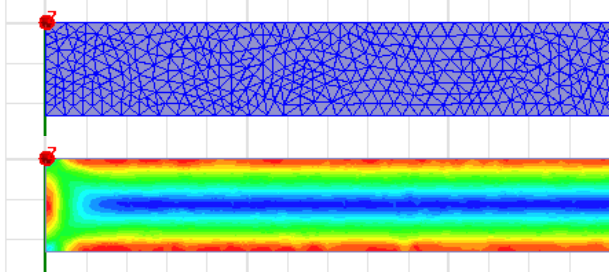
7.3.10.3 Results

Mesh wireframe and Eddy current density map

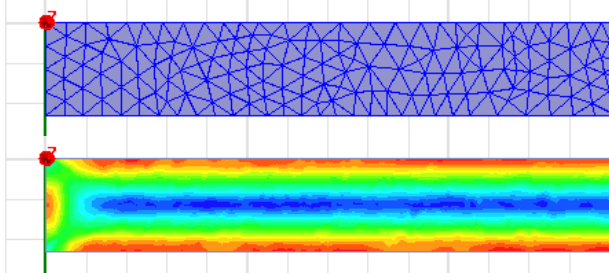
Mesh element size: $3\ \mu\text{m}$



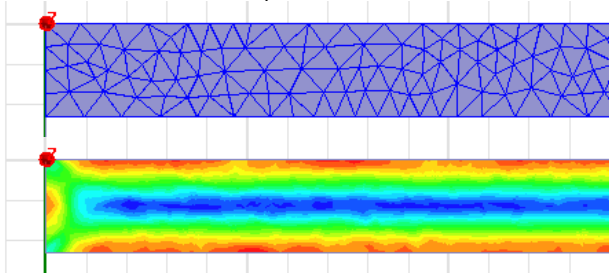
Mesh element size: $5\ \mu\text{m}$



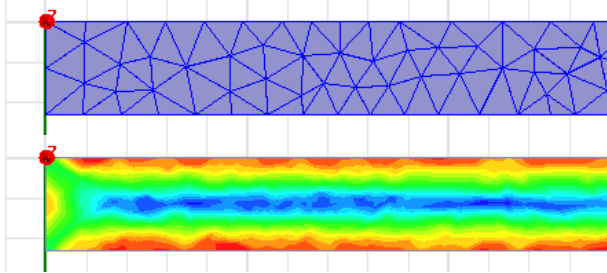
Mesh element size: $8\ \mu\text{m}$



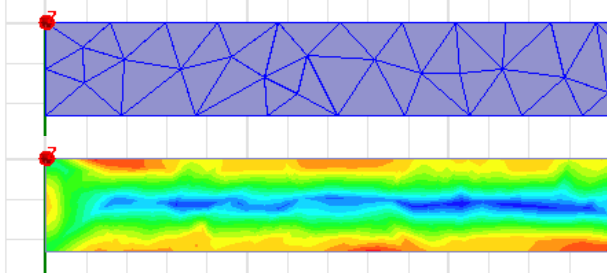
Mesh element size: $10\ \mu\text{m}$



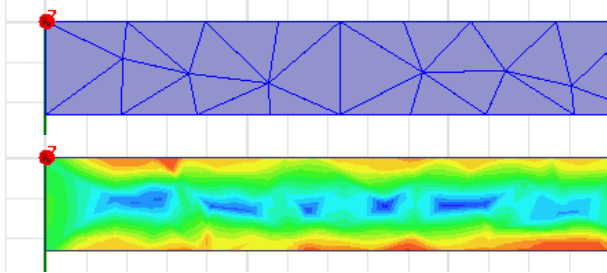
Mesh element size: 15 μm



Mesh element size: 20 μm



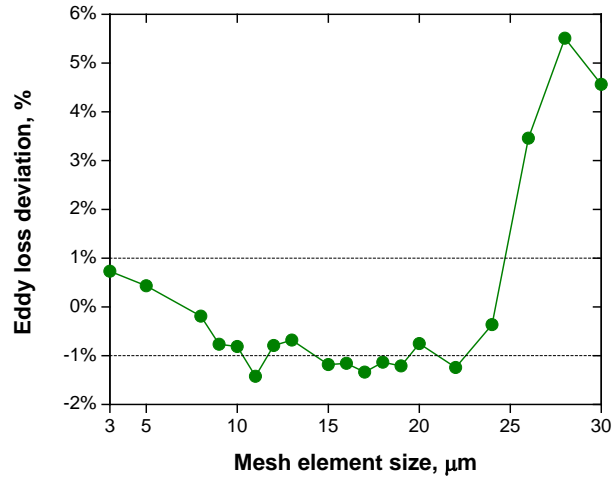
Mesh element size: 30 μm



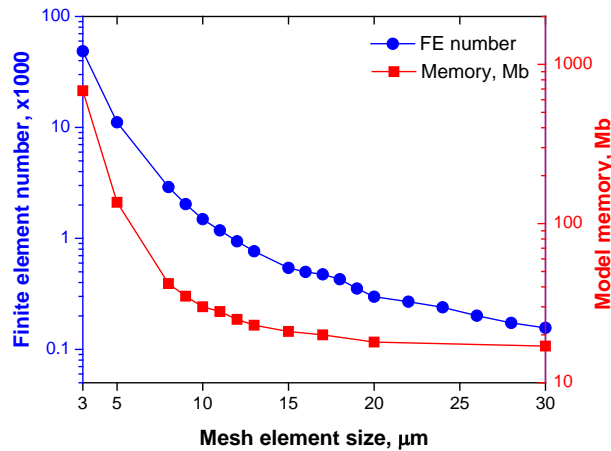
Model statistics

Mesh element size, μm	Number elements	of finite	Model memory, Mb	Calculated Eddy loss p _e , W/m ³	Deviation from theory, %
Theoretical	-	-	-	2.73e+04	-
30	156	17	2.85e+04	4.6	
28	173	17	2.88e+04	5.5	
26	201	17	2.82e+04	3.5	
24	239	17	2.72e+04	-0.4	
22	269	17	2.69e+04	-1.2	
20	298	18	2.71e+04	-0.8	
19	353	18	2.69e+04	-1.2	
18	428	18	2.70e+04	-1.1	
17	474	20	2.69e+04	-1.3	
16	499	20	2.70e+04	-1.2	
15	542	21	2.69e+04	-1.2	
13	765	23	2.71e+04	-0.7	
12	942	25	2.71e+04	-0.8	
11	1180	28	2.69e+04	-1.4	
10	1491	30	2.70e+04	-0.8	
9	2037	35	2.71e+04	-0.8	
8	2899	42	2.72e+04	-0.2	
5	11121	136	2.74e+04	0.4	
3	48598	683	2.75e+04	0.7	

Calculated Eddy loss accuracy compared to theoretical



Number of model finite elements and model PC memory



7.3.10.4 Summary

More accurate current density distribution is obtained with smaller mesh element size as seen from the smoothness of $J(x,y)$ map. Deviation of the calculated Eddy loss from its theoretical value is within 1% for mesh element sizes up to 25 μm .

Even though the $J(x,y)$ distribution does not seem smooth enough for such coarse mesh, it still gives an acceptable result for the integrated Eddy power loss. This is partly due to relatively weak skin effect in the material studied at given frequency of 150 kHz.

Required computer memory increases drastically with higher number of model finite elements. For the lowest acceptable accuracy case (mesh element size 25 μm) the model requires ~230 finite elements for the volume of the simulated metal bar of $3.5\text{e-}14 \text{ m}^3$. Physical inductor core volume is on order of $5\text{e-}5 \text{ m}^3$, which will require $3\text{e}11$ finite elements to model a full size core. Considering a linear dependence of PC memory on the number of FE, such full-scale simulation will need $\sim 10^6$ Gb of computer memory.

7.3.11 Ferrite Core Single Grain Eddy Loss Calculation in Maxwell 3D

7.3.11.1 Objective

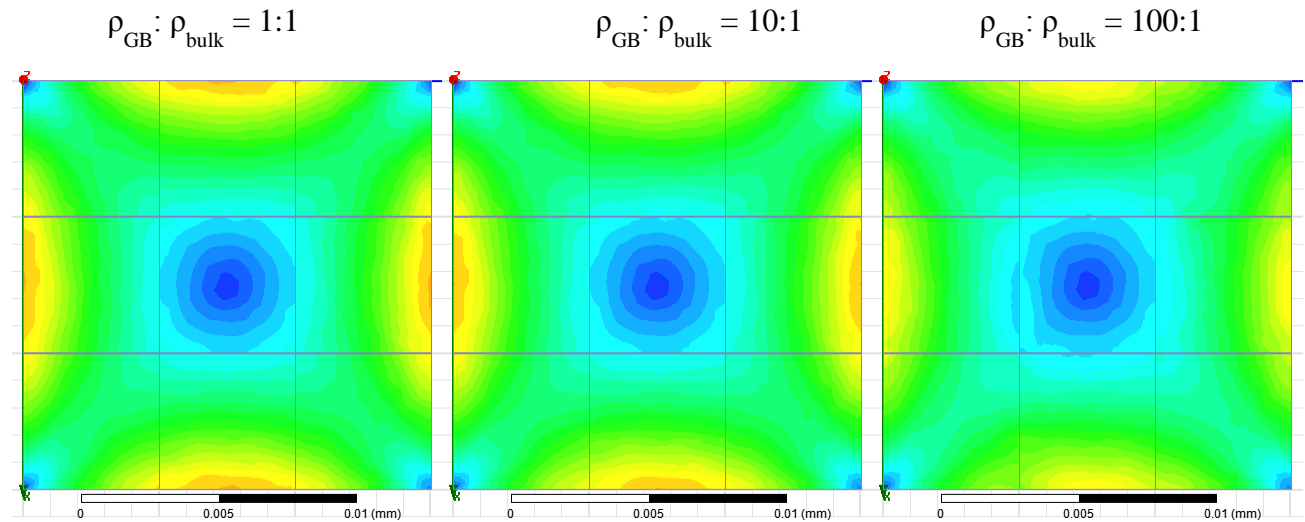
- Create a model of a ferrite core single grain in Maxwell 3D software.
- Estimate the effect of grain boundary resistivity on Eddy current distribution in a ferrite grain cluster.
- Simulate Eddy loss for 300 °C ferrite core material.

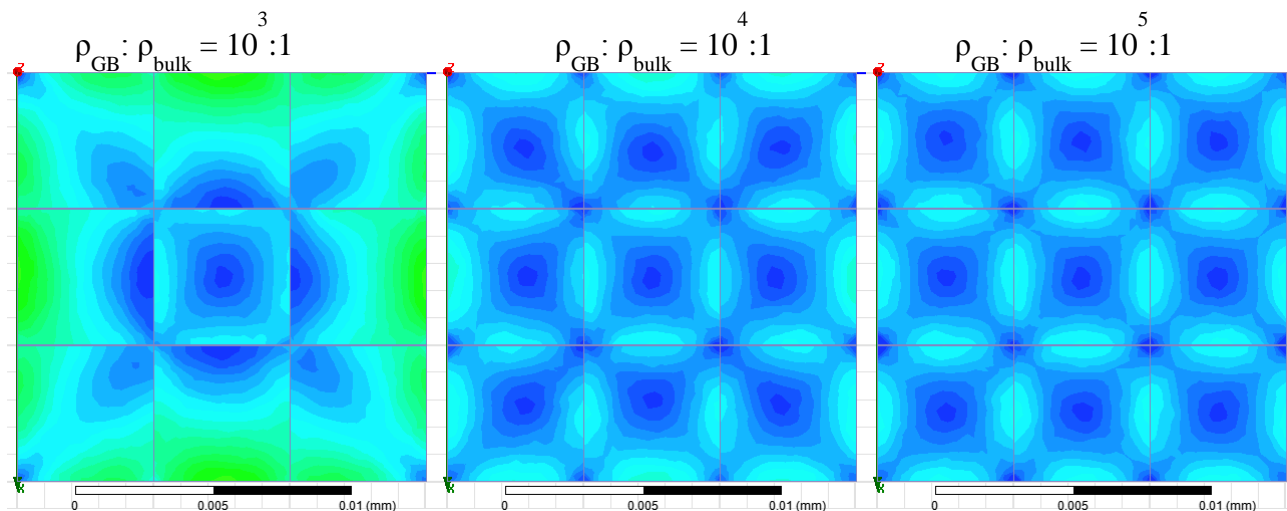
7.3.11.2 Experimental

A Maxwell 3D model of a 3x3 square grain cluster was created using the following parameters: grain size 5 μm , grain boundary width 50 \AA , grain bulk resistivity $\rho_{\text{bulk}}=10 \text{ }\Omega\text{cm}$, relative permeability $\mu_R=500$, grain boundary resistivity $\rho_{\text{GB}}=10^6 \text{ }\Omega\text{cm}$. To study the effect of grain boundary resistivity the total Eddy loss in the grain cluster was calculated at the flux density $B_{\text{max}}=10 \text{ Gauss}$ and frequency 150 kHz for ratios of grain boundary to bulk resistivity $\rho_{\text{GB}}: \rho_{\text{bulk}}$ in the range $1..10^5$. Based on the grain size distribution in 300C ferrite the Eddy micro current loss was calculated using a single grain model.

7.3.11.3 Results

Eddy current complex magnitude. Grain boundary resistivity effect

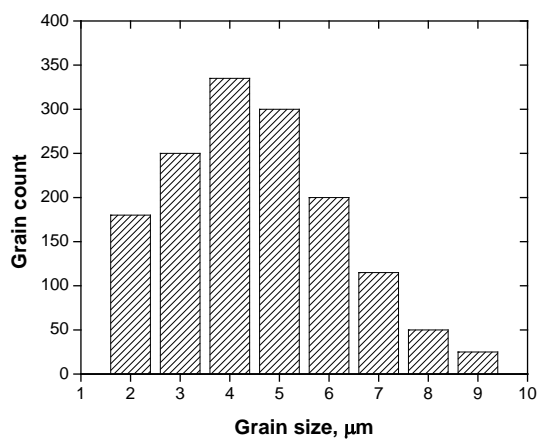




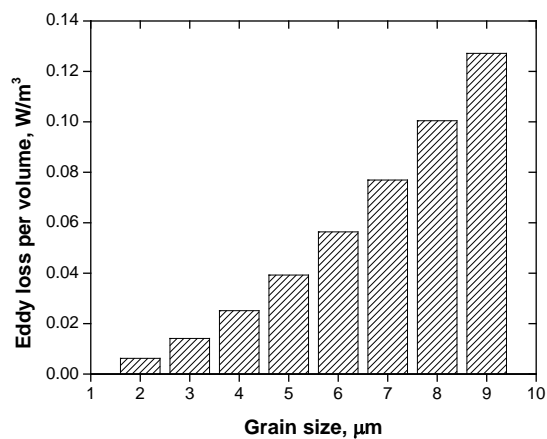
Resistivity ratio $\rho_{GB} : \rho_{bulk}$	Grain cluster total Eddy loss, W
1	9.6218e-21
10	9.4484e-21
10^2	8.0020e-21
10^3	2.9933e-21
10^4	1.1112e-21
10^5	1.0529e-21

Eddy current complex magnitude. Grain size effect

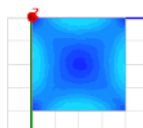
Grain size distribution (Spyker, 2004)



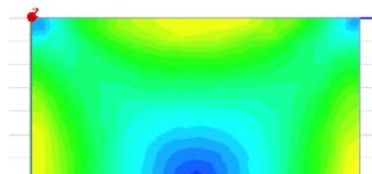
Single grain Eddy loss per volume



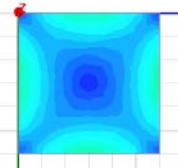
Grain
size
2μm



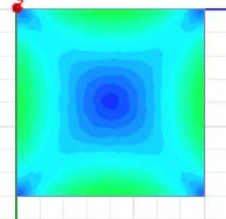
Grain
size
7μm



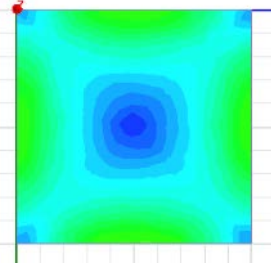
Grain
size
3 μm



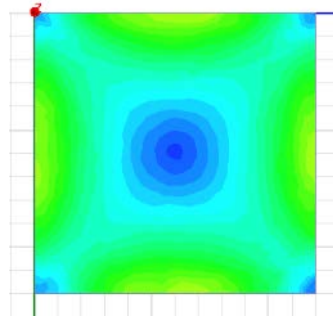
Grain
size
4 μm



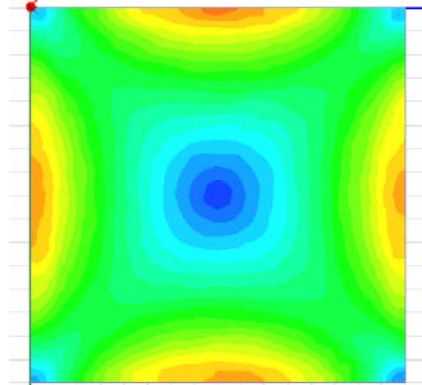
Grain
size
5 μm



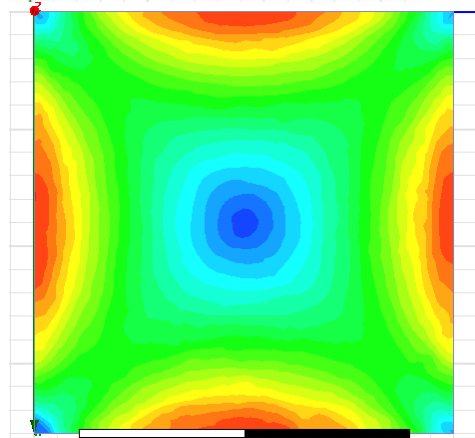
Grain
size
6 μm



Grain
size
8 μm



Grain
size
9 μm



7.3.11.4 Summary

Simulation of Eddy loss in a ferrite grain cluster showed that for the grain boundary resistivity of 10^4 - 10^5 times higher than the bulk resistivity the crossover of micro Eddy currents between individual grains is low and the boundary can be treated as insulating. Experimental measurements report similar ratio of 10^4 - 10^5 .

The average micro Eddy current loss inside a 300 °C ferrite grain was estimated based on the experimentally measured grain size distribution. However, the calculated value of 5.6×10^{-2} W/m³ is substantially lower than actual reported total losses ~ 20 W/m³ for similar flux density (0.1 T) and frequency (150 kHz) in similar ferrite materials.

7.3.12 Summary of Inductor Eddy-current Loss Simulation using ANSYS Maxwell 3D Software

7.3.12.1 Objectives

- Present general idea of ANSYS Maxwell 3D software capabilities in terms of modeling laminated inductor core Eddy-current power losses.
- Based on the simulation results summarize the trends of Eddy losses as a function of operating frequency, lamination thickness and core material resistivity for commercial Metglas and homemade FeCoTa alloys as core materials examples.

7.3.12.2 Experimental

ANSYS Maxwell 3D software package was used to create a 3-dimensional model of a laminated (tape wound) inductor core with material properties equivalent to Metglas 2605SA1 alloy ($\mu_R=45000$, $\sigma=770000$ 1/ Ω m) and core shape AMCC20 (C-core, 72x35x30 mm, tape thickness 23 μ m, lamination stack thickness 11 mm). Simulated magnetic flux density inside the core was ~ 0.1 T and operating frequency in the range 50-150 kHz.

A rendered view of the 3D core model is shown in Figure 7.25, it consists of concentric lamination layers which thickness and number can be controlled through built-in Visual Basic script interface. By progressively increasing the number of layers and decreasing their thickness it has been concluded that available computer memory (8 Gb) is not enough to solve for Eddy-current loss in a model with more than 20 layers due to excessive number of mesh discretization elements. Physical inductor core has ~ 500 lamination layers and projected PC memory requirements for modeling equivalent object is on order of 10^6 Gb. Therefore in order to simplify the model a 2-dimentional crosssection of the core was considered.

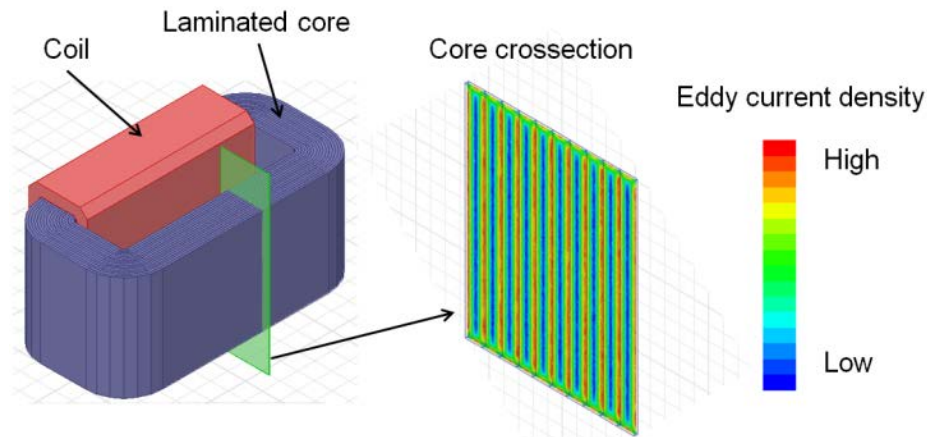


Figure 7.24. Rendering of a tape core inductor 3D model and a 2D cross-section used for accurate Eddy-current calculation

Eddy-current distribution and power loss were accurately solved in a 2D single-sheet model (Figure 7.26), which represents a 23 x 300 μ m part of a lamination layer with detailed geometrical mesh. The simulated results were in a good agreement with theoretical calculations (from Kazimierczuk, 2009) and several sets of data featuring Eddy loss dependence on frequency, lamination thickness and material resistivity were collected. In addition, simulated

results for two different amorphous magnetic alloys were compared: commercial Metglas ($\mu_R=45000$, $\sigma=770000$ 1/ Ω m) and in-house made FeCoTa ($\mu_R=2300$, $\sigma=714000$ 1/ Ω m). In both cases applied magnetic field H_{max} was adjusted to produce same magnetic flux density $B_{max} = 0.1$ T inside the material.

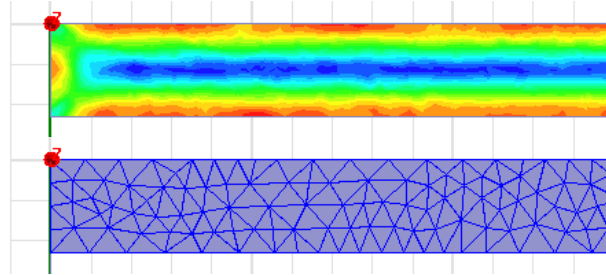


Figure 7.25. Simulated Eddy-current distribution and corresponding mesh discretization in a single lamination layer

Theoretical values were based on the textbook formulas for the Eddy power loss per volume p_e and magnetic field penetration depth δ :

$$p_e = \frac{H_{max}^2 b l}{\sigma \delta} \cdot \frac{\sinh \frac{a}{\delta} - \sin \frac{a}{\delta}}{\cosh \frac{a}{\delta} + \cos \frac{a}{\delta}} \cdot \frac{1}{V} \quad \delta = \frac{1}{\sqrt{\pi f \mu_R \mu_0 \sigma}}$$

where H_{max} is the amplitude of the applied AC magnetic field; a , b , l are lamination layer thickness, depth and height respectively; σ is the material bulk resistivity.

7.3.12.3 Results

Simulated Eddy losses in a layer with thickness $a = 23 \mu\text{m}$ as a function of frequency in the range $f = 10 \dots 10^6$ Hz are shown in Figures 7.27 and 7.28 in logarithmic and linear scales respectively. At lower frequencies, where penetration depth $\delta \gg a$ the power loss increases as f^2 (both Metglas and FeCoTa); while at higher frequencies skin-effect becomes significant, which suppresses Eddy-currents inside the layer (Metglas only, $f > 10^4$ Hz).

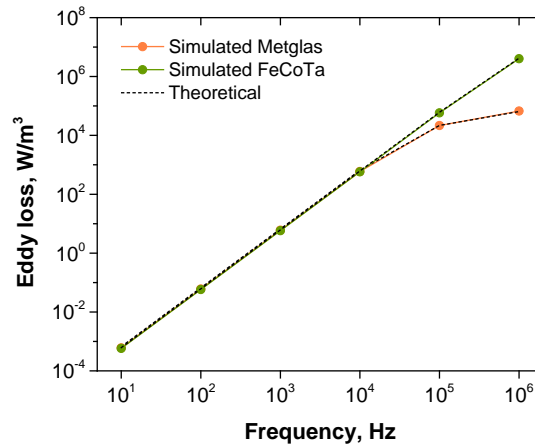


Figure 7.26. Eddy power loss as a function of frequency, logarithmic scale

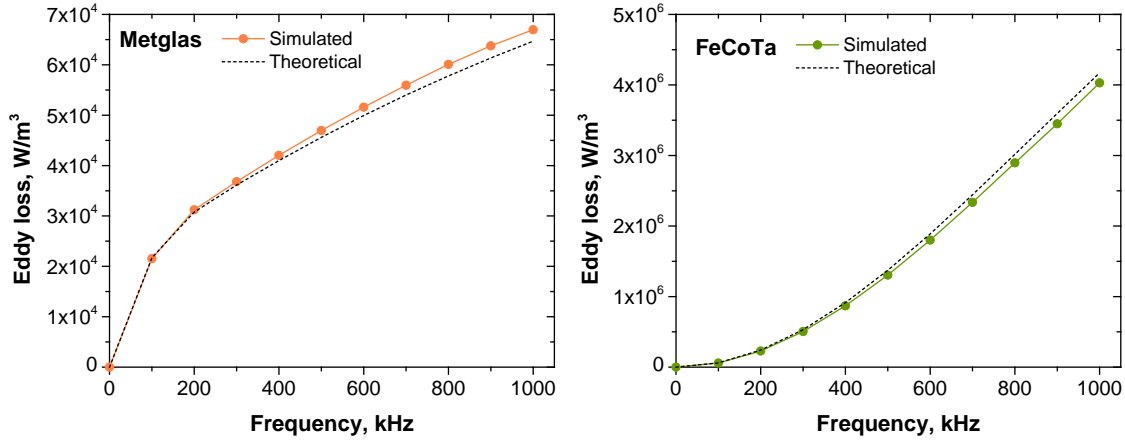


Figure 7.27. Eddy power loss as a function of frequency, linear scale

Eddy power loss dependence on the lamination thickness in the range $a = 5 \dots 65 \mu\text{m}$ at fixed frequency $f = 60 \text{ kHz}$ is shown in Figure 7.29. In the low-frequency approximation $a \ll \delta$, loss is proportional to a^2 , ($a < 20 \mu\text{m}$ for Metglas and full range for FeCoTa). At higher lamination thickness the Eddy-currents circulate only within skin depth at the surface of the layer thus reducing overall loss per volume ($a > 30 \mu\text{m}$ for Metglas).

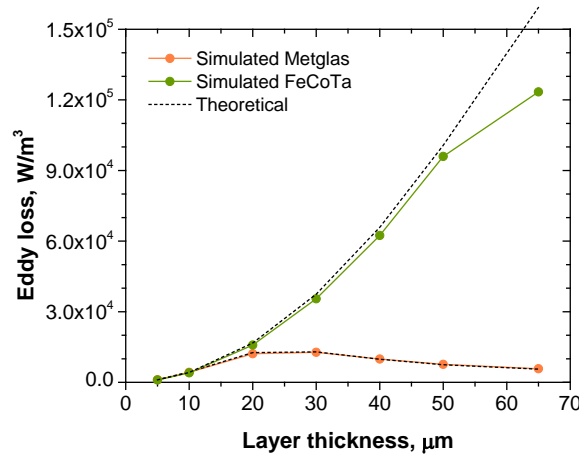


Figure 7.28. Eddy power loss as a function of lamination thickness

Calculated Eddy loss for fixed layer thickness $a = 23 \mu\text{m}$ and frequency $f = 60 \text{ kHz}$ as a function material bulk resistivity $\rho = 50 \dots 300 \mu\Omega \cdot \text{cm}$ is shown in Figure 7.30. Higher resistivity progressively results in reduced Ohmic losses in case of FeCoTa with weak skin effect. On the other hand, Metglas has much higher permeability leading to stronger skin effect and suppressed Eddy loss in low resistivity range.

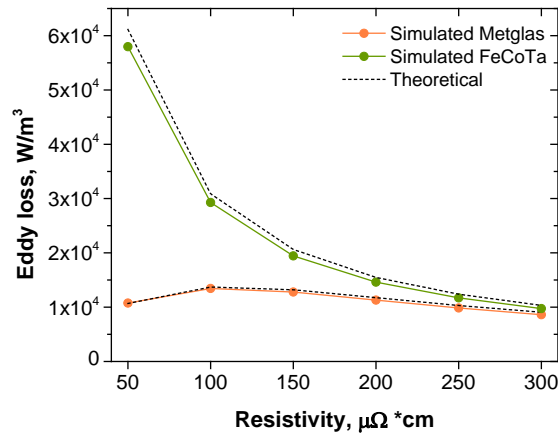


Figure 7.29. Eddy power loss as a function of material resistivity

7.3.12.4 Summary

Based on the results of modeling laminated inductor core Eddy-current losses using conventional PC and ANSYS Maxwell 3D software package the following points can be outlined:

- It is not possible to fully simulate a 3-dimensional laminated core due to extremely high PC memory requirements; a simplified 2D model of a single lamination layer was used instead.
- Eddy power loss was calculated for commercial Metglas and homemade FeCoTa amorphous magnetic alloys; very good agreement between simulated and theoretical results was achieved.
- In the used range of input parameters Metglas alloy exhibits strong skin-effect (field penetration depth much smaller than layer thickness) which reduces Eddy loss per volume of the material, however, the skin-effect also suppresses magnetic flux density in the bulk lowering magnetic performance and should be avoided; the FeCoTa alloy due to much lower permeability does not exhibit skin-effect.
- Eddy losses may be effectively lowered by reducing lamination layer thickness: $\frac{1}{2}$ reduction from 23 μm down to 12 μm will lower Eddy loss by factor of 50% and 75% for Metglas and FeCoTa respectively.
- Lower Eddy loss may also be achieved by increasing alloy bulk resistivity, but less effectively compared to reducing layer thickness. Resistivity doubling from current ~ 150 up to 300 $\mu\Omega \cdot \text{cm}$ will reduce loss by 40% and 45% for Metglas and FeCoTa respectively.

7.3.13 Finite Element Modeling in Maxwell 3D: Permanent Magnet Plate Design

7.3.13.1 Objectives

- Create a magneto-static computer model of a set of magnet plates with controllable magnetization orientation direction and plate thicknesses
- Optimize model parameters to achieve a uniform magnetic field inside a specified region between magnet plates

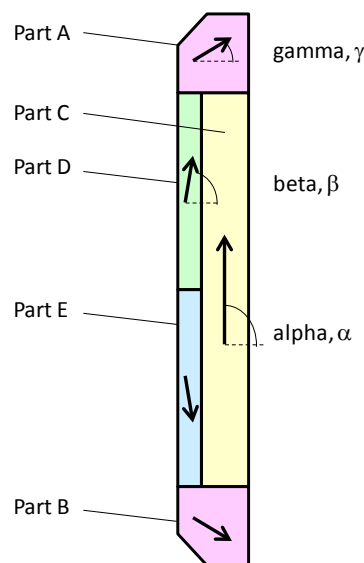
7.3.13.2 Model Design Description and Results

- Flat plate
- Original segmented
- Original segmented, no bevel
- Wedge plate, flat plate
- Wedge plate, original segmented plate
- Closed path, flat plate
- Closed path, flat plate, segmented plate
- Closed path, segmented plate

As a starting point flat plate design (1) have been modeled using structure dimensions as a core size. This design gives good field uniformity along x-axis but not along y- and z- directions. Originally proposed segmented plate design (2) requires much smaller plate thickness for the given central field strength, provides control over x-axis field profile (adjusting angle β) but does not improve either y- or z- axis field uniformity compared to the flat plate. Part A bevel has insignificant effect on the field topology (3).

Slight but insufficient improvement in y-axis field profile was achieved by including wedge plates (4, 5) to the flat and segmented plate models. Addition of side plates to flat plate design in order to create close path (6) greatly improves field uniformity in all directions. Close path segmented plate models (7, 8) can be further fine-tuned to reach <0.3% field variation inside the work zone dimensions.

Segment name and magnetization orientation reference:

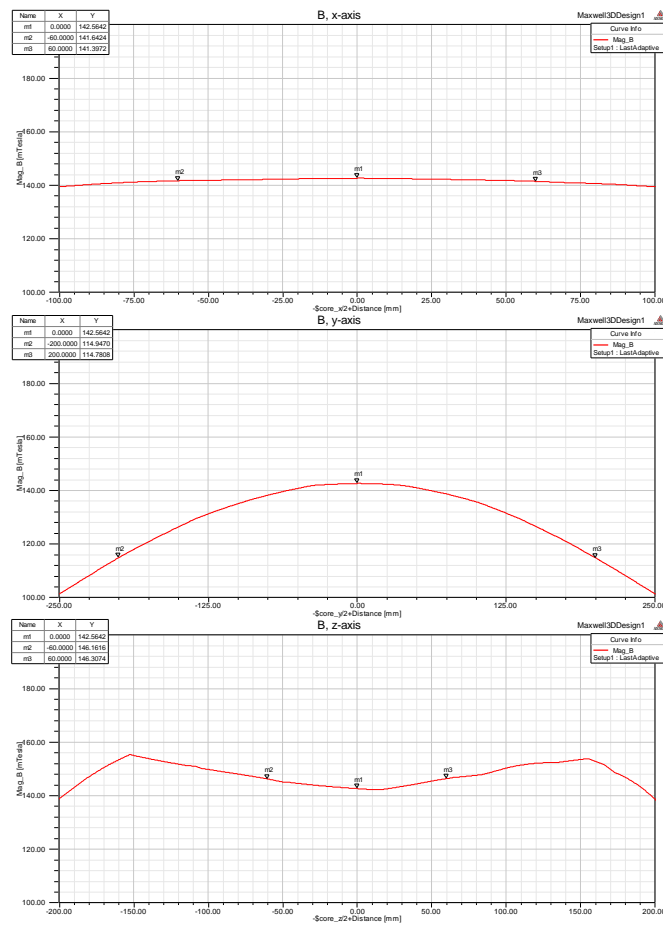
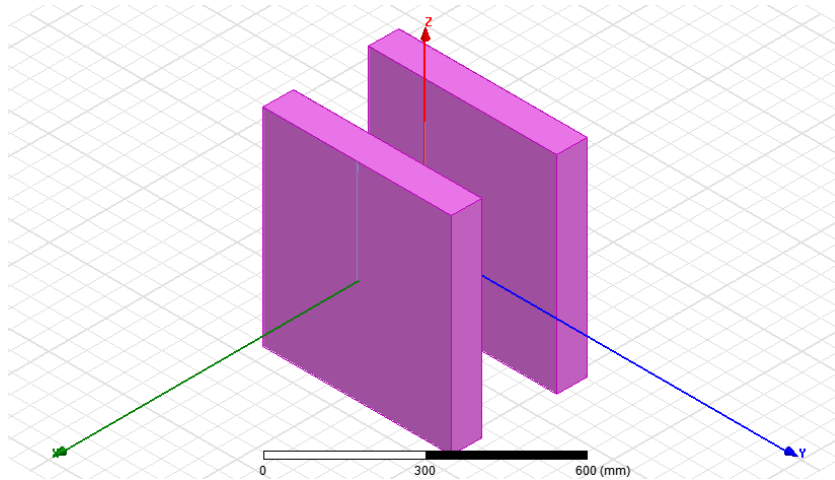


1. Flat plate design: Magnet 0.mxwl

Core dimensions: (core_x,core_y,core_z) 200, 500, 550 mm

Magnet thickness: (mag_x) 80 mm

Magnetization direction angles: (alpha) 90°



Axis	B central, mT	B work zone edge, mT	ΔB , mT	$\Delta B/B$ central
x	142.56	141.64	-0.92	-0.6%
y	142.56	114.95	-27.61	-19.4%
z	142.56	146.16	3.6	2.5%

2. Originally proposed design: Magnet 04.mxl

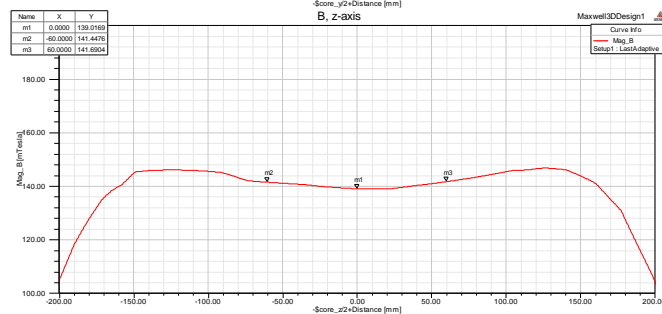
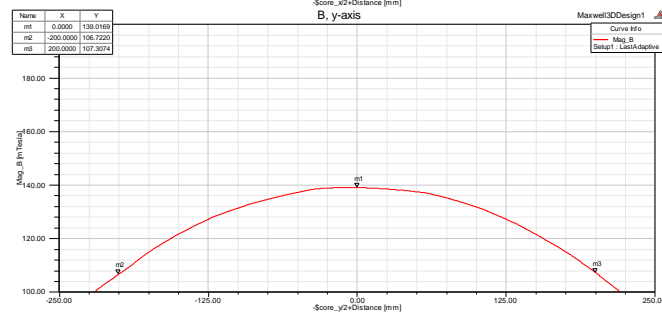
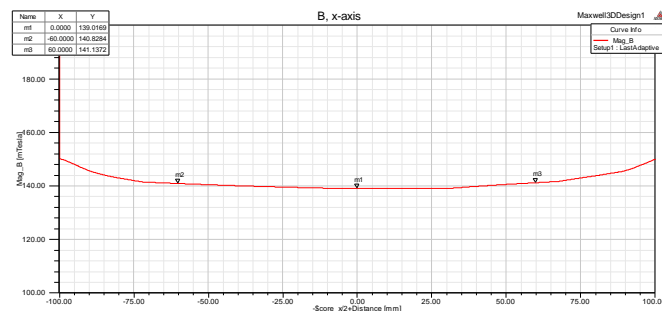
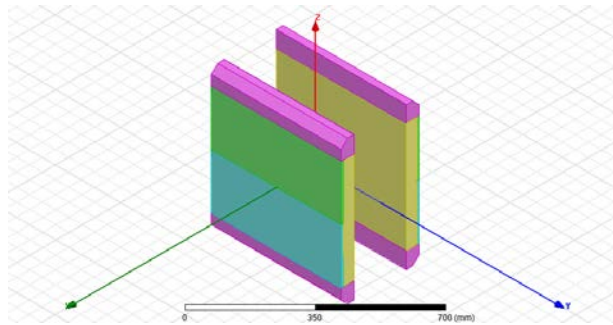
Core dimensions: (core_x,core_y,core_z) 200, 500, 550 mm

Magnet thickness: (mag_x) 50 mm

Part A, height: (part_A_z) 63 mm

Part D thickness: (part_D_x) 8 mm

Magnetization direction angles: (alpha, beta, gamma) 90°, 60°, 30°



Axis	B central, mT	B work zone edge, mT	ΔB , mT	$\Delta B/B$ central
x	139.01	140.83	1.82	1.3%
y	139.01	106.72	-32.29	-23.2%
z	139.01	141.69	2.68	1.9%

3. Originally proposed design: Magnet 04.mxl

No top bevel

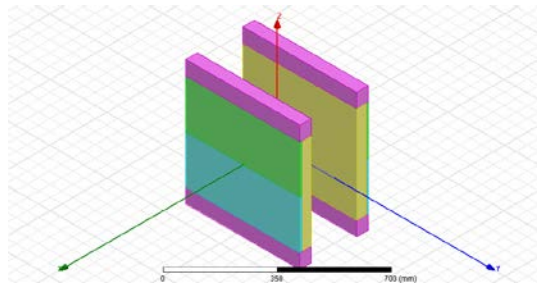
Core dimensions: (core_x,core_y,core_z) 200, 500, 550 mm

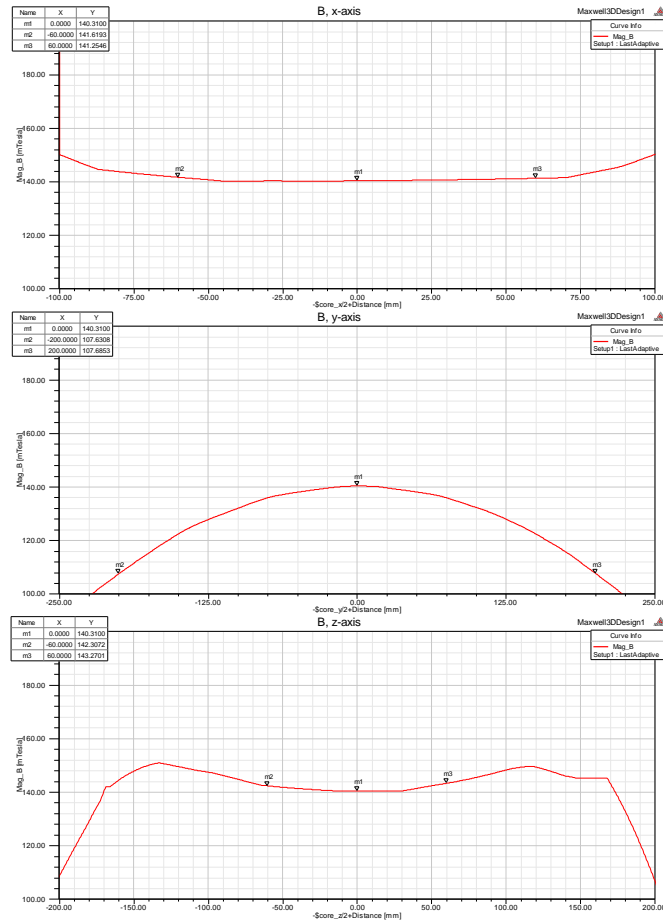
Magnet thickness: (mag_x) 50 mm

Part A, height: (part_A_z) 63 mm

Part D thickness: (part_D_x) 8 mm

Magnetization direction angles: (alpha, beta, gamma) 90°, 60°, 30°





Axis	B central, mT	B work zone edge, mT	ΔB , mT	$\Delta B/B$ central
x	140.31	141.62	1.31	0.9%
y	140.31	107.63	-32.68	-23.3%
z	140.31	142.31	2	1.4%

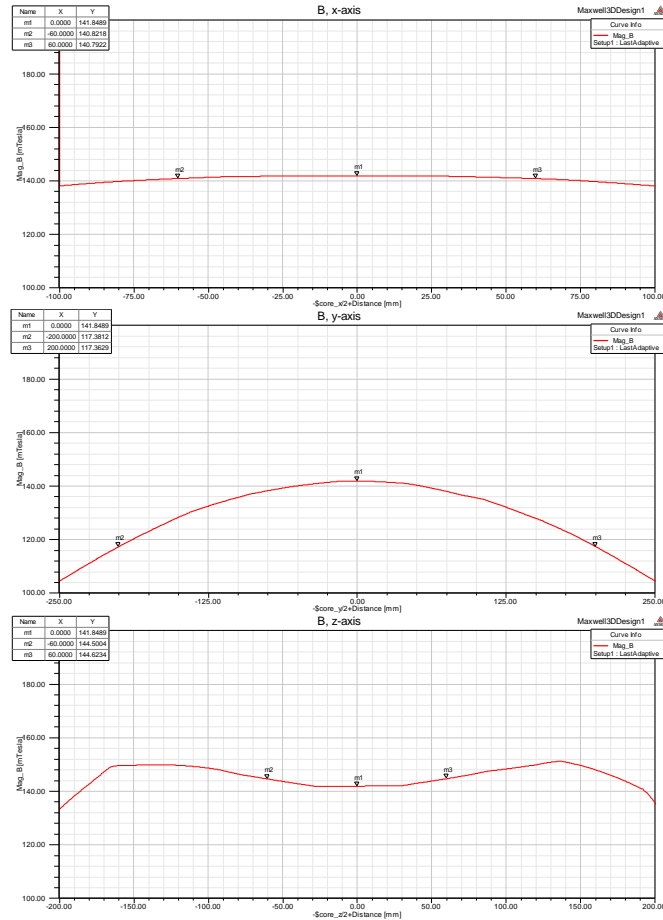
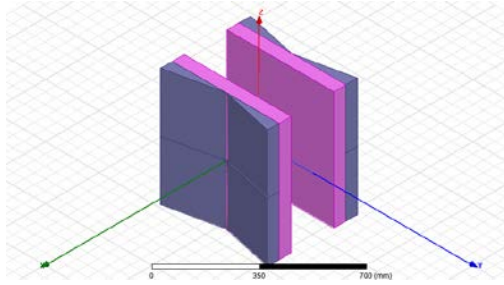
4. Wedge plate, flat plate design: Magnet 05.mxw

Core dimensions: (core_x,core_y,core_z) 200, 500, 550 mm

Inner flat plate thickness: (mag_x) 55 mm

Wedge plate max thickness: 55 mm

Magnetization direction angles: (alpha) 90°



Axis	B central, mT	B work zone edge, mT	ΔB , mT	$\Delta B/B$ central
x	141.85	140.82	-1.03	-0.7%
y	141.85	117.38	-24.47	-17.3%
z	141.85	144.5	2.65	1.9%

5. Wedge plate, original plate design: Magnet 05a.mxl

Core dimensions: (core_x,core_y,core_z) 200, 500, 550 mm

Magnet thickness: (mag_x) 30 mm

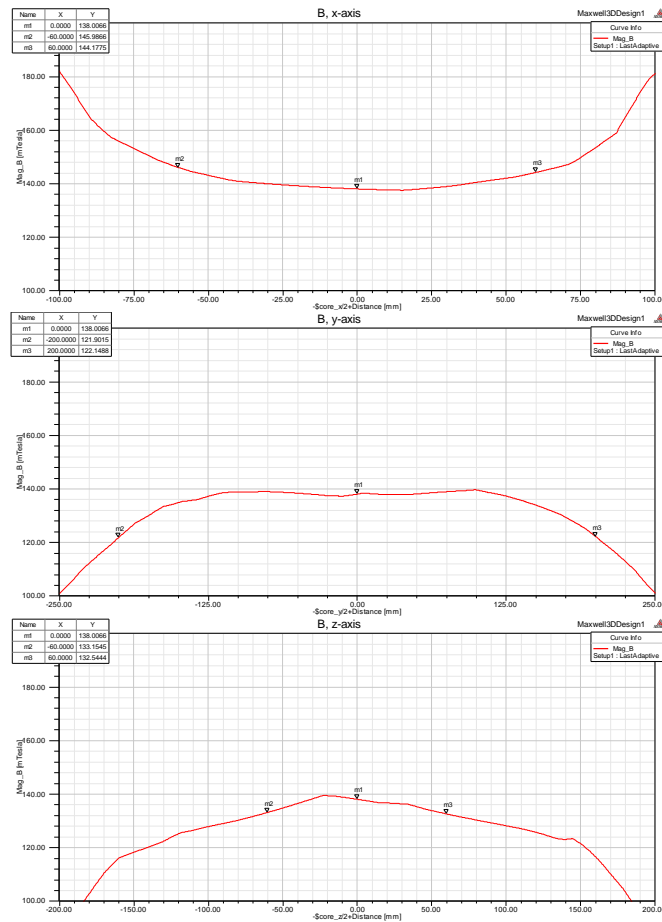
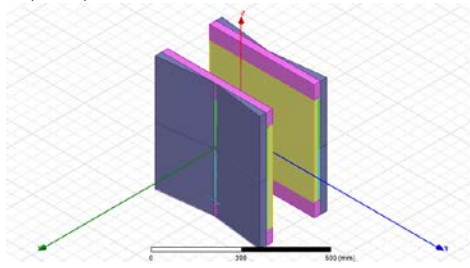
Part A, height: (part_A_z) 63 mm

Part D thickness: (part_D_x) 8 mm

Wedge plate max thickness: 30 mm

Magnetization direction angles: (alpha, beta, gamma) 90°, 60°, 30°

Wedge plate magnetization angle: (beta) 60°



Axis	B central, mT	B work zone edge, mT	ΔB , mT	$\Delta B/B$ central
x	138	145.99	7.99	5.8%
y	138	121.9	-16.1	-11.7%
z	138	133.15	-4.85	-3.5%

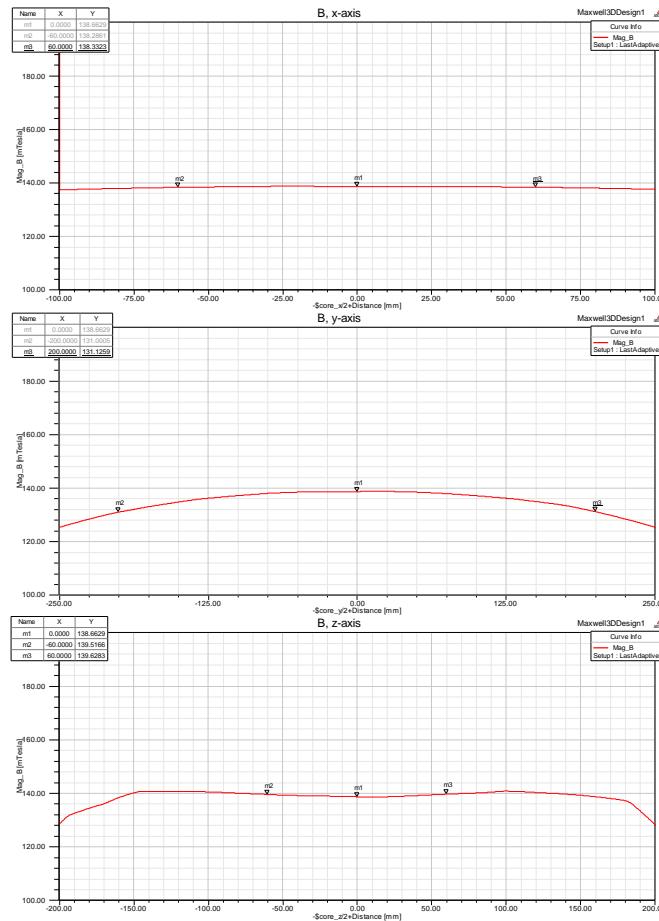
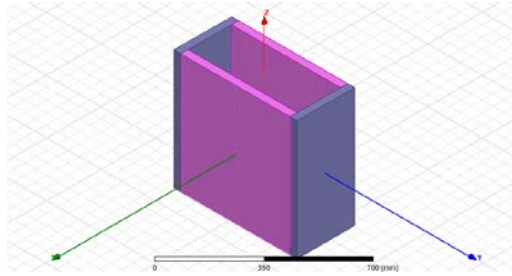
6. Closed path, flat plate design: Magnet 06.mxl

Core dimensions: (core_x, core_y, core_z) 200, 500, 550 mm

Magnet thickness: (mag_x) 32 mm

Side plate thickness: 32 mm

Magnetization direction angles: (alpha) 90°



Axis	B central, mT	B work zone edge, mT	ΔB , mT	$\Delta B/B$ central
x	138.66	138.29	-0.37	-0.3%
y	138.66	131	-7.66	-5.5%
z	138.66	139.52	0.86	0.6%

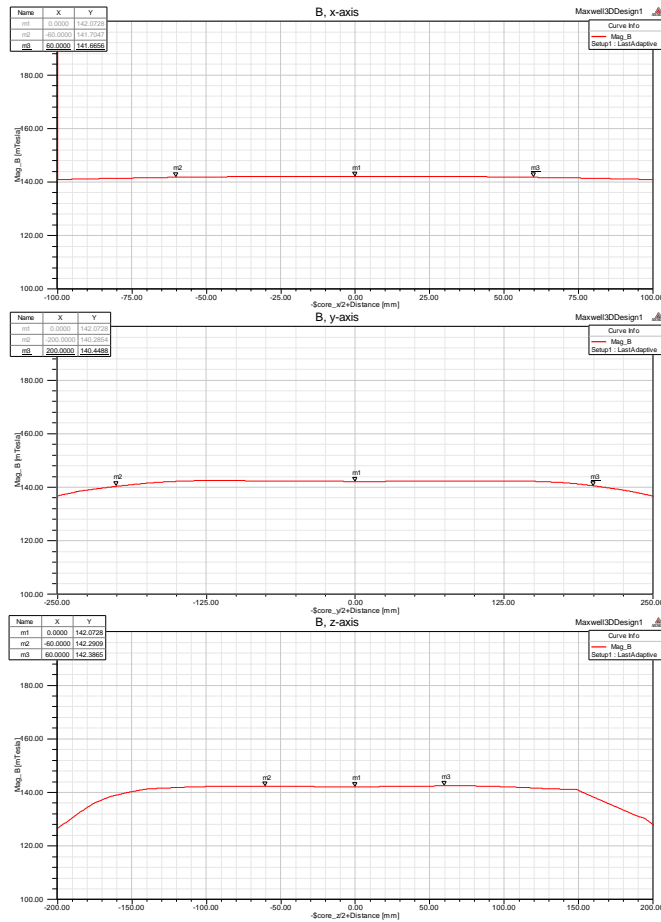
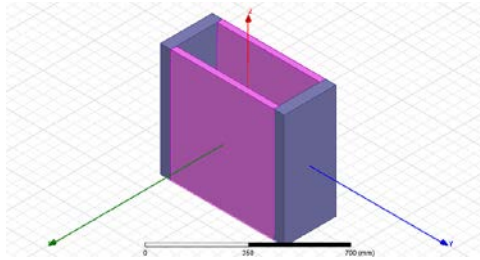
Closed path, flat plate design: Magnet 06.mxw1

Core dimensions: (core_x,core_y,core_z) 200, 500, 550 mm

Magnet thickness: (mag_x) 26 mm

Side plate thickness: 52 mm

Magnetization direction angles: (alpha) 90°



Axis	B central, mT	B work zone edge, mT	ΔB , mT	$\Delta B/B$ central
x	142.07	141.7	-0.37	-0.3%
y	142.07	140.28	-1.79	-1.3%
z	142.07	142.29	0.22	0.2%

7. Closed path, flat plate, segmented plate design: Magnet 07.mxl

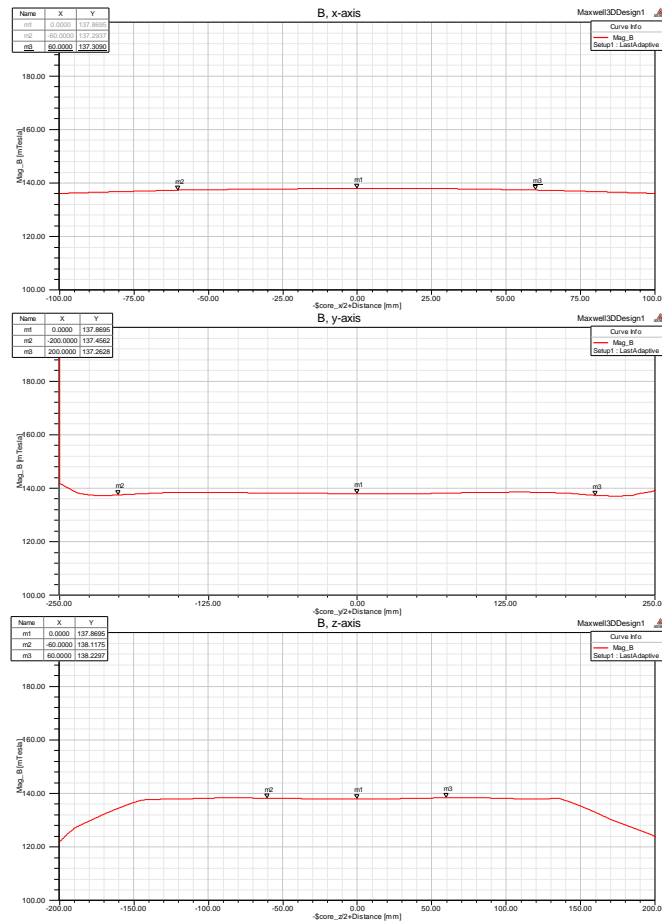
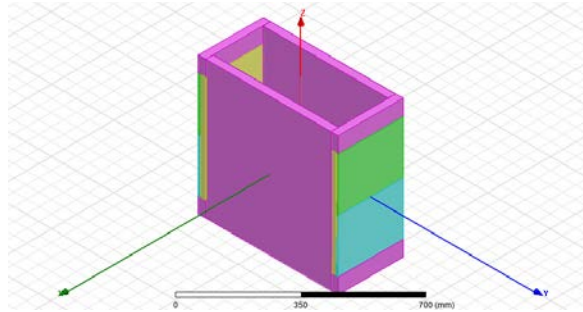
Core dimensions: (core_x,core_y,core_z) 200, 500, 550 mm

Magnet thickness: (mag_x) 30 mm

Part A, height: (part_A_z) 63 mm

Part D thickness: (part_D_x) 8 mm

Magnetization direction angles: (alpha, beta, gamma) 90°, 82°, 30°



Axis	B central, mT	B work zone edge, mT	ΔB , mT	$\Delta B/B$ central
x	137.87	137.29	-0.58	-0.4%
y	137.87	137.46	-0.41	-0.3%
z	137.87	138.12	0.25	0.2%

8. Closed path, segmented plate design: Magnet 08.mxl

Core dimensions: (core_x,core_y,core_z) 200, 500, 550 mm

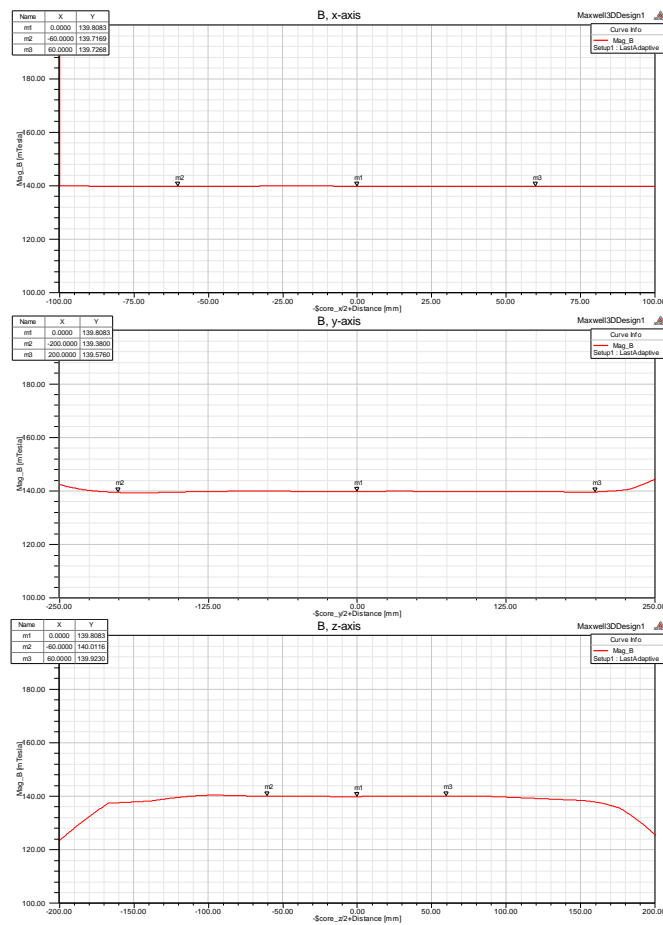
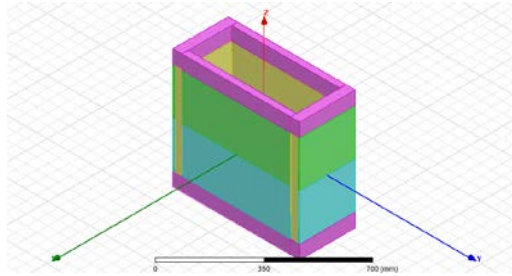
Magnet thickness: (mag_x) 28 mm

Magnet thickness: (mag_y) 42 mm

Part A, height: (part_A_z) 63 mm

Part D thickness: (part_D_x) 8 mm

Magnetization direction angles XZ-plane: (alpha, beta, gamma) 90°, 89°, 90°
Magnetization direction angles YZ-plane: (alpha, beta, gamma) 90°, 80°, 90°



Axis	B central, mT	B work zone edge, mT	ΔB , mT	$\Delta B/B$ central
x	139.8	139.71	-0.09	-0.1%
y	139.8	139.38	-0.42	-0.3%
z	139.8	140.01	0.21	0.2%

Closed path, segmented plate design: Magnet 09.mxl

Core dimensions: (core_x,core_y,core_z) 200, 500, 450 mm

Magnet thickness: (mag_x) 26 mm

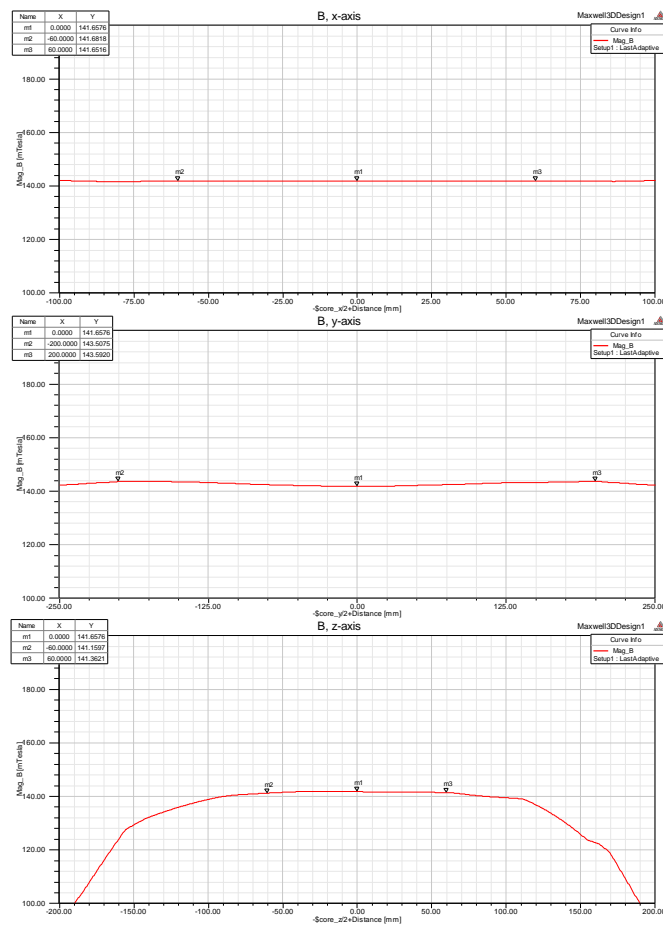
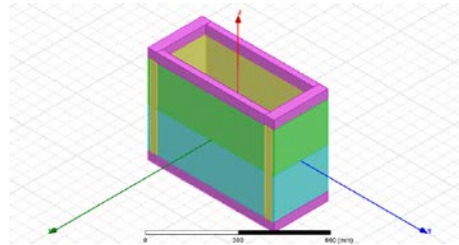
Magnet thickness: (mag_y) 42 mm

Part A, height: (part_A_z) 40 mm

Part D thickness: (part_D_x) 8 mm

Magnetization direction angles XZ-plane: (alpha, beta, gamma) 90°, 89°, 85°

Magnetization direction angles YZ-plane: (alpha, beta, gamma) 90°, 85°, 85°



Axis	B central, mT	B work zone edge, mT	ΔB , mT	$\Delta B/B$ central
x	141.66	141.68	0.02	0.0%
y	141.66	143.51	1.85	1.3%
z	141.66	141.16	-0.5	-0.4%

Other Ongoing Magnetic Material Research Projects

7.3.14 *SmCo₅-FeNi Hard-Soft Composite Magnet*

The objectives for this project were to:

- Prepare FeNi (1:1 atomic ratio) alloy by arc melting
- Heat treat and quench the alloy to obtain FeNi gamma phase
- Ball mill the as-cast and gamma-phase FeNi to obtain nano-scale powder
- Characterize the powder with XRD and M(H)

Based on recently published work of Rai (*J. Mag. and Mag. Mat.* 344, 2013, 211-216) an attempt has been made to produce a two-phase composite magnet using SmCo₅ as hard and FeNi as soft phases via high energy ball milling process. As a first step series of FeNi samples were prepared by arc melting and heat treated to achieve gamma-FeNi phase at room temperature. Treated samples were characterized by XRD for phase purity and SEM (on-going) for investigation of the heat treatment effect on FeNi microstructure.

7.3.14.1 *Results and Discussion*

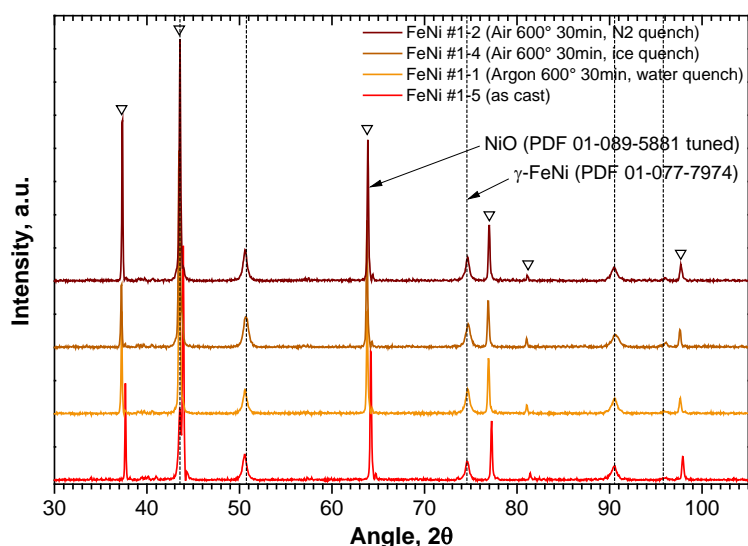
Starting materials: Fe granulas (Alfa Aesar, 99.98%), Ni slugs (Alfa Aesar, 99.995%). Alloy composition: Fe:Ni 1:1 atomic ratio. Each sample was melted in MAM Arcmelter, turned over and remelted two times.

Sample name	Fe, g	Ni, g	Total mass, g	Atomic ratio	Mass after melting, g	Mass loss, %
FeNi 1-1	0.7814	0.8211	1.6025	1.000213	1.5994	-0.19
FeNi 1-2	0.5888	0.6181	1.2069	1.001207	1.2066	-0.02
FeNi 1-3	0.9766	1.0262	2.0028	1.00023	1.9972	-0.27
FeNi 1-4	0.7807	0.8196	1.6003	1.001145	1.609	0.54
FeNi 1-5	0.5854	0.615	1.2004	1.000443	1.2037	0.27
FeNi 1-6	0.9799	1.0293	2.0092	1.000587	2.0092	0

Samples were heat treated at 600 °C for 30 min in a tube furnace using flowing Argon or in Air. After treatment samples were quenched to RT in water, ice or liquid N₂. The idea of treatment + quenching is to stabilize gamma-FeNi phase at room temperature.

Sample name	Anneal temperature	Atmosphere	Dwell time	Quenching method
FeNi 1-1	600°C	Argon	30 min	RT water
FeNi 1-2	600°C	Air	30 min	Iced water
FeNi 1-4	600°C	Air	30 min	Liquid N ₂
FeNi 1-5	As-cast, untreated, for comparison			

Instrument – Bruker Discovery D8, Cu k-alpha, 2 theta = 20-105°, step 0.05°, step time 3 sec. All alloy samples (both as-cast and heat treated) developed gamma-FeNi phase, no residual Fe or Ni were detected (see Fig). In addition to FeNi, a NiO phase was detected – it was assumed that NiO passivation thin film formed on the ingot surface.



7.4 References

- [1] P. G. McCormick, J. Ding, E. H. Feutrill and R. Street, "Mechanically alloyed hard magnetic materials," *J. Magn. Magn. Mater.*, Vols. 157-158, pp. 7-10, May 1996.
- [2] M. Chakka, B. Altuncevahir, Z. Q. Jin, Y. Li and P. Liu, "Magnetic nanoparticles produced by surfactant-assisted ball milling," *J. Appl. Phys.*, vol. 99, p. 08E912, Apr. 2006.
- [3] Y. Wang, Y. Li, C. Rong and J. P. Liu, "Sm–Co hard magnetic nanoparticles prepared by surfactant-assisted ball milling," *Nanotechnology*, vol. 18, p. 465701, Oct. 2007.
- [4] B. Z. Cui, A. M. Gabay, W. F. Li, M. Marinescu, J. F. Liu and G. C. Hadjipanayis, "Anisotropic SmCo₅ nanoflakes by surfactant-assisted high energy ball milling," *J. Appl. Phys.*, vol. 107, p. 09A721, Apr. 2010.
- [5] Y. Shen, M. Q. Huang, A. K. Higgins, S. Liu, J. C. Horwath and C. H. Chen, "Preparation of PrCo₅ bulk magnets using nanograin powders made by surfactant-assisted high energy milling," *J. Appl. Phys.*, vol. 107, p. 09A722, Apr. 2010.
- [6] B. Z. Cui, W. F. Li and G. C. Hadjipanayis, "Formation of SmCo₅ single-crystal submicron flakes and textured polycrystalline nanoflakes," *Acta Mater.*, vol. 59, pp. 563-571, Jan. 2011.
- [7] S. J. Knutson, Y. Shen, J. C. Horwath, P. Barnes and C. H. Chen, "The effect of flake thickness on anisotropic SmCo₅ nanoflakes/submicron-flakes with high energy product," *J. Appl. Phys.*, vol. 109, p. 07A762, Apr. 2011.
- [8] C. Suryanarayana, "Mechanical alloying and milling," *Prog. Mater. Sci.*, vol. 46, pp. 1-184, Jan. 2001.

- [9] L. Zheng, A. M. Gabay, W. Li, B. Cui and G. C. Hadjipanayis, "Influence of the type of surfactant and hot compaction on the magnetic properties of SmCo_5 nanoflakes," *J. Appl. Phys.*, vol. 109, p. 07A721, Apr. 2011.
- [10] C. A. Crouse, E. Michel, Y. Shen, S. J. Knutson, B. K. Hardenstein, J. E. Spowart, S. O. Leontsev, S. L. Semiatin, J. C. Horwath and Z. Turgut, "Effect of surfactant molecular weight on particle morphology of SmCo_5 prepared by high energy ball milling," *J. Appl. Phys.*, vol. 111, p. 07A724, Mar. 2012.
- [11] L. Zheng, B. Cui, N. G. Akdogan, W. Li and G. C. Hadjipanayis, "Influence of octanoic acid on SmCo_5 nanoflakes prepared by surfactant-assisted high-energy ball milling," *J. Alloy Compd.*, vol. 504, pp. 391-394, Aug. 2010.
- [12] P. Saravanan, A. N. Sharma and V. Chandrasekaran, "Highly anisotropic resin-bonded magnets processed with surfactant-coated SmCo_5 nanocrystalline powders," *J. Magn. Magn. Mater.*, vol. 321, pp. 3138-3143, Oct. 2009.
- [13] S. Liu, D. Lee, M. Q. Huang, A. Higgins, Y. Shen, Y. S. He and C. Chen, "Research and development of bulk anisotropic nanograin composite rare earth permanent magnets," *J. Iron Steel Res. Int.*, vol. 13, pp. 123-135, Aug. 2006.
- [14] E. Karapetrova, G. Ice, J. Tischler, H. Hong and P. Zschack, "Design and performance of the 33-BM beamline at the advanced Photon Source," *Nuclear Instruments and Methods in Physics Research A*, vol. 649, p. 52, Sept. 2011.
- [15] P. Sarin, R. P. Haggerty, W. Yoon, M. Knapp, A. Berghaeuser, P. Zschack, E. Karapetrova, N. Yang and W. M. Kriven, "A curved image-plate detector system for high-resolution synchrotron X-ray diffraction," *J. Synchrotron Rad.*, vol. 16, p. 273, Jan. 2009.
- [16] C. H. Chen, S. J. Knutson, Y. Shen, R. A. Wheeler, J. C. Horwath and P. N. Barnes, "The effect of particle size on coercivity and crystallinity of SmCo_5 ," *Appl. Phys. Lett.*, vol. 99, p. 012504, Jul. 2011.
- [17] E. Kneller, "Magnetism and Metallurgy," Academic Press, New York, p. 366, 1969
- [18] H. Zijlstra, "Domain wall processes in SmCo_5 powders," *J. Appl. Phys.*, vol. 41, p. 4881, Nov. 1970.
- [19] E. M. Kirkpatrick, S. A. Majetich and M. E. McHenry, "Magnetic properties of single domain samarium cobalt nanoparticles," *IEEE Trans. Mag.*, vol. 32, p. 4502, Sept. 1996.
- [20] J. Zhang, S. Zhang, H. Zhang and B. Shen, "Structure, magnetic properties, and coercivity mechanism of nanocomposite $\text{SmCo}_5/\alpha\text{-Fe}$ magnets prepared by mechanical milling," *J. Appl. Phys.*, vol. 89, p. 5601, Feb. 2001.
- [21] P. Scherrer, vol. 26, *Nachr Ges Wiss Gott*, 1918, p. 98.
- [22] B. L. Henke, E. M. Gullikson and J. C. Davis, "X-ray interactions: photoabsorption, scattering, transmission, and reflection at $E=50\text{-}30000\text{ eV}$, $Z=1\text{-}92$," *Data and Nuclear Data Tables*, vol. 54, pp. 181-342, Jul. 1993.

List of Acronyms, Abbreviations and Symbols

AC – Alternating current	MPCVD – Microwave plasma chemical vapor deposition
AFM – Atomic force microscopy	MRI – Magnetic resonance imaging
ALD – Atomic layer deposition	MWCNT – Multi-walled carbon nanotube
α – Thermal diffusivity or Seebeck coefficient	PECVD – Plasma enhanced chemical vapor deposition
B – Magnetic flux density	PF – Power factor
BPR – Ball weight ratio	PFSI – Power Factor Screening Instrument
CF – Correction factor	PLD – Pulsed laser deposition
CNT – Carbon nanotube	PPMS – Physical property measurement system
CVD – Chemical vapor deposition	RABiTS TM – Rolling-assisted-biaxially-textured substrate
C _p – Heat capacity	RHEED – Reflection high-energy electron deflection
DM-HP – Dry high energy ball milling – hot pressing	ρ – density or electrical resistivity
DOA – Degree of anisotropy	rpm – rotations per minute
DSC – Differential scanning calorimetry	SAM – Spin around magnet
EDS – Energy dispersive spectroscopy	sccm – Standard cubic centimeters
FCCVD – Floating catalyst chemical vapor deposition	SEM – Scanning electron microscopy
FET – Field-effect transistor	SIMS – Secondary ion mass spectrometry
FFT – Fast Fourier transform	SMES – Superconducting magnet energy storage
F _p – Flux pinning force	STEM – Scanning transmission electron microscopy
F _{pmax} – Flux pinning force maxima	T – Temperature
FWHM – Full width half maximum	T – Tesla
GB – Grain boundary	T _c – Critical transition temperature
H – Magnetic field	TEM – Transmission electron microscopy
HAADF – High angle annular dark field	THCVD – Thermal chemical vapor deposition
HDMS – Hexamethyldisilazane	θ – Bragg angle
HEBM – High energy ball milling	TIM – Thermal interface material
HTS – High temperature superconductor	TTO – Thermal transport option
Hz – Hertz	VA-CNT – Vertically-aligned carbon nanotube
IBAD – Ion-beam assisted deposition	vdP – van der Pauw
I _c – Critical current	VSM – Vibrating sample magnetometer
J _c – Critical current density	XRD – X-ray diffraction
J _{ct} – Transport critical current density	XPS – X-ray photoelectron spectroscopy
J _e – Engineering critical current density	YS – Yield strength
KrF – Krypton-fluoride excimer laser	YSZ – Ytria-stabilized zirconia
λ – Wavelength	zT – Thermoelectric figure-of-merit
LHe – Liquid helium	
LN ₂ – Liquid nitrogen	
LOX – Liquid oxygen	
MOCVD – Metal-organic chemical vapor deposition	
MOD – Metal-organic deposition	